AD-A244 899

FINAL TECHNICAL REPORT

15 July 90 — 14 Jan 91

MOLECULAR OPTICS
Nonlinear Optical Processes in
Organic and Polymeric Crystals and Films

PART II

Principal Investigator   Prof. A.F. Garito

Program Manager   Dr. Charles Lee

92-01059

REPORT DOCUMENTATION PAGE

1. AGENCY USE ONLY	2. REPORT DATE	3. REPORT TYPE AND DATES COVERED
	November 1991	Final Report 7/15/88 - 7/14/91

4. TITLE AND SUBTITLE	5. FUNDING NUMBERS
Molecular Optics: Nonlinear Optical Processes in Organic and Polymeric Crystals and Films **PT. II**	61102F 2303/A3 61101E 4989/08

6. AUTHOR(S)

A. F. Garito

7. PERFORMING ORGANIZATION NAME(S) AND ADDRESS(ES)	8. PERFORMING ORGANIZATION REPORT NUMBER
University of Pennsylvania Department of Physics Philadelphia, PA 19104	

9. SPONSORING MONITORING AGENCY NAME(S) AND ADDRESS(ES)	10. SPONSORING MONITORING AGENCY REPORT
AFOSR/NC Bolling AFB, DC 20332-6448	F49620-88-C-0127

11. SUPPLEMENTARY NOTES

12a. DISTRIBUTION AVAILABILITY STATEMENT	12b. DISTRIBUTION
Approved for public release; distribution is unlimited	

13. ABSTRACT *(Maximum 200 words)*

See Back

14. SUBJECT TERMS	15. NUMBER OF PAGES 520
	16. PRICE

17. SECURITY CLASSIFICATION OF REPORT	18. SECURITY CLASSIFICATION OF THIS PAGE	19. SECURITY CLASSIFICATION OF ABSTRACT	20. LIMITATION
UNCLASSIFIED	UNCLASSIFIED	UNCLASSIFIED	SAR

Optical bistability is a quantum optical realization of a first order phase transition far from equilibrium. A nonlinear optical material contained in an optical cavity driven resonantly by an external coherent optical field undergoes a first order phase transition to a new nonequilibrium stationary state of broken symmetry. Resonant and nonresonant nonlinear optical response of pi-electron excitations in conjugated electronic structure provides the nonlinearity essential to the onset of bistability. Electronic correlation effects in reduced dimensions are responsible for nonresonant nonlinear optical responses. Saturable absorption studies of glassy polymer films consisting of quasi-two dimensional conjugated disc-like structure of silicon naph-thalocyanine demonstrate that on-resonance the system behaves as an optical Bloch system with an intensity dependent refractive index of 1×10^{-10} cm^2/kW. Based on the results of these studies, electronic absorptive optical bistability is observed on a nanosecond time scale in a nonlinear Fabry-Perot interferometer employing the saturable absorbing silicon naphthalocyanine film as the nonlinear optical medium.

PART II
ELECTRON CORRELATION THEORY AND EXPERIMENTAL MEASUREMENTS OF THE THIRD ORDER NONLINEAR OPTICAL PROPERTIES OF CONJUGATED LINEAR CHAINS

ABSTRACT

ELECTRON CORRELATION THEORY AND EXPERIMENTAL MEASUREMENTS OF THE THIRD ORDER NONLINEAR OPTICAL PROPERTIES OF CONJUGATED LINEAR CHAINS

Comprehensive theoretical and experimental studies of the magnitude, sign, dispersion, and length dependence of the third order molecular susceptibility $\gamma_{ijkl}(-\omega_4;\omega_1,\omega_2,\omega_3)$ demonstrate that the microscopic origin of the nonresonant third order nonlinear optical properties of conjugated linear chains is determined by the effects of electron correlation due to electron-electron repulsion. Multiple-excited configuration interaction calculations of $\gamma_{ijkl}(-\omega_4;\omega_1,\omega_2,\omega_3)$ for the archetypal class of quasi-one dimensional conjugated structures known as polyenes reveal for the first time the principal role of strongly correlated, energetically high-lying, two photon ^1A_g virtual states in the largest of the two dominant, competing virtual excitation processes that determine $\gamma_{ijkl}(-\omega_4;\omega_1,\omega_2,\omega_3)$. It is also found in studies of the effects of conformation on $\gamma_{ijkl}(-\omega_4;\omega_1,\omega_2,\omega_3)$ that the origin of the third order optical properties remains basically the same for the all-*trans* and *cis-transoid* polyenes, and the results for the two conformations are unified by a common power law dependence of the dominant tensor

i

component $\gamma_{xxxx}(-\omega_4;\omega_1,\omega_2,\omega_3)$ on the physical end-to-end length L of the chain with an exponent of 3.5. Calculations for a noncentrosymmetric conjugated chain demonstrate that virtual excitation processes involving diagonal transition moments that are forbidden in centrosymmetric structures lead to a more than an order of magnitude enhancement in $\gamma_{xxxx}(-\omega_4;\omega_1,\omega_2,\omega_3)$ compared to the analog centrosymmetric structure. Experimental measurements of the dispersion in the isotropically averaged dc-induced second harmonic susceptibility $<\gamma(-2\omega;\omega,\omega,0)>$ and third harmonic susceptibility $<\gamma(-3\omega;\omega,\omega,\omega)>$ in two important polyene structures confirm the electron correlation description of $\gamma_{ijkl}(-\omega_4;\omega_1,\omega_2,\omega_3)$. The measured values of $<\gamma(-2\omega;\omega,\omega,0)>$ and $<\gamma(-3\omega;\omega,\omega,\omega)>$ at several near infrared fundamental wavelengths for hexatriene, the $N = 6$ carbon site polyene chain, are in excellent agreement with the calculated magnitude, sign, and dispersion. Corresponding measurements for β-carotene, a substituted $N = 22$ polyene chain, together with the results for hexatriene, also verify the calculated power law dependence of $<\gamma(-\omega_4;\omega_1,\omega_2,\omega_3)>$ on L. It was further found in the course of the experimental measurements that the common reference standard for the macroscopic susceptibility $\chi^{(3)}(-3\omega;\omega,\omega,\omega)$ is too large by a factor of 2.0, and an improved standard value is proposed.

TABLE OF CONTENTS

LIST OF TABLES

Chapter 3

:

LIST OF FIGURES

Chapter 3

Chapter 4

Chapter 5

:

Chapter 1

INTRODUCTION

The delocalized, one-dimensional π-electron system of organic conjugated linear chains provides this unique class of materials with novel nonlinear optical and electronic properties.[1-5] However, because the repulsive Coulomb interaction between electrons requires that an exact solution of the electronic structure involves many-electron wavefunctions, the ground state and electronic excitations of conjugated chains have remained not fully understood. Although many approximate theoretical descriptions have been presented that either neglect entirely the electron-electron interaction or treat it in a mean-field theory, there is increasing evidence that electron correlation effects and the many-body nature of the wavefunctions are essential to a complete understanding of the optical and electronic properties of π-electron systems. In fact, it has been clearly and unambiguously established that electron correlation is responsible for the ordering of the low-lying electronic excitations of the short and intermediate length conjugated chains known as polyenes.[6] In this report, the nonresonant nonlinear optical properties of conjugated linear chains are demonstrated to be determined by electron correlation;[7,8] and, in turn, nonlinear optical experiments provide highly sensitive measurements and tests of electron correlation effects on electronic structure. Through a series of combined experimental and theoretical studies of the nonresonant molecular third order susceptibility $\gamma_{ijkl}(-\omega_4;\omega_1,\omega_2,\omega_3)$ of finite linear chains, we demonstrate the essential role of electron-electron interactions in the microscopic origin of the nonlinear optical

1

responses of conjugated structures and achieve agreement between experiment and theory for the magnitude, sign, dispersion, and length dependence of $\gamma_{ijkl}(-\omega_4;\omega_1,\omega_2,\omega_3)$ in quasi-one dimensional systems for the first time.

The large, nonresonant third order nonlinear optical susceptibility of one dimensional conjugated chains is illustrated, for example, by third harmonic generation (THG) measurements of crystalline polydiacetylene TCDU (specified by the side group $R = (CH_2)_4OCONHC_6H_5$) which yielded a macroscopic susceptibility $\chi^{(3)}_{1111}(-3\omega;\omega,\omega,\omega) = 7 \times 10^{-11}$ esu for a fundamental wavelength $\lambda = 1.89$ µm.[9] For $\lambda = 2.62$ µm, such that the third harmonic light at 0.89 µm is still further from the optical absorption peak at 0.56 µm and dispersive effects are less important, the measured susceptibility is only slightly reduced to $\chi^{(3)}_{1111}(-3\omega;\omega,\omega,\omega) = 3.7 \times 10^{-11}$ esu. In a separate comparative study of THG in saturated and conjugated linear chains, it was shown that although the saturated alkane chains exhibit a linear dependence of the isotropically averaged molecular susceptibility $<\gamma(-3\omega;\omega,\omega,\omega)>$ on the length of the chain, $<\gamma(-3\omega;\omega,\omega,\omega)>$ of conjugated linear chains increases in a dramatic supralinear fashion due to the delocalized π-electron system.[10]

The nonresonant nonlinear optical response of conjugated chains has also been demonstrated in a number of studies to occur on ultrafast timescales. Thin films of bis (p-toluene sulfonate) polydiactylene (PTS), for example, were studied by degenerate four wave mixing (DFWM) in which two incident laser pulses form a refractive index grating from which a third (probe) pulse scatters.[11] The decay of the induced grating is a measure of the inherent response time of the nonlinear optical process and can be

2

determined by the scattered light intensity as a function of the temporal delay between the coincident grating-forming pulses and the probe pulse. For laser pulses with 300 femtosecond (fs) temporal width at $\lambda = 652$ nm, just within the onset of the film's optical absorption, the scattered light intensity was found to decay with a lifetime of 1.8 picoseconds (ps). A transient saturable absorption measurement at the same wavelength yielded an excited state lifetime of 2.0 ps and provided verification that the grating measured in this resonant DFWM experiment was due to population of excited electronic states. Most importantly, a DFWM measurement for a wavelength outside the optical absorption ($\lambda = 723$ nm), demonstrated that the nonresonant response time was shorter than the 300 fs pulse width as evidenced by the existence of a scattered signal only when all three pulses were temporally overlapped within the film. Thus, the nonresonant grating induced strictly in the electronic polarization, and not in the excited state population, responds on at least the femtosecond timescale.

One of the earliest evidences of the importance of electron correlation effects in conjugated structures derives from the observation that the first excited state in polyenes is, in fact, the low-lying, two-photon 2^1A_g state.[6] Prior to this discovery, it was believed that the lowest-lying electronic excitation was the large oscillator strength $1^1B_u \leftarrow 1^1A_g$ one-photon transition. The increased oscillator strength and decreased excitation energy of this transition with increased chain length are well-described by one-electron theory that treats the electrons as independent particles. There were, however, a few irreconcilable spectroscopic puzzles. First, the experimentally observed intrinsic fluorescence lifetimes of polyenes are at least an order of magnitude larger than

3

the values obtained by standard analysis of the 1^1B_u absorption band.[12,13] Second, there is a significant separation between the lowest energy peak of the absorption spectrum and the highest energy peak of the fluorescence spectrum. Ordinarily, one would expect these spectra to share a common origin and be mirror images of one another. Finally, the absorption spectrum exhibits a much stronger dielectric shift in polar media than the fluorescence spectrum.

The observation by Hudson and Kohler of a weak, symmetry-forbidden absorption below the $1^1B_u \leftarrow 1^1A_g$ transition in the eight site chain case of all-*trans*-1,8-diphenyloctatetraene resolved these apparent paradoxes.[14] Below the 1^1B_u state lies a state that possesses the same symmetry as the 1^1A_g ground state and is therefore denoted the 2^1A_g state. Schulten and Karplus demonstrated that inclusion of electron correlation by multiple-excited configuration interaction within the Pariser-Parr-Pople (PPP) π-electron Hamiltonian does, in fact, yield a strongly correlated two-photon 2^1A_g state at lower energy than the one-photon allowed 1^1B_u state.[15] Subsequent experimental and theoretical work over the years has clearly shown that the existence of a low-lying, strongly correlated 2^1A_g state is a general feature of all unsubstituted polyenes with number of carbon sites N larger than six.[6,16-20]

In spite of the clear evidence of electron correlation in finite polyenes, the electronic structure of infinite chain conjugated polymers has often been considered within the context of tight-binding[21] or Fermi-liquid models.[22] These theories, which concentrate on the electron-phonon coupling and neglect the electron-electron interaction, have been moderately successful in the interpretation of experimental data

4

from transient optical absorption to resonant Raman scattering to charge transport.[23] Initial mean-field studies of electron-electron interaction within these models concluded that since the on-site Coulomb repulsion tended to destroy the experimentally observed dimerized bonding structure, or bond order wave, of the polymer chain, conjugated polymers must fall in the weak interaction limit.[24] However, less approximate theoretical studies employing Monte Carlo,[25] valence bond,[26] variational,[27] and renormalization group[28] methods have found that the effect of on-site Coulomb repulsion is, in fact, to increase the dimerization amplitude for small and intermediate strengths of the electron-electron interaction. These conclusions remain valid even when off-diagonal interactions in the site representation are included in the Hamiltonian,[29] and it may therefore be concluded that the electron-electron interaction should not be considered to be weak on the basis of the known dimerization of the polymer and that it can, instead, significantly affect the electronic and optical properties of the system.

In light of the above discussion, it is clear that a thorough analysis of the effects of electron correlation on the nonlinear optical properties of conjugated linear chains is necessary to a fundamental understanding of these properties. Although many theoretical studies of the third order susceptibility $\gamma_{ijkl}(-\omega_4;\omega_1,\omega_2,\omega_3)$ of linear polyenes have been published, prior to the work presented in this report,[7,8,30,31] none of them considered electron correlation effects. The independent particle models previously employed include the free-electron model,[32] undimerized[33] and dimerized[34] Huckel models, single-excited configuration interaction of the PPP Hamiltonian,[35] coupled

5

SCF perturbation theory of the CNDO molecular orbital method,[36] perturbative density matrix treatment of the PPP Hamiltonian,[37] and *ab initio* coupled-perturbed Hartree-Fock theory.[38] We present here results from multiple-excited configuration interaction theory applied to a self-consistent-field molecular orbital method that, for the first time, explicitly accounts for the electron-electron interaction and electron correlation. Through examination of the individual third order virtual excitation processes that contribute to $\gamma_{ijkl}(-\omega_4;\omega_1,\omega_2,\omega_3)$, we demonstrate that electron correlation plays a dominant role in the nonlinear optical properties of conjugated linear chains. In particular, virtual transitions that involve previously unexpected, strongly correlated, high-lying, two-photon states are essential in the determination of the magnitude, sign, and dispersion of $\gamma_{ijkl}(-\omega_4;\omega_1,\omega_2,\omega_3)$ in linear polyenes. Our conclusions concerning the importance of electron correlation effects to the nonlinear optical properties of conjugated structures have received subsequent, independent confirmation by exact diagrammatic valence bond theory of the more approximate PPP Hamiltonian[39] and by multiple-excited configuration interaction of the INDO molecular orbital method.[40]

This report presents the electron correlation description of the microscopic origin of third order optical responses in conjugated linear chains and experimental dispersion measurements of dc-induced second harmonic generation (DCSHG) and third harmonic generation (THG) for two important molecular structures that quantitatively verify some of the key theoretical results. In Chapter 2, we describe the theoretical methods employed in the calculation of $\gamma_{ijkl}(-\omega_4;\omega_1,\omega_2,\omega_3)$. Section B presents the Method of Averages technique of time-dependent perturbation theory that expresses

6

excitation energies of the eigenstates of the molecular Hamiltonian. The electron

correlation theory of multiple-excited configuration interactions applied to the self-

consistent-field molecular orbital method that we employ to calculate the ground state

and π-electron excited state electronic wavefunctions of conjugated structures is

reviewed in section C.

Chapter 3 presents the results obtained for calculations of $\gamma_{ijkl}(-\omega_4;\omega_1,\omega_2,\omega_3)$

for all-*trans* polyenes that range in number of carbon atom sites from $N = 4$ to 16. In

short chains, the magnitude, sign, and dispersion of $\gamma_{ijkl}(-\omega_4;\omega_1,\omega_2,\omega_3)$ is found to be

determined by just two competing third order virtual excitation processes. The smaller,

negative contribution involves only the ground state and the large oscillator strength

1^1B_u state. A surprising, larger, positive term additionally involves a high-lying two-

photon ^1A_g state that is highly correlated and couples strongly to the 1^1B_u state. The

dominant tensor component $\gamma_{xxxx}(-\omega_4;\omega_1,\omega_2,\omega_3)$ is found to have a power law

dependence on N with an exponent of 3.9 that therefore leads to very large nonresonant

susceptibilities for intermediate length chains.

The effects of two basic structural alterations to all-*trans* polyenes are considered

in Chapter 4. In section B, we discuss an alternate structural conformation known as

the *cis-transoid* conformation. The results are in direct analogy to those of the all-*trans*

chains with the exception that, for a given N, $\gamma_{xxxx}(-\omega_4;\omega_1,\omega_2,\omega_3)$ is smaller in the *cis-

transoid* conformation. This is understood in terms of the reduced physical length L of

the chain along the conjugation axis in the *cis-transoid* conformation, and the results are

unified by a common power law dependence of $\gamma_{xxxx}(-\omega_4;\omega_1,\omega_2,\omega_3)$ on L with an

exponent of 3.5. Section C describes results for a noncentrosymmetric polyene in which the symmetry is lowered by heteroatomic substitution on the ends of the chain. The introduction of nonzero diagonal elements to the transition moment matrix (*e.g.* ground and excited state dipole moments) is found to enhance $\gamma_{xxxx}(-\omega_4;\omega_1,\omega_2,\omega_3)$ by more than an order of magnitude.

Chapter 5 presents dispersion measurements of DCSHG in hexatriene (HT), the $N = 6$ polyene, and β-carotene, which corresponds to an $N = 22$ polyene; and similar dispersion measurements for THG in these two molecular structures are discussed in Chapter 6. For HT, the experimental magnitude and dispersion of $<\gamma(-2\omega;\omega,\omega,0)>$ and $<\gamma(-3\omega;\omega,\omega,\omega)>$, the isotropically averaged susceptibilities for DCSHG and THG, respectively, are in good agreement with the theoretical results that are discussed in extensive detail in Chapters 3 and 4. Although β-carotene is a longer molecule than can currently be computationally considered, the experimental nonresonant value of $<\gamma(-\omega_4;\omega_1,\omega_2,\omega_3)>$ for β-carotene is in excellent agreement with extrapolation of the theoretical power law chain length dependence providing additional verification of the theoretical results. As a separate issue, by comparison of the DCSHG and THG results we have found that the values for $\chi^{(3)}(-3\omega;\omega,\omega,\omega)$ of quartz and glass that are commonly used as the reference standards for THG measurements of thin films and liquids are too large by a factor of 2.0. $\chi^{(3)}(-3\omega;\omega,\omega,\omega)$ reference standards are discussed in section E of Chapter 6.

8

Chapter 1 References

1. *Nonlinear Optical Properties of Organic and Polymeric Materials*, D.J. Williams, ed., ACS Symp. Series, Vol. 233 (American Chemical Society, Washington, D.C., 1983).

2. *Nonlinear Optical Properties of Polymers*, A.J. Heeger, D. Ulrich, and J. Orenstein, eds. (Mater. Res. Soc. Proc. 109, Pittsburgh, PA, 1988).

3. *Nonlinear Optical Properties of Organic Materials*, G. Khanarian, ed.(Proc. SPIE 971, 1989).

4. *Organic Materials for Nonlinear Optics*, R. A. Hann and D. Bloor, eds. (Royal Soc. of Chem., London, 1989).

5. *Nonlinear Optical Effects in Organic Polymers*, J. Messier *et al.*, eds., NATO ASI Ser. E, Vol. 162 (Kluwer Academic, Boston, 1989).

6. See, for example, B. S. Hudson, B. E. Kohler, and K. Schulten, in *Excited States*, Vol. 6, E. C. Lim, ed. (Academic, New York, 1982); and references therein.

7. J. R. Heflin, K. Y. Wong, O. Zamani-Khamiri and A. F. Garito, Phys. Rev. B38, 1573 (1988); Mol. Cryst. Liq. Cryst. 160, 37 (1988).

8. A. F. Garito, J. R. Heflin, K. Y. Wong, and O. Zamani-Khamiri, in ref. 2, pp. 91 - 102.

9. C. Sauteret *et al.*, Phys. Rev. Lett. 36, 956 (1976).

10. J. P. Herrmann and J. Ducuing, J. Appl. Phys. 45, 5100 (1974).

11. G. M. Carter, J. V. Hryniewicz, M. K. Thakur, Y. J. Chen, and S. E. Meyler, Appl. Phys. Lett. **49**, 998 (1986).

12. S. J. Strickler and R. A. Berg, J. Chem. Phys. **37**, 814 (1962).

13. J. B. Birks and D. J. Dyson, Proc. R. Soc. Lond. A **275**, 135 (1963).

14. B. S. Hudson and B. E. Kohler, Chem. Phys. Lett. **14**, 299 (1972); J. Chem. Phys. **59**, 4984 (1973).

15. K. Schulten and M. Karplus, Chem. Phys. Lett. **15**, 15, 305 (1972).

16. B. S. Hudson and B. E. Kohler, Synth. Metals **9**, 241 (1984).

17. K. Schulten, I. Ohmine, and M. Karplus, J. Chem. Phys. **64**, 4422 (1976).

18. Z. G. Soos and S. Ramasesha, Phys. Rev. **B29**, 5410 (1984).

19. P. Tavan and K. Schulten, J. Chem. Phys. **85**, 6602 (1986).

20. P. Tavan and K. Schulten, Phys. Rev. **B36**, 4337 (1987).

21. W. P. Su, J. R. Scrieffer, and A. J. Heeger, Phys. Rev. **B22**, 2099 (1980).

22. M. Takayama, Y. R. Lin-Liu, and K. Maki, Phys. Rev. **B21**, 2388 (1980).

23. A. J. Heeger, S. Kivelson, J. R. Scrieffer, and W. P. Su, Rev. Mod. Phys. **60**, 781 (1988).

24. S. Kivelson and D. E. Heim, Phys. Rev. **B26**, 4278 (1982).

25. J. E. Hirsch, Phys. Rev. Lett. **51**, 296 (1983).

26. S. Mazumdar and S. N. Dixit, Phys. Rev. Lett. **51**, 292 (1983).

27. D. Baeriswyl and K. Maki, Phys. Rev. **B31**, 6633 (1985).

28. G. W. Hayden and E. J. Mele, Phys. Rev. **B32**, 6527 (1985).

29. D. K. Campbell, J. T. Gammel, E. K. Loh, Jr., Phys. Rev. **B38**, 12043

(1988).

30. A. F. Garito, J. R. Heflin, K. Y. Wong, and O. Zamani-Khamiri, in *Organic Materials for Nonlinear Optics*, R. A. Hann and D. Bloor, eds. (Royal Soc. of Chem., London, 1989) pp.16-27; Proc. SPIE Vol. **971**, 9 (1989); and in *Photoresponsive Materials*, S. Tazuke, ed. (Mat. Res. Soc. Proc. IMAM-12, Pittsburgh, PA, 1989) pp.3-20.

31. J. W. Wu, J. R. Heflin, R. A. Norwood, K. Y. Wong, O. Zamani-Khamiri, A. F. Garito, P. Kalyanaraman, and J. Sounik, J. Opt. Soc. Am. B**6**, 707 (1989).

32. K. C. Rustagi and J. Ducuing, Opt. Comm. **10**, 258 (1974).

33. G. P. Agrawal, C. Cojan, and C. Flytzanis, Phys. Rev. B**17**, 776 (1978).

34. D. N. Beratan, J. N. Onuchic, and J. W. Perry, J. Phys. Chem. **91**, 2696 (1987).

35. O. Zamani-Khamiri and H. F. Hameka, J. Chem. Phys.**73**, 5693 (1980).

36. M. G. Papadopolous, J. Waite, and C. A. Nicolaides, J. Chem. Phys. **77**, 2527 (1982).

37. C. P. de Melo and R. Silbey, J. Chem. Phys. **88**, 2567 (1988).

38. G. J. B. Hurst, M. Dupuis, and E. Clementi, J. Chem. Phys. **89**, 385 (1988).

39. Z. G. Soos and S. Ramasesha, Chem. Phys. Lett. **153**, 171 (1988); J. Chem. Phys. **90**, 1067 (1989).

40. B. M. Pierce, J. Chem. Phys. **91**, 791 (1989).

11

Chapter 2

METHOD FOR CALCULATION OF $\gamma_{ijkl}(-\omega_4;\omega_1,\omega_2,\omega_3)$

A. Introduction

One major motivation of this work was to provide an accurate theoretical description at the molecular level of the third order optical properties of conjugated linear chains that explicitly accounts for the effects of electron correlation. In particular, we wish to understand at the microscopic level the molecular third order susceptibility tensor $\gamma_{ijkl}(-\omega_4;\omega_1,\omega_2,\omega_3)$ which is defined through the constitutive equation

$$p_i^{\omega_4} = \gamma_{ijkl}(-\omega_4;\omega_1,\omega_2,\omega_3)\, E_j^{\omega_1}\, E_k^{\omega_2}\, E_l^{\omega_3} \tag{2.1}$$

where $p_i^{\omega_4}$ is the i-component of the molecular polarization induced at frequency ω_4 in response to the specified components of applied electric fields at frequencies ω_1, ω_2 and ω_3. By consideration of only the electric field amplitudes of the incident light, we have made the generally valid approximation that the electric dipole interaction with the molecule is much stronger than the magnetic and higher order electric interactions.

If the frequencies ω_1, ω_2, and ω_3 are degenerate at frequency ω, then $\gamma_{ijkl}(-3\omega;\omega,\omega,\omega)$ is responsible for the creation of light at 3ω through third harmonic generation (THG). Another important third order optical phenomenon is the intensity dependent refractive index that results from $\gamma_{ijkl}(-\omega;\omega,-\omega,\omega)$, where we have taken the

12

complex conjugate of one of the incident fields. Further, if in addition to the optical field at frequency ω, one applies a dc electric field, the third order process of dc-induced second harmonic generation (DCSHG) occurs via the susceptibility $\gamma_{ijkl}(-2\omega;\omega,\omega,0)$. Thus, it is clear that $\gamma_{ijkl}(-\omega_4;\omega_1,\omega_2,\omega_3)$ governs a multitude of fundamental nonlinear optical processes each determined by the condition $\omega_4 = \omega_1 + \omega_2 + \omega_3$, where each frequency ω_1, ω_2, and ω_3 may be taken as positive or negative.

Of the two principal methods for the calculation of $\gamma_{ijkl}(-\omega_4;\omega_1,\omega_2,\omega_3)$, usually referred to as the summation-over-states[1,2] and finite field[3] techniques, the summation-over-states formalism offers several advantages. Primary among these is the ability to identify specific virtual excitation processes among the eigenstates of the system that make the most significant contributions to $\gamma_{ijkl}(-\omega_4;\omega_1,\omega_2,\omega_3)$. This results from the summation-over-states respresentation of $\gamma_{ijkl}(-\omega_4;\omega_1,\omega_2,\omega_3)$ as a perturbation expansion over all possible virtual excitations. In contrast, the computationally more simple finite field technique, which involves taking derivatives of the perturbed ground state energy or dipole moment of the molecule as a function of applied field strength, yields only a final value for $\gamma_{ijkl}(-\omega_4;\omega_1,\omega_2,\omega_3)$ with no information regarding its origin. Additionally, the summation-over-states method allows one to calculate the frequency-dependence or dispersion of $\gamma_{ijkl}(-\omega_4;\omega_1,\omega_2,\omega_3)$ since it is founded in time-dependent perturbation theory while the finite field technique only calculates the zero-frequency limit $\gamma_{ijkl}(-0;0,0,0)$. A third strength of the summation-over-states method is the capability to include the many-electron nature of the molecular wavefunctions

13

through either multiple-excited configuration interactions or generalized valence bond theory.

The summation-over-states method derives its name from the expression of $\gamma_{ijkl}(-\omega_4;\omega_1,\omega_2,\omega_3)$ through summations over all eigenstates of the system of terms that involve the transition dipole moments and excitation energies of the eigenstates. The calculation of $\gamma_{ijkl}(-\omega_4;\omega_1,\omega_2,\omega_3)$ is therefore no more accurate than the values obtained for the transition moments and excitation energies of the ground and excited states of the molecule. In this thesis, we concentrate on organic conjugated linear chains, a class of molecular structures for which electron correlation effects have been demonstrated to be crucial.[4] The electronic structure of conjugated chains has been studied by a variety of theoretical methods including Huckel, Hubbard, Pariser-Parr-Pople (PPP), and all-valence electron Hartree-Fock theories such as the complete neglect of differential overlap (CNDO) molecular orbital theory. The spectroscopic parametrization of CNDO theory developed by del Bene and Jaffe[5] and modified by Lipari and Duke[6], known as CNDO/S, has been particularly successful in calculation of molecular electronic absorption spectra, and we have therefore chosen to apply the CNDO/S method with multiple-excited configuration interactions to account for electron correlation to the calculation of $\gamma_{ijkl}(-\omega_4;\omega_1,\omega_2,\omega_3)$. Section B of this chapter presents the derivation[7] of the summation-over-states expression of $\gamma_{ijkl}(-\omega_4;\omega_1,\omega_2,\omega_3)$ employing the Method of Averages developed by Bogoliubov and Mitropolsky[8] which eliminates secular divergences that otherwise occur when any subset of the applied frequencies sums to zero. In section C, we review the multiple-excited configuration interaction theory and

14

self-consistent-field molecular orbital method that allow us to calculate the transition

dipole moments and excitation energies of the π-electron molecular states taking account

of electron correlation effects by explicit inclusion of electon-electron interactions.

B. Derivation of $\gamma_{ijkl}(-\omega_4;\omega_1,\omega_2,\omega_3)$ by the Method of Averages

The Method of Averages is a perturbation technique that involves separation of

the wavefunction into slowly and rapidly varying components.[8] The slowly varying

component is responsible for the secular divergences that occur in standard perturbation

theory and leads to shifts of the energy levels while the rapidly varying component

produces the polarization induced in response to the applied fields. We start with the

unperturbed molecular Hamiltonian H_0 possessing eigenstates $|n>$ that satisfy

$$H_0 | n > \; = \hbar\omega_n | n > \; .$$ (2.2)

The time-dependent perturbation $\varepsilon H_1(t)$ leads to a total Hamiltonian

$$H(t) = H_0 + \varepsilon H_1(t)$$ (2.3)

where we will assume $\varepsilon H_1(t) = 0$ for $t \leq 0$. In particular, we consider the semi-classical

interaction of the incident radiation field with the molecule in the electric dipole

approximation such that

15

$$\varepsilon H_1(t) = -e \, \mathbf{E}(t) \cdot \mathbf{r} \qquad (2.4)$$

where $\mathbf{E}(t)$ is the optical electric field amplitude and $e\mathbf{r}$ is the molecular dipole moment operator.

For algebraic simplicity, we use a modified interaction representation with state vector $|\Phi(t)>$ defined by

$$|\Phi(t)> = \exp[iH_0 t / \hbar] \, \exp[i \int_0^t dt' <\varepsilon H_1(t')>_{gg} / \hbar] \, |\Psi(t)> \qquad (2.5)$$

where $|\Psi(t)>$ is the solution to the time-dependent Schrodinger equation

$$\frac{\partial}{\partial t} |\Psi(t)> = (i\hbar)^{-1} \, H(t) \, |\Psi(t)>. \qquad (2.6)$$

We then have

$$\frac{\partial}{\partial t} |\Phi(t)> = \varepsilon \, \bar{H}(t) \, |\Phi(t)> \qquad (2.7)$$

where

$$\bar{H}(t) = (i\hbar)^{-1} \, \exp[iH_0^\dagger t / \hbar] \, H_1(t) \, \exp[-iH_0 t / \hbar] - (i\hbar)^{-1} <H_1(t)>_{gg} \qquad (2.8)$$

with

$$<A>_{ij} \equiv <i \, | \, A \, | \, j> \qquad (2.9)$$

and the barred operator is defined by

$$\bar{A} \equiv A - \overset{\cdot}{<}A>_{gg} \qquad (2.10)$$

The molecular polarization $\mathbf{p}(t)$ is given by

$$p(t) = \langle \Psi(t) | p | \Psi(t) \rangle / \langle \Psi(t) | \Psi(t) \rangle \qquad (2.11)$$

which can be rewritten as

$$p(t) = \langle \Phi(t) | \bar{p} | \Phi(t) \rangle / \langle \Phi(t) | \Phi(t) \rangle + \langle p \rangle_{gg} \qquad (2.12)$$

where

$$\bar{p} = e^{iH_0^\dagger t/\hbar} \, p \, e^{-iH_0 t/\hbar} \qquad . \qquad (2.13)$$

We can express the perturbation Hamiltonian and resultant polarization in terms of Fourier components

$$H_1(t) = H_1^0 + \frac{1}{2} \sum_j \left[H_1^{\omega_j} e^{-i\omega_j t} + H_1^{-\omega_j} e^{i\omega_j t} \right]$$

$$p(t) = p^0 + \frac{1}{2} \sum_\sigma \left[p^{\omega_\sigma} e^{-i\omega_\sigma t} + p^{-\omega_\sigma} e^{i\omega_\sigma t} \right] \quad . \qquad (2.14)$$

We can then specify the particular $\gamma_{ijkl}(-\omega_4;\omega_1,\omega_2,\omega_3)$ of interest by choosing the ω_j corresponding to ω_1, ω_2, and ω_3 and setting $\omega_\sigma = \omega_4$.

The fundamental assumption of the Method of Averages is that the temporal behavior of $| \Phi(t) \rangle$ can be separated into rapidly and slowly varying pieces. We then make the expansion

17

$$| \Phi(t) > = [1 + \sum_{\alpha=1}^{\infty} \epsilon^{\alpha} F^{(\alpha)}] | \xi > \tag{2.15}$$

where the rapid variations are contained in $F^{(\alpha)}$ and the slowly varying part is $| \xi >$

which has temporal evolution given by

$$\frac{\partial}{\partial t} | \xi > = \sum_{\alpha=1}^{\infty} \epsilon^{\alpha} G^{(\alpha)} | \xi > . \tag{2.16}$$

Substitution of Eqs. (2.15) and (2.16) into (2.7) and expansion in powers of ϵ yields.

$$G^{(1)} + \frac{\partial}{\partial t} F^{(1)} = \bar{H}$$

$$G^{(2)} + \frac{\partial}{\partial t} F^{(2)} = \bar{H} F^{(1)} - F^{(1)} G^{(1)}$$

$$G^{(3)} + \frac{\partial}{\partial t} F^{(3)} = \bar{H} F^{(2)} - F^{(1)} G^{(2)} - F^{(2)} G^{(1)} \tag{2.17}$$

which has the general form

$$G^{(\alpha)} + \frac{\partial}{\partial t} F^{(\alpha)} = R^{(\alpha)} \tag{2.18}$$

where $R^{(\alpha)}$ involves only the Hamiltonian and functions of lower order than α. The

utility of the Method of Averages lies in our ability to assign particular matrix elements

18

$< R^{(\alpha)} >_{mn}$ to either $G^{(\alpha)}$ or $F^{(\alpha)}$. If we assume that no excited states achieve significant

population, for which the formal requirement is

$$\frac{< F^{(\alpha)} >_{ng}}{< F^{(\alpha-1)} >_{mg}} = \frac{2 < \bar{H}_1 >_{nm}}{\hbar \Gamma_n} \ll 1 \qquad (2.19)$$

where Γ_n is the inverse radiative lifetime of state $\mid n >$, then the only terms we wish to

assign to $G^{(\alpha)}$ are the secular terms in which some combination of frequencies

$\omega_1 + \omega_2 + ... = 0$, where ω_1, ω_2, ... are the frequencies involved in the perturbation

Hamiltonian.[7] All diagonal terms of $R^{(\alpha)}$ would then diverge if assigned to $F^{(\alpha)}$. This

is because $R^{(\alpha)}$ has the general form

$$< R^{(\alpha)} >_{mn} \propto e^{[it(\omega_{mn} - \omega_1 - \omega_2 - ...)]} \qquad (2.20)$$

where $\omega_{mn} = \omega_m - \omega_n$.

If we expand $\mid \xi >$ in the set of eigenfunctions $\mid n >$ of the unperturbed

Hamiltonian H_0,

$$\mid \xi > = \sum_n \mid n > < n \mid \xi > = \sum_n \mid n > \xi_n, \qquad (2.21)$$

we obtain

$$\frac{\partial}{\partial t} \xi_m = \sum_n \sum_{\alpha=1}^{\infty} \varepsilon^{\alpha} < G^{(\alpha)} >_{mn} \xi_n \quad . \qquad (2.22)$$

Since we have assigned only the diagonal elements of $< R^{(\alpha)} >_{mn}$ to $G^{(\alpha)}$, we have

19

$$\frac{\partial}{\partial t} \xi_n = \sum_{\alpha=1}^{\infty} \varepsilon^{\alpha} < G^{(\alpha)} >_{nn} \xi_n \qquad (2.23)$$

which has the solution

$$\xi_n(t) = \xi_n(0) \, e^{-i \, \Delta E_n \, t / \hbar} \qquad (2.24)$$

where

$$\Delta E_n = i\hbar \sum_{\alpha=1}^{\infty} \varepsilon^{\alpha} < G^{(\alpha)} >_{nn} \, . \qquad (2.25)$$

ΔE_n corresponds to a time-independent energy shift of state $| n >$.

With the initial condition

$$\xi_n(0) = \delta_{ng} \, \xi_g(0), \qquad (2.26)$$

Eq. (2.15) can be rewritten as

$$| \Phi(t) > \, = \, \xi_g \left[1 + \sum_{\alpha=1}^{\infty} \varepsilon^{\alpha} F^{(\alpha)} \right] | g >. \qquad (2.27)$$

We insert Eq. (2.27) into Eq. (2.12) and separate according to order of ε to obtain

$$\mathbf{p}^{(0)}(t) = < \mathbf{p} >_{gg}$$

$$\mathbf{p}^{(1)}(t) = < F^{(1)\dagger} \bar{p} >_{gg} + < \bar{p} \, F^{(1)} >_{gg}$$

$$\mathbf{p}^{(2)}(t) = < F^{(2)\dagger} \bar{p} >_{gg} + < F^{(1)\dagger} \bar{p} \, F^{(1)} >_{gg} + < \bar{p} \, F^{(2)} >_{gg}$$

20

$$\mathbf{p}^{(3)}(t) = <F^{(3)\dagger} \bar{p}>_{gg} + <F^{(2)\dagger} \bar{p} F^{(1)}>_{gg} + <F^{(1)\dagger} \bar{p} F^{(2)}>_{gg} + <\bar{p} F^{(3)}>_{gg}$$

$$- \left[<F^{(2)\dagger}>_{gg} + <F^{(1)\dagger} F^{(1)}>_{gg} + <F^{(2)}>_{gg} \right]$$

$$\left[<F^{(1)\dagger} \bar{p}>_{gg} + <\bar{p} F^{(1)}>_{gg} \right] . \qquad (2.28)$$

For further simplification, let us define a projection operator g that projects out from $\bar{H}$ only those terms that we have assigned to $G^{(1)}$:

$$g \bar{H} = G^{(1)} \qquad (2.29)$$

From Eq. (2.17), we have

$$F^{(1)} = \int dt \, (\bar{H} - g\bar{H}) , \qquad (2.30)$$

and we therefore define a projection operator f through

$$f \bar{H} = \int dt \, (\bar{H} - g\bar{H}) = F^{(1)} . \qquad (2.31)$$

The higher orders of $G^{(\alpha)}$ and $F^{(\alpha)}$ can then be expressed as

$$G^{(2)} = g \bar{H} f \bar{H}$$

$$F^{(2)} = f \bar{H} f \bar{H} - f^2 \bar{H} \, \dot{g} \, \bar{H}$$

21

$$G^{(3)} = g\,\bar{H}\,f\,\bar{H}\,f\,\bar{H} - g\,\bar{H}\,f^2\,\bar{H}\,g\,\bar{H}$$

$$F^{(3)} = f\,\bar{H}\,f\,\bar{H}\,f\,\bar{H} - f\,\bar{H}\,f^2\,\bar{H}\,g\,\bar{H}$$
$$- f^2\,\bar{H}\,g\,\bar{H}\,f\,\bar{H} - f^2\,\bar{H}\,f\,\bar{H}\,g\,\bar{H} + f^3\,\bar{H}\,g\,\bar{H}\,g\,\bar{H} \qquad (2.32)$$

Eqs. (2.28) can now be written in terms of $\bar{p}$, $\bar{H}$, and the projection operators f and g:

$$\mathbf{p}^{(1)}(t) = <\bar{H}^\dagger f^\dagger\,\bar{p}>_{gg} + <\bar{p}\,f\,\bar{H}>_{gg}$$

$$\mathbf{p}^{(2)}(t) = <\bar{H}^\dagger f^\dagger \bar{H}^\dagger f^\dagger\,\bar{p}>_{gg} + <\bar{H}^\dagger f^\dagger\,\bar{p}\,f\,\bar{H}>_{gg} + <\bar{p}\,f\,\bar{H}\,f\,\bar{H}>_{gg}$$

$$\mathbf{p}^{(3)}(t) = <\bar{p}\,f\,\bar{H}\,f\,\bar{H}\,f\,\bar{H}>_{gg} + <\bar{H}^\dagger f^\dagger\,\bar{p}\,f\,\bar{H}\,f\,\bar{H}>_{gg}$$
$$- <\bar{p}\,f^2\,\bar{H}>_{gg}<g\,\bar{H}\,f\,\bar{H}>_{gg} - <f\,\bar{H}\,f\,\bar{H}>_{gg}<\bar{H}^\dagger f^\dagger\,\bar{p}>$$
$$- <\bar{H}^\dagger f^\dagger f\,\bar{H}>_{gg}<\bar{p}\,f\,\bar{H}>_{gg} - <f\,\bar{H}\,f\,\bar{H}>_{gg}<\bar{p}\,f\,\bar{H}>_{gg}$$
$$+ \text{ Hermitian conjugate} \qquad (2.33)$$

where we have made use of $<g\bar{H}>_{gg} = 0$.

As an example, we calculate the linear polarizability $\alpha_{ij}(-\omega;\omega)$ given by

$$p_i^{(1)\,\omega} = \alpha_{ij}(-\omega;\omega)\,E_j^\omega \qquad\qquad . \qquad (2.34)$$

The second term of $\mathbf{p}^{(1)}(t)$ in Eq. (2.33) can be expanded as

22

$$< \bar{p}_i f \bar{H} >_{gg} \; = \; \sum_n < \bar{p}_i >_{gn} < f \bar{H} :_{ng} \tag{2.35}$$

where we now consider the i-component of the polarization. Explicitly writing out $\bar{p}$ and $\bar{H}$, we get

$$< \bar{p}_i f \bar{H} >_{gg} \; = \; \sum_n <g| \, e^{iH_0^\dagger t/\hbar} \, p_i \; e^{-iH_0 t/\hbar} - <p_i>_{gg} \, |n>$$
$$<n| \, (i\hbar)^{-1} f \, (e^{iH_0^\dagger t/\hbar} \, H_1 \; e^{-H_0 t/\hbar} - <H_1>_{gg}) \, |g> \tag{2.36}$$

which reduces to

$$< \bar{p}_i f \bar{H} >_{gg} \; = \; (i\hbar)^{-1} \sum_n{}' \, <g| \, p_i \, |n> \, e^{-i(\omega_n - \omega_g)t} \, <n| f H_1 \, e^{i(\omega_n - \omega_g)t} \, |g> \tag{2.37}$$

where the prime on the summation indicates that the ground state is omitted from the sum ($n \neq g$). Expansion of H_1 as a Fourier series and performance of the time integral involved in the definition of f yield

$$< \bar{p}_i f \bar{H} >_{gg} \; = \; (i\hbar)^{-1} \sum_n{}' \sum_{\omega_j} \frac{<g| \, p_i \, |n> \; <n| \, H_1^{\omega_j} \, |g>}{\omega_{ng} - \omega_j} \, e^{-i\omega_j t} \tag{2.38}$$

The first term of $p^{(1)}(t)$ in Eq. (2.33) is simply the complex conjugate of Eq. (2.35). The polarization $p_i^{(1)\,\omega}$ at frequency ω is then given by

23

$$p_i^{(1)\,\omega} = \frac{1}{\hbar} \sum_n{}' \left[\frac{\langle g| p_i |n\rangle \; \langle n| H_1^\omega |g\rangle}{\omega_{ng} - \omega} + \frac{\langle g| H_1^\omega |n\rangle \; \langle n| p_i |g\rangle}{\omega_{ng} + \omega} \right] \qquad (2.39)$$

and $\alpha_{ij}(-\omega;\omega)$ is

$$\alpha_{ij}(-\omega;\omega) = \frac{e^2}{\hbar} \sum_n{}' \left[\frac{\langle g| r^i |n\rangle \; \langle n| r^j |g\rangle}{\omega_{ng} - \omega} + \frac{\langle g| r^j |n\rangle \; \langle n| r^i |g\rangle}{\omega_{ng} + \omega} \right]. \qquad (2.40)$$

This is the usual expression for the linear susceptibility and is well-behaved in the $\omega \to 0$ limit.

To obtain the third order polarizability $\gamma_{ijkl}(-\omega_4;\omega_1,\omega_2,\omega_3)$ as defined in Eq. (2.1), we must evaluate $p_i^{(3)}(t)$ from Eq. (2.33). Each term in Eq. (2.33) involves three factors of $\overline{H}_1$ which have components that oscillate with frequencies ω_1, ω_2 and ω_3. We define a permutation operator $I_{1,2,3}$ that averages over all permutations of ω_1, ω_2 and ω_3, where the associated indices j, k, and l are also permuted with the frequencies to ensure $\gamma_{ijkl}(-\omega_4;\omega_1,\omega_2,\omega_3) = \gamma_{iljk}(-\omega_4;\omega_3,\omega_1,\omega_2)$ and similar permutations are valid. The susceptibility $\gamma_{ijkl}(-\omega_4;\omega_1,\omega_2,\omega_3)$ is given by

$$\gamma_{ijkl}(-\omega_4;\omega_1,\omega_2,\omega_3) = K(-\omega_4;\omega_1,\omega_2,\omega_3) \left(\frac{e^4}{\hbar^3} \right) I_{1,2,3}$$

$$\left[\sum_{m_1 m_2 m_3}{}' \left\{ \frac{r^i_{g m_3} \, \overline{r}^l_{m_3 m_2} \, \overline{r}^k_{m_2 m_1} \, r^j_{m_1 g}}{(\omega_{m_3 g}-\omega_4)(\omega_{m_2 g}-\omega_1-\omega_2)(\omega_{m_1 g}-\omega_1)} + \frac{r^l_{g m_3} \, \overline{r}^i_{m_3 m_2} \, \overline{r}^k_{m_2 m_1} \, r^j_{m_1 g}}{(\omega_{m_3 g}+\omega_3)(\omega_{m_2 g}-\omega_1-\omega_2)(\omega_{m_1 g}-\omega_1)} \right.$$

$$\left. + \frac{r^j_{g m_3} \, \overline{r}^k_{m_3 m_2} \, \overline{r}^i_{m_2 m_1} \, r^l_{m_1 g}}{(\omega_{m_3 g}+\omega_1)(\omega_{m_2 g}+\omega_1+\omega_2)(\omega_{m_1 g}-\omega_3)} + \frac{r^j_{g m_3} \, \overline{r}^k_{m_3 m_2} \, \overline{r}^l_{m_2 m_1} \, r^i_{m_1 g}}{(\omega_{m_3 g}+\omega_1)(\omega_{m_2 g}+\omega_1+\omega_2)(\omega_{m_1 g}+\omega_4)} \right\}$$

24

$$-\sum_{m_1 m_2}^{\prime} \left\{ \frac{r_{gm_2}^{i}\, r_{m_2 g}^{l}\, r_{gm_1}^{k}\, r_{m_1 g}^{j}}{(\omega_{m_2 g}-\omega_4)(\omega_{m_2 g}-\omega_3)(\omega_{m_1 g}-\omega_1)} + \frac{r_{gm_2}^{i}\, r_{m_2 g}^{l}\, r_{gm_1}^{k}\, r_{m_1 g}^{j}}{(\omega_{m_2 g}-\omega_3)(\omega_{m_1 g}+\omega_2)(\omega_{m_1 g}-\omega_1)} \right.$$

$$\left. + \frac{r_{gm_2}^{l}\, r_{m_2 g}^{i}\, r_{gm_1}^{j}\, r_{m_1 g}^{k}}{(\omega_{m_2 g}+\omega_4)(\omega_{m_2 g}+\omega_3)(\omega_{m_1 g}+\omega_1)} + \frac{r_{gm_2}^{l}\, r_{n_2 g}^{i}\, r_{gm_1}^{j}\, r_{m_1 g}^{k}}{(\omega_{m_2 g}+\omega_3)(\omega_{m_1 g}-\omega_2)(\omega_{m_1 g}+\omega_1)} \right\} \right]$$

$$(2.41)$$

where $r_{m_1 m_2}^{i}$ is the matrix element $<m_1 \mid r^i \mid m_2>$ $(\bar{r}^i = r^i - <r^i>_{gg})$, $\hbar\omega_{m_1 g}$ is the excitation energy of state m_1, and the prime on the summations indicates a sum over all states but g. The factor $K(-\omega_4;\omega_1,\omega_2,\omega_3)$ arises from the distinguishable arrangements of ω_1, ω_2, and ω_3 that can contribute to $\gamma_{ijkl}(-\omega_4;\omega_1,\omega_2,\omega_3)$ and from the factors of 1/2 in the definitions of the Fourier amplitudes of H_1 and $\mathbf{p}$ in Eq. (2.14). The numerical values is given by $K(-\omega_4;\omega_1,\omega_2,\omega_3) = 2^{-m} D$ where m is the number of nonzero input frequencies minus the number of nonzero output frequencies and D is the number of distinguishable orderings of the set $\{\omega_1, \omega_2, \omega_3\}$. Given the transition dipole moments and excitation energies of the electronic states for a particular molecular structure, we can calculate $\gamma_{ijkl}(-\omega_4;\omega_1,\omega_2,\omega_3)$ for any given set of frequenices and for any third order optical process. We note here that some authors choose to include $K(-\omega_4;\omega_1,\omega_2,\omega_3)$ in the constitutive equation (Eq. (2.1)) explicitly rather than incorporate it in $\gamma_{ijkl}(-\omega_4;\omega_1,\omega_2,\omega_3)$.[7] In fact, comparative nonlinear optical measurements are complicated by the many different definitions that have been adopted

25

for $\gamma_{ijkl}(-\omega_4;\omega_1,\omega_2,\omega_3)$. The relationships between the most common notations are given in Appendix A.

C. Multiple-Excited Configuration Interaction Theory and Self-Consistent-Field Molecular Orbital Methods

In order to evaluate Eq. (2.41) for $\gamma_{ijkl}(-\omega_4;\omega_1,\omega_2,\omega_3)$, we require the excitation energies and transition dipole moments for the electronic states of the molecular system. We review here the basic principles of the all-valence electron, self-consistent-field, molecular orbital methods[9,10] employed to calculate the ground state wavefunction as well as the multiple-excited configuration interaction theory[11] that incorporates electron correlation into the determination of excited state properties.

The molecular Hamiltonian H_{total} is given by

$$H_{total}(1,\ 2,...N;\ 1,\ 2,...n)\ =\ -\frac{\hbar^2}{2}\sum_A \frac{1}{M_A}\nabla_A^2\ +\ \sum_{A<B}\frac{e^2 Z_A Z_B}{r_{AB}}$$

$$-\frac{\hbar^2}{2m}\sum_i \nabla_i^2\ -\ \sum_A \sum_i \frac{e^2 Z_A}{r_{Ai}}\ +\ \sum_{i<j}\frac{e^2}{r_{ij}} \tag{2.42}$$

where N and n are the respective numbers of nuclei and electrons, M_A the mass of nucleus A, $Z_A e$ the charge of nucleus A, m and e the electron mass and charge, and r_{ij} the distance between particles i and j. The terms in Eq. (2.42) correspond in order from left to right to the kinetic energy of the nuclei, the Coulomb repulsion between nuclei,

the kinetic energy of the electrons, the Coulomb attraction between nuclei and electrons, and the Coulomb repulsion between electrons. Since the nuclear masses are several thousand times larger than the electronic masses, we make the approximation that at any given time the electrons adjust to the instantaneous nuclear configuration as if the nuclei were motionless. This is, of course, known as the Born-Oppenheimer approximation and reduces the Hamiltonian to

$$H(1, 2,...n) \; = \; -\frac{\hbar^2}{2m}\sum_i \nabla_i^2 \; - \; \sum_A \sum_i \frac{e^2 Z_A}{r_{Ai}} \; + \; \sum_{i<j} \frac{e^2}{r_{ij}} \qquad (2.43)$$

where it is understood that $H(1, 2,...n)$ is also a function of the given nuclear configuration. The many-electron wavefunction $\Psi_m(1, 2,...n)$ is given by the Schrodinger equation

$$H(1, 2,...n) \; \Psi_m(1, 2,...n) \; = \; E_m \Psi_m(1, 2,...n) \; . \qquad (2.44)$$

Equation (2.44) is still too complicated for exact solution because the third term of Eq. (2.43) couples the wavefunction of each electron to all the other electrons in the system. The orbital approximation constructs the many-electron wavefunction from individual wavefunctions determined for each electron. To maintain the antisymmetry of the overall wavefunction, it is taken as the Slater determinant of one electron of each of two possible spins occupying the orbitals Φ_m:

27

$$\Psi(1, 2,....n) = | \Phi_1 \bar{\Phi}_1 \Phi_2 \bar{\Phi}_2 ... \Phi_{n/2} \bar{\Phi}_{n/2} | \qquad (2.45)$$

where Φ_m and $\bar{\Phi}_m$ are one-electron orbitals of opposite spin.

To develop equations that provide Φ_m, we first separate Eq. (2.43) for

$H(1, 2,...n)$ into one-electron and two-electron parts H' and G', respectively :

$$H = H' + G' \qquad (2.46)$$

where

$$H' = \sum_i \left[-\frac{\hbar^2}{2m} \nabla_i^2 - \sum_A \frac{e^2 Z_A}{r_{Ai}} \right] = \sum_i h'(i) \qquad (2.47)$$

and

$$G' = \sum_{i<j} \frac{e^2}{r_{ij}} = \sum_{i<j} g'(i, j) \ . \qquad (2.48)$$

The total electronic energy E is given by

$$E = <\Psi | H | \Psi> = 2 \sum_{i=1}^{n/2} H'_{ii} + \sum_{i=1}^{n/2} \sum_{j=1}^{n/2} (2J_{ij} - K_{ij}) \qquad (2.49)$$

where

$$H'_{ii} = \int \Phi_i^*(1) \, h'(1) \, \Phi_i(1) \, d\tau_1 \qquad (2.50)$$

and i, j sum over the $n/2$ occupied molecular orbitals. The Coulomb integral J_{ij} and

exchange integral K_{ij}, given by

$$J_{ij} = \int \int \Phi_i^*(1) \, \Phi_j^*(2) \frac{1}{r_{12}} \Phi_i(1) \, \Phi_j(2) \, d\tau_1 d\tau_2 \ , \qquad (2.51)$$

28

and

$$K_{ij} = \int\int \Phi_i^*(1) \, \Phi_j^*(2) \frac{1}{r_{12}} \Phi_j(1) \, \Phi_i(2) \, d\tau_1 d\tau_2, \qquad (2.52)$$

respectively, represent the Coulomb repulsion between electrons in orbitals Φ_i and Φ_j and the exchange interaction between electrons of parallel spin in orbitals Φ_i and Φ_j that results from antisymmetry of the total wavefunction. If we define one-electron orbital energies E_i by

$$E_i = H_{ii} + \sum_{j=1}^{n/2} (2J_{ij} - K_{ij}) \qquad (2.53)$$

then

$$E = 2\sum_{i=1}^{n/2} E_i - \sum_{i=1}^{n/2} \sum_{j=1}^{n/2} (2J_{ij} - K_{ij}) \qquad (2.54)$$

where the second term corrects for double-counting of the electron-electron interaction energy.

The solution for Φ_m can be obtained by the method of Lagrange multipliers. When we include the orthonormality constraint that

$$S_{ij} = \int \Phi_i^*(1) \, \Phi_j(1) \, d\tau_1 = \delta_{ij}, \qquad (2.55)$$

the solution is obtained by minimizing the function

$$G = E - 2\sum_{i,j} \epsilon_{ij} S_{ij} = 2\sum_{i} H_{ii}' + \sum_{i,j} (2J_{ij} - K_{ij}) - 2\sum_{i,j} \epsilon_{ij} S_{ij} \qquad (2.56)$$

29

where ε_{ij} are the undetermined Lagrange multipliers. This leads to the differential equations

$$\{ h'(1) + \sum_{j=1}^{n/2} [2J_j(1) - K_j(1)] \} \Phi_i(1) = \varepsilon_i \Phi_i(1) \qquad (2.57)$$

where we have made the unitary transformation in which the only nonzero elements of the Lagrange multipliers ε_{ij} are the diagonal values, denoted ε_i. The Coulomb and exchange operators J_j and K_j, respectively, are defined by

$$J_j(1) \, \Phi_i(1) = [\int \Phi_j^*(2) \frac{1}{r_{12}} \Phi_j(2) \, d\tau_2] \, \Phi_i(1)$$

$$K_j(1) \, \Phi_i(1) = [\int \Phi_j^*(2) \frac{1}{r_{12}} \Phi_i(2) \, d\tau_2] \, \Phi_j(1). \qquad (2.58)$$

The eigenvalues ε_i are equal to the one-electron orbital energies E_i defined in Eq. (2.53).

Equations (2.57) are the Hartree-Fock equations that allow for solution of the set of orbitals Φ_i, but the equations themselves are dependent on Φ_j through the operators J_j and K_j. This requires an iterative solution that is simplified if the orbitals are further approximated as linear combinations of atomic orbitals (LCAO),

$$\Phi_i = \sum_{\mu} C_{\mu i} \, \phi_\mu \qquad (2.59)$$

where ϕ_μ is an atomic orbital. We define the atomic overlap integral $S_{\mu\nu}$ and density matrix $P_{\mu\nu}$ as

$$S_{\mu\nu} = \int \phi_\mu^*(1) \, \phi_\nu(1) \, d\tau_1$$

$$P_{\mu\nu} = 2 \sum_i c_{\mu i}^* \, c_{\nu i} \tag{2.60}$$

where the sum over i in $P_{\mu\nu}$ is over each of the doubly-occupied molecular orbitals. The total electronic energy E given in Eq. (2.49) can be expressed in terms of the atomic orbitals as

$$E = \sum_{\mu\nu} P_{\mu\nu} H_{\mu\nu} + \frac{1}{2} \sum_{\mu\nu\lambda\sigma} P_{\mu\nu} P_{\lambda\sigma} \left[(\mu\nu|\lambda\sigma) - \frac{1}{2}(\mu\lambda|\nu\sigma) \right] \tag{2.61}$$

where

$$H_{\mu\nu} = \int \phi_\mu^*(1) \, h'(1) \, \phi_\nu(1) \, d\tau_1 \tag{2.62}$$

and

$$(\mu\nu|\lambda\sigma) = \int\int \phi_\mu^*(1) \, \phi_\nu(1) \, \frac{1}{r_{12}} \, \phi_\lambda^*(2) \, \phi_\sigma(2) \, d\tau_1 d\tau_2. \tag{2.63}$$

The Lagrange multiplier equation that corresponds to Eq. (2.57) in terms of the atomic orbitals is

$$\sum_\nu (F_{\mu\nu} - \varepsilon_i S_{\mu\nu}) \, c_{\nu i} = 0 \tag{2.64}$$

31

where the Fock matrix $F_{\mu\nu}$ is defined by

$$F_{\mu\nu} = H_{\mu\nu} + \sum_{\lambda\sigma} P_{\lambda\sigma} [(\mu\nu | \lambda\sigma) - \frac{1}{2}(\mu\lambda | \nu\sigma)]. \qquad (2.65)$$

Solution of the algebraic set of equations (2.64) yields the molecular orbitals Φ_i in terms of the atomic orbital coefficients $c_{\nu i}$. Since Eq. (2.64) involves the remaining set of coefficients $c_{\mu i}$ through $P_{\mu\nu}$, it still requires iterative solution.

We now turn to the further approximations and parameterizations that are specific to the CNDO/S method.[5,6] The atomic orbitals ϕ_μ are approximated as Slater-type orbitals when the radial part is given by

$$R_{nl}(r) = (2\zeta)^{n + 1/2} [(2n)!]^{-1/2} r^{n - 1} e^{-\zeta r} \qquad (2.66)$$

where n is the radial quantum number and ζ is the Slater exponent. The angular dependence of the wave functions is given by the spherical harmonics, $Y_{lm}(\theta, \phi)$. In Roothaan's equation (Eq. (2.64)), the zero differential overlap (ZDO) approximation is made for the overlap integrals $S_{\mu\nu}$,

$$S_{\mu\nu} = \delta_{\mu\nu} . \qquad (2.67)$$

The ZDO approximation is also made for the two-electron integrals such that

32

$$(\mu\nu \mid \lambda\sigma) = \delta_{\mu\nu} \, \delta_{\lambda\sigma} (\mu\mu \mid \lambda\lambda) \quad . \tag{2.68}$$

We will use μ_A to denote orbital μ on atomic site A. Then the one-center integral $(\mu_A \mu_A \mid \nu_A \nu_A)$ is taken as an input parameter that is independent of orbital type,

$$(\mu_A \mu_A \mid \nu_A \nu_A) = \gamma_{AA} \, , \tag{2.69}$$

and the two-center integral is given by the Ohno potential,[12]

$$(\mu_A \mu_A \mid \nu_B \nu_B) = \gamma_{AB} = \frac{14.397 \text{ eV Å}}{\left\{ \left[\dfrac{28.794 \text{ eV Å}}{\gamma_{AA} + \gamma_{BB}} \right]^2 + \left[R_{AB}(\text{Å}) \right]^2 \right\}^{1/2}} \quad . \tag{2.70}$$

For the one-electron part of the Fock matrix, denoted by $H_{\mu\nu}$, the diagonal elements are given by

$$H_{\mu\mu} = I_\mu - (Z_A - 1) \gamma_{AA} \tag{2.71}$$

where I_μ is the parameterized ionization potential for orbital μ and Z_A is the net core charge of atom A. The off-diagonal elements of $H_{\mu\nu}$, which represent the bonding energy of a shared electron, are taken as

$$H_{\mu\nu} = \left[(\beta_A + \beta_B) / 2 \right] S_{\mu\nu} \tag{2.72}$$

33

where β_A is the empirical resonance integral of site A and the ZDO approximation is not employed here for $S_{\mu\nu}$.

The final equations from which the orbital coefficients $c_{\nu i}$ are obtained are

$$\sum_{\nu} (F_{\mu\nu} - \varepsilon_i \, \delta_{\mu\nu}) \, c_{\nu i} = 0 \tag{2.73}$$

where

$$F_{\mu\mu} = I_{\mu} - (Z_A - 1) \gamma_{AA} + (P_{AA} - \tfrac{1}{2} P_{\mu\mu}) \gamma_{AA} + \sum_{B \neq A} (P_{BB} - Z_B) \gamma_{AB} \tag{2.74}$$

and

$$F_{\mu\nu} = -(\beta_A + \beta_B)/2 \; S_{\mu\nu} - \tfrac{1}{2} P_{\mu\nu} \gamma_{AB} \qquad (\mu \neq \nu) \tag{2.75}$$

where P_{BB} is the sum of $P_{\lambda\lambda}$ where λ is any orbital centered on atomic site B.

Equation (2.73), together with Eqs. (2.59) and (2.45), yields the ground state electronic wavefunction for the molecular system of interest. In order to obtain the excited state wavefunctions and energies, we perform a double-excited configration interaction calculation.[11] Each state of the system Ψ_n is expanded as

$$\Psi_n = A_{n,0} \Psi_0 + \sum_{k=1}^{n/2} \sum_{p=n/2+1}^{m} A_{n,kp} \Psi_{kp}$$

$$+ \sum_{k=1}^{n/2} \sum_{l=1}^{n/2} \sum_{p=n/2+1}^{m} \sum_{q=n/2+1}^{m} A_{n,kplq} \Psi_{kplq} \tag{2.76}$$

34

where Ψ_0 is the ground state wavefunction, Ψ_{kp} is a spin-singlet, single-excited configuration given by

$$\Psi_{kp} = 2^{-1/2} \left(\; |\Phi_1\bar{\Phi}_1...\Phi_k\Phi_{k+1}\bar{\Phi}_{k+1}...\Phi_{n/2}\bar{\Phi}_{n/2}\bar{\Phi}_p| \right.$$
$$\left. - |\Phi_1\bar{\Phi}_1...\bar{\Phi}_k\Phi_{k+1}\bar{\Phi}_{k+1}...\Phi_{n/2}\bar{\Phi}_{n/2}\Phi_p| \; \right) \qquad (2.77)$$

where p is a virtual orbital that is unoccupied in Ψ_0, and Ψ_{kplq} is an analogous spin-singlet double-excited configuration. The coefficients $A_{n,R}$ where R represents the set of molecular orbitals involved in the configuration, are determined by

$$\sum_R A_{n,R} \, (H_{RS} - E_n \, S_{RS}) = 0 \qquad (2.78)$$

where $H_{RS} = <\Psi_R | H | \Psi_S>$ with H defined in Eq. (2.46), E_n are the eigenvalues of H_{RS}, and S_{RS} is the overlap between Ψ_R and Ψ_S.

The molecular dipole moment operator μ is defined as

$$\mu = -e \sum_i r_i + e \sum_A Z_A \, r_A \qquad (2.79)$$

where i sums over the valence electrons and A over the atomic cores. Within the Born-Oppenheimer approximation, the second term of Eq. (2.79) is constant and only contributes to the diagonal elements of $\mu_{nn'}$ where

35

$$\mu_{nn'} = <\Psi_n | \mu | \Psi_{n'}> . \qquad (2.80)$$

If we rewrite the expansion of the state function Ψ_n as

$$\Psi_n = \sum_R A_{n,R} \ \Psi_R \qquad (2.81)$$

where Ψ_R is either the ground, a single-excited, or a double-excited configuration, we obtain

$$\mu_{nn'} = \sum_{R,S} A_{n,R} A_{n',S} \ <\Psi_R | \mu | \Psi_S> \qquad (2.82)$$

where $<\Psi_R | \mu | \Psi_S>$ is the transition dipole moment between the configurations Ψ_R and Ψ_S.

As an example of the transition moment between configurations, we consider the integral between the ground configuration Ψ_0 and the single-excited configuration Ψ_{ik} that involves promotion of one electron from molecular orbital Φ_i to orbital Φ_k. We wish to evaluate

$$<\Psi_0 | r(1) | \Psi_{ik}> = \int \Psi_0(1, 2,....M) \ r(1) \ \Psi_{ik}(1, 2,....M) \ d\tau_1 \ d\tau_2...d\tau_M \qquad (2.83)$$

where M is the number of valence electrons. Recall that Ψ_0 and Ψ_{ik} are constructed as Slater determinants of orthonormal molecular orbitals. Expansion of Ψ_0 and Ψ_{ik} into the individual terms of the Slater determinants yield many integrals such as

$$\int \Phi_p(2)\, \Phi_q(2)\, d\tau_2 = 0 \quad (p \neq q) \tag{2.84}$$

that vanish by construction of the orbitals. The only terms for which the integrals over $d\tau_2...d\tau_M$ do not yield zero are those for which electrons 2, 3,...M occupy the same orbitals in Ψ_0 and Ψ_{ik}. But we note that Ψ_0 and Ψ_{ik} differ in only one orbital from which they are constructed, and, therefore, the only nonvanishing term is that for which electron 1 is assigned to Φ_i in Ψ_0 and Φ_k in Ψ_{ik}. Integration over $d\tau_2...d\tau_M$ for this term results in

$$< \Psi_0 \mid r(1) \mid \Psi_{ik} > = 2^{1/2} \int \Phi_i(1)\, r(1)\, \Phi_k(1)\, d\tau_1 \tag{2.85}$$

where the factor $2^{1/2}$ is due to the spin-singlet construction of Ψ_{ik}. We can then, finally, evaluate $\gamma_{ijkl}(-\omega_4;\omega_1,\omega_2,\omega_3)$ through Eq. (2.41) with the electronic excitation energies and transition dipole moments for the molecular system obtained as prescribed in this section.

Chapter 2 References

1.   N. Bloembergen, *Nonlinear Optics* (Benjamin, New York, 1965).

2.   J. F. Ward, Rev. Mod. Phys. **37**, 1 (1965).

3.   H. D. Cohen and C. C. J. Roothan, J. Chem. Phys. **43**, 34 (1965).

4.   See, for example, B. S. Hudson, B. E. Kohler, and K. Schulten, in *Excited States*, Vol. **6**, E. C. Lim, ed. (Academic, New York, 1982); and references therein.

5.   J. del Bene and H. H. Jaffe, J. Chem. Phys. **48**, 1807, (1968).

6.   N. O. Lipari and C. B. Duke, J. Chem. Phys. **63**, 1748 (1975).

7.   B. J. Orr and J. F. Ward, Mol. Phys. **20**, 513 (1971).

8.   N. N. Bogoliubov and Y. A. Mitropolsky, *Asymptotic Methods in the Theory of Nonlinear Oscillations* (Gordon and Breach, London, 1961); translated from Russian.

9.   J. A. Pople and D. L. Beveridge, *Approximate Molecular Orbital Theory* (McGraw-Hill, New York, 1970).

10.   J. Sadlej, *Semi-Empirical Methods of Quantum Chemistry* (Ellis Horwood, Chichester, England, 1985); translated from Polish by I. L. Cooper.

11.   D. Lowitz, J. Chem. Phys. **46**, 4698 (1967).

12.   K. Ohno, Theoret. Chim. Acta **2**, 219 (1964).

Chapter 3

ELECTRON CORRELATION DESCRIPTION OF $\gamma_{ijkl}(-\omega_4;\omega_1,\omega_2,\omega_3)$ FOR CONJUGATED LINEAR CHAINS

A. Introduction

In this thesis, we will concentrate on the hydrocarbon chains known as polyenes as the archetypal examples of organic conjugated linear chains.[1] Each carbon atom site in a polyene chain is sp^2 hybrid bonded to its three nearest neighbor carbon and hydrogen atom sites. The first and last carbon sites are each bonded to one carbon and two hydrogens while the internal carbons of the chain are bonded to two carbons and one hydrogen. The carbon sp^2 hybrid orbitals, together with the hydrogen $1s$ orbitals, combine to form bonding molecular orbitals of σ symmetry. To an excellent approximation, the σ bonds lead to a planar molecular structure with each bond pair separated by $120°$. For example, electron diffraction data of hexatriene (HT), the polyene with $N = 6$ carbon sites, are best fit by a planar configuration with minimum and maximum bond angles of $115.0°$ and $124.4°$, respectively.[2]

The remaining electrons (one $2p$ electron per carbon atom site) form a framework of delocalized, π-electron molecular orbitals. These weakly bound π-electrons are responsible for the low-lying electronic excitations of polyenes, and, importantly, through their large transition dipole moments they dominate the molecular nonlinear optical susceptibilities $\beta_{ijk}(-\omega_3;\omega_1,\omega_2)$ and $\gamma_{ijkl}(-\omega_4;\omega_1,\omega_2,\omega_3)$ of these conjugated

39

structures. The π-electrons do not distribute uniformly across the carbon sites; instead, they form a ground state where the charge density is largest at the terminal carbon-carbon bonds and alternates between high and low densities moving inward along the chain. As a result, polyenes have a dimerized bonding structure where the short, double bonds are due to larger bonding electron density. Electron diffraction data for HT yield a short bond length of 1.337 Å and a long bond length of 1.457 Å.[2]

B. Conformation, Symmetry, and Parametrization

Various structural conformations of polyene chains can be considered based on rotations about the carbon-carbon bonds. The two most common conformations, all-*trans* and *cis-transoid*, are shown schematically in Figure 3-1 for the particular case of $N = 6$, HT. Nomenclature for the conformational structures is by reference to the locations of the neighboring carbon-carbon bonds relative to a given bond. The structure is said to be *trans* if the neighboring bonds of a particular bond lie on opposite sides of that bond's axis and *cis* if they lie on the same side. In an all-*trans* polyene, then, all bonds are in the *trans* structure. In a *cis-transoid* polyene, the single bonds on either side of each double bond are in the *cis* structure while the double bonds on either side of each single bond are in the *trans* structure. In this chapter, we will consider only the all-*trans* conformation, hereafter referred to simply as *trans*, which is the energetically most stable conformation. In Chapter 4 we will present results for the *cis-*

40

transoid conformation, hereafter referred to as *cis*, and compare them with the results for the *trans* polyenes.

The *trans* polyenes belong to the C_{2h} symmetry group, where C_2 refers to a two-fold axis of rotation (e.g. a π rotation about a C_2 axis results in an equivalent structure).[3] The C_2 axis lies perpendicular to the molecular plane (out of the page in Figure 3-1) and passes through the center of the central bond. In addition to the C_2 axis, *trans* polyenes also possess a mirror plane which is the molecular plane itself. Since the C_2 axis is defined as the vertical axis, and the two planes that contain it, as vertical planes, the reflection operation that the *trans* polyenes possess is σ_h where the h refers to the horizontal plane, or equivalently, the plane perpendicular to the C_2 axis. Thus, C_{2h} refers to the symmetry group that possesses a two-fold rotational axis and a mirror plane that is perpendicular to that axis.

The C_{2h} symmetry group has four irreducible representations that are labeled A_g, A_u, B_g, and B_u. A and B refer respectively to symmetric and antisymmetric representations with respect to the C_2 operation, and u and g refer respectively to symmetric and antisymmetric representations with respect to the inversion operation. The transformation properties of each irreducible representation of the C_{2h} group under the E (identity), C_2, i (inversion), and σ_h operations are given in Table 3-1. The self-consistent ground state electronic wavefunction is the Slater determinant of the lowest energy molecular orbitals, each doubly occupied, and the MOs are all either of σ or π symmetry where σ is symmetric with respect to the σ_h operation and π is antisymmetric. Double occupation of each orbital leads to a wavefunction that is necessarily symmetric

41

under the σ_h operation and therefore of either A_g or B_u symmetry. Since pairwise filling also leads to a symmetric wavefunction with respect to the C_2 and i operations, the ground state is an A_g symmetry state. Furthermore, we will consider only $\pi \rightarrow \pi^*$ excitations which must also necessarily be symmetric with respect to σ_h. All π-electron states of a *trans* polyene are therefore of either A_g or B_u symmetry.

For complete identification of each individual π-electron state, we number the states according to ascending energy within each of the two symmetry classes. Thus, the ground state is labeled 1^1A_g and the next lowest energy state of the same symmetry is 2^1A_g while the lowest energy state of opposite symmetry than the ground state is denoted 1^1B_u. The superscript 1 indicates that the state is a spin singlet. As a final point with regard to symmetry, we point out that there are strict dipole selection rules within the π-electron states. One-photon transitions are allowed only between states of opposite parity. Thus, the ^1B_u states are one-photon allowed and two-photon forbidden transitions from the 1^1A_g ground state and are therefore known as one-photon states. The excited ^1A_g states, on the other hand, are two-photon allowed and one-photon forbidden and are referred to as two-photon states.

Standard bond lengths, bond angles, and parametrizations of the carbon and hydrogen atomic orbitals were employed for all calculations we carried out of various chain lengths and conformations. The geometry was taken to be planar with $120°$ bond angles, double and single carbon-carbon bond lengths of 1.34 and 1.46 Å, respectively, and carbon-hydrogen bond lengths of 1.09 Å. The parameters for Slater exponents ζ, valence-state ionization energies I, Coulomb repulsion integrals γ, and resonance

42

integrals β for the carbon $2s$ and $2p$ orbitals and the hydrogen $1s$ orbitals are listed in Table 3-2. An earlier theoretical study of the excitation energies of low-lying states of polyenes found that, compared to higher levels of configuration interaction, calculations that include all single and double-excited configurations (SDCI) obtain proper state ordering and yield close results for transition dipole moments but they overcorrelate the ground state relative to the excited states.[4,5] That is to say, the lowering of the ground state energy by inclusion of double-excited configurations is out of proportion to the energy lowering of the excited states. Furthermore, this effect was found to increase roughly linearly with increased chain length. By simply including a fraction of the ground state correlation energy in the excitation energies,

$$\Delta E \ (i \leftarrow \text{ground}) = E_D(i) - (A \ / \ N) \ E_D(ground) \qquad (3.1)$$

where ΔE is the excitation energy of state i, $E_D(i)$ and $E_D(ground)$ are the SDCI energies of the i and ground states relative to the SCF ground state, and N is the number of carbon sites in the chain, the SDCI results are in good agreement with computationally exhaustive, higher levels of configuration interaction.[4,5] In all of our calculations, we have made use of Eq. (3.1) with $A = 3$.

As a demonstration that the theoretical results appropriately describe the π-electron states of polyenes, we compare in Table 3-3 the theoretical and experimental values of the 2^1A_g and 1^1B_u excitation energies for the chain lengths $N = 4$ to 12. The theoretical values are compared to experimental vertical excitation energies rather than

43

0-0 excitation energies since the calculations are performed under the Born-Oppenheimer frozen geometry approximation. Importantly, theory and experiment agree that the 2^1A_g state is of lower energy than the 1^1B_u.

The relative locations of the 1^1B_u and 2^1A_g states has been a critical issue in polyene spectroscopy.[1] For many decades, simple molecular orbital methods had been believed to accurately describe the polyene excitation spectrum since they correctly obtained the large absorption peak due to the $1^1B_u \leftarrow 1^1A_g$ excitation. Hudson and Kohler found, however, in studies of a substituted eight site chain (1,8 diphenyl-1,3,5,7-octatetraene) that an electronic excitation of one-photon forbidden symmetry that lies below the 1^1B_u state is responsible for the displaced origin of the fluorescence spectrum and for the anomalously long fluorescence lifetime following excitation into the 1^1B_u state.[6] Schulten and Karplus subsequently demonstrated that the experimental observation that the 2^1A_g state is lower in energy than the 1^1B_u can be correctly obtained only by calculations that account for electron-electron interactions through multiple-excited configurations.[7] The existence of a low-lying two-photon state is one clear signature that electron correlation effects play a dominant role in polyene electronic structure. One major conclusion of this thesis is that the importance of electron correlation is evidenced just as clearly, if not more so, in the nonlinear optical properties of these conjugated linear chains.

44

C. Hexatriene ($N = 6$)

We begin the discussion of the origin of nonlinear optical properties in polyenes with a detailed discussion of $\gamma_{ijkl}(-\omega_4;\omega_1,\omega_2,\omega_3)$ for HT ($N = 6$) for two principal reasons. Because HT is one of the shortest members of the polyene family, the results of the calculation can be presented and interpreted in an easily manageable manner. In addition, since HT exists at room temperature as a fairly stable liquid and is easily evaporated into the gas phase if needed, it is a suitable system for experimental study. A thorough comparison between the theoretical and experimental results for HT is made in Chapters 5 and 6.

The SCF ground state consists of thirteen doubly-occupied, tightly bound σ-electron molecular orbitals (MOs) and three doubly-occupied π-electron MOs. The occupied π-electron MOs exist at higher energy than the occupied σ MOs, and, in addition, the three lowest energy unoccupied MOs calculated are also π orbitals. The lowest lying electronic excited states therefore involve transitions of electrons from the occupied π MOs to the unoccupied π MOs with the occupied σ orbitals unchanged. Figure 3-2 (a)-(c) and Figure 3-3 (a)-(c) show contour diagrams of the three occupied and three unoccupied π MOs of HT, respectively, in order from lowest to highest energy. Solid and dashed lines correspond to opposite signs of the one-electron wave function, and the contour cut is taken 0.4 Å above the molecular plane since π orbitals vanish on the atoms. The π orbitals are numbered Φ_{13}, Φ_{15}, Φ_{16}, Φ_{17}, Φ_{18}, and Φ_{19} in order from lowest to highest energy. The lowest occupied π MO is numbered Φ_{13}

rather than Φ_{14} because the highest occupied σ MO is, in fact, calculated at a slightly higher energy than the lowest π MO.

The π-electron excited states are obtained by configuration interaction of all single and double-excited configurations from the three occupied π MOs to the three unoccupied π MOs. This leads to a total of 55 calculated states. The excitation energies and x-components of the transition dipole moments of each state with the ground state, $\mu^x_{n,g}$, and the 1^1B_u state, $\mu^x_{n,1^1B_u}$, are listed in Table 3-4 for the lowest-lying calculated states of HT. The 2^1A_g two-photon state at 4.59 eV is the lowest-lying excited state followed by the 1^1B_u state at 4.94 eV. With $\mu^x_{1^1B_u,g} = 6.66$ D, the 1^1B_u state is responsible for the large oscillator strength peak that appears in the HT linear absorption spectrum in the near uv. The $\mu^x_{n,g}$ values that are identically zero for all ^1A_g states and the $\mu^x_{n,1^1B_u}$ that are identically zero for all ^1B_u states clearly demonstrate the dipole selection rules. In addition to the large $\mu^x_{1^1B_u,g}$ between the ground and 1^1B_u states, $\mu^x_{5^1A_g,1^1B_u}$ has the extremely large value 11.40 D. This is a critical virtual transition for $\gamma_{ijkl}(-\omega_4;\omega_1,\omega_2,\omega_3)$ as will be demonstrated below.

The calculated values for the individual tensor components of the dc-induced second harmonic susceptibility $\gamma_{ijkl}(-2\omega;\omega,\omega,0)$ of HT at a nonresonant fundamental photon energy of 0.65 eV ($\lambda = 1907$ nm) are $\gamma_{xxxx} = 24.9$, $\gamma_{xyyx} = 2.0$, $\gamma_{xxyy} = 2.0$, $\gamma_{yxxy} = 2.0$, $\gamma_{yyxx} = 2.0$, and $\gamma_{yyyy} = 0.5 \times 10^{-36}$ esu. Components of the form γ_{ijij} are identically equal to components of the form γ_{iijj} due to the symmetry of their frequency arguments. Components of the form γ_{iijj} and γ_{ijji} are not strictly identical, however, due to dispersion; but at this low photon energy, the dispersion between these

components is weak. The component with all electric fields along the x axis, γ_{xxxx}, where the x direction is defined along the axis of conjugation, is the dominant tensor component of $\gamma_{ijkl}(-2\omega;\omega,\omega,0)$. This is reasonable since the largest transition dipole moments are along the x axis. Transition moments along the transverse y axis are much smaller because of the greater confinement in that direction; and transition moments along the z axis perpendicular to the molecular plane vanish due to the antisymmetry of the π orbitals about the molecular plane.

For the third harmonic susceptibility $\gamma_{ijkl}(-3\omega;\omega,\omega,\omega)$, the calculated tensor components for HT at 0.65 eV are $\gamma_{xxxx} = 4.7$, $\gamma_{xxyy} = 0.4$, $\gamma_{yyxx} = 0.4$, and $\gamma_{yyyy} = 0.1 \times 10^{-36}$ esu. By symmetry of the associated frequency arguments, the γ_{xxyy}, γ_{xyxy}, and γ_{xyyx} components are identical. Again, as expected, the dominant tensor component is γ_{xxxx} where all electric fields are along the axis of conjugation. The larger value of $\gamma_{xxxx}(-2\omega;\omega,\omega,0)$ compared to $\gamma_{xxxx}(-3\omega;\omega,\omega,\omega)$ is a result of the factor $K(-\omega_4;\omega_1,\omega_2,\omega_3)$ in Eq. (2.41). Since $K(-2\omega;\omega,\omega,0) = 3/2$ and $K(-3\omega;\omega,\omega,\omega) = 1/4$, in the limit $\omega \to 0$ we would have $\gamma_{xxxx}(-2\omega;\omega,\omega,0) = 6\,\gamma_{xxxx}(-3\omega;\omega,\omega,\omega)$. Dispersion is responsible for the fact that the calculated value of $\gamma_{xxxx}(-3\omega;\omega,\omega,\omega)$ is actually slightly larger than 1/6 of $\gamma_{xxxx}(-2\omega;\omega,\omega,0)$ at $\hbar\omega = 0.65$ eV.

The values of $\gamma_{ijkl}(-\omega_4;\omega_1,\omega_2,\omega_3)$ were calculated according to Eq. (2.41) from the excitation energies and transition dipole moments of all π-electron states of HT. Of all the terms from the triple and double summations of Eq. (2.41), it was found that a single term dominates each of the two summations. Table 3-5 clearly illustrates this feature where the contributions of each individual term to $\gamma_{xxxx}(-2\omega;\omega,\omega,0)$ are listed in

47

order of decreasing magnitude for the ten largest terms. The columns m_1, m_2, and m_3 indicate the intermediate virtual states according to the notation of Eq. (2.41), and the final column provides the cumulative value of $\gamma_{xxxx}(-2\omega;\omega,\omega,0)$ for all terms of equal or larger magnitude. Terms from the double summation are denoted by $m_2 = 1^1A_g$ and include the overall negative sign of the double summation in the listed contribution. The value of $\gamma_{xxxx}(-2\omega;\omega,\omega,0)$ for the complete summations is determined to better than 85% by the two largest virtual excitation processes. In each of these two terms, the 1^1B_u state is intermediate virtual states m_1 and m_3. The largest term has the 5^1A_g state as the m_2 intermediate state and the second term has the 1^1A_g ground state as m_2.

The significance of these two virtual excitation processes can be understood through examination of Eq. (2.41) and the transition dipole moments of the π-electron states of HT. From Eq. (2.41), it is clear that the virtual π-electron states of polyenes must alternate in parity through the series $1^1A_g \rightarrow a^1B_u \rightarrow b^1A_g \rightarrow c^1B_u \rightarrow 1^1A_g$ as a result of the dipole selection rules where a^1B_u represents intermediate virtual state m_1, b^1A_g represents m_2, and c^1B_u represents m_3. Thus, the m_1 and m_3 states must have ^1B_u symmetry and the m_2 state must have ^1A_g symmetry. The importance of the 1^1B_u state stems from its large transition moment $\mu^x_{1^1B_u,g}$ with the 1^1A_g ground state which is much larger than all other $\mu^x_{n,g}$. The significant m_2 intermediate states will then be those that have the largest $\mu^x_{n,1^1B_u}$. In addition to the 1^1A_g state, the other important ^1A_g state is the 5^1A_g state calculated at 7.97 eV with $\mu^x_{5^1A_g,1^1B_u} = 11.40$ D. The 5^1A_g state is much more significant to $\gamma_{xxxx}(-2\omega;\omega,\omega,0)$ than the low-lying, two-photon 2^1A_g state because of the small value $\mu^x_{2^1A_g,1^1B_u} = 2.42$ D. The magnitude and sign of

48

$\gamma_{xxxx}(-2\omega;\omega,\omega,0)$ is therefore essentially determined by just two virtual excitation processes that contribute with opposite signs, namely, the larger and positive virtual excitation process $1^1A_g \to 1^1B_u \to 5^1A_g \to 1^1B_u \to 1^1A_g$ and the negative process $1^1A_g \to 1^1B_u \to 1^1A_g \to 1^1B_u \to 1^1A_g$.

In general, six types of virtual excitation processes can be identified that contribute to $\gamma_{ijkl}(-\omega_4;\omega_1,\omega_2,\omega_3)$. The six processes, identified as types I through VI, are illustrated in Figure 3-4. Type I involves the same one-photon allowed state in the roles of m_1 and m_3 and the ground state as m_2, and it belongs to the double summation of Eq. (2.41). Type II also involves the same state as m_1 and m_3, but the m_2 intermediate is an excited state. This type of process comes from the triple summation. Types III and IV involve two different states as m_1 and m_3 but are otherwise analogous to types I and II, respectively. The type V and VI processes involve virtual transitions between the same state as represented by the horizontal arrows. Since this virtual transition involves the diagonal matrix element $r^i_{mm} \equiv < m \mid r^i \mid m >$, the type V and VI processes can only be nonzero for noncentrosymmetric molecular structures. In the centrosymmetric case under consideration here, they are identically zero by symmetry.

If there exists one transition moment $\mu^x_{d,g}$ that is significantly larger than all other $\mu^x_{n,g}$, then since the contribution of the corresponding type I term is proportional to $|\mu^x_{d,g}|^4$, while the type III terms are proportional to $|\mu^x_{d,g}|^2 |\mu^x_{n,g}|^2$, the largest of all possible type I and type III terms will be the type I term involving state d. It can be similarly argued that if there are transition moments $\mu^x_{d,g}$ and $\mu^x_{e,d}$ that are much larger than all other $\mu^x_{n,g}$ and $\mu^x_{n,d}$, respectively, where n represents a general state, then the

49

largest of all type II and IV terms will be the type II process $g \rightarrow d \rightarrow e \rightarrow d \rightarrow g$. In the case of HT, the large values of $\mu^x_{1^1B_u,g}$ and $\mu^x_{5^1A_g,1^1B_u}$ are responsible for the dominance of $\gamma_{xxxx}(-2\omega;\omega,\omega,0)$ by the type I term $1^1A_g \rightarrow 1^1B_u \rightarrow 1^1A_g \rightarrow 1^1B_u \rightarrow 1^1A_g$ and the type II term $1^1A_g \rightarrow 1^1B_u \rightarrow 5^1A_g \rightarrow 1^1B_u \rightarrow 1^1A_g$. The larger magnitude of the positive type II term compared to the negative type I term determines the overall sign of the nonresonant $\gamma_{xxxx}(-2\omega;\omega,\omega,0)$ to be positive, a result which is corroborated by experiment[8] and, further, is in distinction from the results of several theoretical methods that omit electron correlation.

The 1^1B_u state is 94% composed of the single-excited configuration of one electron from the highest occupied π-MO to the lowest unoccupied π-MO. The 2^1A_g and 5^1A_g states, on the other hand, are nearly 60% composed of double-excited configurations. The important distinction for $\gamma_{xxxx}(-2\omega;\omega,\omega,0)$ between these two highly electron correlated states is made most evident by the transition density matrix $\rho_{nn'}$ defined through the expression

$$\langle \mu_{nn'} \rangle = -e \int \mathbf{r}\, \rho_{nn'}(\mathbf{r})\, d\mathbf{r} \tag{3.2}$$

with

$$\rho_{nn'}(\mathbf{r}_1) = \int \Psi^*_n (\mathbf{r}_1, \mathbf{r}_2,...\mathbf{r}_M)\, \Psi_{n'}(\mathbf{r}_1, \mathbf{r}_2,...\mathbf{r}_M)\, d\mathbf{r}_2...d\mathbf{r}_M \tag{3.3}$$

where M is the number of valence electrons included in the molecular wavefunction. Contour diagrams for $\rho_{nn'}$ of the ground, 2^1A_g and 5^1A_g states with the 1^1B_u state are shown in Figure 3-5 where solid and dashed lines correspond to increased and

decreased charge density and the contour cut is again taken at 0.4 Å above the molecular plane. The contour diagram of $\rho_{2^1A_g,1^1B_u}$ shows that the $2^1A_g \rightarrow 1^1B_u$ transition results in a charge redistribution concentrated at the center of the molecular structure which yields a small transition moment of 2.42 D, and, correspondingly, a small contribution to $\gamma_{xxxx}(-2\omega;\omega,\omega,0)$. In sharp contrast, $\rho_{5^1A_g,1^1B_u}$ for the virtual transition between the 5^1A_g and 1^1B_u states produces a large charge separation along the chain axis x-direction and an associated large transition moment of 11.40 D which dominates the contributing terms of $\gamma_{xxxx}(-2\omega;\omega,\omega,0)$. This previously unknown feature is key to understanding the nonlinear optical properties of conjugated linear chains.

Table 3-6 lists the four largest configurations that compose the 2^1A_g, 1^1B_u and 5^1A_g states of HT. The notation $\Phi_{16} \rightarrow \Phi_{17}$, for instance, indicates the single-excited configuration in which one electron is promoted from Φ_{16} to Φ_{17}. The 1^1B_u state consists primarily of the single-excited configuration of one electron promoted from the highest occupied π-MO to the lowest unoccupied π-MO and is therefore fairly well described in the independent particle approximation. This explains why simple MO methods were for a long time believed to be sufficient for the polyene structures, since the 1^1B_u state dominates the linear absorption spectrum. The 5^1A_g and 2^1A_g states, however, result from strong electron correlation effects as evidenced by their having significant contributions from several different configurations, especially double-excited configurations. Both the 5^1A_g and 2^1A_g states have large contributions from the double-excited configuration consisting of two electrons promoted from the highest occupied to lowest unoccupied π-MO. Theoretical methods that neglect electron-

51

electron interactions, therefore, inadequately describe the 5^1A_g state that plays a crucial role in $\gamma_{xxxx}(-2\omega;\omega,\omega,0)$.

Figure 3-6 displays the calculated dispersion curve for $\gamma_{xxxx}(-2\omega;\omega,\omega,0)$ of HT from 0.5 eV (λ = 2.48 μm) to 3.0 eV (λ = 0.41 μm). As can be seen in Eq. (2.41) for $\gamma_{ijkl}(-2\omega;\omega,\omega,0)$, there exist 2ω resonances from both ^1B_u and ^1A_g states. The order in which these resonances appear in the DCSHG dispersion is simply the order in which the states occur energetically. Thus, the first singularity in Fig. 3-6 at 2.30 eV, is the 2ω resonance of the 2^1A_g state, and the singularity at 2.47 eV is the 2ω resonance of the 1^1B_u state. Since these two states are so close in energy, there is rapid variation in γ_{xxxx} in this region. Of course, in real systems natural broadening of the electronic states will prevent divergence at the resonances and smooth out this variation. In fact, since the 2^1A_g makes such a small contribution below the resonances, when appropriately broadened, it is not noticeable in the dispersion of $\gamma_{xxxx}(-2\omega;\omega,\omega,0)$.

The natural broadening is accounted for phenomenologically by replacing the transition frequencies ω_{mg} in Eq. (2.41) with the complex quantities $\omega_{mg} - i\Gamma_m$. Figure 3-7 shows the calculated dispersion for $\gamma_{xxxx}(-2\omega;\omega,\omega,0)$ of HT with a representative value $\hbar\Gamma$ = 0.2 eV based on the width of the $1^1B_u \leftarrow 1^1A_g$ peak in the linear absorption spectrum. The divergence that occurs due to the 2ω resonance of the weakly contributing 2^1A_g state for $\hbar\Gamma$ = 0.0 eV in Figure 3-6 is not apparent in Figure 3-7. Inclusion of broadening eliminates the unphysical divergence for strongly contributing states, as well, but $\gamma_{xxxx}(-2\omega;\omega,\omega,0)$ does undergo resonant enhancement in these cases as evidenced in the 2ω resonance of the 1^1B_u state in Figure 3-7. Since the broadening

term makes $\gamma_{xxxx}(-2\omega;\omega,\omega,0)$ complex rather than purely real, we have plotted the real

and imaginary parts of $\gamma_{xxxx}(-2\omega;\omega,\omega,0)$ in Figure 3-7 along with the complex

magnitude. Measurements in a pure sample are sensitive only to the complex magnitude

of $<\gamma(-2\omega;\omega,\omega,0)>$, but sample mixtures allow separation of the real and imaginary

components. It should be noted that at low frequencies, the broadened and unbroadened

dispersions are indistinguishable.

The calculated dispersion of $\gamma_{xxxx}(-3\omega;\omega,\omega,\omega)$ for HT with $\hbar\Gamma = 0.2$ eV is

illustrated in Figure 5-8. Compared to the dispersion of $\gamma_{xxxx}(-2\omega;\omega,\omega,0)$, the first

resonance occurs at lower energy in $\gamma_{xxxx}(-3\omega;\omega,\omega,\omega)$. In THG, the ^1B_u states have

both ω and 3ω resonances while the ^1A_g states have only 2ω resonances. In DCSHG,

the ^1B_u states have ω and 2ω resonances while the ^1A_g states have only 2ω resonances.

Dispersion therefore occurs at lower frequencies in THG than DCSHG due to the 3ω

resonance of the 1^1B_u state. In the $\omega \rightarrow 0$ limit, on the other hand, we have the required

limit $\gamma_{xxxx}(-2\omega;\omega,\omega,0) = 6 \gamma_{xxxx}(-3\omega;\omega,\omega,\omega)$. The details of the mechanism for

nonresonant $\gamma_{xxxx}(-3\omega;\omega,\omega,\omega)$ of HT are in complete analogy to those of

$\gamma_{xxxx}(-2\omega;\omega,\omega,0)$ described earlier in this section.

D. Hexadecaoctaene ($N = 16$)

As an example of a long polyene chain, we now discuss in detail the origin of

$\gamma_{ijkl}(-\omega_4;\omega_1,\omega_2,\omega_3)$ in hexadecaoctaene (HDO), the chain with $N = 16$ carbon sites.

Most of the results are in direct analogy to those discussed in the previous section for

53

HT. The primary exception is the larger number of key virtual transitions involved in $\gamma_{ijkl}(-\omega_4;\omega_1,\omega_2,\omega_3)$ for HDO as compared to only the $1\,^1A_g \rightarrow 1\,^1B_u$ and $1\,^1B_u \rightarrow 5\,^1A_g$ virtual excitations and their corresponding type I and type II terms for HT.

The SCF ground state of HDO includes eight double-occupied π-electron MOs. Complete single and double-excited configuration interaction between the eight occupied and eight unoccupied MOs yields 2145 configurations which are diagonalized to form an equal number of states. More generally, a single and double-excited configuration interaction from n occupied to n unoccupied MOs results in $(n^2+1)\,n^2/2$ double-excited configurations and n^2 single-excited configurations in addition to the SCF ground state configuration. The calculated excitation energies $\hbar\omega_{ng}$ and transition moments $\mu^x_{n,g}$ and $\mu^x_{n,1^1B_u}$ are listed in Table 3-7 for the lowest energy excited states of HDO. The SDCI calculation yields a $1\,^1B_u$ excitation energy 0.06 eV smaller than the $2\,^1A_g$ excitation energy. As a general trend for the SDCI calculation, the energy gap between the $2\,^1A_g$ and $1\,^1B_u$ states decreases with increased chain length until the states become nearly degenerate at $N = 14$. Although this is in contrast to experimental data, in which the $2\,^1A_g - 1\,^1B_u$ gap increases with increased chain length, electron correlation is still well-accounted for at the SDCI level of calculation, and since the $2\,^1A_g$ state is not of primary importance to $\gamma_{ijkl}(-\omega_4;\omega_1,\omega_2,\omega_3)$, the SDCI calculation is an appropriate approximation. This will be confirmed by the agreement of the experimental results of chapters 5 and 6 with the extrapolated length dependence of $\langle\gamma(-\omega_4;\omega_1,\omega_2,\omega_3)\rangle$ from the SDCI calculations.

The calculated values for the individual DCSHG tensor components of HDO at 0.65 eV fundamental photon energy are $\gamma_{xxxx} = 909$, $\gamma_{xxyy} = 38.5$, $\gamma_{xyyx} = 38.0$, $\gamma_{yyxx} = 38.4$, $\gamma_{yxxy} = 37.9$, and $\gamma_{yyyy} = 5.1 \times 10^{-36}$ esu. The $\gamma_{xxxx}(-2\omega;\omega,\omega,0)$ component is even more dominant in the case of the $N = 16$ chain than in the $N = 6$ chain as a result of the increased aspect ratio of the longer chain. For the THG susceptibility $\gamma_{ijkl}(-3\omega;\omega,\omega,\omega)$, the calculated tensor components are $\gamma_{xxxx} = 199$, $\gamma_{xxyy} = 7.8$, $\gamma_{yyxx} = 7.8$, and $\gamma_{yyyy} = 1.0 \times 10^{-36}$ esu. The ratio $\gamma_{xxxx}(-2\omega;\omega,\omega,0) / \gamma_{xxxx}(-3\omega;\omega,\omega,\omega)$ is 4.6 at 0.65 eV, even smaller than the corresponding value 5.3 for HT. The greater deviation for the longer chain from the $\omega \rightarrow 0$ limit value of 6 for this ratio is due to the occurence of the 3ω resonance of the 3.52 eV 1^1B_u state of HDO for $\hbar\omega = 1.17$ eV compared to $\hbar\omega = 1.65$ eV for HT. The lower energy 3ω resonance for HDO increases the degree of dispersion between zero frequency and the fixed, nonresonant fundamental energy 0.65 eV.

The largest contributing terms of $\gamma_{xxxx}(-2\omega;\omega,\omega,0)$ for HDO at 0.65 eV are listed in Table 3-8 according to the same format as Table 3-5. The 1^1B_u state of HDO at 3.52 eV with $\mu^x_{1^1B_u,1^1A_g} = 11.55$ D plays a key role in $\gamma_{xxxx}(-2\omega;\omega,\omega,0)$ as in HT. In addition, the high-lying 10^1A_g two photon state at 5.77 eV with $\mu^x_{10^1A_g,1^1B_u} = 19.38$ D is also important. The two largest contributing virtual excitation processes are then the type II $1^1A_g \rightarrow 1^1B_u \rightarrow 10^1A_g \rightarrow 1^1B_u \rightarrow 1^1A_g$ process and the type I $1^1A_g \rightarrow 1^1B_u \rightarrow 1^1A_g \rightarrow 1^1B_u \rightarrow 1^1A_g$ process. In contrast to the HT case, however, there are other virtual excitation processes that make smaller but significant contributions to

$\gamma_{xxxx}(-2\omega;\omega,\omega,0)$. For instance, the 2^1A_g and 8^1A_g states are important due to their respective $\mu^x_{n,1^1B_u}$ values 6.95 and 5.57 D.

The transition density matrix diagrams for the 1^1A_g, 2^1A_g, and 10^1A_g states of HDO with the 1^1B_u state are illustrated in Figure 3-9. The $1^1A_g \rightarrow 1^1B_u$ virtual transition results in a somewhat modulated charge redistribution that leads to the fairly large $\mu^x_{1^1B_u,1^1A_g} = 11.55$ D whereas the $1^1B_u \rightarrow 2^1A_g$ transition has the charge redistribution concentrated at the center of the molecule such that $\mu^x_{2^1A_g,1^1B_u} = 6.95$ D. The $1^1B_u \rightarrow 10^1A_g$ transition, though, produces a highly charge separated distribution with large $\mu^x_{10^1A_g,1^1B_u} = 19.38$ D.

The $N = 16$ chain, HDO, has $\gamma_{xxxx}(-2\omega;\omega,\omega,0)$ 37 times larger than the corresponding value for the $N = 6$ chain even though the increase in chain length is only slightly larger than a factor of three. This is in large part due to the increase in the transition dipole moments between the 1^1A_g and 1^1B_u states and between the 1^1B_u state and the strongly coupled, highly correlated two-photon state (10^1A_g in the case of HDO). The increase in the transition moments derives from the delocalization of these states across the entire chain length. The large increase in $\gamma_{xxxx}(-2\omega;\omega,\omega,0)$ is also due, however, to other virtual excitation processes that contribute significantly in the long chain but not the short one and to the decrease in the excitation energies for the long chain. As in the case of HT, the statements made here concerning the origin of $\gamma_{xxxx}(-2\omega;\omega,\omega,0)$ in HDO are applicable to all other $\gamma_{xxxx}(-\omega_4;\omega_1,\omega_2,\omega_3)$ at nonresonant frequencies.

E. Length Dependence of $\gamma_{ijkl}(-\omega_4;\omega_1,\omega_2,\omega_3)$

Complete SDCI calculations of $\gamma_{ijkl}(-\omega_4;\omega_1,\omega_2,\omega_3)$ have been performed for the *trans* polyenes of chain length $N = 4$ to 16 carbon sites. In each case, the general origin of $\gamma_{ijkl}(-\omega_4;\omega_1,\omega_2,\omega_3)$ is similar to that described for the $N = 6$ and $N = 16$ cases, HT and HDO, respectively. The calculated individual tensor components of the DCSHG susceptibility $\gamma_{ijkl}(-2\omega;\omega,\omega,0)$ at 0.65 eV are listed in Table 3-9 for each chain length studied. For all chain lengths, the dominant tensor component is $\gamma_{xxxx}(-2\omega;\omega,\omega,0)$ which increases supralinearly with increased chain length. Figure 3-10 shows a log-log plot of $\gamma_{xxxx}(-2\omega;\omega,\omega,0)$ at 0.65 eV versus N. The good linear fit indicates that $\gamma_{xxxx}(-2\omega;\omega,\omega,0)$ possesses a power law dependence on N with an exponent of 3.9. The strong dependence of $\gamma_{xxxx}(-\omega_4;\omega_1,\omega_2,\omega_3)$ on N is the primary reason for the intense interest in conjugated linear chains as nonlinear optical materials. Although various power-law behaviors for $\gamma_{xxxx}(-\omega_4;\omega_1,\omega_2,\omega_3)$ have been previously reported based on delocalized, noninteracting electron models, those calculations are in strong disagreement with experiment in the magnitude, and in some cases, even the sign of $\gamma_{xxxx}(-\omega_4;\omega_1,\omega_2,\omega_3)$, and are therefore incomplete descriptions of third order optical properties.[9-11] The apparent similarity in power law behavior simply reflects the delocalized nature of the conjugated bonds in polyenes as compared to, for example, the linear dependence resulting from the bond additivity rule for localized bonds. We have confirmed the calculated power law dependence of $\gamma_{xxxx}(-\omega_4;\omega_1,\omega_2,\omega_3)$ on chain length

through our experimental DCSHG and THG measurements of HT and, especially, β-carotene, and the results are presented in Chapters 5 and 6.

Tables 3-10 through 3-14 list the calculated excitation energies and transition dipole moments for the lowest lying states of the $N = 4$ to 14 polyenes excluding $N = 6$. The corresponding data for $N = 6$ and 16 are given in Tables 3-4 and 3-7, respectively. For $N = 4$ and 8, there are just three key states and two principal virtual excitation processes in analogy to the case of $N = 6$ described in section C of this chapter. The 1^1A_g and 1^1B_u states are important because of the large transition dipole moment $\mu^x_{1^1B_u,1^1A_g}$ between them that leads to a major type I virtual excitation process. In addition, in each case, there exists a single, strongly correlated, high-lying two-photon state with a very large $\mu^x_{n,1^1B_u}$. For $N = 4$, this is the 4^1A_g state at an energy of 9.18 eV; and for $N = 8$, it is the 6^1A_g state at an energy of 7.16 eV. The type II virtual excitation processes for these respective states make positive contributions to $\gamma_{xxxx}(-\omega_4;\omega_1,\omega_2,\omega_3)$ that are larger in magnitude than the corresponding negative type I terms. The competition between these two processes determines the magnitude and sign of $\gamma_{xxxx}(-\omega_4;\omega_1,\omega_2,\omega_3)$. In the cases of the $N = 10$ and longer chains, $\gamma_{xxxx}(-\omega_4;\omega_1,\omega_2,\omega_3)$ has significant contributions from more than three key states and two virtual excitation processes. As described in Section D of this chapter for $N = 16$, larger numbers of two-photon and one-photon states play important roles in $\gamma_{xxxx}(-\omega_4;\omega_1,\omega_2,\omega_3)$ for the long chains.

In addition to the increase in $\gamma_{xxxx}(-\omega_4;\omega_1,\omega_2,\omega_3)$ with increased chain length due to the larger number of significant contributing virtual excitation processes, there are

two other principal length dependent factors that lead to rapid growth of $\gamma_{xxxx}(-\omega_4;\omega_1,\omega_2,\omega_3)$. First, the electronic excitation energies decrease with increased chain length. As an example, Figure 3-11 shows the calculated $1\,^1B_u$ excitation energy $\hbar\omega_{1\,^1B_u}$ plotted against $1/N$. The $1\,^1B_u$ excitation energy decreases proportionally to the inverse of the chain length with an infinite chain extrapolation of 2.8 eV. The decrease in excitation energies increases the individual terms contributing to $\gamma_{ijkl}(-\omega_4;\omega_1,\omega_2,\omega_3)$ since ω_{mg} appears in the denominator of Eq. (2.41) for each intermediate virtual state m.

Second, the magnitudes of the transition dipole moments along the chain axis x direction increase steadily with chain length. This is illustrated in Figure 3-12 where the calculated transition moment $\mu^x_{1\,^1B_u,1\,^1A_g}$ is plotted against N. Although the increase is less than linear, the transition moment does rise monotonically with increased chain length. The correlated π-electron virtual transitions produce a charge redistribution over a length comparable to that of the chain, and this leads to increased $\gamma_{xxxx}(-\omega_4;\omega_1,\omega_2,\omega_3)$ through the numerators of Eq. (2.41).

F. Single-Excited Configuration Interaction Results: Reduced Correlation

The importance of electron correlations to $\gamma_{ijkl}(-\omega_4;\omega_1,\omega_2,\omega_3)$ of conjugated linear chains is further illustrated by results obtained from calculations at the SCI level that purposely omit double-excited configurations (DCI) but are otherwise identical. As illustrated in Figure 3-13, at this level of calculation, the values calculated for

nonresonant $\gamma_{xxxx}(-2\omega;\omega,\omega,0)$ are negative in sign for all of the polyene chains, contrary to the experimental results. This disagreement occurs because the SCI calculation inadequately describes electron correlation which we have found to be of primary importance, such as in the illustrative case of the critical 5^1A_g state of HT. Instead, at the SCI level, $\gamma_{xxxx}(-\omega_4;\omega_1,\omega_2,\omega_3)$ is predicted to be dominated solely by the type I virtual excitation process which involves only the 1^1A_g and 1^1B_u states. There is no type II term analogous to the one found for the 5^1A_g state. Although the calculated sign of $\gamma_{xxxx}(-2\omega;\omega,\omega,0)$ for each case is negative in contrast to the positive values obtained from the SDCI calculations, the power law dependence of $\gamma_{xxxx}(-2\omega;\omega,\omega,0)$ on N is found to have an exponent of 3.9, the same as for SDCI calculations. This is, however, purely accidental since the SCI calculation omits major virtual excitation processes involved in $\gamma_{xxxx}(-2\omega;\omega,\omega,0)$. Thus, the predicted power law dependence alone does not serve to identify calculations that adequately describe the mechanism of $\gamma_{ijkl}(-\omega_4;\omega_1,\omega_2,\omega_3)$.

G. Linear Polarizability

Attempts have recently been made[12,13] to infer relative magnitudes of $\gamma_{ijkl}(-\omega_4;\omega_1,\omega_2,\omega_3)$ for various molecular structures from calculated results for the linear polarizability $\alpha_{ij}(-\omega;\omega)$ obtained through the expression

$$\alpha_{ij}(-\omega;\omega) = \frac{e^2}{\hbar} \sum_m \left[\frac{r^i_{gm}\, r^j_{mg}}{\omega_{mg} - \omega} + \frac{r^i_{mg}\, r^j_{gm}}{\omega_{mg} + \omega} \right] . \tag{3.4}$$

For each chain from $N = 4$ to 16 we have studied, the term in which the 1^1B_u state is the intermediate is by far the dominant contribution as evidenced, for example, in Table 3-16 where the individual terms contributing to $\alpha_{ij}(-\omega;\omega)$ of HT are listed in decreasing order. Since $\alpha_{ij}(-\omega;\omega)$ involves a summation over just a single intermediate state, for a centrosymmetric molecular structure, only one-photon states can contribute; and $\alpha_{ij}(-\omega;\omega)$ is then dominated by the large oscillator strength transition. Two-photon states cannot contribute to $\alpha_{ij}(-\omega;\omega)$ even though they play a key role in $\gamma_{ijkl}(-\omega_4;\omega_1,\omega_2,\omega_3)$. Since $\alpha_{xx}(-\omega;\omega)$ is dominated by the $1^1A_g \rightarrow 1^1B_u$ virtual transition which is fairly well described by independent particle models, the importance of electron correlation in polyenes that is clear in $\gamma_{ijkl}(-\omega_4;\omega_1,\omega_2,\omega_3)$ and in the two-photon states is not at all apparent in $\alpha_{ij}(-\omega;\omega)$. It is clear from the above discussion that it is inappropriate to draw conclusions concerning $\gamma_{ijkl}(-\omega_4;\omega_1,\omega_2,\omega_3)$ from $\alpha_{ij}(-\omega;\omega)$ since $\alpha_{ij}(-\omega;\omega)$ entirely neglects two-photon states and is insensitive to electron correlation while both of these are critical to an understanding of $\gamma_{ijkl}(-\omega_4;\omega_1,\omega_2,\omega_3)$. The calculated π-electron contributions to $\alpha_{xx}(-\omega;\omega)$ at 1.50 eV, plotted against N on a log-log scale for $N = 4$ to 16 in Figure 3-14, demonstrate a power law dependence with an exponent of 1.7.

Table 3-1. Character Table for the C_{2h} Symmetry Group.

Representation	E	C_2	i	σ_h
A_g	1	1	1	1
B_g	1	-1	1	-1
A_u	1	1	-1	-1
B_u	1	-1	-1	1

Table 3-2. CNDO/S Input Parameters for Carbon and Hydrogen Valence Shells.

| | Carbon | | Hydrogen |
	2s	2p	1s
$\zeta(\text{Å}^{-1})$	3.78	3.78	2.30
$I(\text{eV})$	21.3	11.5	13.6
$\gamma(\text{eV})$	11.1	11.1	12.8
$\beta(\text{eV})$	21.0	16.0	10.0

Table 3-3. Theoretical and Experimental Values for 1^1B_u and 2^1A_g Vertical Excitation Energies as a Function of Polyene Chain Length.

	1^1B_u (eV)		2^1A_g (eV)	
N(sites)	Theo.	Exp.[a]	Theo.	Exp.[a]
4	5.77	5.91	5.31	5.4[b,c]
6	4.94	4.93	4.59	4.0[b,d]
8	4.42	4.40	4.15	3.97
10	4.07	4.02	3.90	3.48
12	3.83	3.65	3.75	2.91

[a] B. S. Hudson, B. E. Kohler, and K. Schulten, in *Excited States*, Vol. 6, E. C. Lim, ed. (Academic, New York, 1982), p. 14.

[b] 0-0 excitation energy.

[c] R. R. Chadwick, D. P. Gerrity, and B. S. Hudson, Chem. Phys. Lett. 115, 24 (1985).

[d] B. S. Hudson and B. E. Kohler, Synth. Metals 9, 241 (1984).

Table 3-4. Calculated Symmetries, Excitation Energies, and Key Transition Dipole
Moments for the Lowest-Lying π-electron States of *trans*-Hexatriene ($N = 6$).

State	$\hbar\omega_{ng}$ (eV)	$\mu^x_{n,g}$ (D)	$\mu^x_{n,1^1B_u}$ (D)
2^1A_g	4.59	0.00	2.42
1^1B_u	4.94	6.66	0.00
2^1B_u	5.22	0.17	0.00
3^1A_g	6.69	0.00	1.68
4^1A_g	6.80	0.00	0.63
3^1B_u	7.55	0.93	0.00
5^1A_g	7.97	0.00	11.40
4^1B_u	8.07	1.05	0.00
6^1A_g	8.62	0.00	0.87
5^1B_u	9.11	0.23	0.00

Table 3-5. Largest Contributing Virtual Excitation Processes to $\gamma_{xxxx}(-2\omega;\omega,\omega,0)$ of

trans-Hexatriene at $\hbar\omega = 0.65$ eV.

m_1	m_2	m_3	Contribution (10^{-36} esu)	Cumulative (10^{-36} esu)
1^1B_u	5^1A_g	1^1B_u	47.5	47.5
1^1B_u	1^1A_g	1^1B_u	-25.9	21.6
1^1B_u	2^1A_g	1^1B_u	3.9	25.5
1^1B_u	8^1A_g	1^1B_u	1.9	27.4
4^1B_u	5^1A_g	1^1B_u	-1.7	25.7
1^1B_u	5^1A_g	4^1B_u	-1.7	24.0
8^1B_u	5^1A_g	1^1B_u	-1.2	22.8
1^1B_u	3^1A_g	1^1B_u	1.2	24.0

Table 3-6. Configuration Compositions of the 2^1A_g, 1^1B_u, and 5^1A_g States of *trans*-Hexatriene.

2^1A_g		1^1B_u	
Configuration	Coefficient	Configuration	Coefficient
$\Phi_{16},\Phi_{16}\rightarrow\Phi_{17},\Phi_{17}$	-0.572	$\Phi_{16}\rightarrow\Phi_{17}$	0.971
$\Phi_{16}\rightarrow\Phi_{18}$	0.473	$\Phi_{15}\rightarrow\Phi_{18}$	0.159
$\Phi_{15}\rightarrow\Phi_{17}$	-0.388	$\Phi_{15},\Phi_{16}\rightarrow\Phi_{17},\Phi_{17}$	-0.090
$\Phi_{15},\Phi_{16}\rightarrow\Phi_{17},\Phi_{18}$	0.274	$\Phi_{16},\Phi_{16}\rightarrow\Phi_{17},\Phi_{18}$	-0.070

5^1A_g	
Configuration	Coefficient
$\Phi_{15}\rightarrow\Phi_{17}$	-0.559
$\Phi_{16},\Phi_{16}\rightarrow\Phi_{17},\Phi_{17}$	0.554
$\Phi_{16}\rightarrow\Phi_{18}$	0.373
$\Phi_{15},\Phi_{16}\rightarrow\Phi_{17},\Phi_{18}$	-0.244

Table 3-7. Calculated Symmetries, Excitation Energies, and Key Transition Dipole

Moments for the Lowest-Lying π-electron States of *trans*-Hexadecaoctaene

($N = 16$).

State	$\hbar\omega_{ng}$ (eV)	$\mu^x_{n,g}$ (D)	$\mu^x_{n,1^1B_u}$ (D)
1^1B_u	3.52	11.55	0.00
2^1A_g	3.58	0.00	6.95
2^1B_u	3.83	0.30	0.00
3^1A_g	4.17	0.00	1.12
3^1B_u	4.48	0.07	0.00
4^1A_g	4.49	0.00	0.54
5^1A_g	4.64	0.00	2.90
6^1A_g	4.79	0.00	0.80
4^1B_u	5.03	0.04	0.00
5^1B_u	5.05	0.12	0.00
7^1A_g	5.12	0.00	0.54
6^1B_u	5.34	3.41	0.00
8^1A_g	5.39	0.00	5.57
9^1A_g	5.45	0.00	0.33
7^1B_u	5.75	0.12	0.00
10^1A_g	5.77	0.00	19.38
8^1B_u	5.81	0.19	0.00
9^1B_u	5.90	1.41	0.00
11^1A_g	6.01	0.00	0.63

68

Table 3-8. Largest Contributing Virtual Excitation Processes to $\gamma_{xxxx}(-2\omega;\omega,\omega,0)$ of

trans-Hexadecaoctaene ($N = 16$) at $\hbar\omega = 0.65$ eV.

m_1	m_2	m_3	Contribution (10^{-36} esu)	Cumulative (10^{-36} esu)
1^1B_u	10^1A_g	1^1B_u	1243.	1243.
1^1B_u	1^1A_g	1^1B_u	-712.	531.
1^1B_u	2^1A_g	1^1B_u	277.	808.
1^1B_u	8^1A_g	1^1B_u	111.	919.
9^1B_u	10^1A_g	1^1B_u	-74.	845.
1^1B_u	10^1A_g	9^1B_u	-71.	774.
6^1B_u	10^1A_g	1^1B_u	-66.	708.
1^1B_u	10^1A_g	6^1B_u	-64.	644.
1^1B_u	20^1A_g	1^1B_u	55.	699.
1^1B_u	18^1A_g	1^1B_u	54.	753.

.

Table 3-9. Calculated Tensor Components $\gamma_{ijkl}(-2\omega;\omega,\omega,0)$ at $\hbar\omega = 0.65$ eV for the

trans-Polyenes in 10^{-36} esu.

N (sites)	$xxxx$	$yyyy$	$xxyy$	$yyxx$	$xyyx$	$yxxy$
4	4.3	0.2	0.5	0.5	0.5	0.5
6	24.9	0.5	2.0	2.0	2.0	2.0
8	81.9	1.2	5.1	5.0	5.0	5.0
10	193.4	2.1	10.2	10.1	10.0	9.9
12	370	3.3	17.7	17.5	17.4	17.2
14	611	4.3	27.3	27.1	26.9	26.7
16	909	5.1	38.5	38.4	38.0	37.9

Table 3-10. Calculated Tensor Components $\gamma_{ijkl}(-3\omega;\omega,\omega,\omega)$ at $\hbar\omega = 0.65$ eV for the *trans*-Polyenes in 10^{-36} esu.

N (sites)	$xxxx$	$yyyy$	$xxyy$	$yyxx$
4	0.78	0.03	0.10	0.09
6	4.7	0.10	0.38	0.36
8	16.0	0.2	1.0	0.9
10	39.1	0.4	2.0	1.9
12	77.1	0.6	3.5	3.4
14	131	0.8	5.5	5.4
16	199	1.0	7.8	7.8

Table 3-11. Calculated Symmetries, Excitation Energies, and Key Transition Dipole Moments for the Lowest-Lying π-electron States of *trans*-Butadiene ($N = 4$).

State	$\hbar\omega_{ng}$ (eV)	$\mu^x_{n,g}$ (D)	$\mu^x_{n,1^1B_u}$ (D)
2^1A_g	5.31	0.00	1.45
1^1B_u	5.77	5.17	0.00
3^1A_g	7.51	0.00	1.14
2^1B_u	9.04	0.65	0.00
4^1A_g	9.18	0.00	8.34
3^1B_u	9.98	0.17	0.00
5^1A_g	10.81	0.00	1.96
4^1B_u	13.20	0.28	0.00

Table 3-12. Calculated Symmetries, Excitation Energies, and Key Transition Dipole Moments for the Lowest-Lying π-electron States of *trans*-Octatetraene $(N = 8)$.

State	$\hbar\omega_{ng}$ (eV)	$\mu^x_{n,g}$ (D)	$\mu^x_{n,1^1B_u}$ (D)
2^1A_g	4.16	0.00	3.43
1^1B_u	4.42	7.91	0.00
2^1B_u	4.78	0.14	0.00
3^1A_g	5.19	0.00	0.55
4^1A_g	6.01	0.00	2.15
5^1A_g	6.07	0.00	0.84
3^1B_u	6.47	0.02	0.00
4^1B_u	7.00	1.73	0.00
6^1A_g	7.16	0.00	13.78
5^1B_u	7.30	0.96	0.00
7^1A_g	7.42	0.00	2.40
8^1A_g	7.56	0.00	0.54

Table 3-13. Calculated Symmetries, Excitation Energies, and Key Transition Dipole

Moments for the Lowest-Lying π-electron States of *trans*-Decapentaene

$(N = 10)$.

State	$\hbar\omega_{ng}$ (eV)	$\mu^x_{n,g}$ (D)	$\mu^x_{n,1^1B_u}$ (D)
2^1A_g	3.90	0.00	4.45
1^1B_u	4.07	8.98	0.00
2^1B_u	4.41	0.16	0.00
3^1A_g	4.92	0.00	0.85
3^1B_u	5.16	0.05	0.00
4^1A_g	5.48	0.00	2.37
5^1A_g	5.53	0.00	1.09
4^1B_u	6.03	0.03	0.00
6^1A_g	6.30	0.00	1.27
5^1B_u	6.48	2.36	0.00
7^1A_g	6.59	0.00	14.72
8^1A_g	6.77	0.00	6.47
6^1B_u	6.78	0.79	0.00
7^1B_u	7.06	0.01	0.00

Table 3-14. Calculated Symmetries, Excitation Energies, and Key Transition Dipole

Moments for the Lowest-Lying π-electron States of *trans*-Dodecahexaene

$(N = 12)$.

State	$\hbar\omega_{ng}$ (eV)	$\mu^x_{n,g}$ (D)	$\mu^x_{n,1^1B_u}$ (D)
2^1A_g	3.75	0.00	5.39
1^1B_u	3.83	9.93	0.00
2^1B_u	4.15	0.21	0.00
3^1A_g	4.60	0.00	0.98
3^1B_u	4.97	0.06	0.00
4^1A_g	5.08	0.00	1.77
5^1A_g	5.13	0.00	2.15
6^1A_g	5.15	0.00	0.61
4^1B_u	5.62	0.06	0.00
7^1A_g	6.02	0.00	2.69
5^1B_u	6.03	2.80	0.00
8^1A_g	6.13	0.00	10.68
6^1B_u	6.19	0.07	0.00
9^1A_g	6.30	0.00	14.04
7^1B_u	6.40	0.91	0.00
8^1B_u	6.59	0.03	0.00

Table 3-15. Calculated Symmetries, Excitation Energies, and Key Transition Dipole Moments for the Lowest-Lying π-electron States of *trans*-Tetradecaheptaene ($N = 14$).

State	$\hbar\omega_{ng}$ (eV)	$\mu_{n,g}^x$ (D)	$\mu_{n,1^1B_u}^x$ (D)
2^1A_g	3.65	0.00	6.23
1^1B_u	3.65	10.78	0.00
2^1B_u	3.96	0.25	0.00
3^1A_g	4.35	0.00	1.06
3^1B_u	4.71	0.07	0.00
4^1A_g	4.75	0.00	0.99
5^1A_g	4.84	0.00	2.75
6^1A_g	5.01	0.00	0.75
4^1B_u	5.13	0.03	0.00
5^1B_u	5.30	0.08	0.00
6^1B_u	5.65	3.14	0.00
7^1A_g	5.69	0.00	4.61
8^1A_g	5.73	0.00	5.46
9^1A_g	5.99	0.00	17.73
7^1B_u	6.01	0.10	0.00
8^1B_u	6.11	1.12	0.00

76

Table 3-16. Contributions of π-electron States to $\alpha_{xx}(-\omega;\omega)$ of *trans*-Hexatriene at $\hbar\omega = 0.65$ eV.

State	Energy (eV)	$\alpha_{xx}(-\omega;\omega)$ (10^{-24} esu)
1^1B_u	4.94	4.12
4^1B_u	8.07	0.06
3^1B_u	7.55	0.05
8^1B_u	11.34	0.006

(a)

(b)

Figure 3-1. Schematic diagrams of the molecular structures for (a) all-*trans* and (b) *cis-transoid* hexatriene (HT).
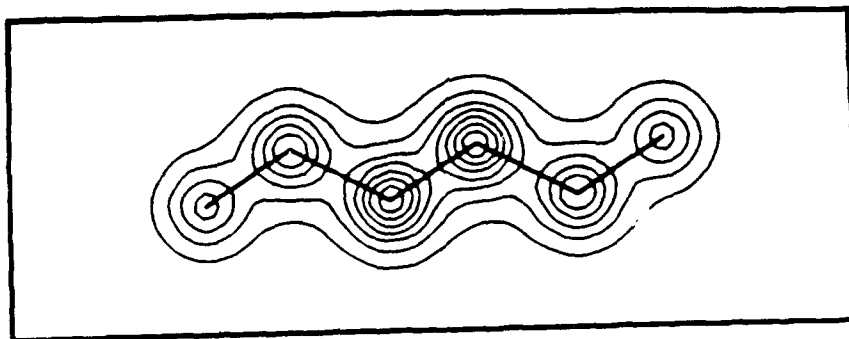
(a)
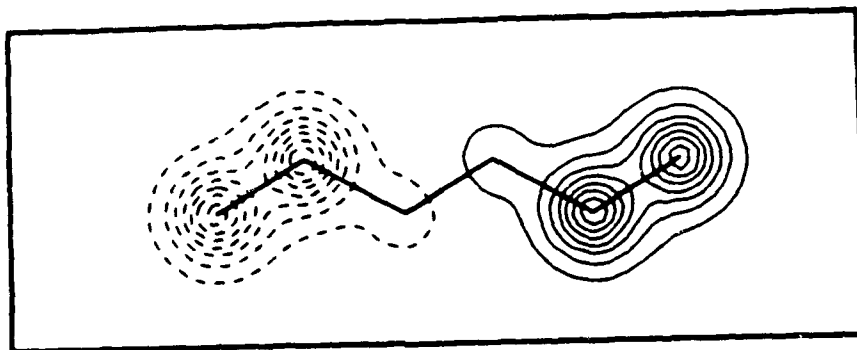
(b)
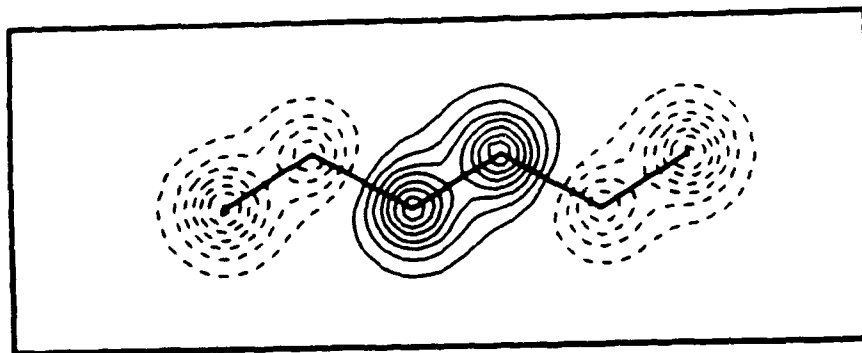
(c)

Figure 3-2. Contour diagrams of the three occupied π-electron molecular orbitals of HT in order of increasing energy. The orbitals are numbered (a) Φ_{13}, (b) Φ_{15}, and (c) Φ_{16}. The contour cuts are taken 0.4 Å above the molecular plane.

79
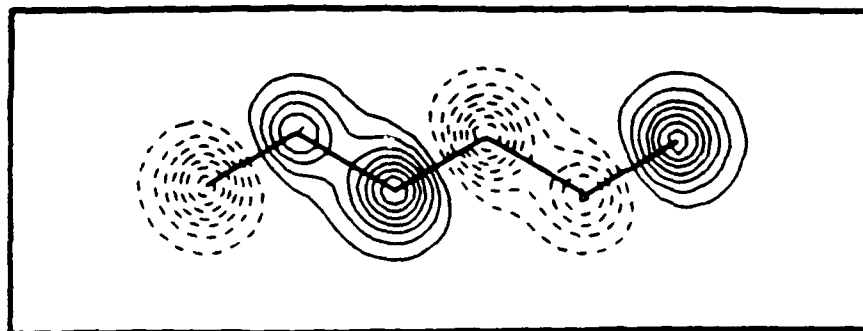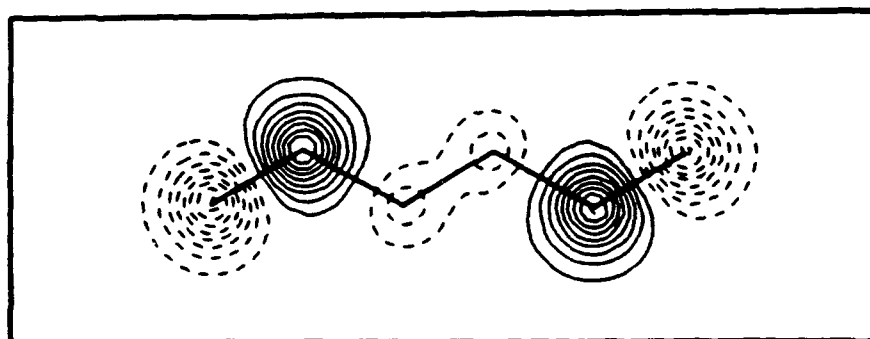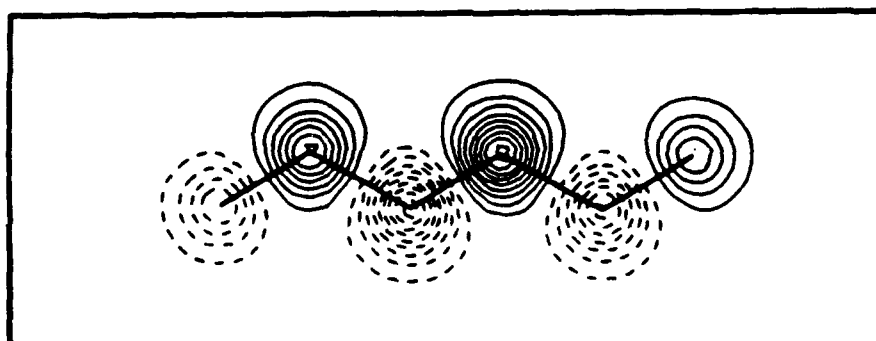
Figure 3-3. Contour diagrams of the three unoccupied π-electron molecular orbitals of HT in order of increasing energy. The orbitals are numbered (a) Φ_{17}, (b) Φ_{18}, and (c) Φ_{19}.
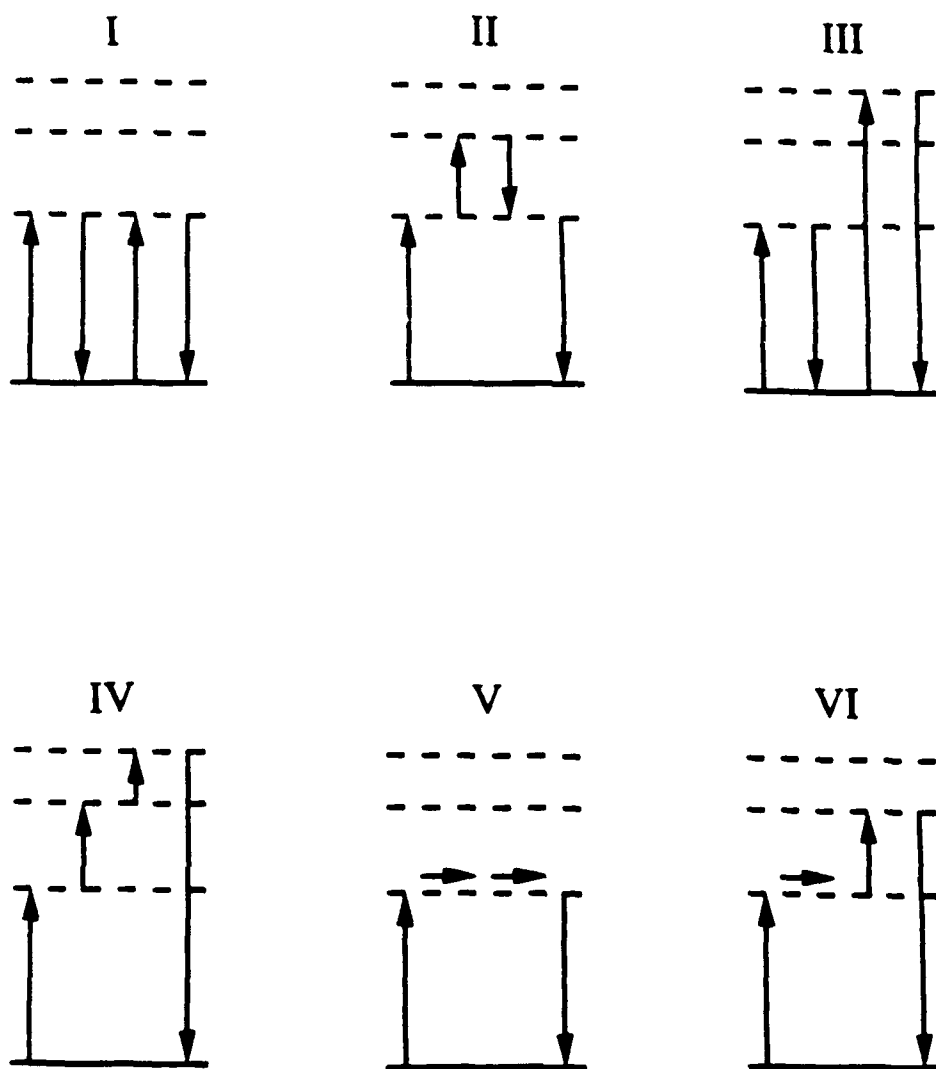
Figure 3-4. The six general types of third order virtual excitation processes that contribute to $\gamma_{ijkl}(-\omega_4;\omega_1,\omega_2,\omega_3)$. Types I - IV are allowed for molecular structures of any symmetry; types V and VI are only allowed for noncentrosymmetric molecular structures.
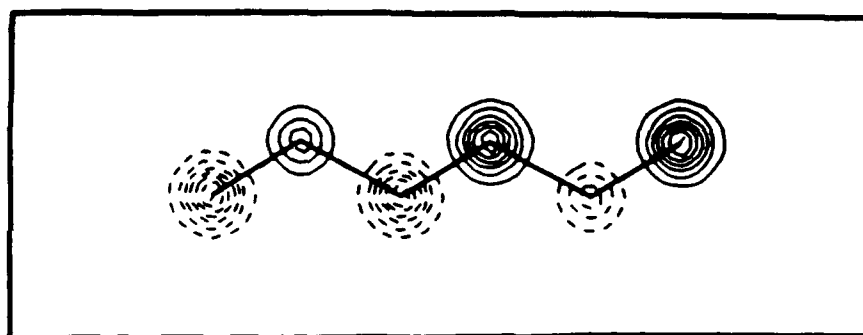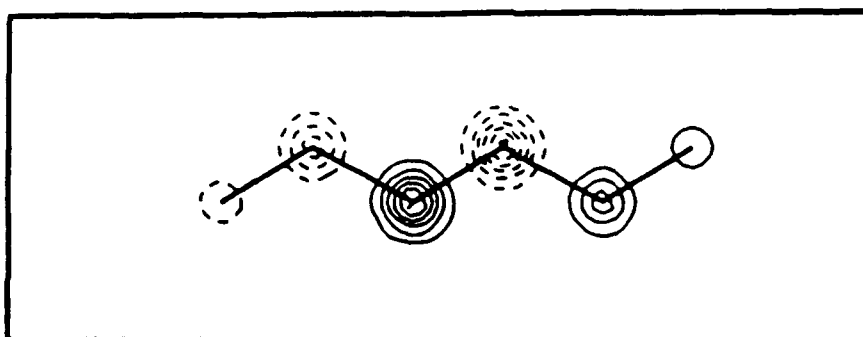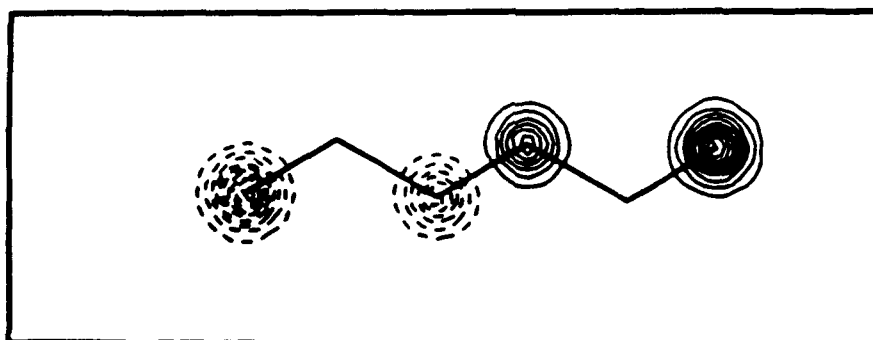
Figure 3-5. Transition density matrix contour diagrams of *trans*-HT for the (a) ground, (b) 2^1A_g, and (c) 5^1A_g states with the 1^1B_u state. The corresponding x-components of the transition dipole moments are 6.66, 2.42, and 11.40 D, respectively. The contour cuts are taken 0.4 Å above the molecular plane.

82
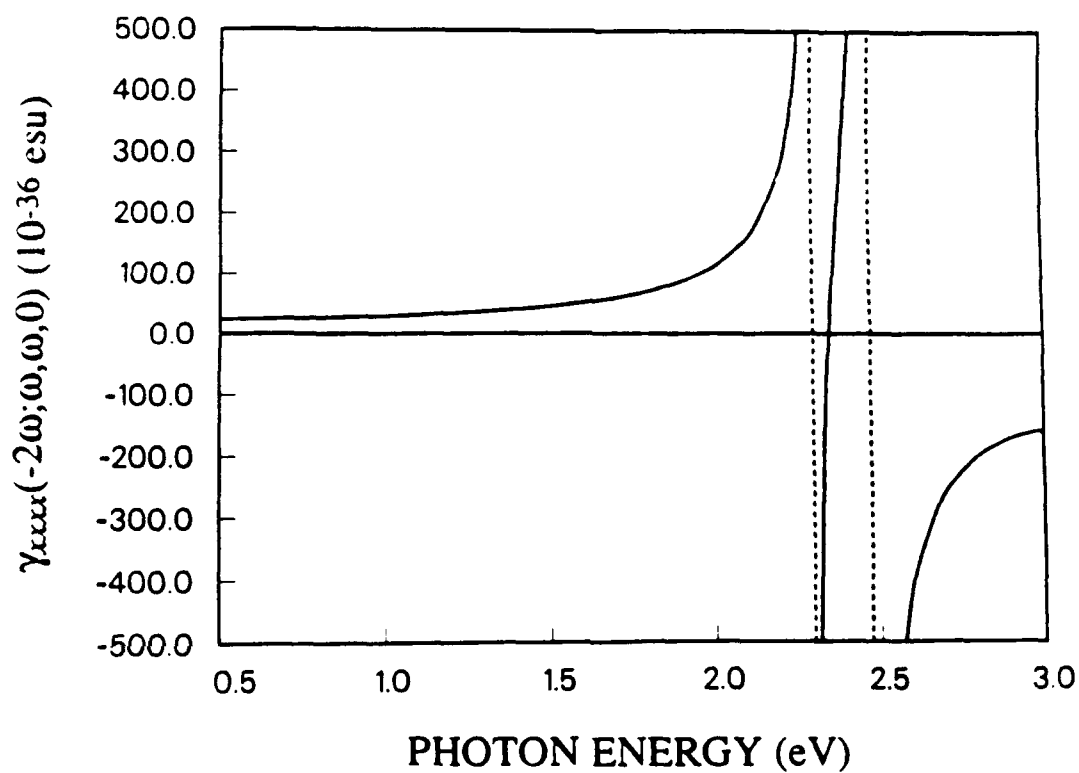
Figure 3-6. Calculated dispersion of $\gamma_{xxxx}(-2\omega;\omega,\omega,0)$ for *trans*-HT with $\hbar\Gamma = 0$. The first vertical dash locates the 2ω resonance of the 1^1A_g state and the second locates the 2ω resonance of the 1^1B_u state.
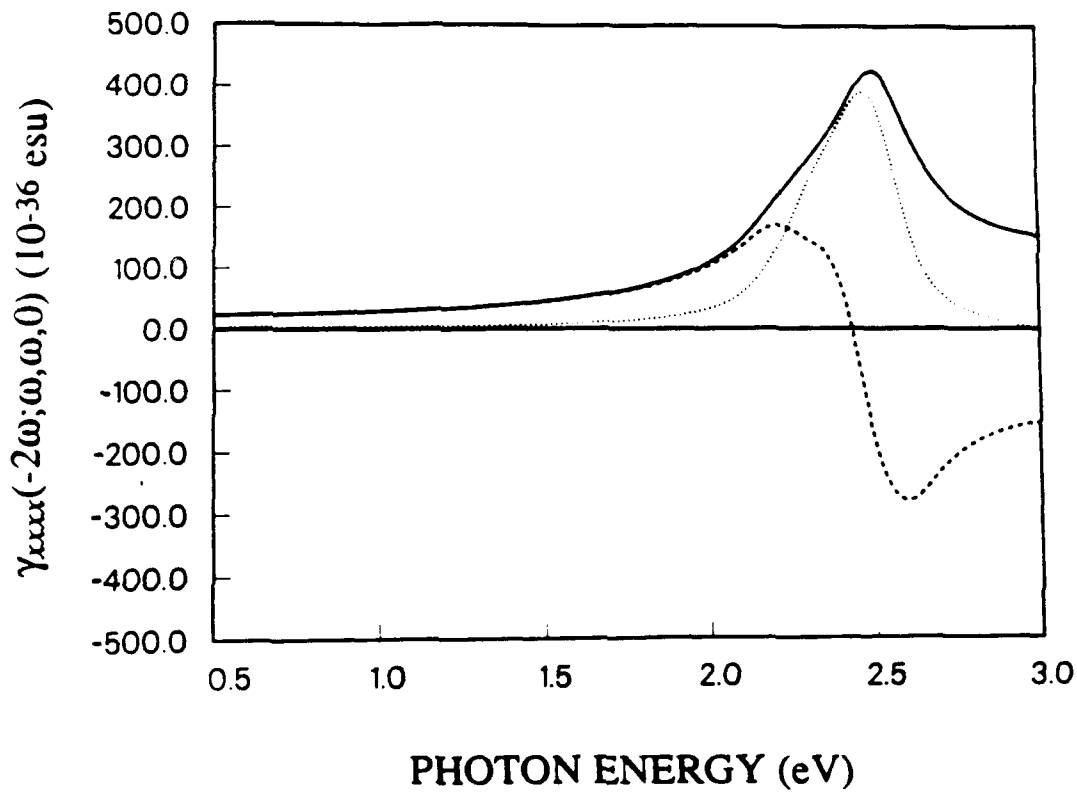
Figure 3-7. Calculated dispersion of $\gamma_{xxxx}(-2\omega;\omega,\omega,0)$ for *trans*-HT with $\hbar\Gamma = 0.2$ eV. The solid curve is $|\gamma_{xxxx}(-2\omega;\omega,\omega,0)|$ and the dashed and dotted curves are $\text{Re}[\gamma_{xxxx}(-2\omega;\omega,\omega,0)]$ and $\text{Im}[\gamma_{xxxx}(-2\omega;\omega,\omega,0)]$, respectively.
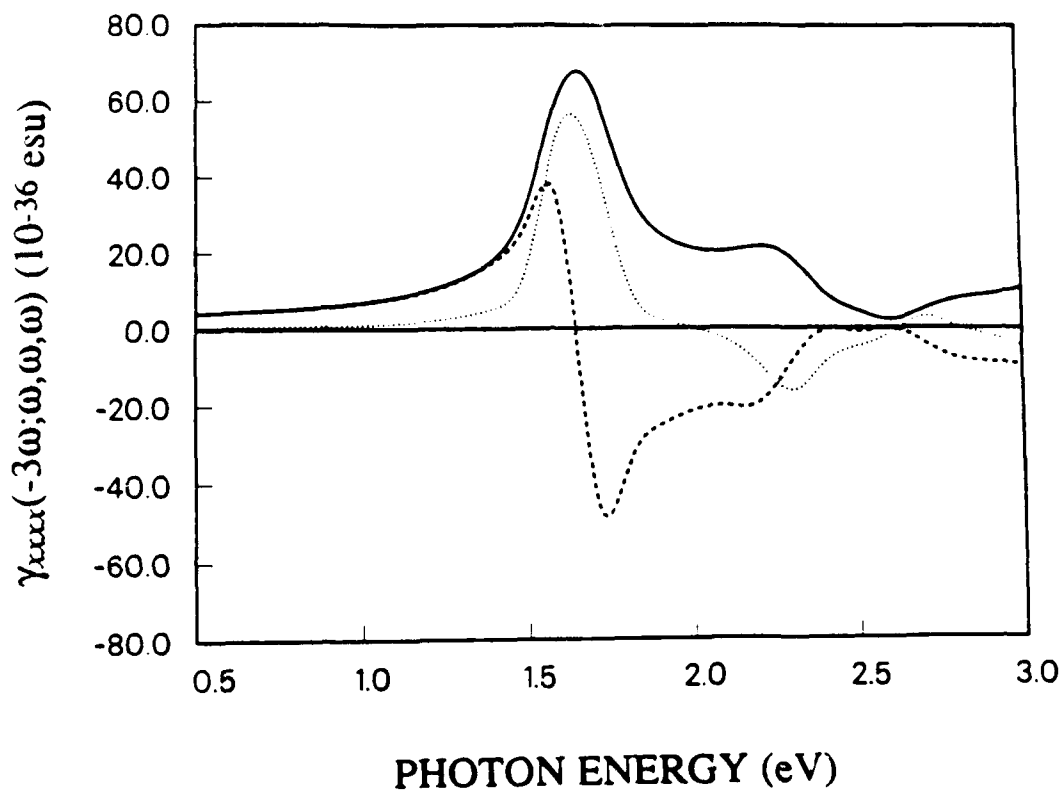
Figure 3-8. Calculated dispersion of $\gamma_{xxxx}(-3\omega;\omega,\omega,\omega)$ for *trans*-HT with $\hbar\Gamma = 0.2$ eV. The solid curve is $|\gamma_{xxxx}(-3\omega;\omega,\omega,\omega)|$ and the dashed and dotted curves are $Re[\gamma_{xxxx}(-3\omega;\omega,\omega,\omega)]$ and $Im[\gamma_{xxxx}(-3\omega;\omega,\omega,\omega)]$, respectively.
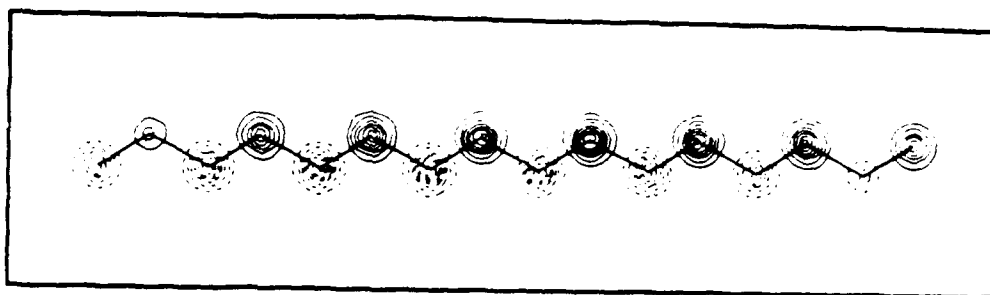
(a)
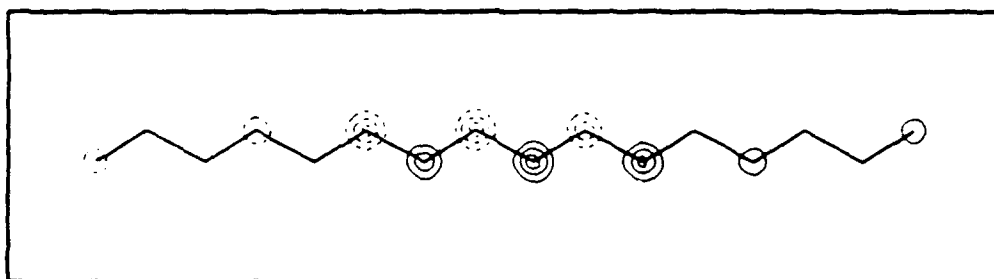
(b)
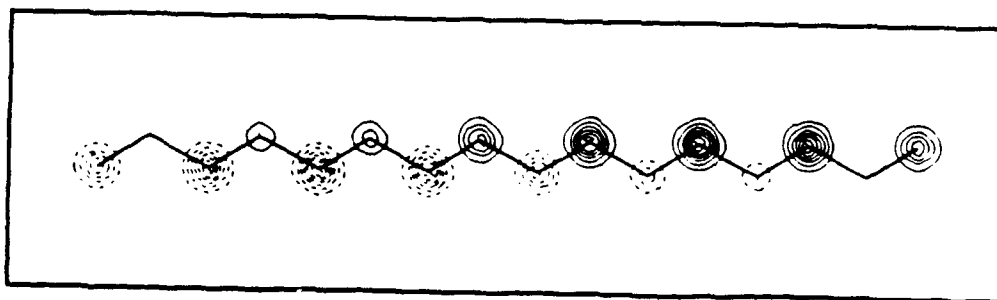
(c)

Figure 3-9. Transition density matrix contour diagrams of *trans*-hexadecaoctaene (HDO) for the (a) ground, (b) 2^1A_g, and (c) 10^1A_g states with the 1^1B_u state. The corresponding *x*-components of the transition dipole moments are 11.55, 6.95, and 19.38 D, respectively.
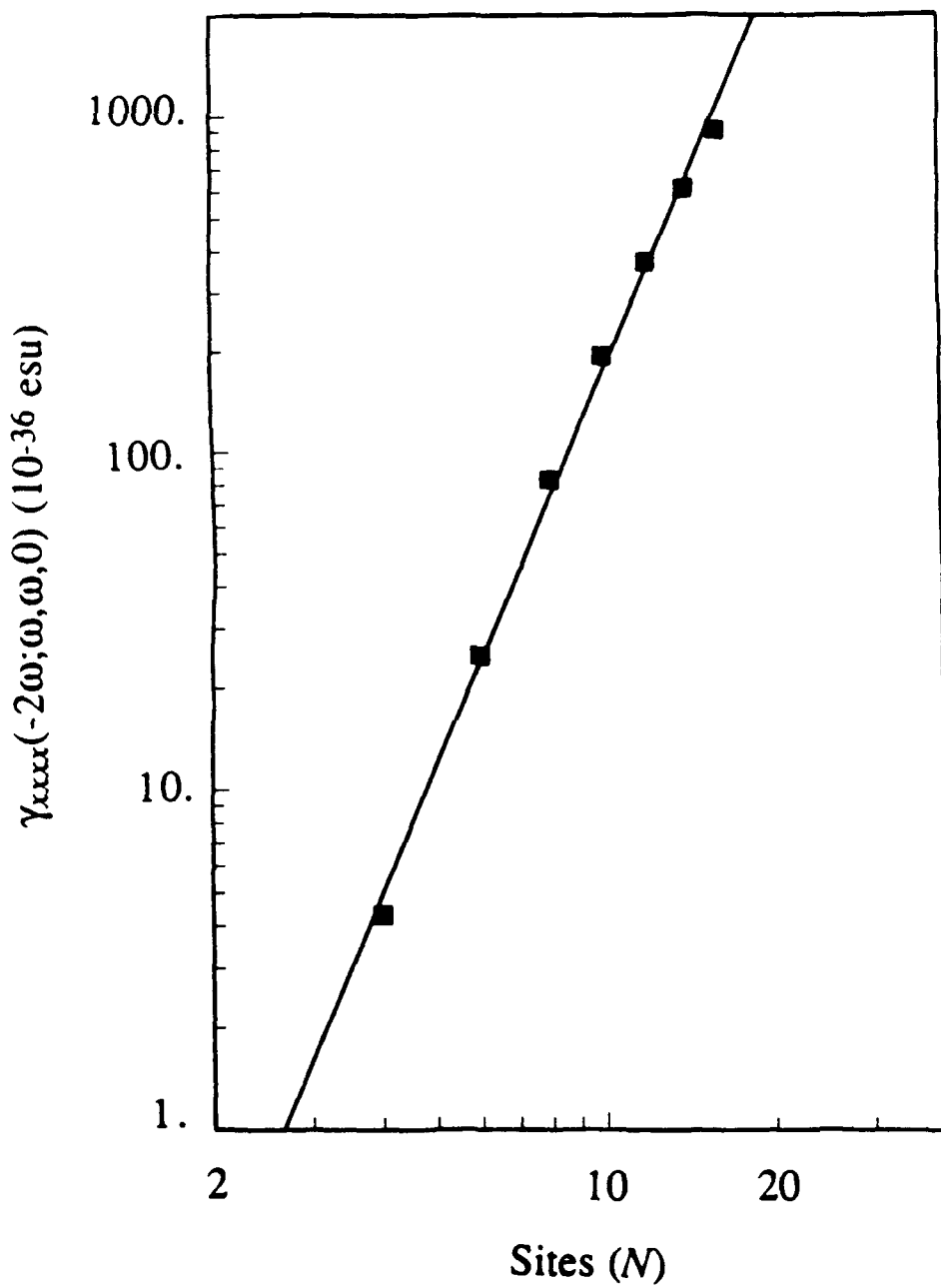
Figure 3-10. Log-log plot of $\gamma_{xxxx}(-2\omega;\omega,\omega,0)$ at $\hbar\omega = 0.65$ eV versus the number N of carbon atom sites in the the polyene chain. The linear fit corresponds to $\gamma_{xxxx}(-2\omega;\omega,\omega,0) \propto N^{3.9}$.
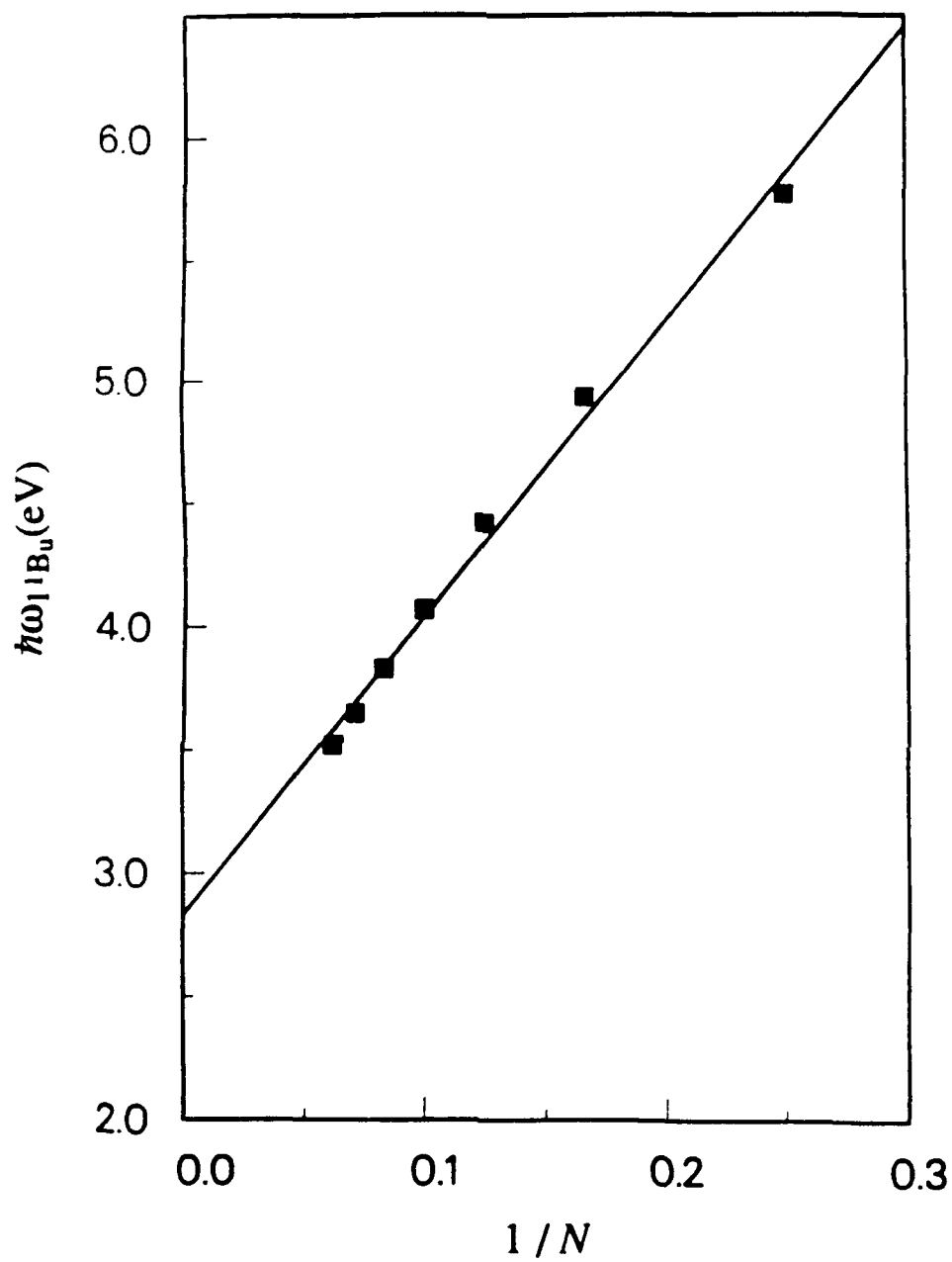
Figure 3-11. The calculated 1^1B_u excitation energy of *trans* polyenes as a function of inverse number of sites in the chain.
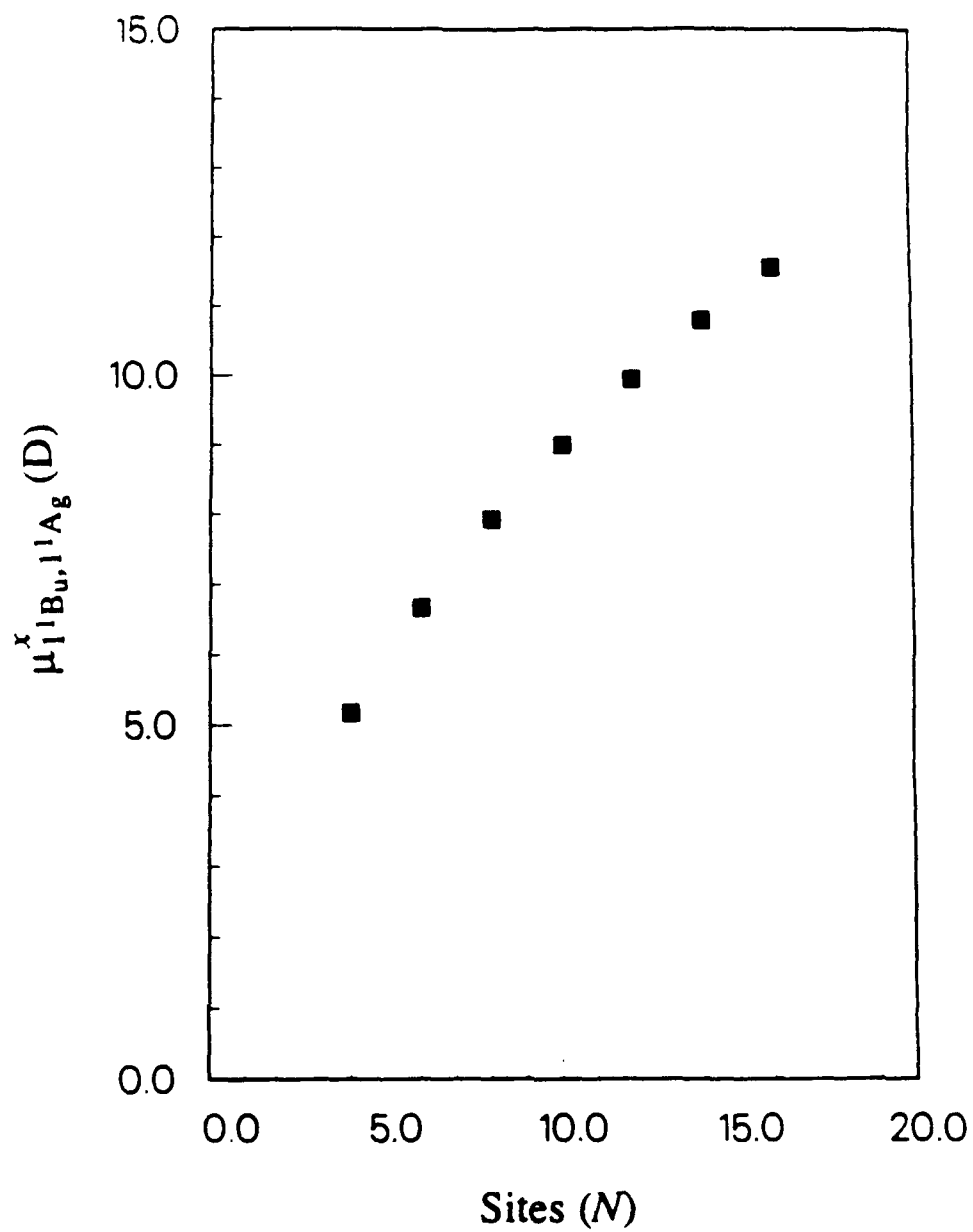
Figure 3-12. The x-component of the transition dipole moment between the ground and $1\,^1B_u$ states as a function of the number of sites in the chain.
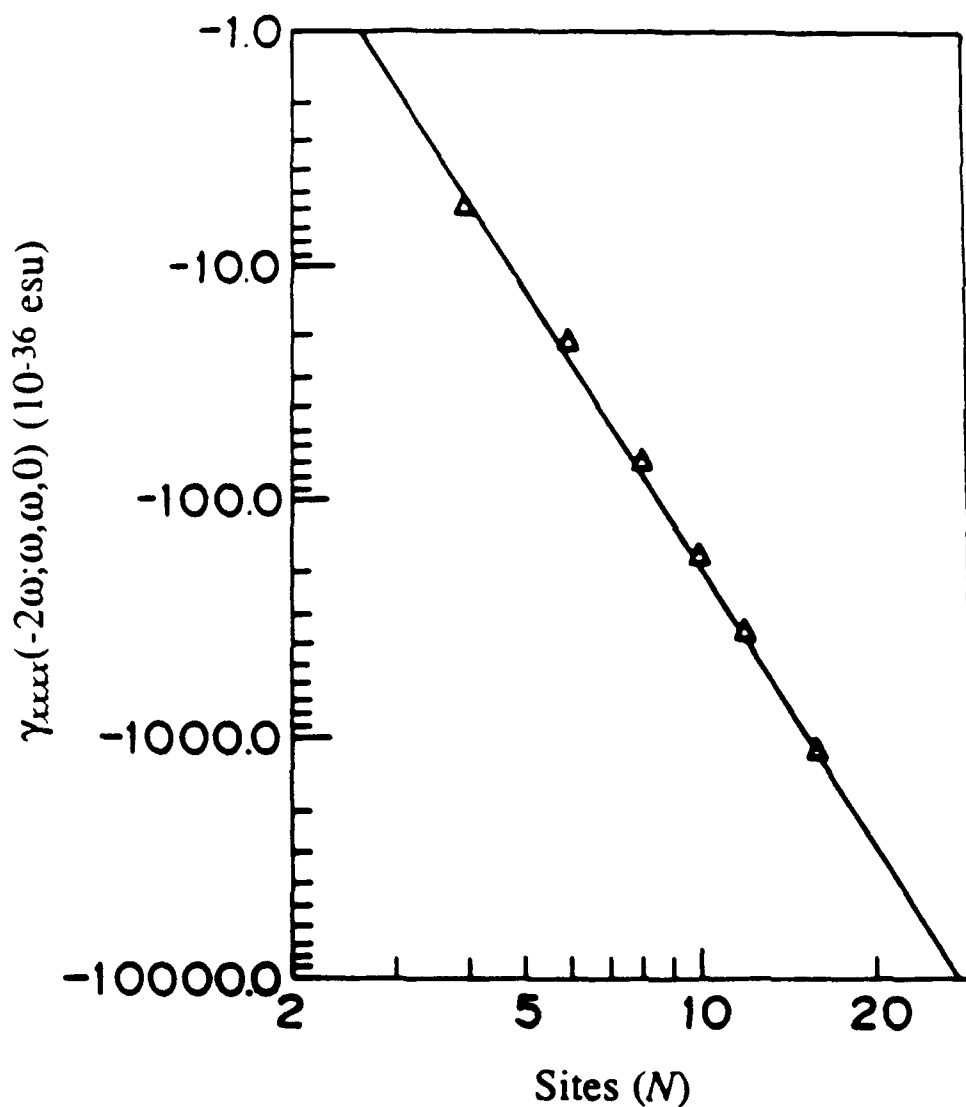
Figure 3-13. Log-log plot of $\gamma_{xxxx}(-2\omega;\omega,\omega,0)$ at 0.65 eV versus the number N of carbon atom sites in the the polyene chain for a calculation at the SCI level. Contrary to experiment and multiple-excited configuration interaction calculations, the values of $\gamma_{xxxx}(-2\omega;\omega,\omega,0)$ are negative for this reduced correlation calculation.
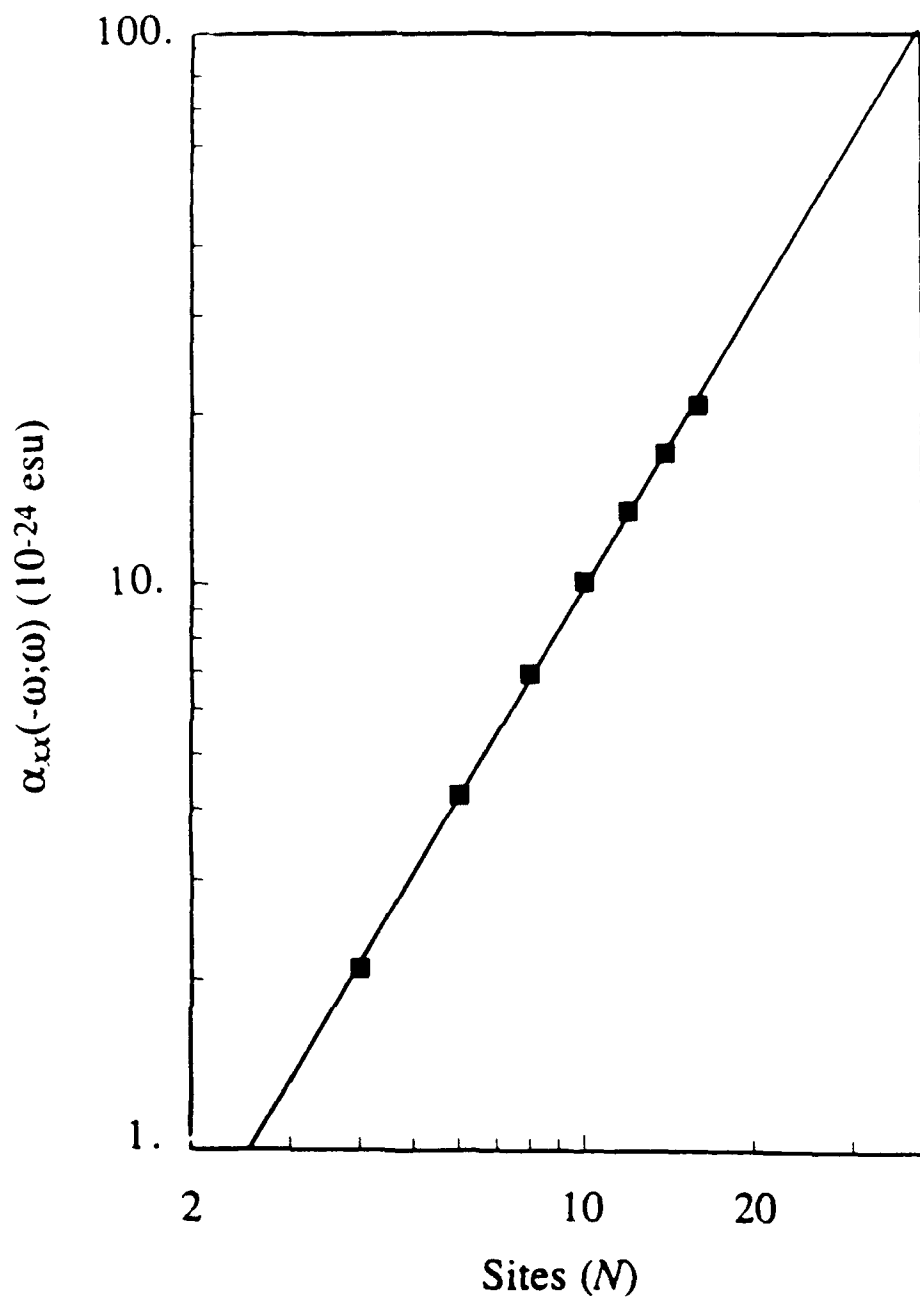
Figure 3-14. Log-log plot of the calculated π-electron contribution to $\alpha_{xx}(-\omega;\omega)$ at $\hbar\omega = 1.50$ eV versus the number of sites N. The linear fit corresponds to $\alpha_{xx}(-\omega;\omega) \propto N^{1.7}$.

Chapter 3 References

1. See B. S. Hudson, B. E. Kohler, and K. Schulten, in *Excited States*, Vol. 6, E. C. Lim, ed. (Academic, New York, 1982); and references therein for an excellent review of the linear optical properties of polyenes.

2. M. Traetteberg, Acta Chem. Scand. **22**, 628 (1968).

3. See, for example, F. A. Cotton, *Chemical Applications of Group Theory* (Wiley, New York, 1971).

4. K. Schulten, U. Dinur, and B. Honig, J. Chem. Phys. **73**, 3927 (1980).

5. I. Ohmine, M. Karplus, and K. Schulten, J. Chem. Phys. **68**, 2298 (1978).

6. B. S. Hudson and B. E. Kohler, Chem. Phys. Lett. **14**, 299 (1972); J. Chem. Phys. **59**, 4984 (1973).

7. K. Schulten and M. Karplus, Chem. Phys. Lett. **15**, 305 (1972).

8. J. F. Ward and D. S. Elliott, J. Chem. Phys. **69**, 5438 (1978).

9. G. P. Agrawal, C. Cojan, and C. Flytzanis, Phys. Rev. **B17**, 776 (1978).

10. E. McIntyre and H. H. Hameka, J. Chem. Phys. **68**, 3481 (1978).

11. D. N. Beratan, J. N. Onuchic, and J. W. Perry, J. Phys. Chem. **91**, 2696 (1987).

12. V. P. Bodart *et al.*, , J. Opt. Soc. Am. **B4**, 1047 (1987).

13. J. L. Bredas, in *Photoresponsive Materials*, S. Tazuke, ed. (Mater. Res. Soc., Pittsburgh, PA, 1989) p. 33.

Chapter 4

EFFECTS OF CONFORMATION AND

NONCENTROSYMMETRY ON $\gamma_{ijkl}(-\omega_4;\omega_1,\omega_2,\omega_3)$

A. Introduction

Having discussed in detail the origin of the third order optical properties of all-trans polyenes, we now consider the effects on $\gamma_{ijkl}(-\omega_4;\omega_1,\omega_2,\omega_3)$ of changes in the structural conformation and symmetry to this archetypal structure for the general class of conjugated linear chains. As a first important case, we discuss the effect of structural conformation by way of the *cis-transoid*, or simply *cis* form. The origin of $\gamma_{ijkl}(-\omega_4;\omega_1,\omega_2,\omega_3)$ in *cis* polyenes is found to be identical to that for *trans*, though the *cis* conformation possesses smaller $\gamma_{xxxx}(-\omega_4;\omega_1,\omega_2,\omega_3)$. The reduction of $\gamma_{xxxx}(-\omega_4;\omega_1,\omega_2,\omega_3)$, as we shall see, is a geometrical result of the reduced physical length of the molecular structure.

The next important effect on $\gamma_{ijkl}(-\omega_4;\omega_1,\omega_2,\omega_3)$ is that of lowered symmetry realized by heteroatom substitution of electron donating and accepting groups to the ends of the polyene chain. The creation of a noncentrosymmetric molecular structure introduces previously forbidden virtual excitation processes to $\gamma_{ijkl}(-\omega_4;\omega_1,\omega_2,\omega_3)$. The new virtual processes, which involve diagonal matrix elements of the dipole moment operator, lead to an order of magnitude enhancement of $\gamma_{xxxx}(-\omega_4;\omega_1,\omega_2,\omega_3)$ compared to the corresponding centrosymmetric conjugated linear chain.

93

B. Structural Conformation: *cis-transoid* Polyenes

The *cis* conformation is schematically illustrated in Figure 3-1(b) for the case of $N = 6$. No *cis-transoid* form of BD ($N = 4$) is possible, so we will make comparison between our *trans* and *cis* calculations for chains from $N = 6$ to 16 sites. The first point to note is that not all of these chains belong to the same symmetry group. The *cis* chains with an odd number of short bonds ($N = 6, 10, 14,...$) are not centrosymmetric and possess C_{2v} symmetry whereas the chains with an even number of short bonds ($N = 8, 12, 16,...$) belong to the C_{2h} group along with the *trans* conformations. The states of the C_{2v} group are identified as A_1, A_2, B_1, and B_2 in contrast to the familliar A_g and B_u of C_{2h}. For $\pi \rightarrow \pi^*$ excitations, the states must be either A_1 or B_2 symmetry, the ground state being always $^1A_1$.

The corresponding one-photon dipole-allowed selection rules are also somewhat different for the two symmetry groups. For C_{2h}, only the ^1B_u states are one-photon allowed transitions from the 1^1A_g ground state for any electric field polarization. However, for the *cis* chains in the C_{2v} symmetry group, where the y-axis is the axis of C_2 two-fold rotational symmetry (perpendicular to the conjugation axis and in the molecular plane), the $^1B_2$ states are one-photon allowed for fields polarized along the x-axis and the excited $^1A_1$ states are the one-photon allowed transitions for polarizations along y. This implies that all of the singlet $\pi \rightarrow \pi^*$ excitations are one-photon allowed transitions for the chains that are members of the C_{2v} group. But it should be noted that

94

because these chains are quasi-one dimensional, the x-components of the transition

dipole moments will, in general, far exceed the y-components, and the oscillator

strengths of the $^1B_2$ states will therefore dominate those of the $^1A_1$ states. We will

therefore consider the $^1A_1$ and $^1B_2$ states of the C_{2v} group to be analogous to the ^1A_g

and ^1B_u states of the C_{2h} group, respectively.

For the range of chain lengths that we have considered, we find that the

transition energies of the 1^1B_u and 2^1A_g states of the *cis* conformations are slightly red-

shifted from the values for the *trans* conformations by 0.02 to 0.10 eV with the shift

constantly increasing with increased chain length. These results are in agreement with

the literature.[1,2] For example, an experimental gas phase absorption study of the *cis*

and *trans* forms of HT[2] found $1^1B_u \leftarrow 1^1A_g$ transition energies of 4.919 and 4.935 eV,

respectively, which is in very good correspondence with our calculated transition

energies of 4.92 and 4.94 eV.

The calculated energies and x and y components of the transition dipole moments

$\mu_{n,g}$ and $\mu_{n,1^1B_2}$ for the low-lying states of *cis*-HT are listed in Table 4-1. The y-

components of the transition moments are seen to be small and non-zero only for states

of like parity. The largest transition moment involving the ground state is $\mu^x_{1^1B_2,g} =$

6.83 D, and the largest transition moment of all is $\mu^x_{5^1A_1,1^1B_2} = 10.49$ D. These two

virtual transitions dominate $\gamma_{xxxx}(-\omega_4;\omega_1,\omega_2,\omega_3)$ in analogy with *trans*-HT.

The calculated values of the independent tensor components of $\gamma_{ijkl}(-2\omega;\omega,\omega,0)$

for *cis*-HT at 0.65 eV are $\gamma_{xxxx} = 20.3$, $\gamma_{xxyy} = 1.9$, $\gamma_{xyyx} = 1.8$, $\gamma_{yyxx}=1.7$, $\gamma_{yxxy} =$

1.8, and $\gamma_{yyyy} = 0.5 \times 10^{-36}$ esu. Although the components involving the y-direction

have different selection rules than those involving x, the dominant tensor component remains $\gamma_{xxxx}(-2\omega;\omega,\omega,0)$. The individual terms that contribute to $\gamma_{xxxx}(-2\omega;\omega,\omega,0)$ are listed in order of descending magnitude in Table 4-2. As in the case of *trans*-HT, the largest term is positive and results from the $g \rightarrow 1^1B_2 \rightarrow 5^1A_1 \rightarrow 1^1B_2 \rightarrow g$ virtual excitation process. This type II term and the negative $g \rightarrow 1^1B_2 \rightarrow 1^1A_1 \rightarrow 1^1B_2 \rightarrow g$ type I term are almost entirely responsible for the sign and magnitude of $\gamma_{xxxx}(-2\omega;\omega,\omega,0)$ in *cis*-HT.

Transition density matrix diagrams of the key virtual excitations of *cis*-HT are shown in Figure 4-1. The transition density matrix diagrams for *cis*-HT are nearly identical to those for *trans*-HT shown in Figure 3-5. The (a) *cis* $1^1A_1 \rightarrow 1^1B_2$ virtual transition results in a somewhat modulated redistribution of charge with a transition moment of 6.83 D. For the transition involving the high-lying, strongly correlated two-photon 5^1A_1 state, however, there is a resultant highly separated charge redistribution in the (b) *cis* $1^1B_2 \rightarrow 5^1A_1$ virtual excitation. The corresponding transition moment is 10.49 D for the *cis* conformation, compared to 11.40 D for *trans*-HT.

Chapters 5 and 6 of this thesis present experimental results for the isotropically averaged susceptibilities $\langle\gamma(-2\omega;\omega,\omega,0)\rangle$ and $\langle\gamma(-3\omega;\omega,\omega,\omega)\rangle$ of HT measured in the neat liquid . The isotropically averaged susceptibility is shown in Appendix B to be given by

$$\langle\gamma(-\omega_4;\omega_1,\omega_2,\omega_3)\rangle = \frac{1}{5}\left[\sum_i \gamma_{iiii} + \frac{1}{3}\sum_{i \neq j}(\gamma_{iijj} + \gamma_{ijij} + \gamma_{ijji})\right]. \qquad (4.1)$$

96

Since the only commercially available HT was found by chromatographic methods[2] to contain 60% of the *trans* conformation and 40% of the *cis*, we will calculate $\langle\gamma(-2\omega;\omega,\omega,0)\rangle$ and $\langle\gamma(-3\omega;\omega,\omega,\omega)\rangle$ weighted accordingly by those fractions of *trans* and *cis* isomers for comparison with experiment.

As a further refinement, we note that although the π-electron contribution to $\langle\gamma(-\omega_4;\omega_1,\omega_2,\omega_3)\rangle$ dominates the σ-electron contribution for long conjugated chains, the two contributions are comparable for HT. Kajzar and Messier have measured $\langle\gamma(-3\omega;\omega,\omega,\omega)\rangle$ in a series of nonconjugated alkane chains and found that the results are well-explained by the bond additivity approximation.[3] The best fit to the experimental data obtains values of 0.0148×10^{-36} esu for each carbon-carbon bond and 0.0250×10^{-36} esu for each carbon-hydrogen bond. These quoted values are 8.0 times smaller than the values listed in Table 7 of Ref. 3 due to a difference in definition of the electric field amplitudes that makes their convention for $\gamma_{ijkl}(-\omega_4;\omega_1,\omega_2,\omega_3)$ 4 times larger than ours and a correction factor of 2.0 for their reference value of $\chi^{(3)}(-3\omega;\omega,\omega,\omega)$ (see Section 6.E). Since HT contains five carbon-carbon bonds and eight carbon-hydrogen bonds, we obtain 0.27×10^{-36} esu for the σ-electron contribution to $\langle\gamma(-3\omega;\omega,\omega,\omega)\rangle$ and 1.64×10^{-36} esu for the σ-electron contribution to $\langle\gamma(-2\omega;\omega,\omega,0)\rangle$.

The calculated values for $\langle\gamma(-2\omega;\omega,\omega,0)\rangle$ and $\langle\gamma(-3\omega;\omega,\omega,\omega)\rangle$ that are to be used for comparison with experiment are then

$$\langle \gamma(-2\omega;\omega,\omega,0) \rangle = 0.6\ \langle \gamma_{trans}(-2\omega;\omega,\omega,0) \rangle$$

$$+ 0.4\ \langle \gamma_{cis}(-2\omega;\omega,\omega,0) \rangle + 1.64 \times 10^{-36}\,\text{esu} \qquad (4.2)$$

and

$$\langle \gamma(-3\omega;\omega,\omega,\omega) \rangle = 0.6\ \langle \gamma_{trans}(-3\omega;\omega,\omega,\omega) \rangle$$

$$+ 0.4\ \langle \gamma_{cis}(-3\omega;\omega,\omega,\omega) \rangle + 0.27 \times 10^{-36}\,\text{esu} \quad . \qquad (4.3)$$

The calculated dispersions of $\langle \gamma(-2\omega;\omega,\omega,0) \rangle$ and $\langle \gamma(-3\omega;\omega,\omega,\omega) \rangle$ are illustrated in Figure 4-2 where $\langle \gamma(-3\omega;\omega,\omega,\omega) \rangle$ has been multiplied by a factor of 6. A broadening term $\hbar\Gamma = 0.2$ eV was included in both instances. At very low fundamental photon energies, the relationship $\langle \gamma(-2\omega;\omega,\omega,0) \rangle = 6\ \langle \gamma(-3\omega;\omega,\omega,\omega) \rangle$ is seen to hold. As the 3ω resonance of the 1^1B_u state at $\hbar\omega = 1.65$ eV is approached, however, $\langle \gamma(-3\omega;\omega,\omega,\omega) \rangle$ increases more rapidly than $\langle \gamma(-2\omega;\omega,\omega,0) \rangle$ and we have $|\langle \gamma(-2\omega;\omega,\omega,0) \rangle| < 6\ |\langle \gamma(-3\omega;\omega,\omega,\omega) \rangle|$. The experimental measurements of $\langle \gamma(-2\omega;\omega,\omega,0) \rangle$ and $\langle \gamma(-3\omega;\omega,\omega,\omega) \rangle$ will be seen to be in very good agreement with the theory for the magnitude, sign, and dispersion of the susceptibility.

The isotropically averaged dc-induced second harmonic susceptibility $\langle \gamma(-2\omega;\omega,\omega,0) \rangle$ has been measured previously in the gas phase for both HT and butadiene (BD), the $N = 4$ site chain, by Ward and Elliott at $\lambda = 694$ nm (1.787 eV).[4] After appropriate conversion of their notation to ours ($\langle \gamma(-2\omega;\omega,\omega,0) \rangle = 3\chi^{(3)}/2$) the experimental values are $\langle \gamma(-2\omega;\omega,\omega,0) \rangle = 3.45 \pm 0.20 \times 10^{-36}$ esu for BD and $11.30 \pm 1.05 \times 10^{-36}$ esu for HT. By performing experiments in gas mixtures, they further determined that the sign of $\langle \gamma(-2\omega;\omega,\omega,0) \rangle$ is positive for both BD and HT. For BD,

which has no *cis-transoid* conformation, we calculate 2.1×10^{-36} esu for the π-electron

contribution to $<\gamma(-2\omega;\omega,\omega,0)>$ at 1.787 eV. Since BD consists of 3 carbon-carbon

bonds and 6 carbon-hydrogen bonds, we obtain 1.2×10^{-36} esu for the σ-electron

contribution to $<\gamma(-2\omega;\omega,\omega,0)>$ based on the bond additivity approximation discussed

above.[3] The resultant value for $<\gamma(-2\omega;\omega,\omega,0)>$ accounting for both π and σ-electrons,

3.3×10^{-36} esu, is in excellent agreement with experiment.

The *trans* conformation of HT is calculated to have a π-electron contribution to

$<\gamma(-2\omega;\omega,\omega,0)>$ of 15.0×10^{-36} esu at 1.787 eV, and the *cis* conformation,

12.2×10^{-36} esu. From Eq. (4.2), $<\gamma(-2\omega;\omega,\omega,0)>$ is 15.5×10^{-36} esu, somewhat

larger than the experimental value. Ward and Elliott measured $<\gamma(-2\omega;\omega,\omega,0)>$ as a

function of temperature, and the reported values correspond to the $T \rightarrow \infty$ limit.[4] In

BD, $<\gamma(-2\omega;\omega,\omega,0)>$ was found to be independent of temperature, while a *decrease in*

the signal for HT with increased temperature was ascribed to a negative $\beta(-2\omega;\omega,\omega)$

second order susceptibility. However, *trans*-HT is centrosymmetric such that the

second order susceptibility is identically zero, and our calculations of the

conformationally-induced $\beta(-2\omega;\omega,\omega)$ for *cis*-HT indicate it is much too small to be

observable. If one neglects the temperature dependence and simply takes the measured

value of $<\gamma(-2\omega;\omega,\omega,0)>$ at room temperature, the experimental value is 12.9×10^{-36}

esu rather than 11.3×10^{-36} esu, which is in much better agreement with theory.

The calculated excitation energies and transition moments $\mu_{n,g}^{x}$, and $\mu_{n,1^1B_u}^{x}$ for

the lowest-lying states of the $N = 8$ to 16 *cis* polyene chains are listed in Tables 4-3

through 4-7 for completeness and to allow comparison with the equivalent results for

the *trans* conformation chains. Table 4-8 contains the values of $\gamma_{xxxx}(-2\omega;\omega,\omega,0)$ and

$\gamma_{xxxx}(-3\omega;\omega,\omega,\omega)$ calculated for the $N = 4$ to 16 *cis* polyenes at fundamental photon

energy 0.65 eV. In each case, the dominant tensor component exhibits a rapid increase

with increased chain length, and the origin of $\gamma_{xxxx}(-\omega_4;\omega_1,\omega_2,\omega_3)$ is entirely analogous

to the description given in Chapter 3 for the *trans* polyenes. For comparison, Figure

4-3 shows a log-log plot of the calculated $\gamma_{xxxx}(-3\omega;\omega,\omega,\omega)$ at 0.65 eV against the

number N of carbon atom sites in the *cis* and *trans* polyenes. The linear fit for the *cis*

chains corresponds to

$$\gamma_{xxxx}(-3\omega;\omega,\omega,\omega) \ \propto \ N^{3.9} \tag{4.4}$$

where the same three length-dependent factors that lead to the power law dependence of

$\gamma_{xxxx}(-\omega_4;\omega_1,\omega_2,\omega_3)$ for the *trans* polyenes are also responsible for the rapid growth in

the *cis* case.

Although there is an excellent qualititative analogy between the descriptions of

$\gamma_{xxxx}(-\omega_4;\omega_1,\omega_2,\omega_3)$ for the *cis* and *trans* polyenes, there is an important quantitative

distinction. For chains with equal numbers of sites, the value of $\gamma_{xxxx}(-\omega_4;\omega_1,\omega_2,\omega_3)$

at a fixed frequency is in all cases calculated to be smaller for the *cis* chain than the *trans*

chain. There is also a slightly lesser rate of growth for $\gamma_{xxxx}(-\omega_4;\omega_1,\omega_2,\omega_3)$ with

increasing N for the *cis*. The power law exponent in $\gamma_{xxxx}(-3\omega;\omega,\omega,\omega)$, for example, in

the *cis* case is 3.9 versus 4.0 for the *trans*.

These differences are well-accounted for in Figure 4-3 in which we also plot on a log-log scale $\gamma_{xxxx}(-3\omega;\omega,\omega,\omega)$ against the actual length L of the chain rather than the number of sites. We have defined L to be the distance in the x-direction (along the chain axis) between the two end carbon sites. The calculated values for both the *cis* and *trans* polyenes are very well fit by a single line. This plot unifies the calculated values for the two conformations and yields

$$\gamma_{xxxx}(-3\omega;\omega,\omega,\omega) \propto L^{3.5} \ . \tag{4.5}$$

The differences in $\gamma_{xxxx}(-\omega_4;\omega_1,\omega_2,\omega_3)$ for an equal number of sites are primarily due to the shorter distance along the conjugation axis produced by the *cis* geometry. For equal numbers of carbon sites, the *cis* conformation is always shorter than the *trans* conformation. Figure 4-3 implies that the values of $\gamma_{xxxx}(-\omega_4;\omega_1,\omega_2,\omega_3)$ will be the same for *cis* and *trans* polyene chains which have equal lengths along the chain axis rather than equal numbers of carbon sites. We conclude that although the *trans* third order susceptibilities are larger than those for the *cis* conformation of an equal number of carbons, $\gamma_{xxxx}(-\omega_4;\omega_1,\omega_2,\omega_3)$ is in fact much more sensitive to the physical length of the chain than to the conformation.

Finally, we can make a rough estimate of the implications of these calculations for the infinite chain polymer by extrapolating to longer chains the power law dependence that we have observed. A typical value of the nonresonant macroscopic third order susceptibility $\chi^{(3)}(-3\omega;\omega,\omega,\omega)$ observed for conjugated polymers is 10^{-10}

esu.[5,6] For an (nearly) isotropic distribution of chains considered as independent sources of nonlinear response with a single dominant tensor component $\gamma_{xxxx}(-3\omega;\omega,\omega,\omega)$, we have

$$\chi^{(3)}_{1111}(-3\omega;\omega,\omega,\omega) = \frac{1}{5} \ N \ (f^\omega)^3 \ f^{3\omega} \ \gamma_{xxxx}(-3\omega;\omega,\omega,\omega) \tag{4.6}$$

where N is the number density of chains and f^ω is the Lorentz-Lorenz local field factor. Using typical values of $N = 10^{20}$ molecules/cm^3 and 1.8 for the refractive index, we derive a $\gamma_{xxxx}(-3\omega;\omega,\omega,\omega)$ of roughly 2 x 10^{-31} esu. An extrapolation of our power law dependence of $\gamma_{xxxx}(-3\omega;\omega,\omega,\omega)$ on N for the *trans*-polyenes yields a value for N in the range 50 to 100 carbon sites or, equivalently, a length of approximately 50 - 100 Å. Since many of these polymers consist of much longer chains, we infer that $\gamma_{xxxx}(-3\omega;\omega,\omega,\omega)$ must deviate from the power law dependence and begin to saturate at a length shorter than 100 Å. It is then concluded that large nonresonant values of $\gamma(-\omega_4;\omega_1,\omega_2,\omega_3)$, and, correspondingly, $\chi^{(3)}(-\omega_4;\omega_1,\omega_2,\omega_3)$, may only require chains of intermediate length of order 50 - 100 Å with little to be gained by increasing the chain length beyond this limit.

C. Noncentrosymmetric Polyenes

Thus far, we have considered the third order nonlinear optical properties of centrosymmetric linear chains and have illustrated the important role of definite parity

selection rules in the third order virtual excitation processes. We will demonstrate in this section that lowering the symmetry to a noncentrosymmetric structure can act as a mechanism for the enhancement of nonresonant $\gamma_{ijkl}(-\omega_4;\omega_1,\omega_2,\omega_3)$. As seen in Eq. (2.41), for noncentrosymmetric structures the Bogoliubov-Mitropolsky formalism admits new types of virtual excitation processes otherwise forbidden under centrosymmetric conditions.

The symmetry is lowered by heteroatomic substitution on the linear chain. A principal noncentrosymmetric analog to the $N = 8$ site chain, octatetraene (OT), is 1,1-dicyano-8-N,N-dimethylamino-1,3,5,7-octatetraene (which we will refer to as NOT) having dicyano acceptor groups on one end and a dimethylamino donor group on the other as shown in Figure 4-4 and which has been synthesized in our laboratories. Comparison with the earlier detailed discussion of unsubstituted polyenes will allow direct understanding of the effect of lowered symmetry on $\gamma_{ijkl}(-\omega_4;\omega_1,\omega_2,\omega_3)$.

The calculation of the electronic states and nonlinear optical properties of NOT involved all single and double-excited configurations of the six occupied and six unoccupied π-electron molecular orbitals. This leads to 703 configurations in the CI matrix which is then diagonalized to produce 703 singlet π-electron states. The complete calculation including computation of all transition dipole moments of Eq. (2.41) for $\gamma_{ijkl}(-\omega_4;\omega_1,\omega_2,\omega_3)$ required $5\frac{1}{2}$ CPU hours on a CRAY-X/MP. The calculated excitation energies and transition moments $\mu_{n,n}^x$, $\mu_{n,g}^x$, and $\mu_{n,2^1A'}^x$ of NOT are given in Table 4-9. The dominant excitation is that from the lowest energy π-electron singlet excited state located at 2.81 eV. This is 1.6 eV lower than the energy of

103

the dominant one-photon 1^1B_u state of OT. There is a secondary peak predicted in the optical absorption spectrum at 3.58 eV which actually corresponds to the 2^1A_g state of OT. Because of the lowered symmetry of NOT, there are no one-photon selection rules as there are in OT. Instead, all of the π-electron states of NOT possess A' symmetry and all are one-photon allowed excitations from the ground state. Thus, in addition to the lowering in energy of the analog to the 1^1B_u state, the symmetry lowering has two interesting effects on linear optical properties. The analog of the 2^1A_g state becomes a one-photon allowed transition which turns out to have a sizable oscillator strength, and the ordering of the analogs of the 2^1A_g and 1^1B_u states is inverted. We wish to emphasize, however, that although the existence of the 2^1A_g below the 1^1B_u provided the first definitive evidence of the importance of electron correlation in polyenes, the inverted order in the substituted chains is not due to any less correlation. The $3^1A'$ state of NOT, which is the 2^1A_g analog, is still composed of more than 40% double excited configurations.

The principal symmetry constraint in the case of centrosymmetric structures that the intermediate virtual states must alternate between one-photon states and two-photon states is lifted upon symmetry lowering. Matrix elements of the form $< n| r^i | n >$ are no longer symmetry-forbidden and can have an important role in $\gamma_{ijkl}(-\omega_4;\omega_1,\omega_2,\omega_3)$. Diagonal transitions of this form are best illustrated in the difference density matrix $\Delta\rho_n$ where

$$\Delta\rho_n(r) = \rho_n(r) - \rho_g(r) \qquad (4.7)$$

and

$$<\Delta\mu_n> = -e \int r \; \rho_n(r) \, dr \; . \tag{4.8}$$

The function $\rho_n(r)$ is given by Eq. (3.3) with n equal to n'. The contour diagram of $\Delta\rho_{2^1A'}(r)$ is shown in Figure 4-5(a) where the solid and dashed lines correspond to increased and decreased electron density, respectively. There is a large redistribution of electron density along the dipolar x-axis leading to a large dipole moment difference $\Delta\mu^x_{2^1A'}$ of 14.49 D. The calculated ground state dipole moment $\mu^x_{1^1A'}$ is 10.93 D in good agreement with the experimental value 11.8 ± 0.3 D. The sign for $\Delta\mu^x_{2^1A'}$ is seen to be positive as electron density is decreased in the region of the electron donor and increased in the region of the electron acceptor group upon excitation. This is consistent with the experimentally observed shift to lower energies of the first optical absorption peak in increasingly polar solvents. The magnitude of $\Delta\mu^x_{2^1A'}$ is relatively large and leads to important terms in $\gamma_{ijkl}(-\omega_4;\omega_1,\omega_2,\omega_3)$ that involve the matrix element $< 2^1A' | x | 2^1A' >$. There are no analogous terms in $\gamma_{ijkl}(-\omega_4;\omega_1,\omega_2,\omega_3)$ in the case of centrosymmetric linear chains since the dipole moments of the ground state and all excited states are zero by symmetry. Transition density matrix diagrams for the (b) ground and (c) $7^1A'$ states with the $2^1A'$ state are also shown in Figure 4-5.

For the third harmonic susceptibility $\gamma_{ijkl}(-3\omega;\omega,\omega,\omega)$, it is found, once again, that the $\gamma_{xxxx}(-3\omega;\omega,\omega,\omega)$ component is by far the largest. At 0.65 eV, the independent tensor components are $\gamma_{xxxx} = 407$, $\gamma_{xxyy} = 3.0$, $\gamma_{yyxx} = 1.2$, and $\gamma_{yyyy} = 0.7 \times 10^{-36}$ esu. The calculated dispersion curve of $\gamma_{xxxx}(-3\omega;\omega,\omega,\omega)$ in Figure 4-6 smoothly

105

increases *to the first* resonance occurring at 0.94 eV which is the 3ω resonance of the $2^1A'$ state. Because of the lowered symmetry of NOT, the 3ω and 2ω resonance selection rules for the centrosymmetric polyenes are no longer applicable. Thus, every excited state has allowed 3ω, 2ω and ω resonances, and the dispersive behavior of $\gamma_{xxxx}(-3\omega;\omega,\omega,\omega)$ exhibits all of these many resonances at frequencies beyond the first resonance.

The individual virtual excitation processes that contribute to $\gamma_{xxxx}(-3\omega;\omega,\omega,\omega)$ of NOT at 0.65 eV are listed in Table 4-10 in order of decreasing magnitude. The value of $\gamma_{xxxx}(-3\omega;\omega,\omega,\omega)$ is essentially determined by three terms. As described earlier, for centrosymmetric structures there are two important types of virtual excitation processes that dominate $\gamma_{xxxx}(-\omega_4;\omega_1,\omega_2,\omega_3)$. We have found for the noncentrosymmetric chains a third type of process is allowed and, in fact, makes a larger contribution to $\gamma_{xxxx}(-\omega_4;\omega_1,\omega_2,\omega_3)$ than the other two. These three types of virtual excitation processes in NOT are illustrated in Figure 4-7. The processes illustrated in Figures 4-7(a) and (b) are analogous to the dominant processes for centrosymmetric polyenes. For NOT, the $2^1A'$ state plays the role of the 1^1B_u state of HT because it has the largest transition dipole moment (9.34 D) with the ground state. The type I term is a result of the double summation in the Bogoliubov-Mitropolsky formalism and has the ground state as the middle intermediate state. The largest term of this type is the one with $2^1A'$ as the first and last intermediate state because of its large transition moment with the ground state. The type I term illustrated in Figure 4-7(a) makes a negative contribution to $\gamma_{xxxx}(-3\omega;\omega,\omega,\omega)$ because although the numerator and denominator are both positive,

106

the double sum makes a negative contribution to $\gamma_{xxxx}(-3\omega;\omega,\omega,\omega)$. In the type II

process, there is a high-lying middle intermediate state that has a large transition moment

with $2^1A'$. The analog to the $5^1A'$ state of HT is the $7^1A'$ state of NOT. The type II

term makes a positive contribution to $\gamma_{xxxx}(-3\omega;\omega,\omega,\omega)$ because the numerator is

effectively the square of two matrix elements and the denominator is positive when

below all resonances.

Most importantly, however, for noncentrosymmetric structures, there is a new

type of process which is allowed. This process is illustrated in Figure 4-7(c) and

corresponds to a type V process from Figure 3-3. For NOT, this is the dominant type

of term contributing to $\gamma_{xxxx}(-3\omega;\omega,\omega,\omega)$. Type V terms involve a diagonal matrix

element and are therefore forbidden in centrosymmetric structures which cannot possess

a permanent dipole moment. The important quantity in this term is the dipole moment

difference between an excited state and the ground state $\Delta\mu_n$. For the $2^1A'$ state, the

$\Delta\mu^x_{2^1A'}$, value of 14.49 D leads to a very large term in the triple sum in which all three

intermediate states are the $2^1A'$. Since the numerator and denominator are both positive,

the contribution of this term to γ_{xxxx} is positive. The lowered symmetry of NOT, as

compared to OT, produces a new type of virtual excitation process which dominates

$\gamma_{xxxx}(-3\omega;\omega,\omega,\omega)$ and causes the value of $\gamma_{xxxx}(-3\omega;\omega,\omega,\omega)$ to be more than an order

of magnitude larger for NOT compared to OT. For example, the calculated nonresonant

values of $\gamma_{xxxx}(-3\omega;\omega,\omega,\omega)$ at 0.65 eV for NOT and OT are 407 and 16.0×10^{-36} esu,

respectively. Therefore, although regular conformational changes affect

$\gamma_{xxxx}(-\omega_4;\omega_1,\omega_2,\omega_3)$ only through the change in the physical length of the molecular

structure, lowering of the symmetry by attachment of donor and acceptor groups significantly enhances $\gamma_{xxxx}(-\omega_4;\omega_1,\omega_2,\omega_3)$ through the introduction of previously symmetry-forbidden virtual excitation processes.

Table 4-1. Calculated Symmetries, Excitation Energies, and Key Transition Dipole

Moments for the Lowest-Lying π-electron States of *cis*-Hexatriene ($N = 6$).

State	$\hbar\omega_{ng}$ (eV)	$\mu^x_{n,g}$ (D)	$\mu^y_{n,g}$ (D)	$\mu^x_{n,1^1B_2}$ (D)	$\mu^y_{n,1^1B_2}$ (D)
2^1A_1	4.55	0.00	0.08	1.72	0.00
1^1B_2	4.92	6.83	0.00	0.00	0.01
2^1B_2	5.24	0.14	0.00	0.00	1.67
3^1A_1	6.75	0.00	1.11	1.55	0.00
4^1A_1	6.80	0.00	0.62	0.24	0.00
3^1B_2	7.46	1.52	0.00	0.00	0.30
4^1B_2	7.72	1.84	0.00	0.00	0.09
5^1A_1	7.86	0.00	0.11	10.49	0.00
6^1A_1	8.78	0.00	1.73	1.12	0.00
5^1B_2	9.12	0.24	0.00	0.00	2.88

Table 4-2. Largest Contributing Virtual Excitation Processes to $\gamma_{xxxx}(-2\omega;\omega,\omega,0)$ of

cis-Hexatriene at $\hbar\omega = 0.65$ eV.

m_1	m_2	m_3	Contribution (10^{-36} esu)	Cumulative (10^{-36} esu)
1^1B_2	5^1A_1	1^1B_2	43.7	43.7
1^1B_2	1^1A_1	1^1B_2	-29.1	14.6
1^1B_2	8^1A_1	1^1B_2	3.8	18.4
1^1B_2	10^1A_1	1^1B_2	2.5	20.9
4^1B_2	5^1A_1	1^1B_2	-2.4	18.5
1^1B_2	5^1A_1	4^1B_2	-2.3	16.2
1^1B_2	2^1A_1	1^1B_2	2.1	18.3

Table 4-3. Calculated Symmetries, Excitation Energies, and Key Transition Dipole

Moments for the Lowest-Lying π-electron States of cis-Octatetraene

$(N = 8)$.

State	$\hbar\omega_{ng}$ (eV)	$\mu^x_{n,g}$ (D)	$\mu^x_{n,1^1B_u}$ (D)
2^1A_g	4.11	0.00	2.78
1^1B_u	4.37	8.00	0.00
2^1B_u	4.77	0.05	0.00
3^1A_g	5.22	0.00	0.32
4^1A_g	6.03	0.00	1.77
5^1A_g	6.08	0.00	0.68
3^1B_u	6.47	0.16	0.00
4^1B_u	6.82	2.97	0.00
6^1A_g	7.03	0.00	12.62
5^1B_u	7.09	0.08	0.00
7^1A_g	7.41	0.00	0.69
8^1A_g	7.42	0.00	0.44

Table 4-4. Calculated Symmetries, Excitation Energies, and Key Transition Dipole Moments for the Lowest-Lying π-electron States of *cis*-Decapentaene $(N = 10)$.

State	$\hbar\omega_{ng}$ (eV)	$\mu^x_{n,g}$ (D)	$\mu^x_{n,1^1B_2}$ (D)
2^1A_1	3.85	0.00	3.80
1^1B_2	4.00	9.04	0.00
2^1B_2	4.38	0.02	0.00
3^1A_1	4.91	0.00	0.56
3^1B_2	5.19	0.04	0.00
4^1A_1	5.48	0.00	2.06
5^1A_1	5.53	0.00	0.56
4^1B_2	6.02	0.27	0.00
5^1B_2	6.24	3.35	0.00
6^1A_1	6.29	0.00	2.11
7^1A_1	6.47	0.00	14.08
6^1B_2	6.61	0.09	0.00
8^1A_1	6.72	0.00	2.15
7^1B_2	7.06	0.04	0.00

Table 4-5. Calculated Symmetries, Excitation Energies, and Key Transition Dipole

Moments for the Lowest-Lying π-electron States of cis-Dodecahexaene

$(N = 12)$.

State	$\hbar\omega_{ng}$ (eV)	$\mu_{n,g}^x$ (D)	$\mu_{n,1^1B_u}^x$ (D)
2^1A_g	3.69	0.00	4.73
1^1B_u	3.74	9.98	0.00
2^1B_u	4.11	0.04	0.00
3^1A_g	4.58	0.00	0.69
3^1B_u	4.97	0.04	0.00
4^1A_g	5.09	0.00	2.27
5^1A_g	5.11	0.00	0.51
6^1A_g	5.17	0.00	0.33
4^1B_u	5.61	0.22	0.00
5^1B_u	5.82	3.71	0.00
7^1A_g	6.00	0.00	7.22
8^1A_g	6.06	0.00	12.19
9^1A_g	6.18	0.00	6.98
6^1B_u	6.19	0.09	0.00
7^1B_u	6.22	0.21	0.00

Table 4-6. Calculated Symmetries, Excitation Energies, and Key Transition Dipole Moments for the Lowest-Lying π-electron States of cis-Tetradecaheptaene $(N = 14)$.

State	$\hbar\omega_{ng}$ (eV)	$\mu^x_{n,g}$ (D)	$\mu^x_{n,1^1B_2}$ (D)
1^1B_2	3.55	10.85	0.00
2^1A_1	3.59	0.00	5.55
2^1B_2	3.92	0.07	0.00
3^1A_1	4.32	0.00	0.77
3^1B_2	4.69	0.04	0.00
4^1A_1	4.77	0.00	1.08
5^1A_1	4.82	0.00	2.20
6^1A_1	5.02	0.00	0.58
4^1B_2	5.16	0.01	0.00
5^1B_2	5.29	0.15	0.00
6^1B_2	5.50	3.96	0.00
7^1A_1	5.67	0.00	7.82
8^1A_1	5.71	0.00	3.96
9^1A_1	5.83	0.00	14.41
7^1B_2	5.89	0.73	0.00
8^1B_2	6.01	0.02	0.00

114

Table 4-7. Calculated Symmetries, Excitation Energies, and Key Transition Dipole

Moments for the Lowest-Lying π-electron States of cis-Hexadecaoctaene

$(N = 16)$.

State	$\hbar\omega_{ng}$ (eV)	$\mu^x_{n,g}$ (D)	$\mu^x_{n,1^1B_u}$ (D)
1^1B_u	3.41	11.65	0.00
2^1A_g	3.52	0.00	6.27
2^1B_u	3.78	0.01	0.00
3^1A_g	4.13	0.00	0.84
3^1B_u	4.46	0.03	0.00
4^1A_g	4.50	0.00	0.82
5^1A_g	4.62	0.00	2.39
6^1A_g	4.79	0.00	0.64
4^1B_u	5.04	0.08	0.00
5^1B_u	5.04	0.04	0.00
7^1A_g	5.15	0.00	0.54
6^1B_u	5.24	4.10	0.00
8^1A_g	5.36	0.00	5.84
9^1A_g	5.43	0.00	0.50
10^1A_g	5.60	0.00	16.66
7^1B_u	5.63	1.36	0.00
8^1B_u	5.74	0.12	0.00

115

Table 4-8. Calculated Values for $\gamma_{xxxx}(-2\omega;\omega,\omega,0)$ and $\gamma_{xxxx}(-3\omega;\omega,\omega,\omega)$ at $\hbar\omega = 0.65$ eV for the *cis*-Polyenes in 10^{-36} esu.

N (sites)	$\gamma_{xxxx}(-2\omega;\omega,\omega,0)$	$\gamma_{xxxx}(-3\omega;\omega,\omega,\omega)$
6	20.3	3.83
8	63.8	12.5
10	150.1	30.4
12	290.1	60.9
14	488.2	105.8
16	742.0	165.5

Table 4-9. Calculated Symmetries, Excitation Energies, and Key Transition Dipole Moments for the Lowest-Lying π-electron States of NOT.

State	$\hbar\omega_{ng}$ (eV)	$\mu^x_{n,n}$ (D)	$\mu^x_{n,g}$ (D)	$\mu^x_{n,2^1A'}$ (D)
$1^1A'$	0.00	10.93	10.93	9.34
$2^1A'$	2.81	25.42	9.34	25.42
$3^1A'$	3.58	13.27	4.12	2.22
$4^1A'$	4.10	14.78	0.54	1.41
$5^1A'$	4.40	15.21	0.50	2.21
$6^1A'$	4.84	14.14	0.31	1.59
$7^1A'$	5.01	19.25	2.80	10.94
$8^1A'$	5.21	16.49	0.60	4.54
$9^1A'$	5.72	19.04	0.79	1.40
$10^1A'$	5.90	12.95	0.3	2.02
$11^1A'$	6.04	12.74	1.17	9.24
$12^1A'$	6.29	20.39	0.05	1.08
$13^1A'$	6.68	15.76	0.23	0.09
$14^1A'$	6.78	14.23	0.35	1.91

Table 4-10. Largest Contributing Virtual Excitation Processes to $\gamma_{xxxx}(-3\omega;\omega,\omega,\omega)$ of

NOT at $\hbar\omega = 0.65$ eV.

m_1	m_2	m_3	Contribution (10^{-36} esu)	Cumulative (10^{-36} esu)
$2^1A'$	$2^1A'$	$2^1A'$	550.3	550.3
$2^1A'$	$1^1A'$	$2^1A'$	-172.6	377.7
$2^1A'$	$7^1A'$	$2^1A'$	135.4	513.1
$2^1A'$	$11^1A'$	$2^1A'$	76.6	589.7
$7^1A'$	$2^1A'$	$2^1A'$	-63.1	526.6
$2^1A'$	$2^1A'$	$7^1A'$	-45.8	480.8
$3^1A'$	$2^1A'$	$2^1A'$	-27.8	453.0
$3^1A'$	$11^1A'$	$2^1A'$	26.0	479.0
$2^1A'$	$2^1A'$	$3^1A'$	-22.5	456.5

118
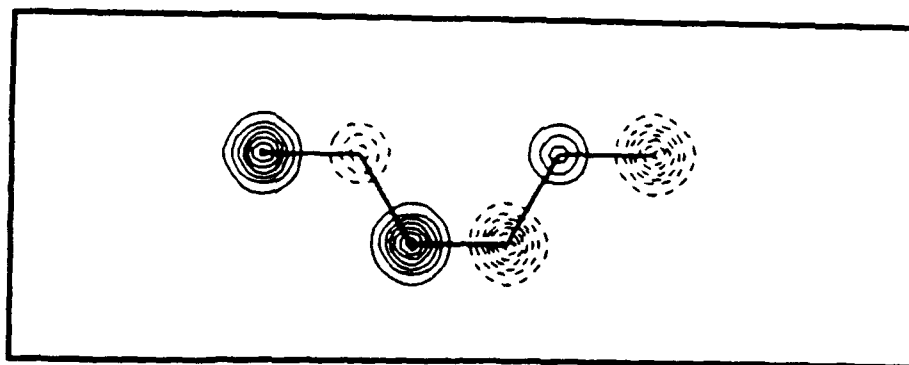
(a)
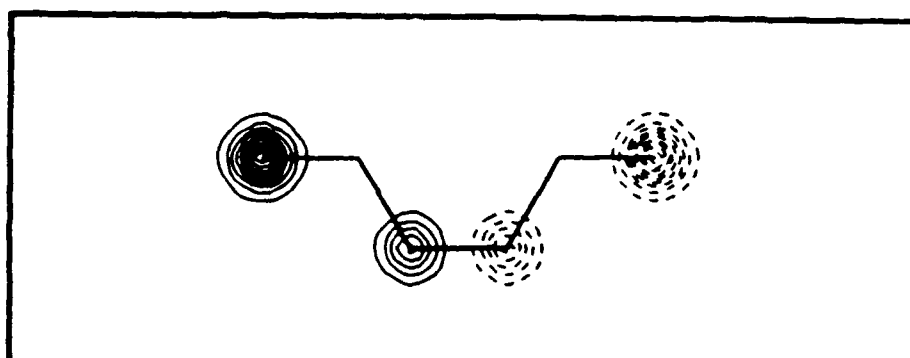
(b)

Figure 4-1. Transition density matrix contour diagrams of *cis*-HT for the (a) ground and (b) 5^1A_g states with the 1^1B_u state. The x-components of the transition dipole moments are 6.83 and 10.49 D, respectively. The contour cuts are taken 0.4 Å above the molecular plane.
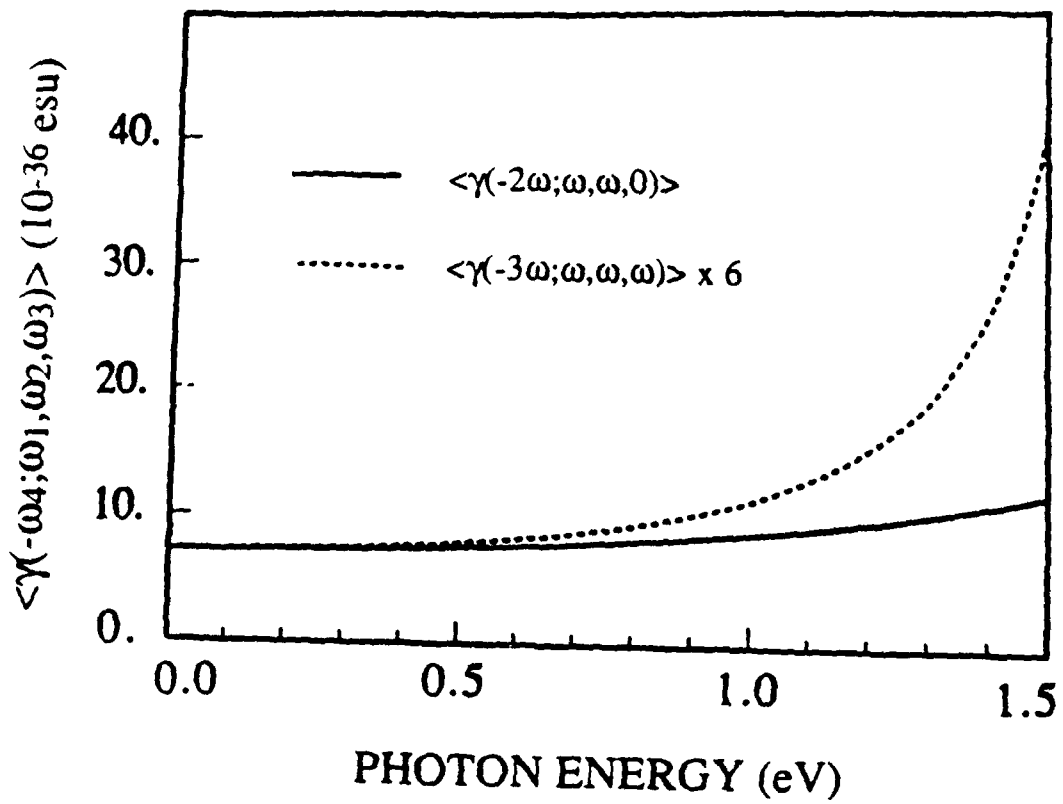
Figure 4-2. The calculated dispersions of $\langle\gamma(-2\omega;\omega,\omega,0)\rangle$ (solid) and $\langle\gamma(-3\omega;\omega,\omega,\omega)\rangle$ (dashed) for HT. The values of $\langle\gamma(-3\omega;\omega,\omega,\omega)\rangle$ have been multiplied by a factor of 6.

120
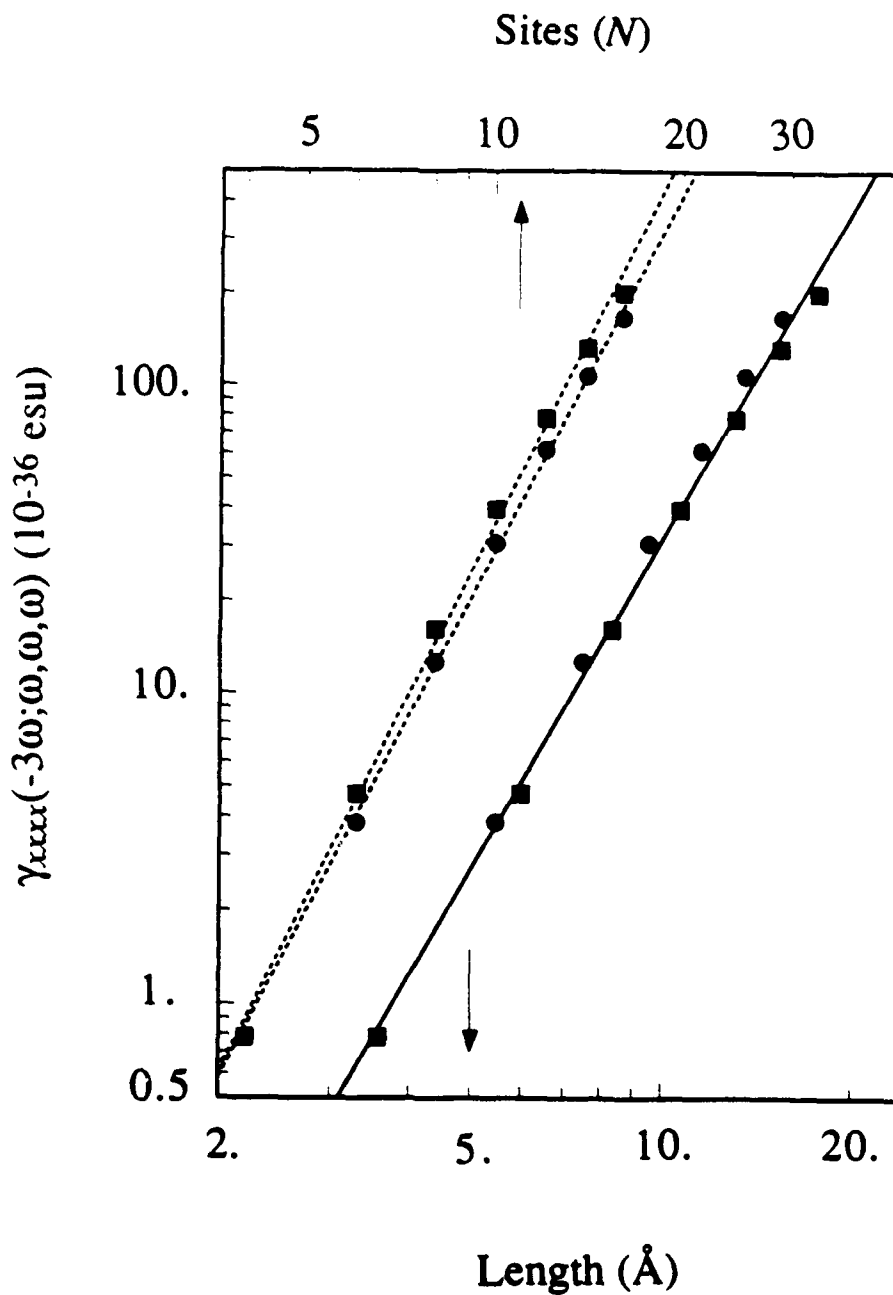
Figure 4-3. Log-log plot of $\gamma_{xxxx}(-3\omega;\omega,\omega,\omega)$ at $\hbar\omega = 0.65$ eV versus the number N of carbon sites (upper axis and dashed lines) and length L (lower axis and solid line). The values for *trans* chains are represented by squares; and the values for *cis* chains, by circles. The linear fit of the solid line corresponds to $\gamma_{xxxx}(-3\omega;\omega,\omega,\omega) \propto L^{3.5}$.

121
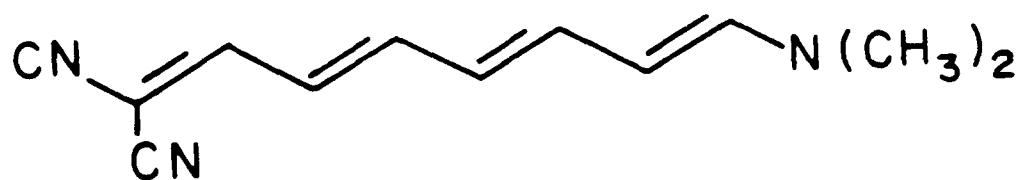
Figure 4-4. Schematic diagram of the molecular structure of 1,1-dicyano-8-N,N-dimethylamino-1,3,5,7-octatetraene (NOT).
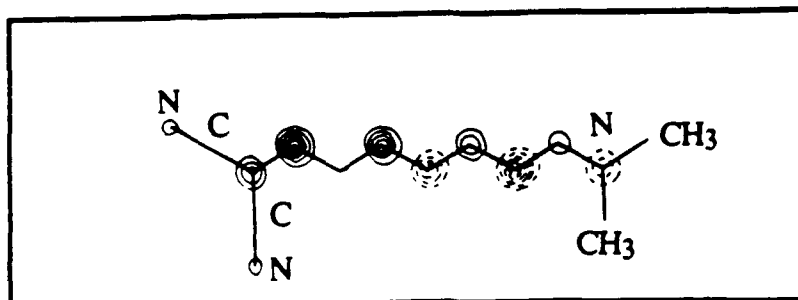
(a)
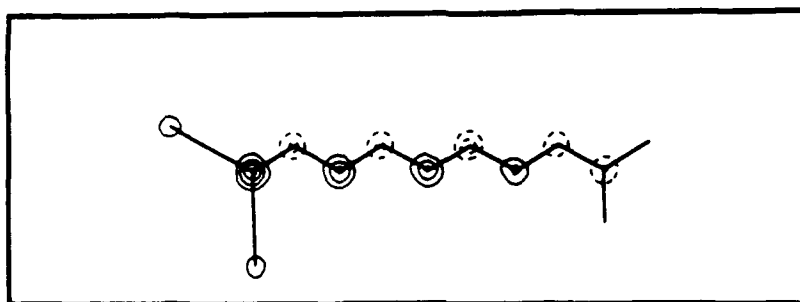
(b)
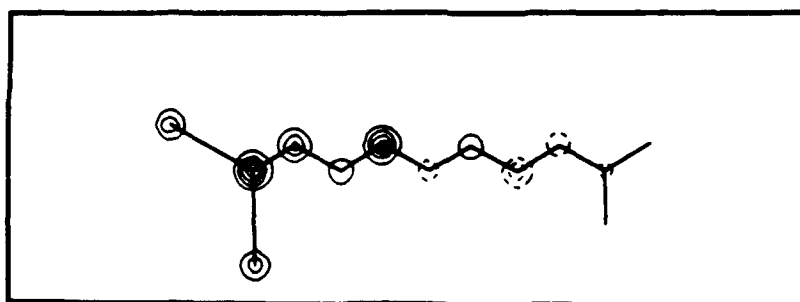
(c)

Figure 4-5. Contour diagrams for NOT of (a) the difference density matrix for the $2^1A'$ state, and transition density matrices of the (b) ground and (c) $7^1A'$ states with the $2^1A'$ state. The increased charge near the cyano groups in (a) represents a large increase in the x-component of the dipole moment from 10.93 D in the ground state to 25.42 D in the $2^1A'$ state.

123
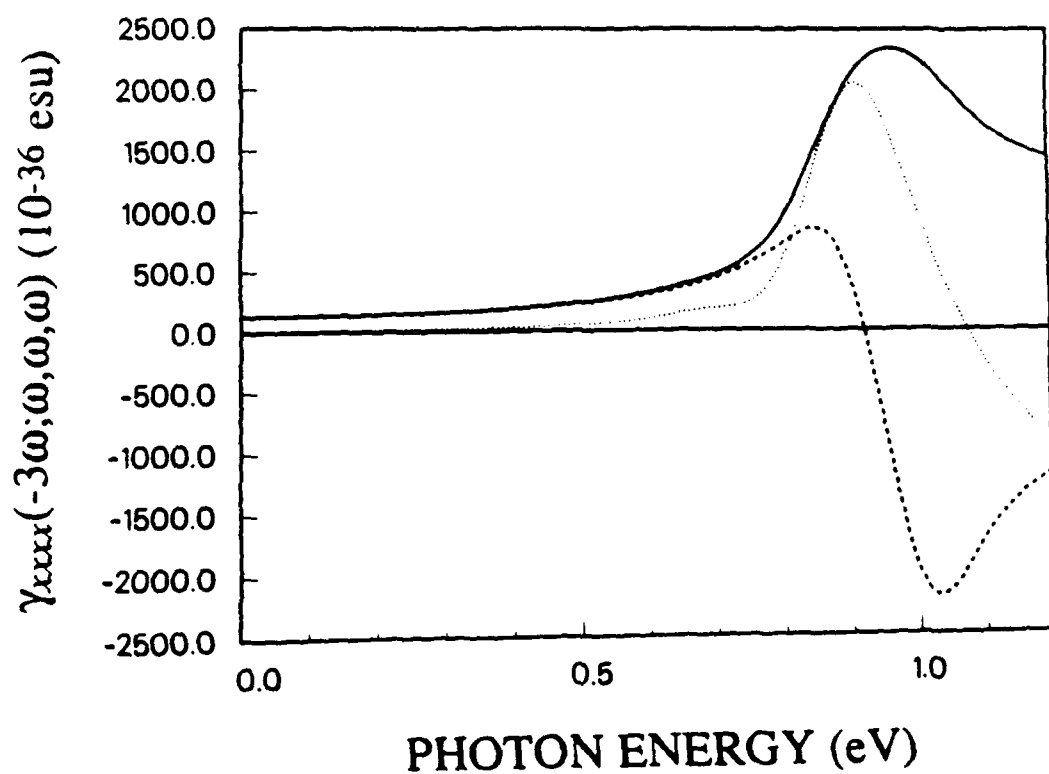
Figure 4-6. Calculated dispersion of $\gamma_{xxxx}(-3\omega;\omega,\omega,\omega)$ for NOT with $\hbar\Gamma = 0.2$ eV. The solid curve is $|\gamma_{xxxx}(-3\omega;\omega,\omega,\omega)|$ and the dashed and dotted curves are $\text{Re}[\gamma_{xxxx}(-3\omega;\omega,\omega,\omega)]$ and $\text{Im}[\gamma_{xxxx}(-3\omega;\omega,\omega,\omega)]$, respectively.
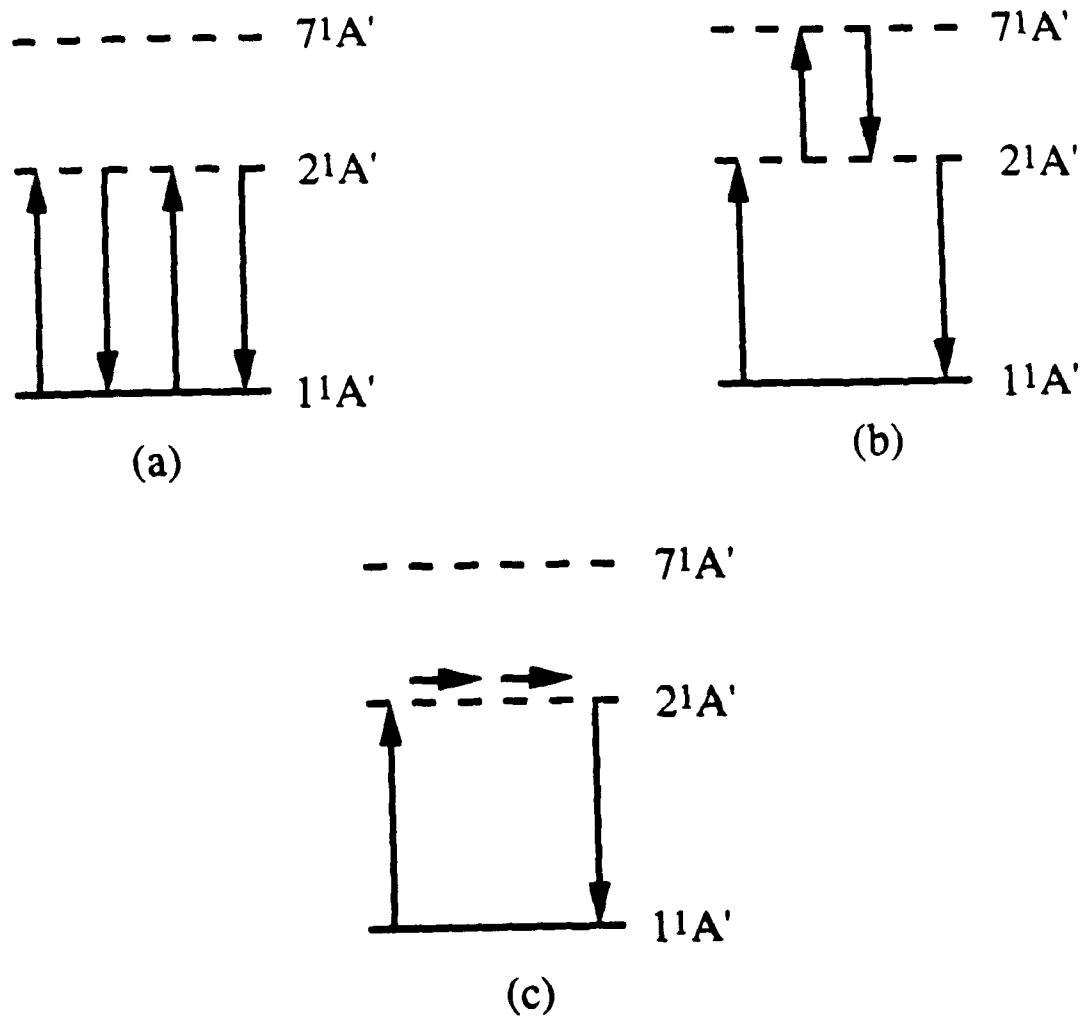
Figure 4-7. The three principal third order virtual excitation processes for NOT. The diagram in (c) corresponds to a process that can only occur in noncentrosymmetric structures and dominates $\gamma_{xxxx}(-3\omega;\omega,\omega,\omega)$ in NOT.

Chapter 4 References

1. Z. G. Soos and S. Ramasesha, Phys. Rev. B29, 5410 (1984).

2. R. M. Gavin, Jr., S. Risemberg, and S. M. Rice, J. Chem. Phys. 58, 3160 (1973).

3. F. Kajzar and J. Messier, J. Opt. Soc. Am. B4, 1040 (1987).

4. J. F. Ward and D. S. Elliott, J. Chem. Phys. 69, 5438 (1978).

5. C. Sauteret et al., Phys. Rev. Lett. 36, 956 (1976).

6. F. Kajzar and J. Messier, Polym. J. 19, 275 (1987).

Chapter 5

DISPERSION OF $\langle\gamma(-2\omega;\omega,\omega,0)\rangle$ IN HEXATRIENE AND β-CAROTENE

Chapters 3 and 4 presented the detailed results of the electron correlation description of the nonlinear optical properties of conjugated linear chains. In order to test the validity of these results, the frequency dependence of the isotropically averaged molecular third order susceptibility $\langle\gamma(-\omega_4;\omega_1,\omega_2,\omega_3)\rangle$ has been measured for two fundamentally important conjugated molecular systems, hexatriene (HT) and β-carotene, through two separate nonlinear optical processes. The hexatriene results allow us direct comparison with the theoretical predictions for the magnitude and dispersion of $\langle\gamma(-\omega_4;\omega_1,\omega_2,\omega_3)\rangle$ for HT presented in chapters 3 and 4 while the length dependence of $\langle\gamma(-\omega_4;\omega_1,\omega_2,\omega_3)\rangle$ is experimentally determined by the measurements on β-carotene, a symetrically substituted polyene corresponding to $N = 22$. This chapter describes the measurement of $\langle\gamma(-2\omega;\omega,\omega,0)\rangle$ in HT and β-carotene at 1907, 1543, and 1064 nm by dc-induced second harmonic generation (DCSHG). Chapter 6 will present third harmonic generation experiments, which measure the related quantity $\langle\gamma(-3\omega;\omega,\omega,\omega)\rangle$.

A. Introduction to DCSHG

Electric field-induced second harmonic generation is now well-established as a primary method for the determination of the molecular *second* order susceptibility $\beta_{ijk}(-2\omega;\omega,\omega)$ in gases, liquids, and solids.[1-4] Use of this technique has allowed rapid

127

and direct measurement of molecular second order optical properties in a variety of conjugated structures to aid in understanding the microscopic origin of $\beta_{ijk}(-2\omega;\omega,\omega)$ and the effect substituents and different parent structures have on $\beta_{ijk}(-2\omega;\omega,\omega)$. In addition, DCSHG provides a method for evaluation of candidate molecular structures for their potential in electrooptics or frequency doubling applications in noncentrosymmetric crystals[5,6] or poled, doped polymers.[7-9] The measurement of $\chi_{ijk}^{(2)}(-\omega_3;\omega_1,\omega_2)$, which requires a macroscopically noncentrosymmetric medium, is easily accomplished in DCSHG, where removal of centrosymmetry in a polar solution is achieved by application of a static electric field, as compared to direct second harmonic generation or linear electrooptic effect measurements of crystals or poled polymers for which extensive sample preparation is required.

Despite its primary role in measurement of $\beta_{ijk}(-2\omega;\omega,\omega)$, DCSHG is, in fact, a third order nonlinear optical process defined through the polarization expression

$$P_i^{2\omega} = \Gamma_{ijkl}\ E_j^{\omega}\ E_k^{\omega}\ E_l^{0} \tag{5.1}$$

where $P_i^{2\omega}$ is the macroscopic polarization at a frequency 2ω induced by two applied optical electric fields of amplitude E_j^{ω} and E_k^{ω} and an applied static field of amplitude E_l^{0}. The magnitude of the second harmonic polarization is governed by the effective DCSHG susceptibility tensor Γ_{ijkl} which has three potential contributing mechanisms.[1] We note here that Γ_{ijkl} is equivalent to $\chi_{ijkl}^{(3)}(-2\omega;\omega,\omega,0)$ and is a prevalent notation in the

128

DCSHG literature. We will use the notation Γ_{ijkl} throughout the remainder of this chapter.

The electronic molecular third order susceptibility for DCSHG, $\gamma_{ijkl}(-2\omega;\omega,\omega,0)$, results in a microscopic polarization

$$p_i^{2\omega} = \gamma_{ijkl}(-2\omega;\omega,\omega,0)\ E_j^\omega\ E_k^\omega\ E_l^0\ . \tag{5.2}$$

This purely electronic polarization effect does not involve any vibrational, rotational, or orientational motion of the molecule and corresponds to the $\gamma_{ijkl}(-2\omega;\omega,\omega,0)$ calculated in chapters 3 and 4. For an isotropic medium, when the static, fundamental, and harmonic electric fields are all parallel to the X axis in the laboratory coordinate frame,

$$p_X^{2\omega} = \langle\gamma(-2\omega;\omega,\omega,0)\rangle\ E_X^\omega\ E_X^\omega\ E_X^0 \tag{5.3}$$

where the microscopic isotropically averaged DCSHG susceptibility $\langle\gamma(-2\omega;\omega,\omega,0)\rangle$ is given by (see Appendix B)

$$\langle\gamma(-2\omega;\omega,\omega,0)\rangle = \frac{1}{5}\Big\{ \sum_i \gamma_{iiii}(-2\omega;\omega,\omega,0) + \frac{1}{3}\sum_{i\neq j} [\gamma_{iijj}(-2\omega;\omega,\omega,0)$$
$$+ \gamma_{ijij}(-2\omega;\omega,\omega,0) + \gamma_{ijji}(-2\omega;\omega,\omega,0)] \Big\}\ . \tag{5.4}$$

Eq. (5.4) has often[1,2] been written as

$$\langle\gamma\rangle = \frac{1}{5}\ (\gamma_{xxxx} + \gamma_{yyyy} + \gamma_{zzzz} + 2\gamma_{xxyy} + 2\gamma_{xxzz} + 2\gamma_{yyzz}) \tag{5.5}$$

129

where the frequency arguments have been omitted. It is assumed in Eq. (5.5) that

$$\gamma_{xxyy} = \gamma_{xyyx} = \gamma_{xyxy} = \gamma_{yyxx} = \gamma_{yxxy} = \gamma_{yxyx} \tag{5.6}$$

and that the corresponding equalities involving the subscript pairs x,z and y,z also hold; but this is strictly valid only in the zero frequency limit ($\omega = 2\omega = 0$). For nonzero frequencies, dispersion leads to violation of most of these proposed equalities, and the only strict identities are of the form

$$\gamma_{ijkl}(-2\omega;\omega,\omega,0) = \gamma_{ikjl}(-2\omega;\omega,\omega,0) \quad . \tag{5.7}$$

Thus, making use of

$$\gamma_{ijij}(-2\omega;\omega,\omega,0) = \gamma_{iijj}(-2\omega;\omega,\omega,0) \tag{5.8}$$

from Eq. (5.7), Eq. (5.4) can be simplified to[3]

$$<\gamma(-2\omega;\omega,\omega,0)> = \frac{1}{15} \sum_{i,j} \ [2\gamma_{iijj}(-2\omega;\omega,\omega,0) + \gamma_{ijji}(-2\omega;\omega,\omega,0)] \quad . \tag{5.9}$$

In nonlinear optical processes involving only optical frequencies, such as THG, the exclusive contribution to $\gamma_{ijkl}(-\omega_4;\omega_1,\omega_2,\omega_3)$ is of electronic origin since molecular vibrational and rotational excitations cannot follow the optical frequency oscillations. The static field in DCSHG, however, can couple to the vibrational normal modes of the

130

molecule through the hyper-Raman susceptibility that contributes a second harmonic polarization

$$p_i^{2\omega} = \sum_{\sigma} \xi_{ijk,\sigma} \, E_j^{\omega} \, E_k^{\omega} \, Q_{\sigma} \tag{5.10}$$

where $\xi_{ijk,\sigma}$ is the hyper-Raman susceptibiity and Q_{σ} the vibrational normal coordinate for mode σ. Using the vibrational equation of motion

$$m_{\sigma} \, \omega_{\sigma}^2 \, Q_{\sigma} = e_{l,\sigma}^{*} E_i^0 \tag{5.11}$$

where m_{σ} is the reduced mass, ω_{σ} the vibrational frequency, and $e_{l,\sigma}^{*}$ the effective charge, we have

$$p_i^{2\omega} = \gamma_{jkl}^{v}(-2\omega;\omega,\omega,0) \, E_j^{\omega} \, E_k^{\omega} \, E_l^0 \tag{5.12}$$

where

$$\gamma_{ijkl}^{v}(-2\omega;\omega,\omega,0) = \sum_{\sigma} (\xi_{ijk,\sigma} \, e_{l,\sigma}^{*}) / (m_{\sigma} \, \omega_{\sigma}^2) \tag{5.13}$$

is the vibrational contribution to the third order susceptibility. The isotropic average of $\gamma_{ijkl}^{v}(-2\omega;\omega,\omega,0)$ is also of the form of Eq. (5.4).

Finally, for noncentrosymmetric molecular structures, $\beta_{ijk}(-2\omega;\omega,\omega)$ is nonvanishing and leads to a microscopic second harmonic polarization

131

$$p_i^{2\omega} = \beta_{ijk}(-2\omega;\omega,\omega) \; E_j^{\omega} \; E_k^{\omega} \qquad . \qquad (5.14)$$

In an isotropic medium such as a gas or liquid, however, the average of $p_i^{2\omega}$ over the uniform molecular orientational distribution function leads to a vanishing net second harmonic polarization and no SHG is observed. In DCSHG, with the application of a dc electric field, the medium becomes anisotropic. In the case of the dc and optical electric fields all applied along the X-axis in the laboratory coordinate frame, the isotropically averaged contribution of $\beta_{ijk}(-2\omega;\omega,\omega)$ to $p_X^{2\omega}$ can be shown to be

$$\langle p_X^{2\omega} \rangle = \frac{\mu\beta_x}{5kT} \; E_X^{\omega} \; E_X^{\omega} \; E_X^0 \qquad (5.15)$$

where μ is the magnitude of the molecular dipole moment and

$$\beta_x = \beta_{xxx}(-2\omega;\omega,\omega) + \beta_{xyy}(-2\omega;\omega,\omega) + \beta_{xzz}(-2\omega;\omega,\omega) \qquad (5.16)$$

is the vector part of $\beta_{ijk}(-2\omega;\omega,\omega)$ along the molecular dipolar axis x.

Combining the electronic third order, vibrational third order, and static field induced second order contributions to $p_x^{2\omega}$, we obtain

$$p_X^{2\omega} = [<\gamma(-2\omega;\omega,\omega,0)> + <\gamma^v(-2\omega;\omega,\omega,0)> + \frac{\mu\,\beta_x(-2\omega;\omega,\omega)}{5kT}] \; E_X^{\omega} \; E_X^{\omega} \; E_X^0. \qquad (5.17)$$

132

Comparison of third order susceptibilities of several centrosymmetric organic structures measured by DCSHG and by frequency-mixing has shown that the measured susceptibilities are essentially identical in the two processes.[1,10] Since γ^{ν} contributes to DCSHG but not to frequency-mixing, these results demonstrate that, in general, the electronic term $<\gamma(-2\omega;\omega,\omega,0)>$ dominates the hyper-Raman term $<\gamma^{\nu}(-2\omega;\omega,\omega,0)>$. Furthermore, for centrosymmetric molecules μ and $\beta_{ijk}(-2\omega;\omega,\omega)$ are identically zero reducing Eq. (5.17) to

$$p_X^{2\omega} = <\gamma(-2\omega;\omega,\omega,0)> (E_X^{\omega})^2 E_X^0 \ . \tag{5.18}$$

The DCSHG experiments presented in this chapter were performed on centrosymmetric molecular structures in the liquid phase such that the experiments are governed by Eq. (5.18), and only the electronic third order susceptibility $<\gamma(-2\omega;\omega,\omega,0)>$ is measured.

In gaseous media, the relationship between Eqs. (5.1) and (5.18) is simply

$$\Gamma_{XXXX} = \sum_m [N_m <\gamma_m(-2\omega;\omega,\omega,0)>] \tag{5.19}$$

where N_m is the number density of molecular species m. For condensed media, such as liquids, it is necessary to additionally take into account the effect of linear polarization of the medium on the magnitude of the local electric field experienced at the molecular site. This is done via the local field factors f^{ω} yielding

133

$$\Gamma_{XXXX} = f^{2\omega} (f^{\omega})^2 f^0 \sum_m [N_m <\gamma_m(-2\omega;\omega,\omega,0)>] \qquad (5.20)$$

where the local fields have been taken as spa̶ uniform and independent of the molecular species. Onsager[11] showed for nonassociating liquids that

$$f^{\omega} = \frac{(\varepsilon_\infty + 2) \varepsilon_\omega}{\varepsilon_\infty + 2\varepsilon_\omega} \qquad (5.21)$$

where ε_∞ is the non-dipole contribution to the dielectric constant (effectively n^2 at optical frequencies). Thus, we finally have

$$\Gamma_{XXXX}(-2\omega;\omega,\omega,0) = \left(\frac{n_{2\omega}^2 + 2}{3}\right) \left(\frac{n_\omega^2 + 2}{3}\right)^2 \left(\frac{(n_\omega^2 + 2)\varepsilon}{n_\omega^2 + 2\varepsilon}\right)$$

$$\sum_m [N_m <\gamma_m(-2\omega;\omega,\omega,0)>] \qquad (5.22)$$

where ε is the static dielectric constant and n_ω is the refractive index at frequency ω.

B. Derivation of Second Harmonic
Intensity in the DCSHG Configuration

In this section we derive the expression for the second harmonic intensity at the output of the DCSHG configuration[2] illustrated schematically in Figure 5-1. Four

interfaces must be considered: air-glass, glass-liquid, liquid-glass, and glass-air. The static field electrodes extend over the entire liquid region and part of the glass windows such that the electric field is constant over the entire liquid length but is negligible at the air-glass interfaces. Since air, glass, and liquid are all isotropic, there is an effective second order susceptibility only in the region where the static field is nonzero. We will consider the fundamental and second harmonic beams to be monochromatic plane waves (e.g. the confocal parameter $z_0 > z_1 + z_2$) and allow for absorption at both the fundamental and second harmonic frequencies within the liquid.

The nonlinear wave equation that governs the second harmonic electric field $E^{2\omega}(z)$ is

$$\frac{\partial^2 E^{2\omega}}{\partial z^2} + \alpha_{2\omega} \frac{\partial E^{2\omega}}{\partial z} + k_f^2 \, E^{2\omega} = -\frac{16\pi\omega^2}{c^2} d_{eff}(z) \, [E^{\omega}(z)]^2 \, e^{ik_b z} \qquad (5.23)$$

where $\alpha_{2\omega}$ is the absorption coefficient at the harmonic frequency, $d_{eff}(z)$ the effective second harmonic susceptibility $(d_{eff}(z) = \Gamma(-2\omega;\omega,\omega,0)E^0(z))$, $E^{\omega}(z)$ the amplitude of the fundamental field that decreases with increased z due to α_{ω}, and $k_f = (2\omega\, n_{2\omega})/c$ and $k_b = (2\omega\, n_{\omega})/c$ are the wave vectors of the free and bound harmonic waves, respectively. The free wave is the solution to the homogeneous differential equation and the bound wave is the particular solution for the nonlinear polarization source term leading to the solution

$$E^{2\omega}(z) = E_f \, e^{-\alpha_{2\omega} z/2} \, e^{ik_f z} + E_b(z) \, e^{ik_b z} \qquad (5.24)$$

135

where E_f and $E_b(z)$ are the free and bound electric field amplitudes, respectively.

Insertion of Eq.(5.24) into Eq. (5.23) yields

$$\frac{\partial^2 E_b}{\partial z^2} + (\alpha_{2\omega} + 2ik_b) \frac{\partial E_b}{\partial z} + (k_f^2 - k_b^2 + ik_b\alpha_{2\omega}) E_b(z) = -\frac{16\pi\omega^2}{c^2} d_{eff}(z) [E^\omega(z)].$$

(5.25)

Because the spacing of the electrodes is large compared to the coherence length l_C = $\pi / |k_f - k_b|$, the variation of $d_{eff}(z)$ due to the fringe electric fields is weak such that the first two terms of Eq. (5.25) are small compared to the third. In this limit, the solution for $E_b(z)$ is

$$E_b(z) = -\frac{16\pi\omega^2}{c^2(k_f^2 - k_b^2 + ik_b\alpha_{2\omega})} d_{eff}(z) [E^\omega(z)]^2$$

(5.26)

which further reduces to

$$E_b(z) = -\frac{4\pi}{n_{2\omega}^2 - n_\omega^2} d_{eff}(z) [E^\omega(z)]^2$$

(5.27)

for the usual case of $\alpha_{2\omega} \ll |k_f - k_b|$.

We first consider the general case of a single boundary at $z = z_0$ between media 1 and 2 and then apply the solution to the particular configuration of Figure 5-1. The second harmonic electric field in medium 1 is composed of the free $E_f^{(1)}$, bound $E_b^{(1)}$, and reflected free $E_R^{(1)}$ waves,

136

$$E^{2\omega}(z) = E_f^{(1)} e^{[ik_f - (\alpha_{2\omega}/2)]z} + E_b^{(1)}(z) e^{[ik_b - \alpha_\omega]z} + E_R^{(1)} e^{-[ik_f - (\alpha_{2\omega}/2)]z} \quad . \quad (5.28)$$

Any possible absorption at the fundamental frequency is here explicitly accounted for in the phase factor accompanying $E_b^{(1)}(z)$ and will therefore be omitted from $[E^\omega(z)]^2$ when Eq. (5.26) is used for $E_b(z)$. We can now solve for the free wave in medium 2, $E_f^{(2)}$, in terms of $E_f^{(1)}$, $E_b^{(1)}$, and $E_b^{(2)}$ by applying the boundary conditions on $E^{2\omega}$ and $H^{2\omega}$ at z_0. We have

$$E_f^{(1)} e^{i\varphi_f} + E_b^{(1)}(z_0) e^{i\varphi_b} + E_R^{(1)} e^{-i\varphi_f} = E_f^{(2)} + E_b^{(2)}(z_0) e^{i\varphi_b}$$

$$n_{2\omega}^{(1)} E_f^{(1)} e^{i\varphi_f} + n_\omega^{(1)} E_b^{(1)}(z_0) e^{i\varphi_b} - n_{2\omega}^{(1)} E_R^{(1)} e^{-i\varphi_f} = n_{2\omega}^{(2)} E_f^{(2)} + n_\omega^{(2)} E_b^{(2)}(z_0) e^{i\varphi_b}$$

$$(5.29)$$

where the free and bound wave phases, $\varphi_f = (k_f + i\alpha_{2\omega}/2)z_0$ and $\varphi_b = (k_b + i\alpha_\omega)z_0$, respectively, refer to medium 1. Elimination of $E_R^{(1)}$ yields

$$E_f^{(2)} = T_{2\omega} E_f^{(1)} e^{i\varphi_f} + [T_1 E_b^{(1)}(z_0) - T_2 E_b^{(2)}(z_0)] e^{i\varphi_b} \quad (5.30)$$

where

$$T_{2\omega} = \frac{2n_{2\omega}^{(1)}}{n_{2\omega}^{(1)} + n_{2\omega}^{(2)}}$$

.

$$T_1 = \frac{n_\omega^{(1)} + n_{2\omega}^{(2)}}{n_{2\omega}^{(2)} + n_{2\omega}^{(1)}}$$

137

$$T_2 = \frac{n_{\omega}^{(2)} + n_{2\omega}^{(1)}}{n_{2\omega}^{(2)} + n_{2\omega}^{(1)}} \quad . \tag{5.31}$$

The phase of $E_b^{(2)}(z_0)$ in Eq. (5.29) is $e^{i\varphi_b}$ because it, like $E_b^{(1)}(z_0)$, derives from the propagation of E^{ω} through medium 1.

We can now apply Eq. (5.30) to the boundaries of the actual DCSHG configuration. At the first boundary, $z = z_1$, $E^0(z_1) = 0$ and no second harmonic is generated. Therefore, at the $z = 0$ glass-liquid interface, there is no incident free wave $E_f^{(1)}$, and the bound waves are given by

$$E_b^{(1)}(0) = E_b^G = \frac{-4\pi}{(n_{2\omega}^G)^2 - (n_{\omega}^G)^2} \Gamma_G E_0 (E_\omega t_\omega^{(1)})^2$$

$$E_b^{(2)}(0) = E_b^L = \frac{-4\pi}{(n_{2\omega}^L)^2 - (n_{\omega}^L)^2} \Gamma_L E_0 (E_\omega t_\omega^{(1)} t_\omega^{(2)})^2 \tag{5.32}$$

from Eq. (5.27) where G and L refer to glass and liquid, respectively, E_ω is the amplitude of the fundamental field incident on the air-glass boundary, and $t_\omega^{(1)} = 2 / (1 + n_\omega^G)$ and $t_\omega^{(2)} = 2n_\omega^G / (n_\omega^G + n_\omega^L)$ are the Fresnel transmission factors for E_ω at the air-glass and glass-liquid interfaces, respectively. From Eq. (5.30) the free wave created in the liquid at the glass-liquid interface is

$$E_f^L = T_1 E_b^G - T_2 E_b^L \tag{5.33}$$

138

where the phase $e^{i\varphi_b}$ is unity since the fundamental absorption in the glass is negligible.

As the free wave propagates through the liquid to the liquid-glass interface at $z = l$ it becomes

$$E_f(l) = E_f^L e^{[ik_f - (\alpha_{2\omega}/2)] l}.$$

(5.34)

The bound wave in the liquid at $z = l$ is still E_b^L and the bound wave in the glass at $z = l$ is equal to the bound wave in the glass at $z = 0$ reduced by the Fresnel factors $t_\omega^{(2)}$ and $t_\omega^{(3)} = 2n_\omega^L / (n_\omega^L + n_\omega^G)$ corresponding to the glass-liquid and liquid-glass interfaces, respectively. We therefore make the identifications $E_f^{(1)} = E_f^L$, $E_b^{(1)} = E_b^L$, $E_b^{(2)} = E_b^G (t_\omega^{(2)} t_\omega^{(3)})^2$, and $z_0 = l$ for insertion into (5.30) and obtain

$$E_f^G = T_{2\omega}^L E_f^L e^{i\varphi_f} + [T_L E_b^L - T_G (t_\omega^{(2)} t_\omega^{(3)})^2 E_b^G] e^{i\varphi_b}$$

(5.35)

with

$$T_{2\omega}^L = \frac{2n_{2\omega}^L}{n_{2\omega}^G + n_{2\omega}^L}$$

$$T_L = \frac{n_\omega^L + n_{2\omega}^L}{n_{2\omega}^G + n_{2\omega}^L}$$

139

$$T_G = \frac{n_\omega^G + n_{2\omega}^L}{n_{2\omega}^G + n_{2\omega}^L} \quad . \tag{5.36}$$

Because all of the glass and liquid refractive indices in the current experiments lie in the range 1.40 to 1.52, we can make the following approximations: $t_\omega^{(2)} \, t_\omega^{(3)} \cong 1$, $T_1 \, t_{2\omega}^L \cong T_G$, and $T_2 \, t_{2\omega}^L \cong T_L$. This simplifies Eq. (5.35) to

$$E_f^G = (T_G \, E_b^G - T_L \, E_b^L) \, (e^{i\varphi_f} - e^{i\varphi_b}) \quad . \tag{5.37}$$

Finally, at the glass-air interface $z = z_2$, the static electric field is negligible and there is no bound wave. The free wave E_f^G simply propagates through the boundary with the transmission factor $T_{2\omega}^G = 2n_{2\omega}^G / (1 + n_{2\omega}^G)$. The total second harmonic electric field out of the DCSHG cell is then

$$E^{2\omega} = T_{2\omega}^G \, (T_G \, E_b^G - T_L \, E_b^L) \, (e^{[ik_f - (\alpha_{2\omega}/2)]l} - e^{[ik_b - \alpha_\omega]l}) \quad , \tag{5.38}$$

and the second harmonic intensity $I^{2\omega}$ is

$$I_L^{2\omega}(0) = \frac{2c}{8\pi} \, [T_{2\omega}^G \, (T_G \, E_b^G - T_L \, E_b^L)]^2 \, e^{-[\alpha_\omega + (\alpha_{2\omega}/2)]l}$$
$$\{\cosh [(\alpha_\omega - \frac{\alpha_{2\omega}}{2})l] - \cos [(k_f - k_b)l]\} \tag{5.39}$$

If there is no absorption, Eq. (5.39) reduces to

$$I_L^{2\omega}(l) = \frac{c}{2\pi} \, [T_{2\omega}^G (T_G \, E_b^G - T_L \, E_b^L)]^2 \, \sin^2 [(k_f - k_b) l \, / \, 2] \qquad (5.40)$$

which oscillates periodically with increased pathlength through the liquid. In the wedged Maker fringe configuration, the liquid is confined between windows that make a small angle, α. As the wedge is translated perpendicularly to the beam, the path length l is increased producing oscillations in the output second harmonic intensity that are known as Maker fringes. The effect on the Maker fringes of absorption at either ω or 2w is to decrease the amplitude and introduce a nonzero minimum as can be seen in Eq. (5.39).

The second harmonic intensity is seen in Eqs. (5.39) and (5.40) to depend on both $\Gamma_G(-2\omega;\omega,\omega,0)$ and $\Gamma_L(-2\omega;\omega,\omega,0)$. In order to determine the desired quantity $\Gamma_L(-2\omega;\omega,\omega,0)$, we must have previous knowledge of $\Gamma_G(-2\omega;\omega,\omega,0)$ for the BK-7 glass cell windows. Furthermore, rather than attempt an absolute calibration of Eq. (5.40) with every experimental run, the Maker fringes from the DCSHG cell containing sample liquid are compared with the fringes obtained from a known reference standard. A careful absolute determination of the second harmonic coefficient of quartz has yielded[12] $d_{11}^Q = \chi^{(2)}(-2\omega;\omega,\omega) = 1.2 \times 10^{-9}$ esu, and this value is commonly used as the standard for both second harmonic susceptibility $\chi^{(2)}(-2\omega;\omega,\omega)$ and dc-induced second harmonic susceptibility $\chi^{(3)}(-2\omega;\omega,\omega,0)$ measurements. We fix the absolute magnitude of Γ_L, then, by bracketing the DCSHG measurements with second harmonic measurements of a quartz wedge without a static electric field applied. The analysis for the SH intensity observed from the quartz wedge is similar to the one given above, but

141

there are only two boundaries and the bound wave in the air at each one is zero. The final result is[2]

$$I_Q^{2\omega}(l) = \frac{c}{2\pi} (T_Q E_b^Q)^2 \sin^2 [(k_f^Q - k_b^Q)l/2] \tag{5.41}$$

where

$$T_Q = \frac{n_\omega^Q + n_{2\omega}^Q}{1 + n_{2\omega}^Q} \tag{5.42}$$

and

$$E_b^Q = \frac{-4\pi \, d_{11}^Q}{(n_{2\omega}^Q)^2 - (n_\omega^Q)^2} \left(\frac{2n_\omega^Q}{1 + n_\omega^Q}\right)^2 E_\omega^2 . \tag{5.43}$$

In the absence of absorption, one can simply compare the peak heights of the liquid DCSHG and quartz SHG Maker fringes to obtain Γ_L. From Eqs. (5.40) and (5.41), one finds

$$\Gamma_L = \frac{n_\omega^L + n_{2\omega}^L}{l_c^L T_L (t_\omega^{(1)} t_\omega^{(2)})^2} \left[T_G \frac{l_c^G \Gamma_G (t_\omega^{(1)})^2}{n_\omega^G + n_{2\omega}^G} \right.$$

$$\left. \pm \frac{T_Q}{E_0} \left(\frac{1 + n_{2\omega}^G}{2n_{2\omega}^G}\right) \frac{l_c^Q d_{11}^Q}{(n_\omega^Q + n_{2\omega}^Q)} \left(\frac{2n_\omega^Q}{1 + n_\omega^Q}\right)^2 \left(\frac{I_L^{2\omega}}{I_Q^{2\omega}}\right)^{1/2} \right] \tag{5.44}$$

where $l_c = \pi/(k_f - k_b) = \lambda/4(n^{2\omega} - n^\omega)$ is the coherence length and $t_\omega^{(1)}, t_\omega^{(2)}$ are defined in Eq. (5.32), T_L and T_G in Eq. (5.36), and T_Q in Eq. (5.42). Thus, in addition to the

142

refractive indices of liquid, glass and quartz at the fundamental and second harmonic frequencies, one must also know Γ_G, d_{11}^Ω, and E_0. The static field strength is $E_0 = \dfrac{V}{d}$ where V is the applied high voltage and d is the electrode spacing.

C. Implementation of DCSHG Experiment

Laser Source

The optical source for the DCSHG experiment is a Quanta-Ray DCR-1 neodymium-doped yttrium aluminum garnet (Nd:YAG) laser. The YAG laser is actively Q-switched at 10 Hz and produces 8 ns pulses at a wavelength of 1064 nm with a maximum output energy of 300 mJ per pulse. For the dispersion measurements of DCSHG in hexatriene and β-carotene, it was determined that appropriate, accessible wavelengths are 1064, 1543, and 1907 nm. The latter two wavelengths were obtained by frequency conversion of the YAG fundamental through the stimulated Raman scattering process.

The Stokes and anti-Stokes Raman processes illustrated in Figure 5-2 correspond to the subtraction and addition, respectively, of a quantum of energy of the material system from the incident photon. In Stokes Raman processes, the Raman medium makes a transition from an initial eigenstate $|i>$ to a higher-energy eigenstate $|f>$; whereas in anti-Stokes processes, the $|i>$ state is of higher energy. For our purposes, energies on the order of 1 mJ/pulse at the desired wavelengths were obtained by focusing the 1064 nm YAG fundamental into a 1m long metal cell that contained

hydrogen or methane gas at a pressure of 300 psi. The vibrational Stokes shift of hydrogen at 4155 cm^{-1} and of methane at 2916 cm^{-1} produced first Stokes lines of 1907 and 1543 nm, respectively. Higher order Stokes conversion is also observed due to the interaction of multiple vibrational quanta with the incident photon, and the available wavelengths are listed in Table 5-1.

Optical Layout

A schematic illustration of the DCSHG experimental layout is shown in Figure 5-3. The YAG fundamental at 1064 nm was steered by prism P_1 and focused by lens L_1 into the gas Raman cell. The reflection from P_1 was focused onto the gate photodiode PD which served as an optical trigger for the data collection electronics as discussed later. The output from the Raman cell consisting of many discrete wavelengths was recollimated by lens L_2 and steered by prism P_2 towards the dispersive prism P_3. Rotation of P_3 allows selection of the desired wavelength by aligning it through the pinhole PH while the other Raman lines are blocked. The beam was further filtered by the band pass filter F_1. Prism P_5 steered the beam towards the DCSHG sample cell while the reflection from P_5 was guided by prism P_6 into the reference arm.

In the sample arm, after steering by P_5, the beam was focused into the DCSHG sample cell S to be described in detail below. The cell was mounted on a configuration of four translation stages that controlled the height of the cell with respect to the beam, the position of the cell along the beam path, and the position of the cell transverse to the beam path. Control of the position along the beam path was required to adjust the beam

waist to the center of the cell, a condition required for optimization of the Maker fringes. Two stages adjusted the cell position transverse to the beam path, one to rapidly select between the sample cell and a quartz wedge mounted beside it on the stage assembly and the second driven by a stepper motor to allow fine adjustment of the transverse beam position for the Maker fringe data collection. The quartz wedge served to set the absolute magnitude of Γ_L by comparison of quartz SHG Maker fringes to the liquid DCSHG Maker fringes through Eq. (5.44). The stepper motor was controlled by a PDP-11 computer to translate the wedge sample in fine steps across the beam, thereby increasing the beam pathlength through the sample and generating Maker fringes. The output of the sample, consisting of the strong fundamental light and relatively weak second harmonic, was passed through filters (i.e. $CuSO_4$ solution) to absorptively remove the fundamental, further spectrally filtered by the monochromator M, and then weakly focused on the photomultiplier cathode PMT_1.

The reference beam was focused on a separate quartz crystal R that was used to reduce the fluctuations in the SH intensity $I^{2\omega}$. Because stimulated Raman conversion is a nonlinear process, fluctuations in the YAG fundamental are amplified in the Raman output, and further amplification of the fluctuations occurs in the SH conversion. Under the assumption that the intensities in the sample and reference arms are linearly related independent of the Raman fluctuations (e.g. linear beam splitting, detection, etc.), $I^{2\omega} \propto (I^\omega)^2$ of each arm is also linearly related. Thus division of the sample $I_S^{2\omega}$ by the reference $I_R^{2\omega}$ should remain constant. Pulse-to-pulse variations in beam profile and focal plane position still lead to slight variation in $I_S^{2\omega} / I_R^{2\omega}$, but the pulse-to-pulse signal

145

stability was drastically improved by this referencing technique. Further reduction in

fluctuation was accomplished by averaging over at least 20 to 30 shots for each data

point and rejecting all shots in which $I_R^{2\omega}$ varied by more than 30% from the mean value.

The reference beam was passed through absorptive filters to remove the fundamental and

weakly focused on PMT_2.

Liquid Sample Cell

There are three primary requirements to be incorporated into the design of the

sample cell: 1) The boundary conditions leading to Eq. (5.39) require that the electrodes

be wide enough that E^0 is essentially constant across the liquid but narrow enough that

E^0 is negligible at the front and back window-air interfaces. Analysis of the electrode

fringe fields demonstrates that the electrodes must extend a distance d beyond the glass-

liquid boundaries and be at least $4d$ away from the glass-air boundaries, where d is the

spacing between the electrodes.[13] 2) The wedge angle α of the liquid must be chosen

such that several fringes may be obtained in full translation of the cell for typical

coherence lengths l_c on the order of 15 to 30 μm. 3) The mean thickness l of the liquid

compartment should be relatively small so that the contrast between the Maker fringe

maximum and minimum is not "washed out" in weakly absorptive liquids as determined

by Eq. (5.39).

The cell, illustrated in Figure 5-4, consists primarily of two fine annealed BK-7

glass windows of dimension 8 x 24 x 1.6 mm formed into a wedge of α = 0.0227

radian with two stainless steel electrodes of dimension 6 x 28 mm attached at the top and

bottom. This configuration is encased in a larger glass cell with the two glass windows protruding slightly through the cell. The joints are sealed by Omega high temperature ceramic adhesive and coated by silicone rubber to ensure a leak-proof seal. The mean thickness of the liquid between the windows is about 1 n.m and the electrode spacing is 1.6 mm, the thickness of the windows.

Photomultiplier Tubes

For applications of DCSHG with a fundamental wavelength of 1907 nm, it is necessary to have a detector with high sensitivity in the near infrared out to 954 nm. For most photomultiplier tubes, the quantum efficiency is negligible beyond 900 nm. The Varian VPM-159A PMT with InGaAsP photocathode, however, has a typical quantum efficiency of 5% at 900 nm and 2% at 1060 nm. A gain of 10^4 - 10^5 is obtained from the 12 stage dynode configuration at the typical applied voltage of -1300 V. The PMT output pulse is longer than the laser pulse since the tube has a rise time of ~10 ns, but the output pulse is shorter than 100 ns and falls well within the opening of the ADC gate. Permanent cooling to below -20°C is required for the VPM-159A to avoid irreversible damage to the cathode. The PMT cooled housing obtained from Products for Research, Inc. also serves to drastically reduce the dark current that results from thermionic emission of electrons from the cathode and dynodes. As an additional consideration, too high an input intensity to the PMT can lead to saturation of the photocathode and, therefore, nonlinearity of the PMT response. The focusing conditions, input intensity, and high voltage were carefully maintained in the linear response regime.

147

Electronics and Data Acquisition

The high voltage pulse applied to the sample cell electrodes, the analog-to-digital converter (ADC) gate pulse provided by the photodiode, and the PMT output pulse must all be carefully synchronized. Rather than supply a constant high voltage to the electrodes, a 5 kV, 10 μs pulse is provided by a Cober 60S high voltage pulse generator to minimize the ionic conductivity and polarization of the electrodes. The laser pulse is synchronized to arrive near the 8 μs mark within the rectangular HV pulse; and since the laser pulse is of only 8 ns duration, the HV may be considered to provide a static E^0. The laser pulse is adjusted to arrive towards the end of the HV pulse in order to allow orientational equilibrium to occur in the liquid. Relative timing between the HV and laser pulses was achieved by triggering the HV generator on a pulse provided by the YAG laser upon firing of the flashlamps. The HV is triggered 250 μs after flashlamp firing, and the laser Q-switch is triggered 8μs later still. The 250 μs delay maximizes the laser output by allowing energy buildup in the cavity prior to Q-switching.

The PMT output is digitized through a LeCroy 2249w 12 channel ADC inserted into a standard CAMAC crate controller (Kinetic Systems model 3912) interfaced to a PDP-11. The ADC inputs have a common gate that is provided by a circuit triggered on the gate photodiode. The 600 ns gate covers the entire PMT output pulse with synchronization between the gate and PMT pulses achieved by delay boxes. After averaging the ratio PMT_1/PMT_2 over the desired number of shots, the computer stores

148

the result and advances the stepper motor to increase the beam pathlength. The fringes

are also plotted in real time on an x - y recorder as a monitor during the measurements.

Materials Handling and Preparation

Hexatriene, which was measured in the neat liquid, was obtained from Aldrich

Chemical Company in fused, glass ampules containing 1 gm of HT each. These were

stored in a freezer and allowed to warm to room temperature only a couple of hours

before use. The DCSHG cell was sealed with septa and filled with nitrogen for fifteen

minutes. After all other preparations for the measurement had been made, the ampule

was cracked open and HT was immediately transferred to the sealed DCSHG cell. After

data-taking of no more than thirty minutes, the HT was discarded. In this way,

exposure of HT to light, oxygen, and water was kept to a minimum.

β-carotene was obtained in microcrystalline form, also from Aldrich, and stored

in a refrigerator. Structural transformation in β-carotene is known to occur in solutions

with exposure to water or UV light and is manifested in a strong blue-shift in the optical

absorption spectrum accompanied by a striking color change from red to yellow.[14,15] In

order to prepare stock solutions, then, 150 mg β-carotene was quickly but carefully

weighed out on a Mettler H20 electronic balance, transferred to a flask, and placed in a

glove box. After evacuation of the glove box and inflow of nitrogen, 30 ml 1,4 dioxane

was added to the flask which was then capped with a septum, sealed with Parafilm, and

wrapped in aluminum foil for protection from light. The tendency of dioxane to absorb

water from the atmosphere was prevented by storage in an Aldrich "sure-seal" bottle and transfer into a nitrogen-filled flask.

Dilution of the stock solution for concentration-dependence measurements was carried out by transfer from the stock solution flask to small vials sealed with septa containing nitrogen and pure dioxane. The DCSHG sample cell was always filled with nitrogen before the addition of solution. Measurements of one week old solutions yielded a 20% decrease in $<\gamma(-2\omega;\omega,\omega,0)>$ of β-carotene compared to fresh solutions. Therefore, all measurements reported here were performed in less than two days after preparation of the stock solution.

D. Experimental Results and Analysis

Quartz, Glass, and Dioxane

As discussed in conjunction with Eq. (5.44), several quantities must be precisely known in order to achieve accurate measurements of the liquid DCSHG susceptibility Γ_L. In particular, the refractive indices, coherence lengths, and susceptibilities of quartz, BK-7 glass, and dioxane must be well-characterized. In this subsection, we present the reference values used for these quantities at the relevant wavelengths of 1907, 1543, and 1064 nm and discuss the internal consistency of these results.

The value of the second harmonic susceptibility d_{11} of quartz has been carefully determined[12] to be 1.20×10^{-9} esu at a fundamental wavelength of 1064 nm and this value is universally accepted in the community as the reference standard. To obtain d_{11}

150

at 1907 and 1543 nm, we applied the generalized form of Miller's rule. Miller

discovered in a survey of d_{11} values of inorganic crystals that, for crystals with d_{11}

values that vary over three orders of magnitude, d_{11} could be described by

$$d_{11} = \chi_{11}^{2\omega} \, \chi_{11}^{\omega} \, \chi_{11}^{\omega} \, \delta_{11} \tag{5.45}$$

where χ_{11} is the linear susceptibility and δ_{11}, known as the Miller's coefficient, has a

variation of less than a factor of two.[16] This empirical rule has been generalized to

describe the dispersion of d_{11} in inorganic crystals in the weakly dispersive regime,

leading to

$$d_{11}^{\omega'} = d_{11}^{\omega} \, \frac{\chi_{11}^{2\omega'} \, \chi_{11}^{\omega'} \, \chi_{11}^{\omega'}}{\chi_{11}^{2\omega} \, \chi_{11}^{\omega} \, \chi_{11}^{\omega}} \, . \tag{5.46}$$

Table 5-2 lists the values obtained for d_{11}^{ϱ} from Eq. (5.46) along with the tabulated[17]

refractive indices at the fundamental and second harmonic wavelengths.

An example of the Maker fringes obtained from quartz is compared to the fringes

obtained from the DCSHG cell filled with dioxane in Figure 5-5 for $\lambda = 1543$ nm.

Because quartz generates SH intensity via $\chi_{ijk}^{(2)}$ $(-2\omega;\omega,\omega)$ and the DCSHG cell via the

higher order $\chi_{ijkl}^{(3)}$ $(-2\omega;\omega,\omega,0)$, the quartz signal is several orders of magnitude larger.

The quartz fringe amplitude in Fig. 5-5 was depressed by a factor of 3.72×10^3 with

neutral density filters (OD = 3.57) relative to the dioxane fringe. The Maker fringes are

least-squares fit to a function of the form

$$I^{2\omega}(l) = A_1 \sin^2\left(\frac{\pi l}{2A_3} + A_4\right) + A_2 \qquad (5.47)$$

where A_1 is the fringe amplitude, A_2 the fringe minimum, A_3 the coherence length l_c, and A_4 an arbitrary phase factor. In evaluation of Γ_L from Eq. (5.44), we use the mean fringe height $A_m = \frac{A_1}{2} + A_2$ for $I^{2\omega}$ rather than the fringe maximum in order to properly account for any non-zero minimum that results from finite beam size effects.[2,18]

The Maker fringe analysis directly yields l_c as well as $I^{2\omega}$ for insertion into Eq. (5.44). Since we also have the relation

$$l_c = \frac{\pi}{(k_f - k_b)} = \frac{\lambda}{4(n^{2\omega} - n^{\omega})} , \qquad (5.48)$$

if we have the necessary refractive index values, we can verify the consistency of the measured l_c with the expected value. Experimentally, l_c is determined by the angle of the wedge and the transverse displacement l of the cell from a fringe minimum to a maximum through

$$l_c = l \, \sin \alpha \qquad (5.49)$$

The quartz wedge angle α was independently measured to be 0.0195 radian. The calculated values of l_c for quartz from Eq. (5.48) and refractive index data are in excellent agreement with the experimental values of l_c as shown in Table 5-2.

The refractive indices of the BK-7 glass windows at the pertinent wavelengths were calculated from the dispersion relation

$$n^2(\lambda) = A_0 + A_1 \lambda^2 + A_2 \lambda^{-2} + A_3 \lambda^{-4} + A_4 \lambda^{-6} + A_5 \lambda^{-8} \qquad (5.50)$$

where λ is the wavelength in microns and the dispersion constants A_0 through A_5 obtained from Schott-Glass Technologies[19] are listed in Table 5-3. The DCSHG susceptibility of BK-7 glass Γ_G has been measured at 1064 nm by Oudar to be 3.50 x 10^{-14} esu using a glass wedge with HV electrodes attached and in direct comparison with d_{11} of quartz.[2] Γ_G values at 1907 and 1543 nm were obtained through this value in conjunction with the generalized Miller's rule. Table 5-4 lists the calculated values of n^ω, $n^{2\omega}$, Γ_G, and l_c^G for BK-7 at the wavelengths 1064, 1543, and 1907 nm.

The measurement of Γ_L for pure 1,4 dioxane at each of the three fundamental wavelengths was required for the determination of $<\gamma(-2\omega;\omega,\omega,0)>$ for β-carotene from concentration dependence studies of solutions and serves to illustrate the basic procedure for DCSHG experiments in liquids. For example, the least squares fit to Eq. (5.47) of the fringes taken for quartz and dioxane at $\lambda = 1064$ nm yields values for A_m^Q, l_c^Q, A_m^L and l_c^L. The value for A_m^Q must then be scaled up by 10^{OD} where OD is the optical density of the filters used to reduce the quartz SH intensity on PMT_1 to maintain linearity of the PMT signal. The measured angle for the DCSHG cell of $\alpha = 0.0277$ rad is used in the calculation of l_c^L. From Aldrich Chemical Company, the refractive index of dioxane at $\lambda = 590$ nm (Sodium d line) is 1.4215. Our measured value of l_c for

153

dioxane, 26.67 μm, yields $n^{2\omega}(532 \text{ nm}) - n^{\omega}(1064 \text{ nm}) = 0.010$. We therefore use n^{ω} = 1.41 and $n^{2\omega} = 1.42$ where the lesser precision of the refractive indices of dioxane in comparison to BK-7 and quartz introduces less than 1% uncertainty into Γ_L. The full set of parameters used to determine Γ_L of dioxane at 1064 nm are listed in Table 5-5. Insertion into Eq. (5.44) yields $\Gamma_L = 5.71 \times 10^{-14}$ esu.

The coherence lengths of dioxane at 1907 and 1543 nm allow us to approximate the refractive index at these wavelengths as well. At 1543 nm, $l_c = 71.1$ μm gives $\Delta n = n^{2\omega} - n^{\omega} = 0.005$; and at 1907 nm, for $l_c = 105.7$ μm, $\Delta n = 0.005$. The refractive index is well-enough approximated for our purposes by 1.41 at 1907, 1543, 1064, and 953 nm and 1.42 at 771 and 532 nm. The values of the refractive index at the fundamental and second harmonic frequencies, the coherence length, and the measured Γ_L for dioxane at $\lambda = 1064$, 1543, and 1907 nm are listed in Table 5-6.

Finally, we can calculate the molecular susceptibility $<\gamma(-2\omega;\omega,\omega,0)>$ from

$$\Gamma_L = N \left(\frac{n_{\omega}^2 + 2}{3}\right)^2 \left(\frac{n_{2\omega}^2 + 2}{3}\right) \left[\frac{(n_{\omega}^2 + 2)\varepsilon}{n_{\omega}^2 + 2\varepsilon}\right] <\gamma(-2\omega;\omega,\omega,0)> \qquad (5.51)$$

where N is the number density of molecules and ε is the static dielectric constant of the liquid. The number density is given by

$$N = \frac{N_A}{MW} d \qquad (5.52)$$

154

where N_A is Avogadro's number, MW the molecular weight and d the density. For

dioxane, with MW = 88.1 gm/mole and d = 1.034 gm/cm^3, we obtain N = 7.065 x 10^{21}

cm^{-3}. The static dielectric constant is ε = 2.209 at room temperature. The values thus

obtained for $<\gamma(-2\omega;\omega,\omega,0)>$ from the measured Γ_L are also listed in Table 5-6. Since

the optical absorption of dioxane begins near λ = 300 nm, the dispersion of

$<\gamma(-2\omega;\omega,\omega,0)>$ is expected to be weak in our experimental wavelength regime. The

weak, montonic increase in the experimental $<\gamma(-2\omega;\omega,\omega,0)>$ with decreased

wavelength is a satisfying indication that our experimental technique is consistent from

wavelength to wavelength and possesses high precision.

Hexatriene

The optical absorption spectrum of liquid HT in the vicinity of the $1\,^1B_u \leftarrow 1\,^1A_g$

π-electron transition is shown in Figure 5-6. The 0-0 transition occurs at 274 nm (4.53

eV) and the vertical transition at 243 nm (5.10 eV). In comparison with the vapor phase

absorption spectrum in which both the 0-0 and vertical transitions occur at 251 nm (4.93

eV), it is seen that the primary effect on the spectrum in going from the gaseous to

condensed phase is a red-shift of the low-energy shoulder of the spectrum while the

peak of the oscillator strength (vertical transition) shifts only slightly. Since the second

harmonic wavelengths in the current study are at 953, 771 and 532 nm, all well below

the $1\,^1B_u \leftarrow 1\,^1A_g$ absorption, it is expected that the dispersion of $<\gamma(-2\omega;\omega,\omega,0)>$ will

be weak, in analogy to the dioxane results.

155

The refractive indices of HT, required for evaluation of Γ_L from the Maker fringe data as well as for determination of $<\gamma(-2\omega;\omega,\omega,0)>$, were obtained from the value $n = 1.56135$ at 590 nm from Aldrich in conjunction with the $\Delta n = n^{2\omega} - n^\omega$ values derived from l_c at each fundamental wavelength. The measured values of l_c at 1907, 1543 and 1064 nm, 49.5, 29.1 and 7.9 μm, respectively, yield $\Delta n = 0.010$, 0.013, and 0.034. The consistent set of refractive indices determined by these values to a precision of ± 0.01 is listed in Table 5-7.

Γ_L at each fundamental wavelength was calculated for neat HT from the Maker fringe data and the quartz and BK-7 values given in Tables 5-2 and 5-4 in the same manner as described above for dioxane. The dispersion is fairly weak as expected. Primarily through the significantly shorter l_c of HT compared to dioxane, but also due to as much as 60% increase in fringe height, Γ_L of HT at the various wavelengths is 3.5 to 4.2 times larger than that of dioxane. Table 5-7 lists the experimental values for Γ_L of HT at each wavelength.

From the HT molecular weight of 80.13 and density $d = 0.737$ gm/cm^{-3}, we determine the number density N to be 5.54×10^{21} cm^{-3} in the neat liquid. Using this value of N, $\varepsilon = 2.276$,[20] the refractive indices from Table 5-7, and Eq. (5.51), we obtain $<\gamma(-2\omega;\omega,\omega,0)> = 8.2$, 7.5, and 10.0×10^{-36} esu for 1907, 1543, and 1064 nm, respectively. These values as well as those of Γ_L have an associated experimental uncertainity of $\pm 15\%$ determined from the reproducibility of the Maker fringes and uncertainities in the standard and derived values employed for quartz and BK-7 glass. Comparison of the measured values for $<\gamma(-2\omega;\omega,\omega,0)>$ with the theoretically predicted

156

values as described in Chapter 4 is made in Table 5-8. At each of the three fundamental

wavelengths, experiment and theory are in agreement within the 15% experimental

uncertainity. As discussed in Chapter 4, the theoretical values are for a mixture of 60%

trans and 40% *cis* conformations of HT and include a small σ-electron contribution to

$<\gamma(-2\omega;\omega,\omega,0)>$ determined from bond additivity analysis of alkane chains.

The experimental values of $<\gamma(-2\omega;\omega,\omega,0)>$ are also plotted against the

theoretically predicted dispersion curve in Figure 5-7. Since the first 2ω resonance is

predicted to occur for a fundamental wavelength of 502 nm, far shorter than our shortest

experimental wavelength, the dispersion is predicted to result in only a 25% increase in

$<\gamma(-2\omega;\omega,\omega,0)>$ in the experimental region. Indeed, the difference between the smallest

and largest experimental values is 33%. The 8% larger measured value at 1907 nm

relative to 1543 nm is considered a fluctuation within the experimental uncertainty and is

not evidence for anomalous dispersion. The experimental results demonstrate that the

theoretical method accounting for electron correlation described in Chapters 2 through 4

accurately determines the magnitude and dispersion of $<\gamma(-2\omega;\omega,\omega,0)>$ in HT.

β-Carotene

The optical absorption spectrum of β-carotene in solution with dioxane, shown

in the vicinity of the $1^1B_u \leftarrow 1^1A_g$ π-electron transition in Figure 5-8, exhibits the onset

of absorption near 530 nm (2.34 eV), the 0-0 transition at 484 nm (2.56 eV), and the

vertical transition at 455 nm (2.73 eV). The second harmonic wavelengths 953 and 771

nm are quite far from the $1\,^1B_u$ excitation, but we expect the second harmonic at 532 nm to exhibit strong resonant enhancement due to its proximity to the optical absorption.

Under certain conditions, DCSHG measurements in solution at a single concentration can yield unreliable results due to solute-solute interactions.[3] In order to eliminate this possibility as well as to obtain more precise values of $<\gamma(-2\omega;\omega,\omega,0)>$, we have measured Γ_L as function of β-carotene concentration. In the analysis of these measurements, we have assumed that each molecular species contributes to Γ_L in a weighted average of $<\gamma(-2\omega;\omega,\omega,0)>$, that the local field factors are independent of the molecular species, and that n and ε are independent of concentration in these relatively dilute solutions of nonpolar solvent and solute. With these approximations, we have

$$\Gamma_L = (\frac{n_\omega^2 + 2}{3})^2 \ (\frac{n_{2\omega}^2 + 2}{3}) \ [\frac{(n_\omega^2 + 2)\varepsilon}{n_\omega^2 + 2\varepsilon}]$$

$$[\ N_1 <\gamma_1(-2\omega;\omega,\omega,0) > \ + \ N_2 <\gamma_2(-2\omega;\omega,\omega,0) > \ ] \qquad (5.53)$$

where the subscripts 1 and 2 refer to solvent and solute, respectively. Furthermore, in the limit $|<\gamma_2(-2\omega;\omega,\omega,0)>| >> |<\gamma_1(-2\omega;\omega,\omega,0)>|$, $\frac{\partial \Gamma_L}{\partial C}$, where C is the concentration in mole / litre; depends only on $<\gamma_2(-2\omega;\omega,\omega,0)>$. We then have,

$$<\gamma_2(-2\omega;\omega,\omega,0) > \ = \ (\frac{3}{n_\omega^2 + 2})^2 (\frac{3}{n_2^{2\omega} + 2})$$

$$[\frac{n_\omega^2 + 2\varepsilon}{(n_\omega^2 + 2)\varepsilon}] \ (\frac{1}{6.02 \times 10^{20}}) \ \frac{\partial \Gamma_L}{\partial C} \ . \qquad (5.54)$$

158

We used stock concentrations of 8 - 9 x 10^{-3} mole / liter and measured Γ_L at several more dilute concentrations for each fundamental wavelength. In all cases, Γ_L was quite linearly dependent on C indicating that the approximations that lead to Eq. (5.54) are valid. At 1907 and 1543 nm, l_c of the solutions decreased by no more than 3% relative to pure dioxane, while at 1064 nm, a 10% decrease was observed. The larger change in l_c at 1064 nm is due to the strong dispersion in the linear susceptibility of β-carotene as the second harmonic wavelength approaches the $1^1B_u \leftarrow 1^1A_g$ excitation wavelength. Nevertheless, the decrease in l_c at 1064 nm from 26.7 to 24.2 μm results from a change in $n^{2\omega} - n^{\omega}$ from 0.010 to 0.011 since the solution is dilute, and the approximation of constant refractive index remains valid. The SH fringe height, however, increases by 95% for the stock solution relative to pure solvent at 1064 nm and by 50% at 1907 and 1543 nm.

The concentration dependences of $\Gamma_L = \chi^{(3)}(-2\omega;\omega,\omega,0)$ at λ = 1907, 1543, and 1064 nm are shown in Figures 5-9, 5-10, and 5-11, respectively. The measurements at 1543 and 1064 nm were made in solutions of β-carotene in dioxane while at 1907 nm the solvent was benzene. Γ_L at each concentration was determined as described above. The refractive indices of benzene, for the 1907 nm measurements, are $n^{\omega} \cong n^{2\omega} \cong 1.50$. Table 5-9 lists the slopes $\frac{\partial \Gamma_L}{\partial C}$ determined from each concentration dependence and the values for $<\gamma(-2\omega;\omega,\omega,0)>$ of β-carotene obtained from Eq. (5.54). The closeness of the measured values at 1907 and 1543 nm in the weak dispersion regime demonstrates that solvent-solute interactions are relatively weak. As expected based on the optical

159

absorption spectrum, $\langle\gamma(-2\omega;\omega,\omega,0)\rangle$ at 1064 nm is, however, much larger than the values at the two longer wavelengths.

In Figure 5-12, the experimental value for $\langle\gamma(-2\omega;\omega,\omega,0)\rangle$ of β-carotene at 1907 nm is plotted against the length of the chain along with the theoretical results from Chapter 4. For β-carotene, the length L is taken as 25.4 Å which corresponds to the $N = 22$ linear $trans$-polyene. The β-carotene experimental value is in excellent agreement with extrapolation of the theoretically predicted power law dependence $\langle\gamma(-2\omega;\omega,\omega,0)\rangle \propto L^{3.4}$. This result taken together with the agreement between experiment and theory for the magnitude of $\langle\gamma(-2\omega;\omega,\omega,0)\rangle$ for HT, both validates the theoretical power law dependence and extends the region of chain lengths over which it holds beyond the largest length addressable with current computational resources.

Table 5-1. Vibrational Raman Lines from Hydrogen and Methane Pumped by a

Nd:YAG Laser.

Raman Medium :	H$_2$	CH$_4$	H$_2$	CH$_4$
Pump Wavelength (nm) :	1064	1064	532	532
Second Stokes (nm)	----	2804	954	771
First Stokes (nm)	1907	1543	683	630
First anti-Stokes (nm)	738	812	436	461
Second anti-Stokes (nm)	565	657	369	406
Third anti-Stokes (nm)	457	551	320	363

Table 5-2. Fundamental and Second Harmonic Refractive Indices, Calculated and Experimental Coherence Lengths, and Derived d_{11} Values for Quartz.

λ(nm)	n^{ω}	$n^{2\omega}$	$l_c = \dfrac{\lambda}{4(n^{2\omega} - n^{\omega})}$ (μm)	$l_c^{exp.}$ (μm)	d_{11} (10^{-9} esu)
1907	1.5224	1.5358	35.6 ± 1.6	36.3 ± 0.2	1.14
1543	1.5278	1.5390	34.4 ± 2.0	34.9 ± 0.2	1.16
1064	1.5341	1.5470	20.6 ± 1.0	21.2 ± 0.2	1.20

Table 5-3. Constants for Refractive Index Dispersion Relation of BK-7 Glass.

$$[n(\lambda)]^2 = A_0 + A_1 \lambda^2 + A_2 \lambda^{-2} + A_3 \lambda^{-4} + A_4 \lambda^{-6} + A_5 \lambda^{-8} \qquad (\lambda \text{ in } \mu m)$$

A_0 : 2.2718929

A_1 : -1.0108077 x 10^{-2}

A_2 : 1.0592509 x 10^{-2}

A_3 : 2.0816965 x 10^{-4}

A_4 : -7.6472538 x 10^{-6}

A_5 : 4.9240991 x 10^{-7}

Table 5-4.   Fundamental and Second Harmonic Refractive Indices, Coherence Lengths, and Γ_G for BK-7 Glass.

λ (nm)	n^{ω}	$n^{2\omega}$	l_c (μm)	Γ_G (10^{-14} esu)
1907	1.4960	1.5082	39.08	3.32
1543	1.5008	1.5114	36.39	3.39
1064	1.5067	1.5191	21.37	3.50

Table 5-5. Parameters for Γ_L of Dioxane at $\lambda = 1064$ nm.

d_{11} Quartz	:	1.20×10^{-9} esu
l_c Quartz	:	21.4 μm
n^{ω} Quartz	:	1.5341
$n^{2\omega}$ Quartz	:	1.5470
Γ_G BK-7	:	3.50×10^{-14} esu
l_c BK-7	:	21.37 um
n^{ω} BK-7	:	1.5067
$n^{2\omega}$ BK-7	:	1.5191
n^{ω} Dioxane	:	1.41
$n^{2\omega}$ Dioxane	:	1.42
l_c Dioxane	:	26.7 μm
E_0	:	5.10 kV $/ 0.16$ cm
A_m Quartz	:	4.41×10^4
A_m Dioxane	:	0.758

Table 5-6. Fundamental and Second Harmonic Refractive Indices, Coherence Length, Γ_L, and $<\gamma(-2\omega;\omega,\omega,0)>$ for Dioxane.

λ (nm)	n^ω	$n^{2\omega}$	l_c (μm)	Γ_L (10^{-14} esu)	$<\gamma(-2\omega;\omega,\omega,0)>$ (10^{-36} esu)
1907	1.41	1.41	105.7	4.50	1.95
1543	1.41	1.42	71.1	4.93	2.14
1064	1.41	1.42	26.7	5.71	2.48

166

Table 5-7. Fundamental and Second Harmonic Refractive Indices, Coherence Length, and Γ_L for HT.

λ (nm)	n^{ω}	$n^{2\omega}$	l_c (μm)	Γ_L (10^{-14} esu)
1907	1.48	1.49	49.6	17.7
1543	1.48	1.50	26.3	16.1
1064	1.49	1.51	7.9	22.0

Table 5-8.   Experimental and Theoretical Values of $<\gamma(-2\omega;\omega,\omega,0)>$ for HT.

λ (nm)	Experiment (10^{-36} esu)	Theory (10^{-36} esu)
1907	8.2 ± 1.2	7.1
1543	7.5 ± 1.1	7.5
1064	10.0 ± 1.5	8.9

Table 5-9. $\partial\Gamma_L / \partial C$ and $\langle\gamma(-2\omega;\omega,\omega,0)\rangle$ for β-Carotene.

λ (nm)	$\frac{\partial\Gamma_L}{\partial C}$ (10^{-12} esu/M)	$\langle\gamma(-2\omega;\omega,\omega,0)\rangle$ (10^{-36} esu)
1907	1.50 ± 0.15	616 ± 62
1543	1.16 ± 0.07	592 ± 36
1064	3.09 ± 0.25	1580 ± 130

169
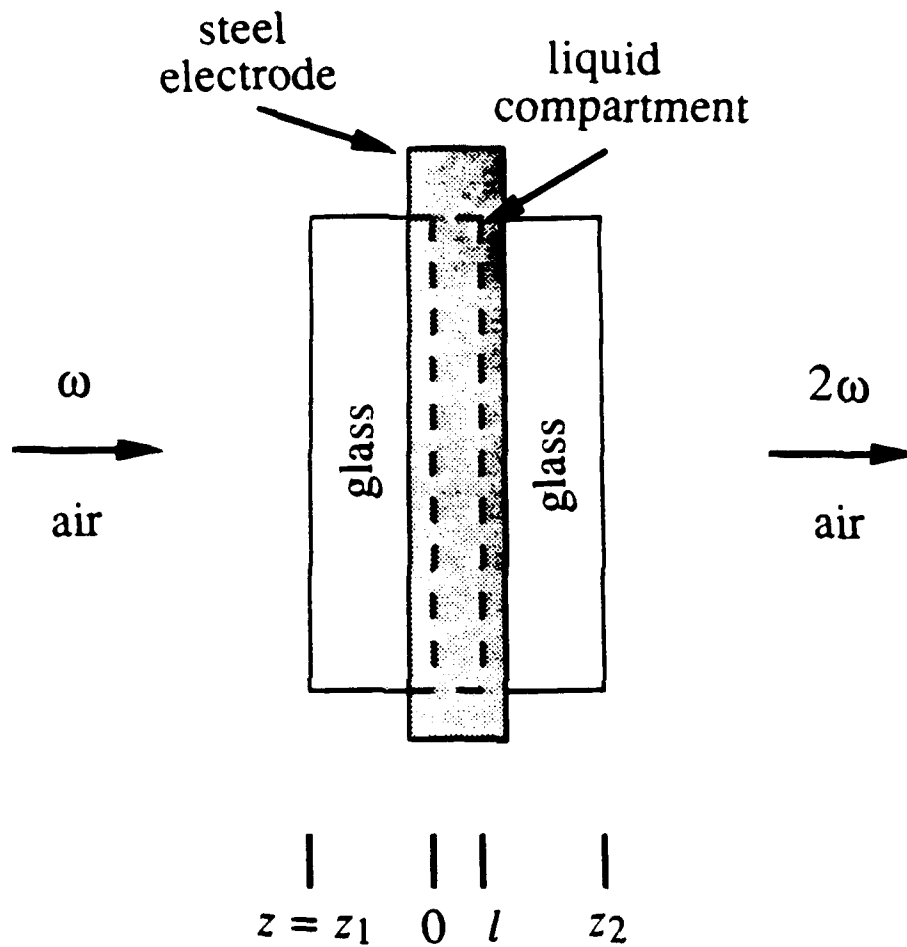
Figure 5-1. Schematic illustration of the DCSHG cell configuration. The top and bottom steel HV electrodes extend entirely over the liquid compartment of width l and partially over the glass windows. In the actual cell, the windows form a wedge such that the pathlength l varies across the transverse dimension.
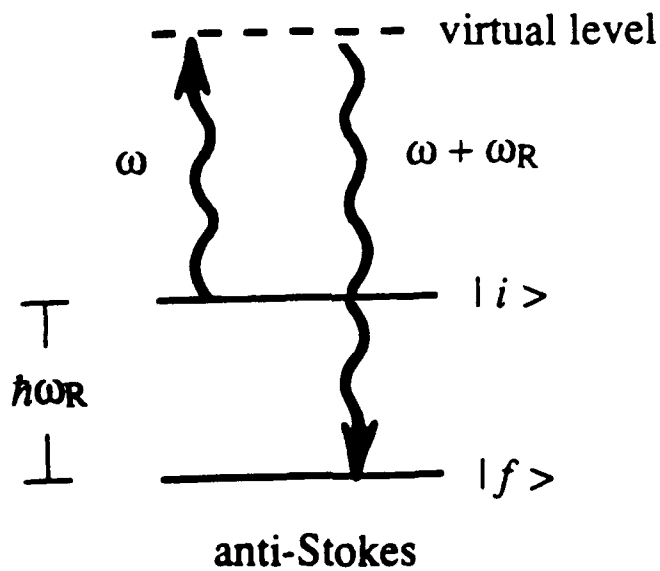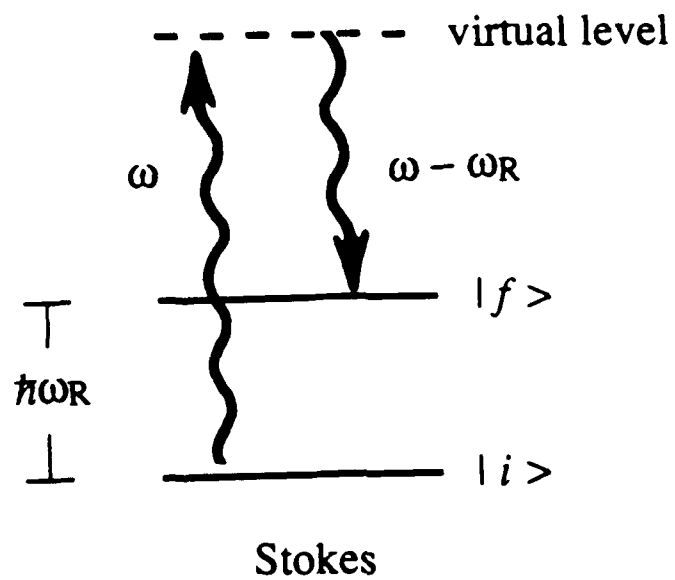
Figure 5-2. Schematic illustrations of the Stokes and anti-Stokes Raman processes that are used for frequency conversion of the Nd:YAG laser output.
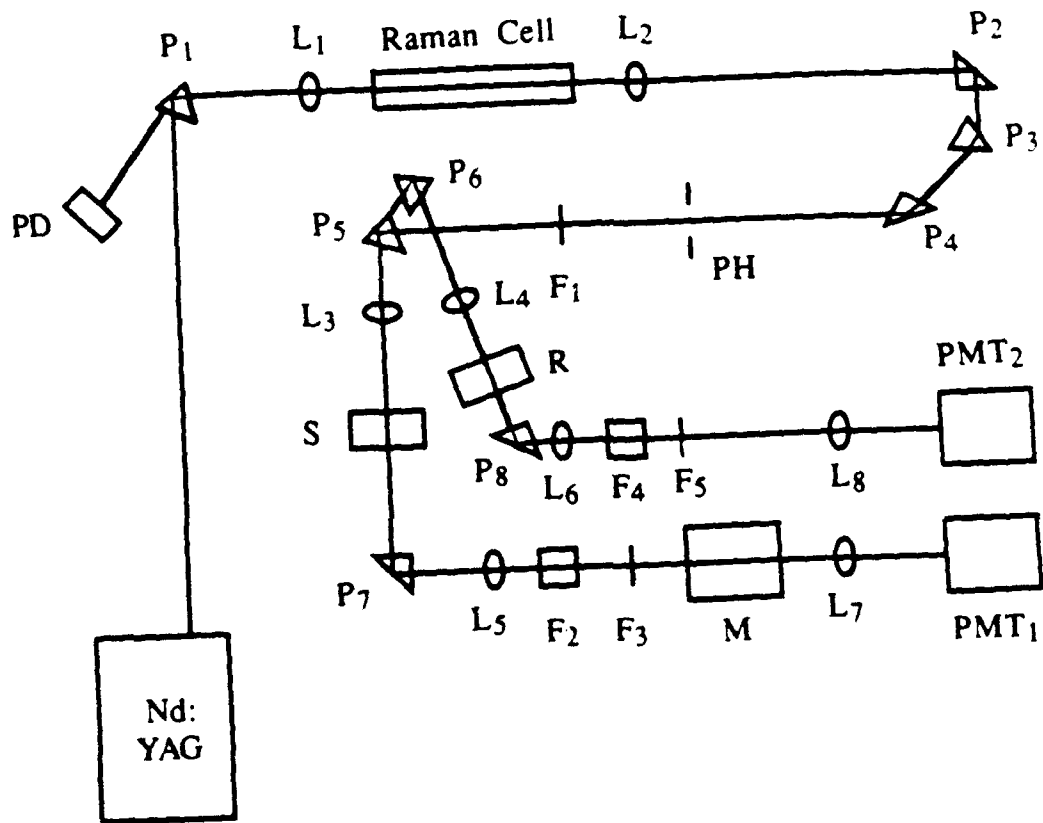
171

Figure 5-3. Experimental layout of the dc-induced second harmonic generation (DCSHG) experiment.
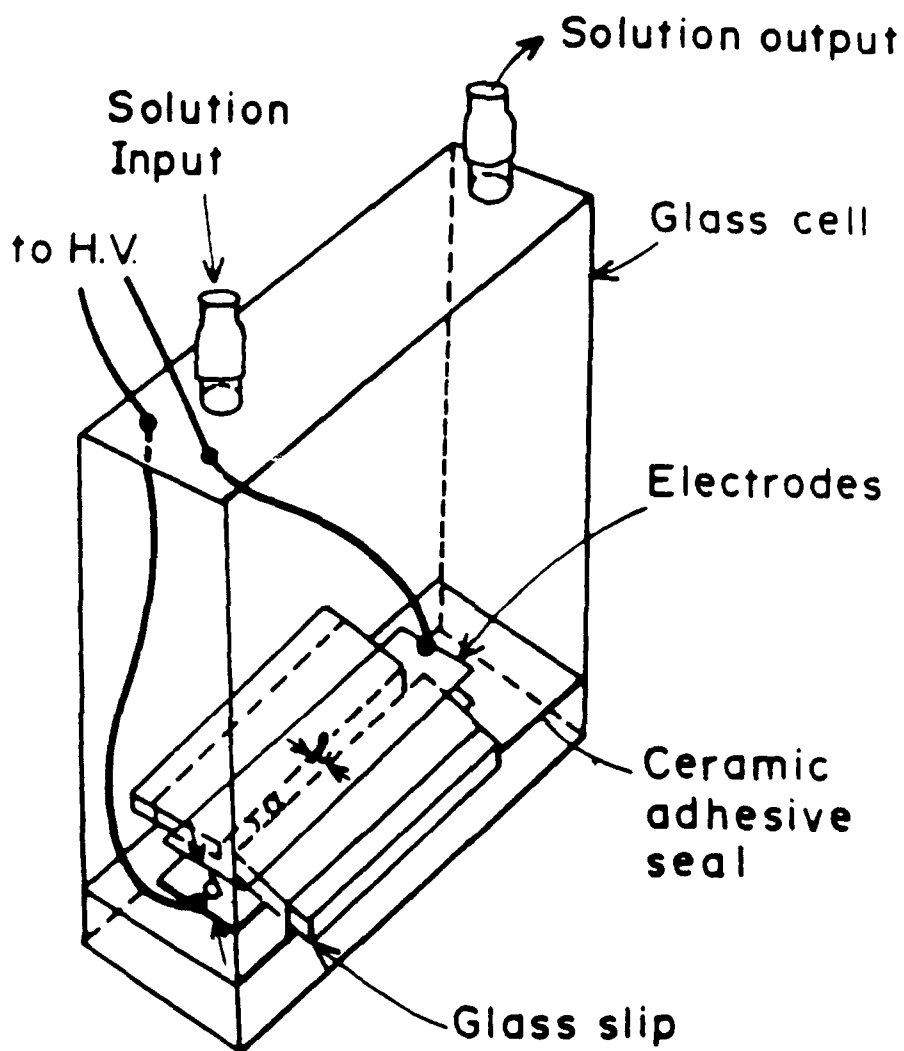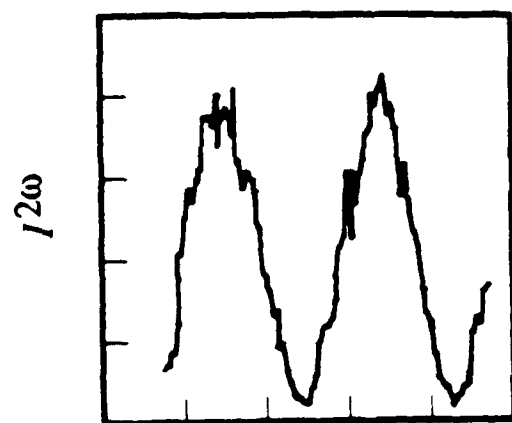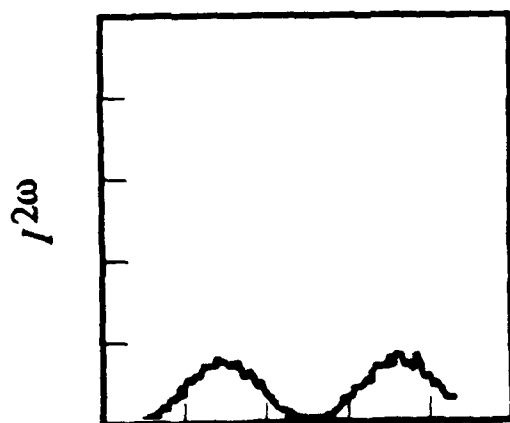
Figure 5-4. The DCSHG liquid sample cell. The BK-7 glass windows form a wedge angle $\alpha = 0.0227$ rad with a mean pathlength of 1.0 mm. The HV electrodes are separated by 1.6 mm.

Figure 5-5. Sample DCSHG Maker fringes obtained for (a) quartz and (b) 1,4-dioxane at a fundamental wavelength $\lambda = 1543$ nm. The quartz second harmonic intensity is attenuated by an optical density of 3.57.
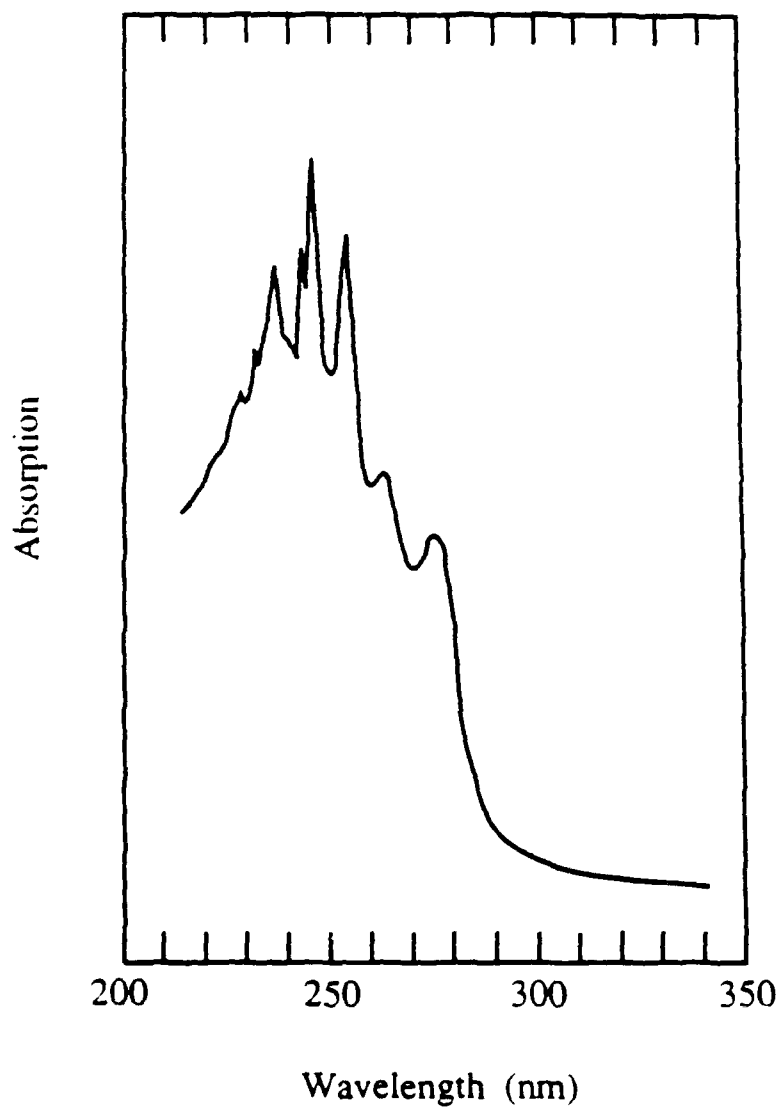
174

Figure 5-6. The linear absorption spectrum of hexatriene (HT) in the neat liquid in the region of the $1^1B_u \leftarrow 1^1A_g$ π-electron transition.
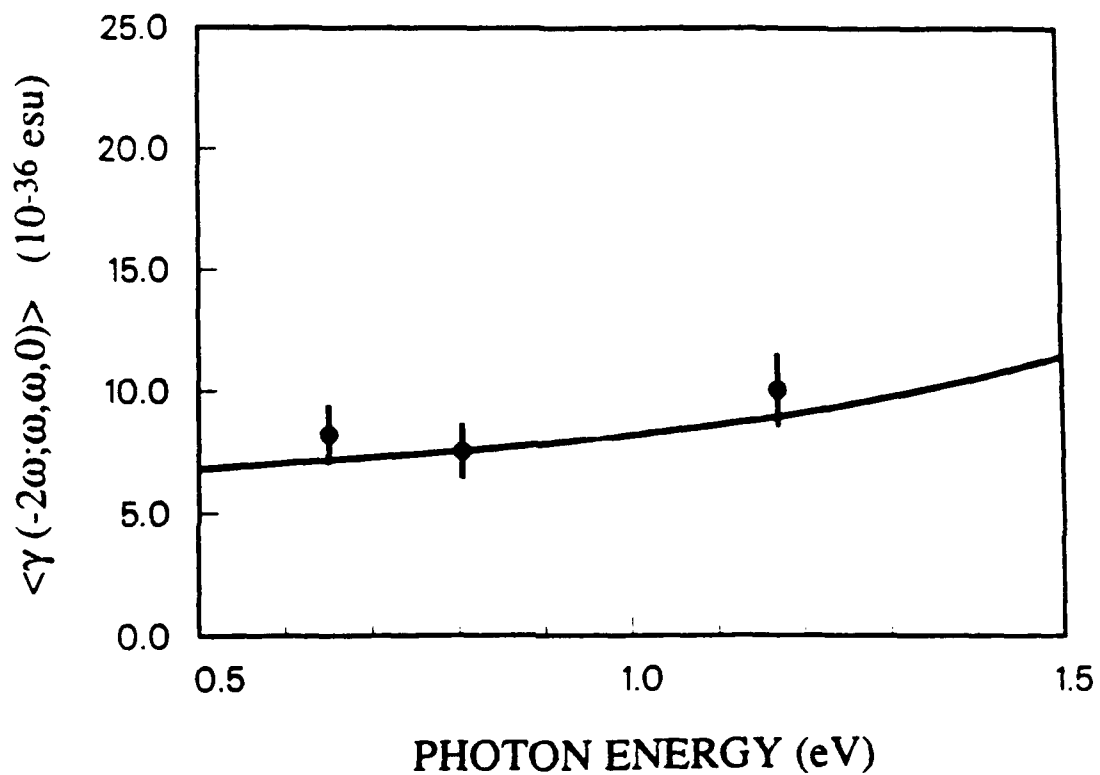
Figure 5-7. The experimentally determined values of $<\gamma(-2\omega;\omega,\omega,0)>$ for HT at $\lambda =$ 1907, 1543, and 1064 nm and the theoretical dispersion curve.
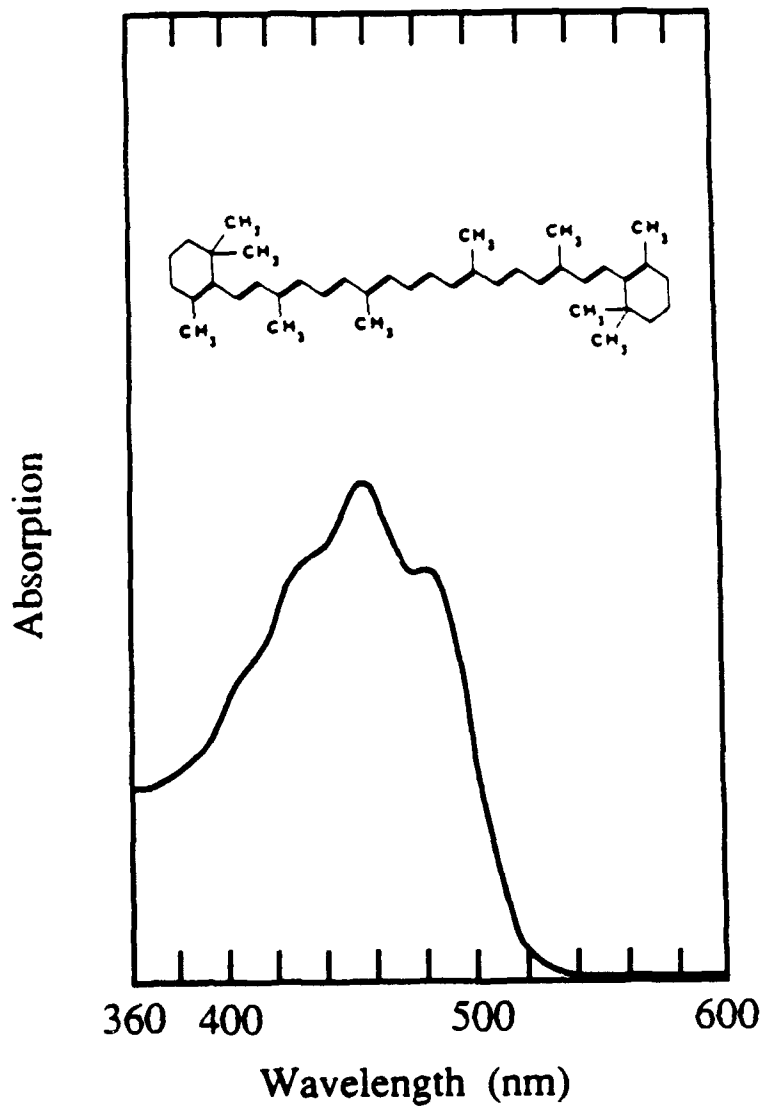
Figure 5-8. The linear absorption spectrum of β-carotene in solution with 1,4-dioxane in the region of the $1\,^1B_u \leftarrow 1\,^1A_g$ π-electron transition. The molecular structure of β-carotene is also shown.
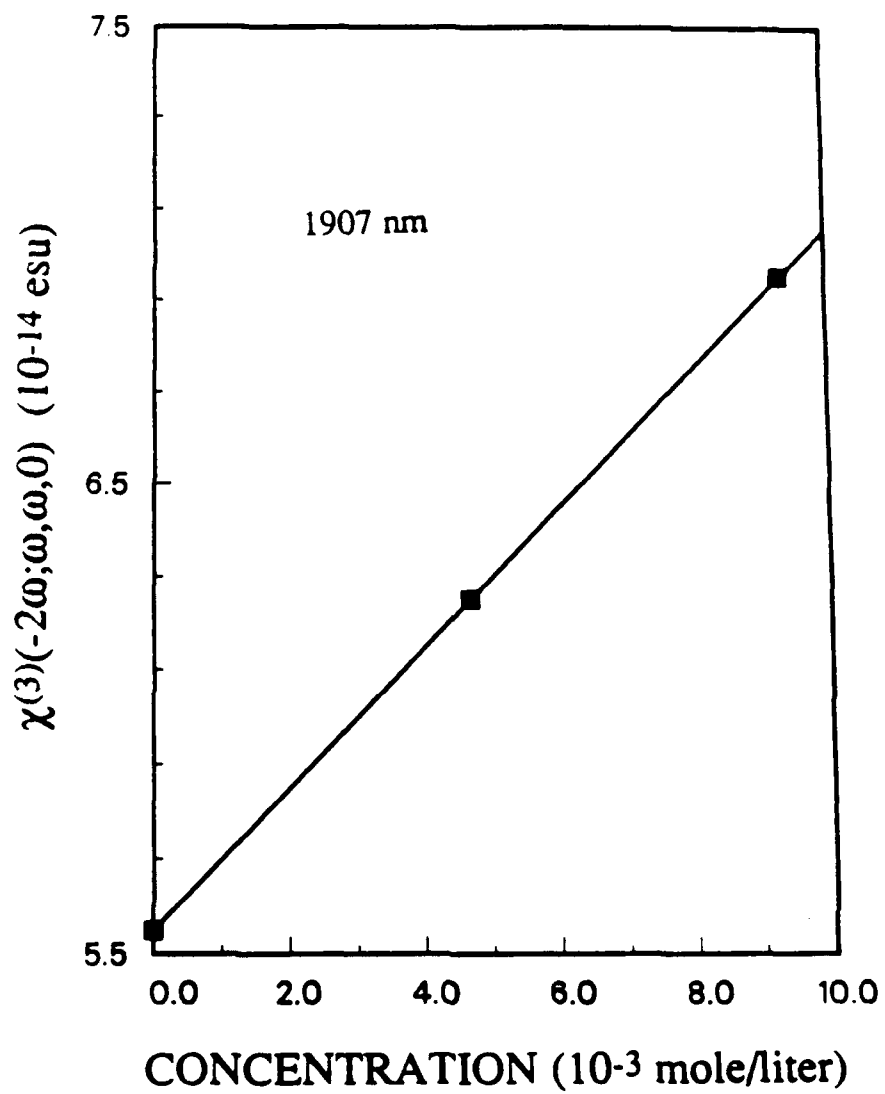
177

Figure 5-9. Concentration dependence of $\chi^{(3)}(-2\omega;\omega,\omega,0)$ for β-carotene in solution with benzene at $\lambda = 1907$ nm.
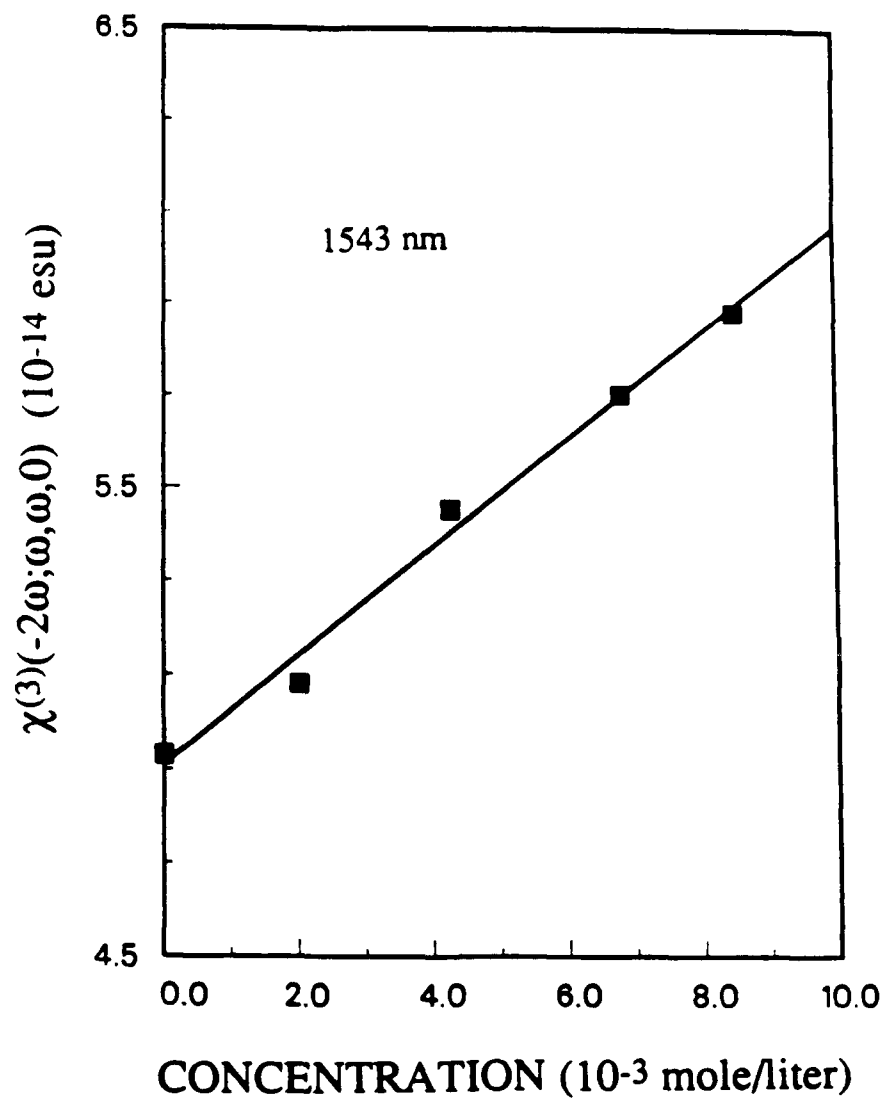
Figure 5-10. Concentration dependence of $\chi^{(3)}(-2\omega;\omega,\omega,0)$ for β-carotene in solution with dioxane at λ = 1543 nm.
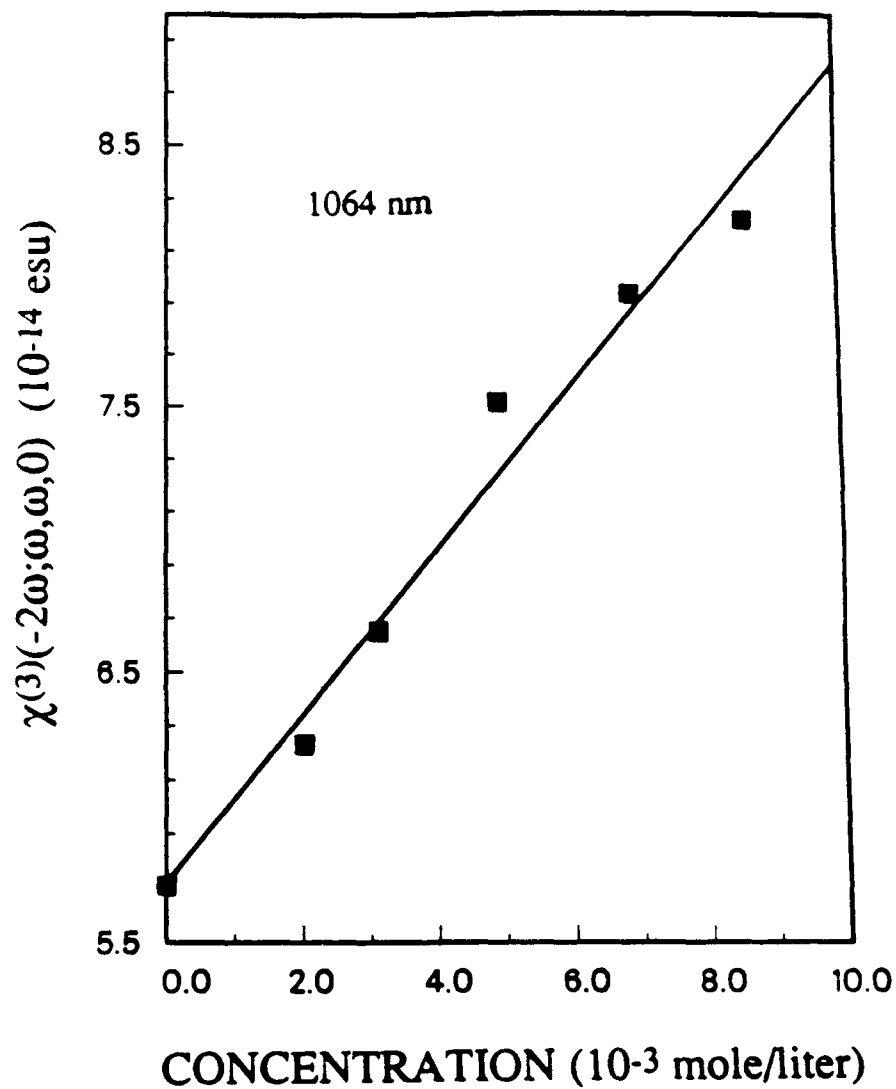
Figure 5-11. Concentration dependence of $\chi^{(3)}(-2\omega;\omega,\omega,0)$ for β-carotene in solution with dioxane at $\lambda = 1064$ nm.
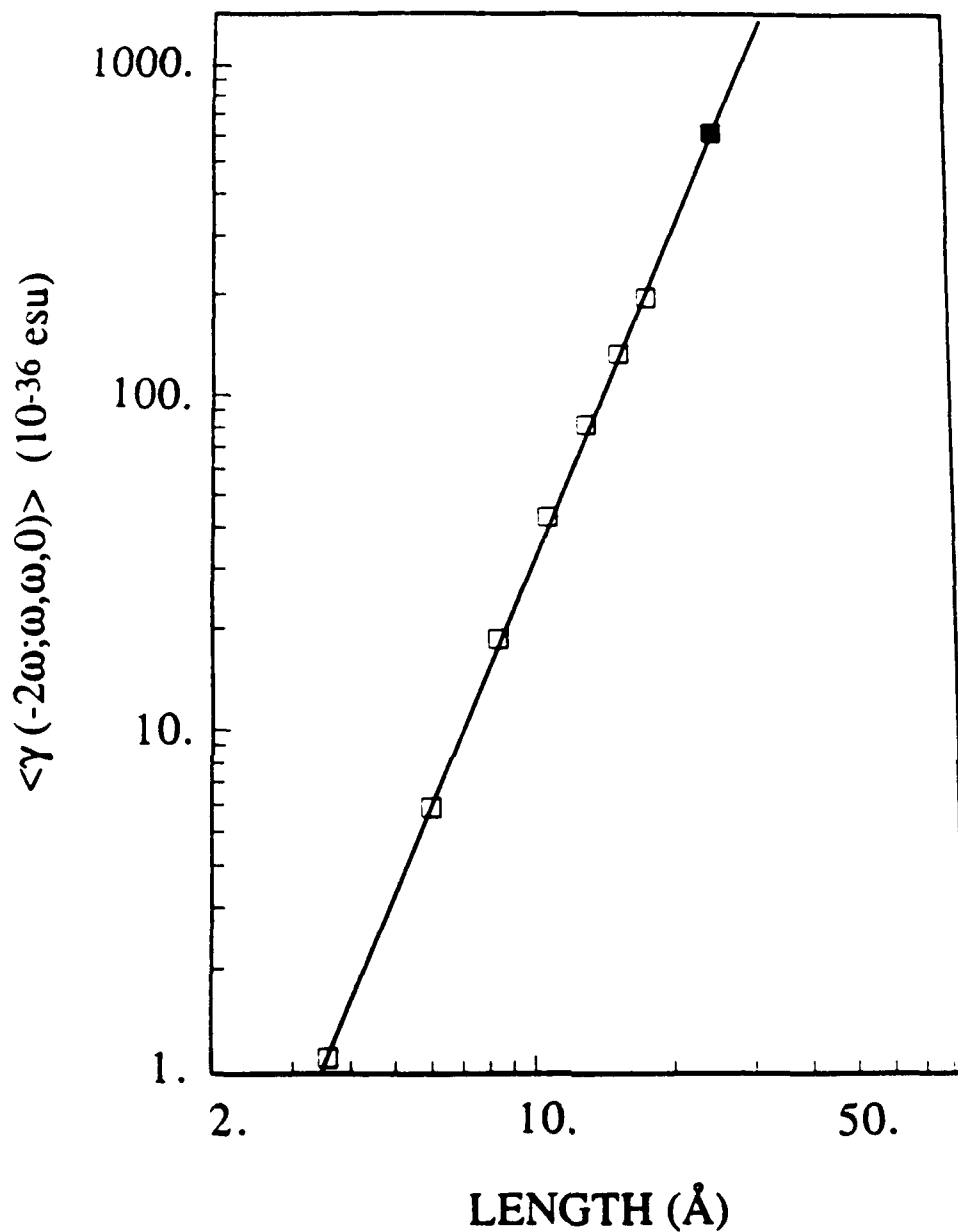
Figure 5-12. The experimental value of $\langle\gamma(-2\omega;\omega,\omega,0)\rangle$ for β-carotene at $\lambda = 1907$ nm ($\hbar\omega = 0.65$ eV) (solid square) compared with the theoretical values for the $N = 4$ to 16 *trans* polyenes (open squares) as a function of chain length L. The β-carotene experimental value confirms the theoretical power law dependence $\langle\gamma(-2\omega;\omega,\omega,0)\rangle \propto L^{3.4}$ represented by the solid line.

Chapter 5 References

1. B. F. Levine and C. G. Bethea, J. Chem. Phys. **63**, 2666 (1975).

2. J. L. Oudar, J. Chem. Phys. **67**, 446 (1977).

3. K. D. Singer and A. F. Garito, J. Chem. Phys. **75**, 3572 (1981).

4. C. C. Teng and A. F. Garito, Phys. Rev. Lett. **50**, 350 (1983); Phys. Rev.

   B28, 6766 (1983).

5. C. H. Grossman, Ph.D. Thesis, University of Pennsylvania (1987).

6. C. H. Grossman, T. Wada, S. Yamada, A. Yamada, H. Sasabe, and A. F.

   Garito, in *Nonlinear Optics of Organics and Semiconductors*, T. Kobayashi, ed.

   (Springer-Verlag, Berlin, 1989) p. 214.

7. K. D. Singer, J. E. Sohn, and S. J. Lalama, Appl. Phys. Lett. **49**, 248 (1986).

8. C. Ye, T. J. Marks, J. Yang, and G. K. Wong, Macromolecules **20**, 2324

   (1987).

9. K. D. Singer, S. J. Lalama, J. E. Sohn, and R. D. Small, in *Nonlinear Optical*

   Properties of Organic Molecules and Crystals, Vol. 1, D. S. Chemla and J.

   Zyss, eds. (Academic, New York, 1987).

10. G. Haucerone, F. Kerherve, and G. Mayer, J. Phys. **32**, 47 (1971).

11. L. Onsager, J. Am. Chem. Soc. **58**, 1486 (1936).

12. M. Choy and R. L. Byer, Phys. Rev. **B14**, 1693 (1976).

13. K. D. Singer, Ph.D. Thesis, University of Pennsylvania (1981).

14. P. S. Song and T. A. Moore, Photochem. Photobiol. **19**, 45 (1974).

15. L. V. Haley and J. A. Konigstein, J. Phys. Chem. **87**, 621 (1983).

16. R. C. Miller, Appl. Phys. Lett. **5**, 17 (1964).

17. American Institute of Physics Handbook, Third Ed., p. 6-27.

18. D. S. Chemla and P. J. Kupecek, Rev. Phys. Appl. **6**, 31 (1971).

19. *Optical Glass*, Schott Glass Technologies (Duryea, PA).

20. N. Gee, K. Shinsaka, J. Dodelet, and G. R. Freeman, J. Chem.

    Thermodynamics **18**, 221 (1986).

Chapter 6

DISPERSION OF $\langle\gamma(-3\omega;\omega,\omega,\omega)\rangle$ IN HEXATRIENE AND β-CAROTENE

A.   Introduction

The technique of third harmonic generation (THG) is ideally suited to the measurement of third order optical nonlinearities of electronic origin. In contrast to DCSHG, which possesses potential contributions both from the second order susceptibility $\beta_{ijk}(-2\omega;\omega,\omega)$ and from the vibrationally-derived third order hyper-Raman susceptibility $\xi_{ijk,\sigma}$ as described in the previous chapter, THG involves only optical input and output frequencies that oscillate too rapidly ($> 10^{14}$ Hz) for molecular orientations, vibrations, or rotations to follow. THG possesses the additional advantage over degenerate four-wave mixing (DFWM) measurements, governed by $\gamma_{ijkl}(-\omega;\omega,-\omega,\omega)$, for example, that it involves detection of a frequency different than that of the input light. In DFWM experiments, one detects the scattered signal of an incident probe beam from a refractive-index grating formed in the medium by two other incident beams. In addition to grating formation in the electronic polarization of the medium, thermal, acoustic, and population gratings may also form and scatter the incident beam. While deconvolution of the various mechanisms is a difficult problem in DFWM, it is clear that thermal, acoustic and population variations cannot lead to the creation of a new frequency and thus cannot contribute to THG.

184

An additional motivation for THG dispersion measurements in HT and β-carotene is to make careful comparison between DCSHG and THG results. In the limit $\omega \to 0$, the molecular susceptibilities $\gamma_{ijkl}(-2\omega;\omega,\omega,0)$ and $\gamma_{ijkl}(-3\omega;\omega,\omega,\omega)$ are related by a simple multiplicative factor. From the convention defined in Chapter 2, the relationship is

$$\gamma_{ijkl}(-2\omega;\omega,\omega,0) = 6\ \gamma_{ijkl}(-3\omega;\omega,\omega,\omega)\ . \tag{6.1}$$

For optical frequencies that lie below the first 3ω THG resonance, dispersion increases the magnitude of each $\gamma_{ijkl}(-\omega_4;\omega_1,\omega_2,\omega_3)$ above its $\omega = 0$ limit. In this frequency region, the dispersion of $\gamma_{ijkl}(-3\omega;\omega,\omega,\omega)$ is larger than that of $\gamma_{ijkl}(-2\omega;\omega,\omega,0)$, and therefore, for a given ω, the multiplicative factor between $\gamma_{ijkl}(-2\omega;\omega,\omega,0)$ and $\gamma_{ijkl}(-3\omega;\omega,\omega,\omega)$ is less than 6 and monotonically decreases with increased ω. Thus, although comparisons between measured values of $\gamma_{ijkl}(-2\omega;\omega,\omega,0)$ and $\gamma_{ijkl}(-3\omega;\omega,\omega,\omega)$ have been made previously, they have been hampered by the uncertainty in the degree of dispersion. In the present work, since the experimental and theoretical values of $<\gamma(-2\omega;\omega,\omega,0)>$ have been shown to be in excellent agreement, a similar comparison between theory and experiment for $<\gamma(-3\omega;\omega,\omega,\omega)>$ allows us to also address the relationship between $<\gamma(-2\omega;\omega,\omega,0)>$ and $<\gamma(-3\omega;\omega,\omega,\omega)>$ as a function of dispersion.

The derivation of the TH intensity in the THG wedge Maker fringe configuration and the implementation of the THG experiment are very similar to what was described in

185

the previous chapter for the DCSHG experiments. In fact, the THG and DCSHG experiments were performed on the same optical table, used the same laser source, and had many optical components in common. The intentional versatility of the experimental design allowed us to switch between the THG and DCSHG arrangements with only slightly more effort than is required to change the fundamental wavelength within either of the two experimental configurations. Because of the similarity of THG to DCSHG, the derivation of the TH intensity and the description of experimental design in this chapter will primarily focus only on the aspects that are different than those described in the previous chapter.

B. Derivation of Third Harmonic Intensity in the THG Configuration

The following derivation closely follows the one given in Section 5.B. The macroscopic polarization induced in a medium at a frequency 3ω by three applied optical electric fields at frequency ω with amplitudes E_j^ω, E_k^ω, and E_l^ω in the j, k and l directions is given by

$$P_i^{3\omega} = \chi_{ijkl}^{(3)}(-3\omega;\omega,\omega,\omega)\ E_j^\omega\ E_k^\omega\ E_l^\omega \qquad (6.2)$$

where $\chi_{ijkl}^{(3)}(-3\omega;\omega,\omega,\omega)$ is the macroscopic THG susceptibility tensor. In the case where the polarizations of all fields are parallel, the corresponding nonlinear wave equation that determines the third harmonic electric field $E^{3\omega}(z)$ is given by

186

$$\frac{\partial^2 E^{3\omega}}{\partial z^2} + \alpha_{3\omega}\frac{\partial E^{3\omega}}{\partial z} + k_f^2\, E^{3\omega} = -\frac{36\pi\omega^2}{c^2}\,\chi_{1111}^{(3)}(-3\omega;\omega,\omega,\omega)\ [E^\omega(z)]^3\ e^{ik_b z} \qquad (6.3)$$

where $\alpha_{3\omega}$ is the absorption coefficient at the harmonic frequency, $E^\omega(z)$ is the amplitude

of the fundamental field and decreases due to α_ω, $k_f = (3\omega\, n_{3\omega})/c$ and $k_b = (3\omega\, n_\omega)/c$

are the wave vectors of the free and bound harmonic waves, respectively, and the z-axis

is the direction of wave propagation. Eq. (6.3) has the solution

$$E^{3\omega}(z) = E_f\, e^{-\alpha_{3\omega}z/2}\ e^{ik_f z} + E_b(z)\, e^{ik_b z} \qquad (6.4)$$

where the bound wave amplitude is given by

$$E_b(z) = -\frac{4\pi}{n_{3\omega}^2 - n_\omega^2}\,\chi_{1111}^{(3)}(-3\omega;\omega,\omega,\omega)\ [E^\omega(z)]^3 \qquad . \qquad (6.5)$$

For the general case of a boundary at $z = z_0$ between two media, we find for the free

wave in the second medium

$$E_f^{(2)} = T_{3\omega}\, E_f^{(1)}\, e^{i\varphi_f} + [T_1\, E_b^{(1)}(z_0) - T_2\, E_b^{(2)}(z_0)]\, e^{i\varphi_b} \qquad (6.6)$$

where $\varphi_f = (k_f + i\alpha_{3\omega}/2)z_0$, $\varphi_b = (k_b + i3\alpha_\omega/2)z_0$, and

$$T_{3\omega} = \frac{2n_{3\omega}^{(1)}}{n_{3\omega}^{(i)} + n_{3\omega}^{(2)}}$$

187

$$T_1 = \frac{n_\omega^{(1)} + n_{3\omega}^{(1)}}{n_{3\omega}^{(2)} + n_{3\omega}^{(1)}}$$

$$T_2 = \frac{n_\omega^{(2)} + n_{3\omega}^{(1)}}{n_{3\omega}^{(2)} + n_{3\omega}^{(1)}} \quad . \tag{6.7}$$

Since all materials have a nonzero $\chi_{1111}^{(3)}(-3\omega;\omega,\omega,\omega)$, in our THG configuration, air, glass, and liquid sample all generate TH light. This is in contrast to the DCSHG experiment in which SH light is only generated in regions where the static electric field is nonzero. We can, however, simplify the THG analysis and mimic the DCSHG configration by using long glass windows in the THG sample cell. We choose focusing conditions such that the electric field amplitudes at the air-glass interfaces are less than one-tenth of the amplitudes at the glass-liquid interfaces. Thus, since for air $l_c \sim 50$ mm and $\chi^{(3)} \sim 10^{-18}$ esu and for glass $l_c \sim 20$ μm and $\chi^{(3)} \sim 10^{-14}$ esu, the bound wave due to air is less than 0.001 of the bound waves generated in the glass and liquid and can be neglected. More detail will be provided in section 6.C with the description of the THG sample cell; in the following, we neglect the air-glass interfaces and consider only the glass-liquid interfaces for generation of TH light.

By solving for the free wave in the liquid E_f^L after the $z = 0$ glass-liquid boundary, we obtain

$$E_f^L = T_1 E_b^G - T_2 E_b^L \qquad (6.8)$$

where

$$E_b^G = \frac{-4\pi}{(n_{3\omega}^G)^2 - (n_\omega^G)^2} \, \chi_G^{(3)}(-3\omega;\omega,\omega,\omega) \, (E^\omega t_\omega^{(1)})^3$$

$$E_b^L = \frac{-4\pi}{(n_{3\omega}^L)^2 - (n_\omega^L)^2} \, \chi_L^{(3)}(-3\omega;\omega,\omega,\omega) \, (E^\omega t_\omega^{(1)} t_\omega^{(2)})^3 \qquad (6.9)$$

with $t_\omega^{(1)} = 2/(1+n_\omega^G)$ and $t_\omega^{(2)} = 2n_\omega^G/(n_\omega^G + n_\omega^L)$. Following the $z = l$ liquid glass

boundary, the free wave in the rear window of the sample cell, E_f^G, is given by

$$E_f^G = T_{3\omega}^L E_f^L \, e^{i\varphi_f} + [T_L E_b^L - T_G (t_\omega^{(2)} t_\omega^{(3)})^3 E_b^G] \, e^{i\varphi_b} \qquad (6.10)$$

where

$$T_{3\omega}^L = \frac{2n_{3\omega}^L}{n_{3\omega}^G + n_{3\omega}^L}$$

$$T_L = \frac{n_\omega^L + n_{3\omega}^L}{n_{3\omega}^G + n_{3\omega}^L}$$

$$T_G = \frac{n_\omega^G + n_{3\omega}^L}{n_{3\omega}^G + n_{3\omega}^L} \, , \qquad (6.11)$$

$t_\omega^{(3)} = 2n_\omega^L / (n_\omega^L + n_\omega^G)$, $\varphi_f = (k_f + i\alpha_{3\omega}/2)l$, $\varphi_b = (k_b + i3\alpha_\omega/2)l$. The total third harmonic electric field that leaves the THG cell is then found to be

$$E^{3\omega} = T_{3\omega}^G (T_G E_b^G - T_L E_b^L)\, (e^{[ik_f - (\alpha_{3\omega}/2)]l} - e^{[ik_b - (3\alpha_\omega/2)]l}) \ , \qquad (6.12)$$

where $T_{3\omega}^G = 2n_{3\omega}^G / (1 + n_{3\omega}^G)$, after we propagate E_f^G through the final glass-air boundary and make approximations on the refractive index factors similar to those made for Eq. (5.37).

The third harmonic intensity $I^{3\omega}$ as a function of the path length l through the liquid sample is given by

$$I^{3\omega}(l) = \frac{2c}{8\pi} [T_{3\omega}^G (T_G E_b^G - T_L E_b^L)]^2\, e^{-[(3\alpha_\omega/2) + (\alpha_{3\omega}/2)]l}$$

$$\left\{ \cosh\left[\left(\frac{3\alpha_\omega}{2} - \frac{\alpha_{3\omega}}{2}\right) l\right] - \cos[(k_f - k_b)\, l]\right\} \qquad (6.13)$$

which reduces for the conditions $\alpha_\omega = \alpha_{3\omega} = 0$ to

$$I^{3\omega}(l) = \frac{c}{2\pi} [T_{3\omega}^G (T_G E_b^G - T_L E_b^L)]^2 \sin^2\left(\frac{\pi l}{2 l_c^L}\right) \qquad (6.14)$$

where $l_c^L = \lambda/6(n_{3\omega}^L - n_\omega^L)$. If we define A_m as the mean amplitude of the Maker fringes, then for measurements made on two different liquids, we find the ratio of A_m is

$$\frac{A_m^L}{A_m^R} = \frac{\left[T_{GL} \dfrac{\ell_c^G \chi_G^{(3)}}{n_{3\omega}^G + n_\omega^G} - T_L \dfrac{\ell_c^L \chi_L^{(3)}}{n_{3\omega}^L + n_\omega^L}(t_L^{(2)})^3\right]^2}{\left[T_{GR} \dfrac{\ell_c^G \chi_G^{(3)}}{n_{3\omega}^G + n_\omega^G} - T_R \dfrac{\ell_c^R \chi_R^{(3)}}{n_{3\omega}^R + n_\omega^R}(t_R^{(2)})^3\right]^2} \tag{6.15}$$

where R refers to the reference liquid and $t_L^{(2)}$, T_{GL}, $t_R^{(2)}$, and T_{GR} are $t_\omega^{(2)}$ and T_G

evaluated for the sample and reference liquids, respectively. Finally, solving for $\chi_L^{(3)}$ in

Eq. (6.15), we get

$$\chi_L^{(3)} = \frac{n_{3\omega}^L + n_\omega^L}{\ell_c^L T_L (t_L^{(2)})^3}\left[T_{GL} \dfrac{\ell_c^G \chi_G^{(3)}}{n_{3\omega}^G + n_\omega^G} \pm \right.$$

$$\left. \left(\frac{A_m^L}{A_m^R}\right)^{1/2} \left|T_{GR} \dfrac{\ell_c^G \chi_G^{(3)}}{n_{3\omega}^G + n_\omega^G} - T_R \dfrac{\ell_c^R \chi_R^{(3)}}{n_{3\omega}^R + n_\omega^R}(T_R^{(2)})^3\right| \right]. \tag{6.16}$$

Thus, $\chi_L^{(3)}(-3\omega;\omega,\omega,\omega)$ can be obtained from the refractive indices of the glass, reference

liquid, and sample liquid, $\chi_G^{(3)}$ and ℓ_c^G of the glass windows, $\chi_R^{(3)}$ of the reference liquid,

and A_m^L, A_m^R, ℓ_c^L, and ℓ_c^R determined from the Maker fringe analysis.

C.   Implementation of THG Experiment

The optical layout for THG is nearly identical to the one for DCSHG illustrated

in Figure 5-3, the only major difference being that THG does not require an HV source.

The Quanta-Ray DCR-1 Nd:YAG 8 ns laser was used as the light source, and the THG fundamental wavelengths were the Nd:YAG fundamental and Raman lines generated in hydrogen and methane gas cells. In addition to the 1064, 1543 and 1907 nm wavelengths employed in the DCSHG experiments, for the THG dispersion of β-carotene we also used the 2148 nm first vibrational-rotational Stokes line generated in hydrogen. The 2148 nm line, which results from subtracting one vibrational quantum at 4155 cm^{-1} and one rotational quantum at 587 cm^{-1} from the Nd:YAG fundamental output of 9398.5 cm^{-1}, was obtained with circularly polarized light incident on the Raman cell in order to efficiently couple the beam to the hydrogen rotational modes. Before it was split into the sample and reference arms of the layout, the Raman output was converted back to vertical linear polarization with a Glan-Taylor polarizer. We used the 2148 nm line in the β-carotene dispersion measurements in lieu of 1064 nm since the third harmonic of 1064 nm, 355 nm, is strongly absorbed within the $1^1B_u \leftarrow 1^1A_g$ absorption band.

As opposed to the DCSHG configuration in which the laser flashlamp trigger signal is used to trigger the HV pulse, is delayed, and then triggers the Q-switch, since no HV pulse is needed in THG, the laser internal delay and firing electronics were employed. It was still necessary, of course, to gate the ADC and synchronize the data collection electronics with the gate photodiode. One other minor difference in the two experiments is in the use of the reference arm signal. The small intensity split off into the reference arm was not sufficient to generate a substantial third harmonic signal, and, therefore, the quartz second harmonic signal was again employed for referencing. Since

the SH signal is proportional to the square of the fundamental intensity and the TH signal, the cube, the reference signal was raised to the 3/2 power for each laser pulse before the sample to reference signal ratio was taken. This produced a very stable THG signal. The design of the THG sample cell is the final difference in the THG and DCSHG experiments. See Section 5.C for details on the laser source, optical layout, PMTs, data collection electronics, and materials handling that are all applicable to THG as well as DCSHG.

THG Sample Cell

Because all media have nonzero $\chi_{ijkl}^{(3)}(-3\omega;\omega,\omega,\omega)$ regardless of their symmetry, the environmental air surrounding a THG cell can make a measurable contribution to the third harmonic intensity. Two independent studies employing conventional THG cell configurations determined $I_{vac}^{3\omega}/I_{air}^{3\omega} \cong 4$ where $I_{vac}^{3\omega}$ and $I_{air}^{3\omega}$ are the peak third harmonic intensities observed for glass in vacuum and at 1 atmosphere, respectively.[1,2] In order to eliminate the contributions of air to the TH signal and to simplify and make more reliable the analysis, we adopted the cell design developed by Kajzar and Messier.[3] The design takes advantage of the focusing conditions employed in THG by moving the air-glass boundaries to positions where the fundamental intensity is reduced to less than 10% of its value at the focus in the center of the cell. The corresponding contribution of air to the TH signal through $\chi^{(3)}(-3\omega;\omega,\omega,\omega)$ is therefore reduced by more than 10^3 relative to the liquid and glass contributions. This is achieved by making the BK-7 glass windows 5.0 cm long and focusing with an $f = 30$ cm lens.

193

The THG sample cell is shown schematically in Figure 6-1. Each of the 1.0 x 2.0 x 5.0 cm BK-7 glass windows is polished to flatter than $\lambda/4$ and the ends are made parallel to within 5 seconds. The windows are leakproof sealed to the aluminum holder with RTV silicone rubber, and threaded screw holes through the aluminum allow fine adjustment of the window positions. The cell can be disassembled for cleaning or replacement of the windows. During the course of the present experiments, the windows were adjusted to form a wedge of angle $\alpha = 0.0125$ radian with mean pathlength $l = 0.44$ mm.

D. Experimental Results and Analysis

Glass and Pure Solvents

To measure $\chi^{(3)}_{1111}(-3\omega;\omega,\omega,\omega)$ of a given liquid, one requires the values of $\chi^{(3)}$ and l_c of the BK-7 glass windows and a reference liquid at the desired frequency. After Maker fringe analysis of both sample and reference and determination of the fundamental and harmonic refractive indices, $\chi^{(3)}_L(-3\omega;\omega,\omega,\omega)$ is obtained through Eq. (6.16). For glass, we use a value of $\chi^{(3)}_{1111}(-3\omega;\omega,\omega,\omega) = 0.58 \times 10^{-14}$ esu at $\lambda = 1907$ nm as a standard and employ Miller's rule to obtain values at 2148, 1543, and 1064 nm. The origin of this standard value for BK-7 glass will be described at the end of the chapter. The refractive indices at each fundamental and harmonic wavelength obtained through the BK-7 dispersion relation of Eq. (5.50) fix the value $\chi^{(3)}_G (\lambda)$ of BK-7 glass at a given fundamental wavelength through Miller's rule

194

$$\chi_G^{(3)}(\lambda) = \chi_G^{(3)}(1907 \text{ nm}) \; \frac{[\chi_G^{(1)}(\lambda)]^3 \; \chi_G^{(1)}(\lambda/3)}{[\chi_G^{(1)}(1907 \text{ nm})]^3 \; \chi_G^{(1)}(636 \text{ nm})} \tag{6.17}$$

and the coherence length l_c through

$$l_c = \frac{\lambda}{6(n^{3\omega} - n^{\omega})} \; . \tag{6.18}$$

Table 6-1 lists the resultant values for $\chi_G^{(3)}(-3\omega;\omega,\omega,\omega)$, l_c, n^{ω} and $n^{3\omega}$ for each of the four fundamental wavelengths at which we performed THG measurements.

Two surveys of $\chi^{(3)}(-3\omega;\omega,\omega,\omega)$ for organic liquids exist in the literature. Meredith, Buchalter, and Hanzlik performed THG measurements at 1907 nm with a wedge cell configuration maintained in vacuum that is valid only in the instance of negligible absorption at the fundamental and harmonic wavelengths.[4] Kajzar and Messier developed an analysis of the effects of air on Maker fringes and employed it to measure several organic liquids at fundamental wavelengths of 1907 and 1064 nm.[2] The results of Kajzar and Messier are in agreement with those of Meredith, Buchalter, and Hanzlik to within 10% for all but one solvent. Kajzar and Messier observed reasonable agreement, as well, in separate measurements employing the cell configuration we use that eliminates the contributions of air.[3] In the present experiments, we use the measurements of Kajzar and Messier for acetone at 1907 and 1064 nm as our liquid reference values. The reported values of $\chi^{(3)}(-3\omega;\omega,\omega,\omega)$ for acetone are 0.513 and 0.586 x 10^{-14} esu at 1907 and 1064 nm, respectively.[2] We point

195

out here that the values above are different than those reported in Ref. 2, due to a factor of 4 difference in conventions (see Appendix A) and a factor of 2.0 difference in the reference value for the glass windows that will be explained later in the chapter.

At 1064 nm, we measured $\chi^{(3)}(-3\omega;\omega,\omega,\omega)$ of several liquids for comparison with Kajzar and Messier. The values we obtained for $\chi^{(3)}(-3\omega;\omega,\omega,\omega)$, l_c, and $<\gamma(-3\omega;\omega,\omega,\omega)>$ of methanol, dimethylformamide, water, and cyclohexane are compared to the results of Ref. 2 in Table 6-2. In the case of the discrepancy for cyclohexane, we point out the l_c and refractive index values of Ref. 2 for cyclohexane are in good agreement with our results for cyclohexanone and suggest that the measurements in Ref. 2 were actually performed on cyclohexanone rather than cyclohexane.

Since our β-carotene measurements were performed in dioxane solutions, we chose to use pure dioxane as the reference liquid in each data-taking run where the value for $\chi^{(3)}(-3\omega;\omega,\omega,\omega)$ of dioxane at each wavelength was determined by a separate comparison of dioxane Maker fringes with acetone. For $\chi^{(3)}(-3\omega;\omega,\omega,\omega)$ of acetone at 1543 nm, we used the value 0.534×10^{-14} esu obtained from interpolation of the measured values at 1907 and 1064 nm. For dioxane at 2148 nm, since no value is available for acetone at this wavelength, we assumed that dioxane has the same 2% dispersion determined for BK-7 glass, and our relative uncertainty in this value is therefore less than 2%. We list in Table 6-3 the measured values of $\chi^{(3)}(-3\omega;\omega,\omega,\omega)$, l_c, and $<\gamma(-3\omega;\omega,\omega,\omega)>$ for dioxane together with the values of the refractive index at

196

the fundamental and harmonic wavelengths. In analogy with Eq. (5.51), $\langle\gamma(-3\omega;\omega,\omega,\omega)\rangle$ was obtained through

$$\chi^{(3)}(-3\omega;\omega,\omega,\omega) = N \left(\frac{n_\omega^2 + 2}{3} \right)^3 \left(\frac{n_{3\omega}^2 + 2}{3} \right) \langle\gamma(-3\omega;\omega,\omega,\omega)\rangle \qquad (6.19)$$

where N is the molecular number density and the local field factors are taken as isotropic Lorentz-Lorenz terms.

Hexatriene

$\chi^{(3)}(-3\omega;\omega,\omega,\omega)$ and, correspondingly, $\langle\gamma(-3\omega;\omega,\omega,\omega)\rangle$ were measured for HT at 1907, 1543, and 1064 nm. In addition to the $\chi^{(3)}(-3\omega;\omega,\omega,\omega)$, l_c, n^ω, and $n^{3\omega}$ values for BK-7 glass and dioxane listed in Tables 6-1 and 6-3, respectively, evaluation of $\chi^{(3)}(-3\omega;\omega,\omega,\omega)$ for HT requires the values for n^ω and $n^{3\omega}$ of HT. From the measured coherence lengths l_c of 11.8, 6.2, and 1.18 μm at 1907, 1543, and 1064 nm, respectively, we obtain for $\Delta n = n^{3\omega} - n^\omega$ the values 0.027, 0.041 and 0.16 from Eq. (6.18). The extremely large dispersion in the HT refractive index between 1064 and 355 nm results from the proximity of 355 nm to the strong $1^1B_u \leftarrow 1^1A_g$ π-electron transition that begins at 290 nm. The values for n^ω and $n^{3\omega}$ that are consistently determined from these results, the refractive index at 590 nm obtained from Aldrich, and the l_c's measured by THG are listed in Table 6-4.

The values obtained for $\chi^{(3)}(-3\omega;\omega,\omega,\omega)$ of HT at each wavelength from the Maker fringe analysis through Eq. (6.16) are also listed in Table 6-4. As in DCSHG,

197

the values for HT are several times larger than those for dioxane, but, importantly, at 1064 nm $\chi^{(3)}(-3\omega;\omega,\omega,\omega)$ of HT increases to 6.5 times larger than dioxane. As in the linear refractive index, the nearness of the third harmonic wavelength to the HT π-electron absorption produces a large dispersion in $\chi^{(3)}(-3\omega;\omega,\omega,\omega)$.

We compare in Table 6-5 the experimental values of $\langle\gamma(-3\omega;\omega,\omega,\omega)\rangle$ for HT, obtained from Eq. (6.19) with the molecular number density $N = 5.54 \times 10^{21}$ cm^{-3} and the refractive index values given in Table 6-4, with the theoretical values from Chapter 4. The theoretical values include a small σ-electron contribution to $\langle\gamma(-3\omega;\omega,\omega,\omega)\rangle$ in addition to the directly calculated π-electron contribution and consider the liquid to consist of 60% *trans* conformation and 40% *cis*. We observe good agreement between experiment and theory for the magnitude of $\langle\gamma(-3\omega;\omega,\omega,\omega)\rangle$. Furthermore, the larger dispersion theoretically predicted for THG compared to DCSHG is clearly observed. The degree of dispersion predicted by theory is quantified by the ratio of $\langle\gamma(-3\omega;\omega,\omega,\omega)\rangle$ calculated at fundamental wavelength 1064 nm to $\langle\gamma(-3\omega;\omega,\omega,\omega)\rangle$ at 1907 nm which has a value of 1.77. The experimentally determined ratio of $\langle\gamma(-3\omega;\omega,\omega,\omega)\rangle$ at these two wavelengths is 1.87 in good agreement with the theoretical ratio. For comparison, the theoretically predicted ratio for the less dispersive DCSHG process at these wavelengths is 1.25. The experimental values for $\langle\gamma(-3\omega;\omega,\omega,\omega)\rangle$ are also plotted with the theoretical dispersion curve in Figure 6-2 for visual comparison of experiment and theory.

In the case of the Maker fringes for HT at $\lambda = 1064$ nm, since the coherence length l_c is extremely short (1.18 μm) due to the large dispersion in the refractive index

between the fundamental and harmonic wavelengths, an interesting effect occurs due to the finite width of the laser beam at the sample. The Maker fringe technique relies on the fact that the output harmonic intensity from the sample cell is a periodic function of the pathlength of the beam through the liquid. In the wedge configuration we employ, a beam with a finite waist w necessarily samples an interval of pathlength rather than one single, well-defined pathlength. A consequence of finite beam waist, then, is that if the interval of pathlength covered is sufficiently large, although the beam may be centered on the pathlength that yields zero harmonic output intensity, the edges of the beam traverse pathlengths that yield non-zero harmonic intensity. The net effect of finite beam waist is an increase in the minimum of the Maker fringe from zero to a finite magnitude. The observed fringes for HT, shown in Figure 6-3(a), have a minimum value that is 35% of the peak value. In contrast, the fringes for acetone of Figure 6-3(b) demonstrate a perfect zero for the minimum. The measured l_c of acetone is 6.6 μm, 5.6 times larger than l_c of HT. For clarity, the horizontal scale of Figure 6-3(a) was expanded by a factor of 3 compared to the scale of 6-3(b).

To calculate the effect of finite beam width on the fringe shape, we approximate the beam profile by a constant intensity disc of diameter w. (The actual output of the Quanta-Ray DCR-1 resonator cavity is a multimode "donut" profile that consists of a high intensity annulus surrounding the lower intensity central region.) For a liquid sample wedge of angle α, the beam covers a pathlength interval $\Delta l = \alpha w$. From Eq. (6.14), we note that, in the absence of absorption, the pathlength dependent part of the harmonic intensity is given by

$$f(l) = \sin^2\left(\frac{\pi l}{2l_c}\right) \tag{6.20}$$

If we define $d = \pi(\Delta l) / 2l_c$, then the normalized fringe height when the beam is centered on a path l' with $c = \pi l' / 2l_c$) is

$$I(c) = \frac{1}{d} \int_{c-d/2}^{c+d/2} \sin^2 x \, dx \tag{6.21}$$

The normalization of Eq. (6.21) is chosen such that, when d is small enough that $f(l)$ is constant over the beam width, we have $I(c) = f(l')$. The minimum value of the fringe is then given by

$$I_{min} = \frac{1}{d} \int_{-d/2}^{d/2} \sin^2 x \, dx = \frac{1}{2} - \frac{\sin d}{2d} \tag{6.22}$$

and the maximum value by

$$I_{max} = \frac{1}{d} \int_{p/2 - d/2}^{p/2 + d/2} \sin^2 x \, dx = \frac{1}{2} + \frac{\sin d}{2d} \tag{6.23}$$

where it is clear that the reduction in the fringe peak amplitude due to finite beam width is equal to the increase in the minimum. The value $I_{min}/I_{max} = 0.35$ observed for HT in Figure 6-3(a) corresponds to $d = 1.94$ rad or $\Delta l/l_c = 1.24$. Since $l_c = 1.18$ μm and $\alpha = 0.0125$ rad, we therefore expect to observe this ratio of I_{min}/I_{max} for a beam diameter w

200

= 106 μm. This is quite reasonable since our focusing conditions have been directly measured to yield a typical beam diameter of 100-400 μm at the sample. In Table 6-5 are listed the ratios I_{min}/I_{max} calculated from Eqs. (6.22) and (6.23) for other values of $\Delta l/l_c$. It can be seen from the table that for $\Delta l/l_c$ five times smaller than for HT, the minimum is only 1% of the maximum peak height. This explains why the other measured solvents, all possessing l_c's many times greater than that of HT, do not exhibit nonzero minima.

β-Carotene

We measured the concentration dependence of $\chi^{(3)}(-3\omega;\omega,\omega,\omega)$ for β-carotene solutions in dioxane at fundamental wavelengths of 2148, 1907, and 1543 nm. THG measurements at $\lambda = 1064$ nm were not possible since the solution strongly absorbs the third harmonic at 355 nm. As was found in the DCSHG measurements, l_c was weakly dependent on concentration. For example, at 1907 nm, $l_c = 32.7$ μm for pure dioxane and 31.8 μm for the stock solution concentration 8.15×10^{-3} mole/litre. At each concentration, therefore, $\chi^{(3)}(-3\omega;\omega,\omega,\omega)$ was calculated with the directly measured l_c at that concentration, but with the refractive indices of pure dioxane. From the concentration dependence of $\chi^{(3)}(-3\omega;\omega,\omega,\omega)$, we determined $<\gamma(-3\omega;\omega,\omega,\omega)>$ of β-carotene according to

$$<\gamma(-3\omega;\omega,\omega,\omega)> = \left(\frac{3}{n_\omega^2 + 2}\right)^3 \left(\frac{3}{n_{3\omega}^2 + 2}\right) \left(\frac{1}{6.02 \times 10^{20}}\right) \frac{\partial\chi^{(3)}(-3\omega;\omega,\omega,\omega)}{\partial C} \quad (6.24)$$

201

where C is the concentration in mole/litre and the same valid approximations are made that led to Eq. (5.54).

The concentration dependences of $\chi^{(3)}(-3\omega;\omega,\omega,\omega)$ at $\lambda = 2148$, 1907, and 1543 nm are illustrated in Figures 6-4, 6-5, and 6-6, respectively. In each case, $\chi^{(3)}(-3\omega;\omega,\omega,\omega)$ shows good linearity with concentration. Table 6-6 lists $\partial\chi^{(3)}(-3\omega;\omega,\omega,\omega) / \partial C$ determined from each concentration dependence and the corresponding values obtained for $<\gamma(-3\omega;\omega,\omega,\omega)>$. The strong near-resonant enhancement at 1543 nm results from the proximity of the third harmonic wavelength 514 nm to the $1^1B_u \leftarrow 1^1A_g$ absorption band that peaks at 455 nm.

In Figure 6-7, the experimental value for $<\gamma(-3\omega;\omega,\omega,\omega)>$ of β-carotene at 1907 nm is plotted against the length of the chain along with the theoretical results from Chapter 4. As in the case of DCSHG, the THG experimental value for $<\gamma(-3\omega;\omega,\omega,\omega)>$ of β-carotene is in agreement with the extrapolation of the theoretical power law dependence $<\gamma(-3\omega;\omega,\omega,\omega)> \propto L^{3.5}$. This serves as a separate experimental confirmation that the theoretically predicted power law dependence of $<\gamma(-3\omega;\omega,\omega,\omega)>$ on chain length is correct and that it is valid for chains at least as long as 25 Å or $N = 22$.

The β-carotene molecular structure is longer than we can accurately calculate, and we therefore are unable to make the same comparison between experiment and theory for the dispersion of $<\gamma(-3\omega;\omega,\omega,\omega)>$ that we made for HT. We have, however, based on the theoretical results for shorter chains presented in Chapters 3 and 4, developed a model that adequately describes the experimentally observed dispersion of $<\gamma(-3\omega;\omega,\omega,\omega)>$ and $<\gamma(-2\omega;\omega,\omega,0)>$. We pointed out in Chapter 3 that for very short

chains, $N = 4, 6$, and 8, the nonresonant $\langle\gamma(-\omega_4;\omega_1,\omega_2,\omega_3)\rangle$ is determined almost exclusively by three states. These three key states are the 1^1A_g ground state, the 1^1B_u lowest-lying one-photon state, and a high-lying ^1A_g two-photon state that strongly couples to 1^1B_u. For increased chain length, we found that there were larger numbers of both ^1B_u and ^1A_g states that made significant contributions to $\langle\gamma(-\omega_4;\omega_1,\omega_2,\omega_3)\rangle$. The first strong resonance that occurs both in $\langle\gamma(-3\omega;\omega,\omega,\omega)\rangle$ and in $\langle\gamma(-2\omega;\omega,\omega,0)\rangle$, however, in all cases results from the 1^1B_u state. In $\langle\gamma(-3\omega;\omega,\omega,\omega)\rangle$, the 3ω resonance of 1^1B_u is the lowest-frequency electronic resonance that can occur; in $\langle\gamma(-2\omega;\omega,\omega,0)\rangle$, the first resonance that occurs, the 2ω resonance of the 2^1A_g state, is weak because of the small transition moment between 2^1A_g and 1^1B_u, and the low frequency dispersion is therefore dominated by the 2ω resonance of the 1^1B_u state.

We have found that the experimental dispersions are well-described by a three-level model with one free parameter that fixes the magnitude of the nonresonant $\langle\gamma(-\omega_4;\omega_1,\omega_2,\omega_3)\rangle$. The expression for $\langle\gamma(-3\omega;\omega,\omega,\omega)\rangle$ for a system that has only a ground state (labeled 0), a one-photon state (1), and a two-photon state (2) is

$$
\gamma_{xxxx}(-3\omega;\omega,\omega,\omega) = \frac{e^4}{4\hbar^3} \Big\{ \; x_{01}^2 \, x_{12}^2
$$
$$
\{ \, [\, (\omega_{10} - 3\omega)(\omega_{20} - 2\omega)(\omega_{10} - \omega) \,]^{-1} + [\, (\omega_{10} + \omega)(\omega_{20} - 2\omega)(\omega_{10} - \omega) \,]^{-1}
$$
$$
+ [\, (\omega_{10} + \omega)(\omega_{20} + 2\omega)(\omega_{10} - \omega) \,]^{-1} + [\, (\omega_{10} + \omega)(\omega_{20} + 2\omega)(\omega_{10} + 3\omega) \,]^{-1} \, \}
$$
$$
- x_{01}^4 \, \{ \, [\, (\omega_{10} - 3\omega)(\omega_{10} - \omega)(\omega_{10} - \omega) \,]^{-1} + [\, (\omega_{10} - \omega)(\omega_{10} + \omega)(\omega_{10} - \omega) \,]^{-1}
$$
$$
+ [\, (\omega_{10} + 3\omega)(\omega_{10} + \omega)(\omega_{10} + \omega) \,]^{-1} + [\, (\omega_{10} + \omega)(\omega_{10} - \omega)(\omega_{10} + \omega) \,]^{-1} \, \} \, \Big\}
$$

(6.25)

203

where x_{01} and x_{12} are the x-components of the transition moments between states 0 and 1 and states 1 and 2, respectively, and $\hbar\omega_{10}$ and $\hbar\omega_{20}$ are the excitation energies of states 1 and 2, respectively. In this three-level model, state 1 corresponds to the 1^1B_u state of β-carotene. We therefore take $\hbar\omega_{10} = 2.71$ eV from the peak of the β-carotene absorption spectrum and $x_{01} = 15.0$ D from extrapolation of the calculated $\mu_{1^1A_g,1^1B_u}$ values to $N = 22$. For $\hbar\omega_{20}$, we use 4.6 eV by extrapolation of the dominant high-lying two-photon state energies of Chapter 3, though this value is not critical since $\hbar\omega_{20}$ and x_{12} together effectively fix the magnitude of the nonresonant $\langle\gamma(-3\omega;\omega,\omega,\omega)\rangle$. Choice of a smaller value for $\hbar\omega_{20}$ could be compensated by a smaller value for x_{12} as well. We have taken the representative values $\hbar\Gamma_{10} = \hbar\Gamma_{20} = 0.2$ eV based on the width of the $1^1B_u \leftarrow 1^1A_g$ peak in the experimental linear absorption spectrum.

The remaining value to be determined in the three-level model is x_{12}. State 2 acts as a representative state here, taking the role of the several other two-photon and one-photon states that actually determine $\langle\gamma(-3\omega;\omega,\omega,\omega)\rangle$. We thus consider x_{12} to be a free parameter that is used to fit the experimental dispersion data by fixing the correct magnitude of the low frequency $\langle\gamma(-3\omega;\omega,\omega,\omega)\rangle$. The best fit to the experimental data was found for $x_{12} = 21.8$ D and is illustrated in Figure 6-8. The fit of the three-level model dispersion curve to the data is quite satisfactory considering the simplicity of the model. The observed dispersion is clearly due predominantly to the 3ω resonance of the 1^1B_u state.

For DCSHG, the expression for the three-level model is

$$\gamma_{xxxx}(-2\omega;\omega,\omega,0) = \frac{e^4}{2\hbar^3} \{ \ x_{01}^2 \, x_{12}^2$$

$$\{ \ [\ (\omega_{10} - 2\omega)(\omega_{20} - 2\omega)(\omega_{10} - \omega) \ ]^{-1} + [\ (\omega_{10} + 0)(\omega_{20} - 2\omega)(\omega_{10} - \omega) \ ]^{-1}$$

$$+ [\ (\omega_{10} + \omega)(\omega_{20} + 2\omega)(\omega_{10} - 0) \ ]^{-1} + [\ (\omega_{10} + \omega)(\omega_{20} + 2\omega)(\omega_{10} + 2\omega) \ ]^{-1}$$

$$+ [\ (\omega_{10} - 2\omega)(\omega_{20} - \omega)(\omega_{10} - \omega) \ ]^{-1} + [\ (\omega_{10} + \omega)(\omega_{20} - \omega)(\omega_{10} - \omega) \ ]^{-1}$$

$$+ [\ (\omega_{10} + \omega)(\omega_{20} + \omega)(\omega_{10} - \omega) \ ]^{-1} + [\ (\omega_{10} + \omega)(\omega_{20} + \omega)(\omega_{10} + 2\omega) \ ]^{-1}$$

$$+ [\ (\omega_{10} - 2\omega)(\omega_{20} - \omega)(\omega_{10} - 0) \ ]^{-1} + [\ (\omega_{10} + \omega)(\omega_{20} - \omega)(\omega_{10} - 0) \ ]^{-1}$$

$$+ [\ (\omega_{10} - 0)(\omega_{20} + \omega)(\omega_{10} - \omega) \ ]^{-1} + [\ (\omega_{10} - 0)(\omega_{20} + \omega)(\omega_{10} + 2\omega) \ ]^{-1} \ \}$$

$$- x_{01}^4 \ \{ \ [\ (\omega_{10} - 2\omega)(\omega_{10} - 0)(\omega_{10} - \omega) \ ]^{-1} + [\ (\omega_{10} - 0)(\omega_{10} + \omega)(\omega_{10} - \omega) \ ]^{-1}$$

$$+ [\ (\omega_{10} + 2\omega)(\omega_{10} + 0)(\omega_{10} + \omega) \ ]^{-1} + [\ (\omega_{10} + 0)(\omega_{10} - \omega)(\omega_{10} + \omega) \ ]^{-1}$$

$$+ [\ (\omega_{10} - 2\omega)(\omega_{10} - \omega)(\omega_{10} - \omega) \ ]^{-1} + [\ (\omega_{10} - \omega)(\omega_{10} + 0)(\omega_{10} - \omega) \ ]^{-1}$$

$$+ [\ (\omega_{10} + 2\omega)(\omega_{10} + \omega)(\omega_{10} + \omega) \ ]^{-1} + [\ (\omega_{10} + \omega)(\omega_{10} - 0)(\omega_{10} + \omega) \ ]^{-1}$$

$$+ [\ (\omega_{10} - 2\omega)(\omega_{10} - \omega)(\omega_{10} - 0) \ ]^{-1} + [\ (\omega_{10} - \omega)(\omega_{10} + \omega)(\omega_{10} - 0) \ ]^{-1}$$

$$+ [\ (\omega_{10} + 2\omega)(\omega_{10} + \omega)(\omega_{10} + 0) \ ]^{-1} + [\ (\omega_{10} + \omega)(\omega_{10} - \omega)(\omega_{10} + 0) \ ]^{-1} \ \} \ \}$$

$$(6.26)$$

We again set x_{01} = 15.0 D, $\hbar\omega_{10}$ = 2.71 eV, $\hbar\omega_{20}$ = 4.6 eV, and $\hbar\Gamma_{10} = \hbar\Gamma_{20}$ = 0.2 eV as described above. Figure 6-9 shows the calculated dispersion curve for the DCSHG three-level model with x_{12} = 23.7 D. Again, the essential features of the dispersion are well-described by the three-level model. The slight discrepancy in the values for x_{12} in the THG and DCSHG three-level models is reasonable considering the level of approximation. We point out, however, that an accurate calculation of dispersion requires determination of the complete π-electron excited state manifold, especially for

long chains, even though the three-level model successfully demonstrates that the low-frequency dispersion is dominated by the first multi-photon resonance of the 1^1B_u state.

E. Reference Standard for $\chi^{(3)}(-3\omega;\omega,\omega,\omega)$

The currently accepted reference values for THG measurements of liquids and thin films are $\chi_G^{(3)}(-3\omega;\omega,\omega,\omega) = 1.17 \times 10^{-14}$ esu for BK-7 glass and $\chi_S^{(3)}(-3\omega;\omega,\omega,\omega) = 0.70 \times 10^{-14}$ esu for fused silica at $\lambda = 1907$ nm. These values, which have been converted into our convention for $\chi^{(3)}(-3\omega;\omega,\omega,\omega)$ through division by a factor of 4 (see Appendix A), were determined by Buchalter and Meredith by comparison to $\chi_Q^{(3)}(-3\omega;\omega,\omega,\omega) = 0.95 \times 10^{-14}$ esu for α-quartz.[5] The quartz $\chi_Q^{(3)}(-3\omega;\omega,\omega,\omega)$ value is derived from an analysis of interference fringes between 3ω light due to $\chi_Q^{(3)}(-3\omega;\omega,\omega,\omega)$ and 3ω light generated by the cascading of $\chi_Q^{(2)}(-2\omega;\omega,\omega)$ and $\chi_Q^{(2)}(-3\omega;2\omega,\omega)$.[6] It was pointed out that the silica and glass $\chi^{(3)}(-3\omega;\omega,\omega,\omega)$ values were not in agreement with measurements by other third order processes, and this was attributed as most likely due to the incompatibility of the multi-mode laser source in the quartz experiment with the experimental analysis that assumed a single-mode source.[5] Nonetheless, these values were taken as the standard reference values for THG measurements.

Until the present experiments, no comparisons have been made between theory and experimental values of $<\gamma(-3\omega;\omega,\omega,\omega)>$ obtained using the above reference standards. As a result, only relative experimental values of $<\gamma(-3\omega;\omega,\omega,\omega)>$ were

206

meaningful. In the course of our measurements, it became clear that the experimental values for $\langle\gamma(-3\omega;\omega,\omega,\omega)\rangle$ of HT that we derived based on Buchalter and Meredith's value of $\chi_G^{(3)}$ $(-3\omega;\omega,\omega,\omega)$ were in conflict with our theoretical results and with our experimental values for $\langle\gamma(-2\omega;\omega,\omega,0)\rangle$. A survey of the literature yielded six independent measurements of $\chi^{(3)}(-\omega_4;\omega_1,\omega_2,\omega_3)$ for BK-7 glass via four separate third order processes, namely DCSHG,[7-9] non-degenerate three-wave mixing (NDTWM),[10] time-resolved interferometry (TRI),[11] and ellipse rotation (ER),[12] that give consistent values to better than 10%. These values are listed in Table 6-7 along with the THG measurement of Buchalter and Meredith. Each value has been converted into the convention for $\chi^{(3)}(-3\omega;\omega,\omega,\omega)$. For instance, since we have the relation $\chi^{(3)}(-2\omega;\omega,\omega,0) = 6\,\chi^{(3)}$ $(-3\omega;\omega,\omega,\omega)$ in the extreme nonresonant limit, the DCSHG values have been divided by a factor of 6.

The $\chi^{(3)}(-3\omega;\omega,\omega,\omega)$ value of BK-7 glass from Buchalter and Meredith is clearly too large compared to the other values. In the experimental results for $\langle\gamma(-3\omega;\omega,\omega,\omega)\rangle$ presented in section D of this chapter, we instead took $\chi^{(3)}(-3\omega;\omega,\omega,\omega) = 0.58 \times 10^{-14}$ esu for BK-7 glass. This value, in addition to being consistent with the measurements of Table 6-7, provides much better agreement between experiment and theory. We would like to mention here that our calculations for $\langle\gamma(-2\omega;\omega,\omega,0)\rangle/\langle\gamma(-3\omega;\omega,\omega,\omega)\rangle$ for HT yielded a ratio of 5.3 rather than 6.0 at 1907 nm. Even at this long wavelength, dispersion increases $\langle\gamma(-3\omega;\omega,\omega,\omega)\rangle$ more quickly than $\langle\gamma(-2\omega;\omega,\omega,0)\rangle$. Thus, as regards our comparison of $\chi^{(3)}(-\omega_4;\omega_1,\omega_2,\omega_3)$ in Table 6-7, we expect

$\chi^{(3)}(-3\omega;\omega,\omega,\omega)$ should in fact be 5-15% larger than $\chi^{(3)}(-\omega_4;\omega_1,\omega_2,\omega_3)$ of other processes.

We conclude, then, that the common reference values for $\chi^{(3)}(-3\omega;\omega,\omega,\omega)$ of BK-7 glass and silica are too large by a factor of 2.0. Until a careful absolute measurement of $\chi^{(3)}(-3\omega;\omega,\omega,\omega)$ is performed as an additional check, we recommend that the value of $\chi^{(3)}(-3\omega;\omega,\omega,\omega) = 0.58 \times 10^{-14}$ esu for BK-7 glass at $\lambda = 1907$ nm be used as the standard reference value.

Table 6-1. Fundamental and Third Harmonic Refractice Indices, Coherence Length, and

$\chi^{(3)}(-3\omega;\omega,\omega,\omega)$ of BK-7 Glass.

λ(nm)	n^{ω}	$n^{3\omega}$	l_c (μm)	$\chi^{(3)}(-3\omega;\omega,\omega,\omega)$ (10^{-14} esu)
2148	1.4925	1.5127	17.72	0.568
1907	1.4960	1.5150	16.72	0.580
1543	1.5008	1.5205	13.03	0.600
1064	1.5067	1.5382	5.63	0.635

Table 6-2. Comparison of Measured l_c, $\chi^{(3)}(-3\omega;\omega,\omega,\omega)$, and $<\gamma(-3\omega;\omega,\omega,\omega)>$ at 1064 nm for Several Common Liquids.

Liquid	$l_c(\mu m)$	$l_c(\mu m)$[a]	$\chi^{(3)}$ (10^{-14} esu)	$\chi^{(3)}$ [a]	$<\gamma>$ (10^{-36} esu)	$<\gamma>$ [a]
Acetone	6.90	6.86	0.586[b]	0.586	0.225	0.225
Methanol	8.45	8.41	0.386	0.373	0.106	0.104
DMF	4.42	4.43	0.792	0.696 (0.766)[c]	0.314	0.303[c]
Water	7.35	7.40	0.359	0.350	0.107	0.104
Cyclohexane	6.32	5.94	0.728	0.809	0.374	0.415
Cyclo-hexanone	5.86		0.788		0.378	

[a] From Kajzar and Messier, Phys. Rev. A32, 2352 (1985).

[b] Taken as reference.

[c] From Kajzar and Messier, Rev Sci. Instrum. 58, 2081 (1987).

Table 6-3. Fundamental and Third Harmonic Refractive Indices, Coherence Length, $\chi^{(3)}(-3\omega;\omega,\omega,\omega)$, and $<\gamma(-3\omega;\omega,\omega,\omega)>$ of Dioxane.

λ(nm)	n^ω	$n^{3\omega}$	l_c (μm)	$\chi^{(3)}(-3\omega;\omega,\omega,\omega)$ (10^{-14} esu)	$<\gamma(-3\omega;\omega,\omega,\omega)>$($10^{-36}$ esu)
2148	1.41	1.42	38.7	0.621	0.279
1907	1.41	1.42	32.7	0.643	0.289
1543	1.41	1.42	19.6	0.702	0.316
1064	1.41	1.44	6.4	0.738	0.327

Table 6-4. Fundamental and Third Harmonic Refractive Indices, Coherence Length, and $\chi^{(3)}(-3\omega;\omega,\omega,\omega)$ of HT.

λ(nm)	n^{ω}	$n^{3\omega}$	l_c (μm)	$\chi^{(3)}(-3\omega;\omega,\omega,\omega)$ (10^{-14} esu)
1907	1.48	1.51	11.7	2.25
1543	1.48	1.52	6.2	2.57
1064	1.48	1.63	1.18	4.55

Table 6-5. Experimental and Theoretical Values for $<\gamma(-3\omega;\omega,\omega,\omega)>$ of HT.

λ (nm)	Experiment (10^{-36} esu)	Theory (10^{-36} esu)
1907	1.04 ± 0.16	1.30
1543	1.18 ± 0.18	1.45
1064	1.94 ± 0.29	2.30

Table 6-6. Effect of Finite Beam Diameter on Ratio of Minimum to Maximum Maker Fringe Intensity.

$\Delta l / l_c$	I_{min} / I_{max}
0.25	0.01
0.50	0.05
0.75	0.12
1.00	0.22
1.25	0.35

Table 6-7. $\partial\chi^{(3)}(-3\omega;\omega,\omega,\omega) / \partial C$ and $<\gamma(-3\omega;\omega,\omega,\omega)>$ for β-carotene.

λ (nm)	$\partial\chi^{(3)}(-3\omega;\omega,\omega,\omega) / \partial C$ (10^{-12} esu)	$<\gamma(-3\omega;\omega,\omega,\omega)>$ (10^{-36} esu)
2148	0.098 ± 0.003	51.8 ± 1.3
1907	0.174 ± 0.004	92.0 ± 2.1
1543	0.49 ± 0.10	358 ± 64

215

Table 6-8. Measured Values for $\chi^{(3)}(-\omega_4;\omega_1,\omega_2,\omega_3)$ of BK-7 Glass Through Several

Nonlinear Optical Processes.

$\chi^{(3)}(-\omega_4;\omega_1,\omega_2,\omega_3)$ (10^{-14} esu)	Process	Reference[a]
0.58	DCSHG	Oudar
0.58	DCSHG	Levine and Bethea
0.53	DCSHG	Teng
0.52	Nondegenerate Three Wave Mixing	Adair *et al.*
0.50	Time-Resolved Interferometry	Milam and Weber
0.56	Ellipse Rotation	Hellwarth
1.17	THG	Buchalter and Meredith

a Complete references are given in the Chapter 6 References.

liquid compartment

BK-7   BK-7

teflon cap

aluminum frame

top view
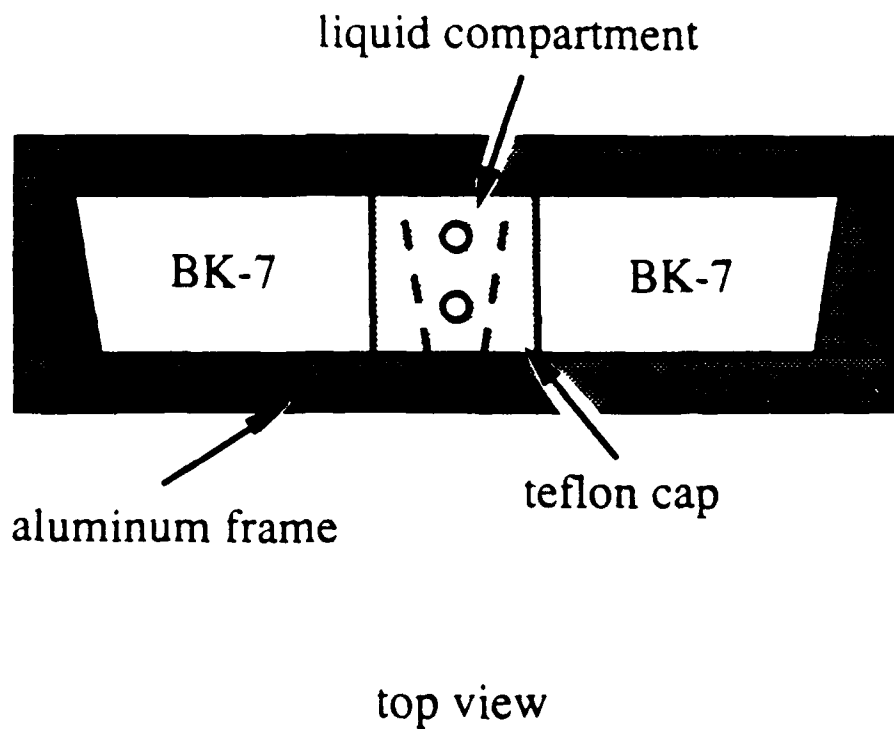
Figure 6-1. Illustration of the third harmonic generation (THG) liquid sample cell. The 5.0 cm long BK-7 glass windows eliminate the $\chi^{(3)}(-3\omega;\omega,\omega,\omega)$ contribution of air. The liquid compartment wedge angle α is 0.0125 rad with mean pathlength 0.44 mm.
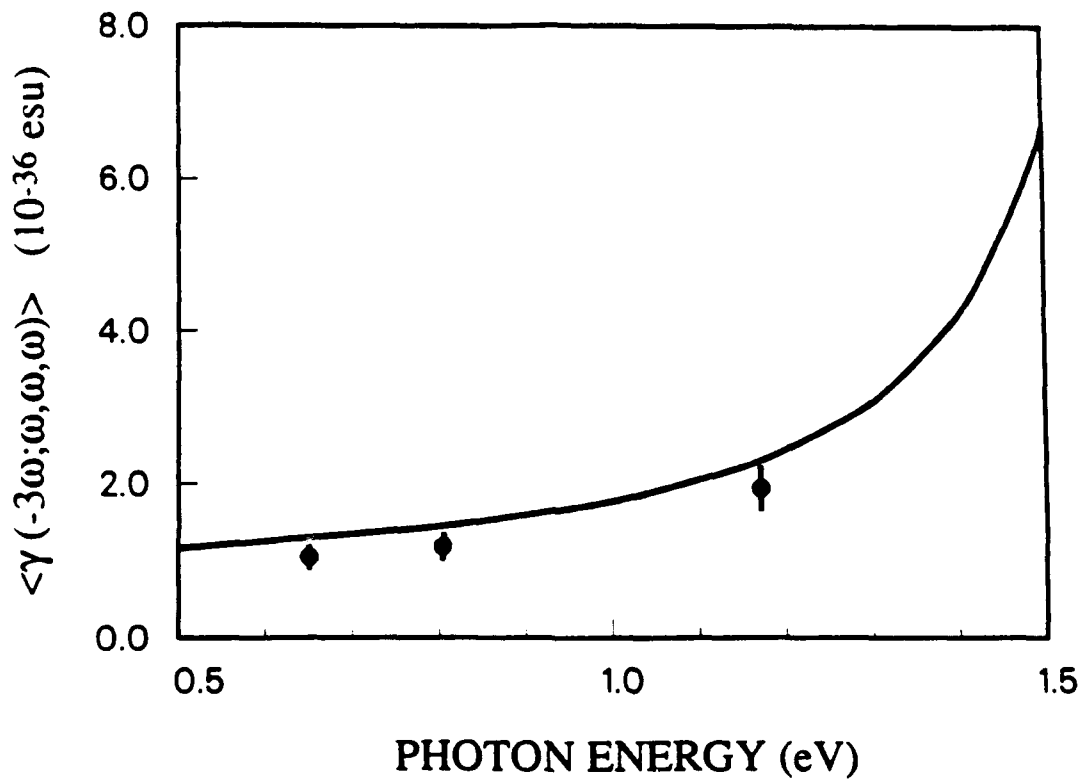
Figure 6-2. The experimentally determined values of $<\gamma(-3\omega;\omega,\omega,\omega)>$ for HT at $\lambda =$ 1907, 1543, and 1064 nm and the theoretical dispersion curve.
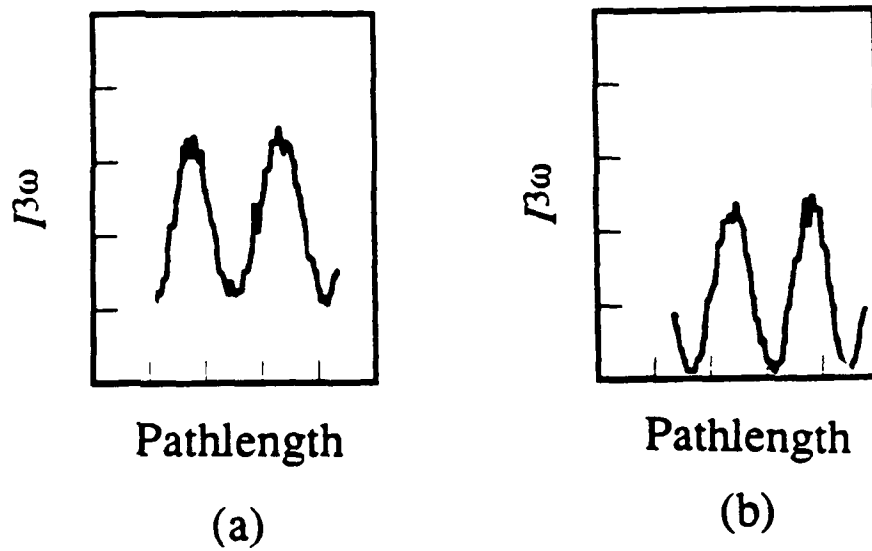
Figure 6-3. Sample THG Maker fringes for (a) HT and (b) acetone at $\lambda = 1064$ nm. The nonzero minimum in the case of the fringes for HT is due to the finite beam size effect. For HT, the coherence length $l_c = 1.18$ μm, while for acetone, $l_c = 6.6$ μm. The horizontal scale of (a) is expanded by a factor of 3 compared to (b) for clarity.
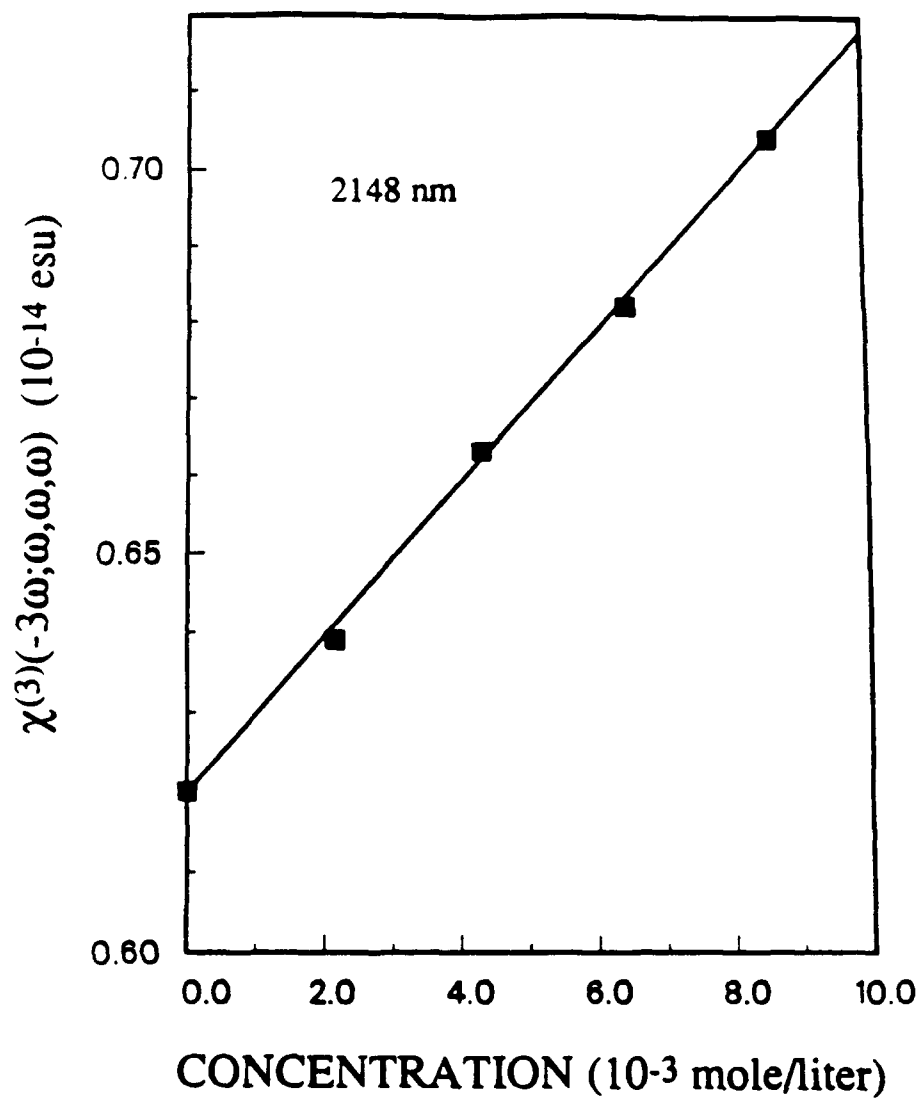
Figure 6-4. Concentration dependence of $\chi^{(3)}(-3\omega;\omega,\omega,\omega)$ for β-carotene in solution with dioxane at λ = 2148 nm.
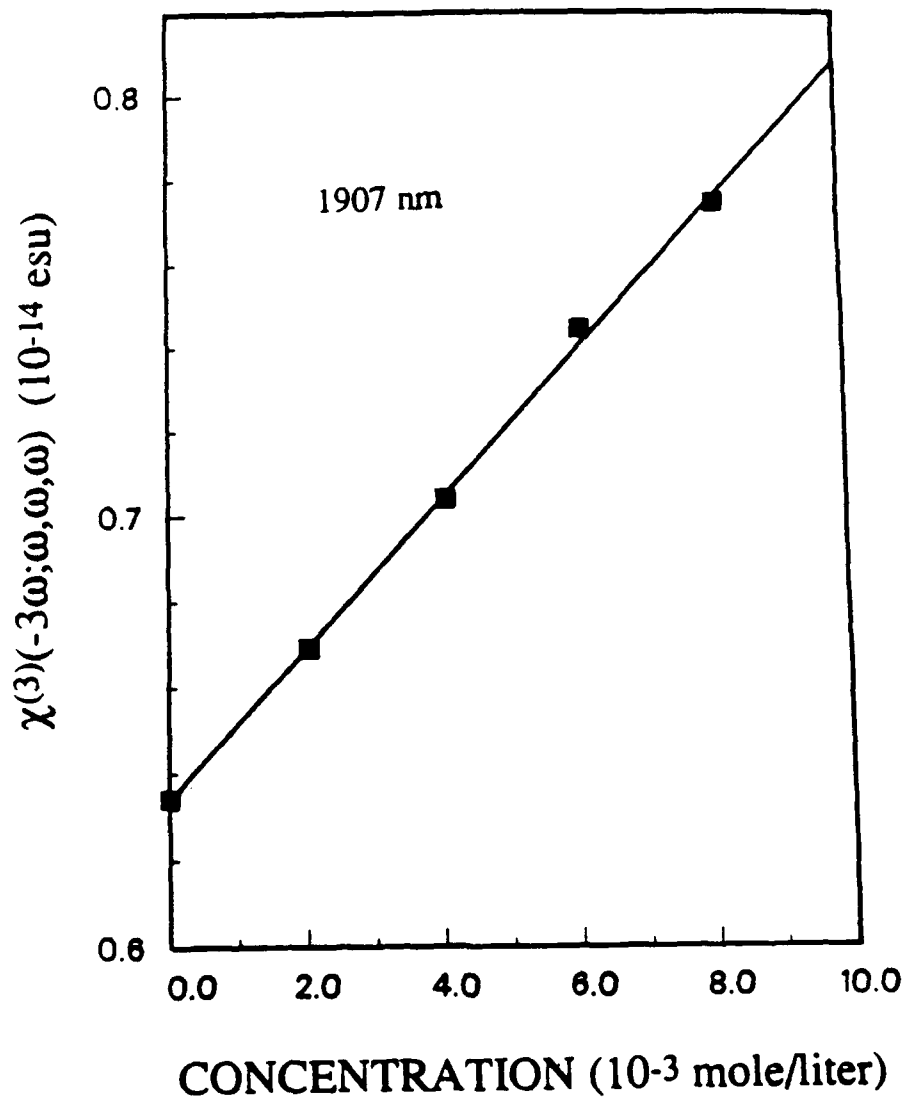
Figure 6-5. Concentration dependence of $\chi^{(3)}(-3\omega;\omega,\omega,\omega)$ for β-carotene in solution with dioxane at $\lambda = 1907$ nm.
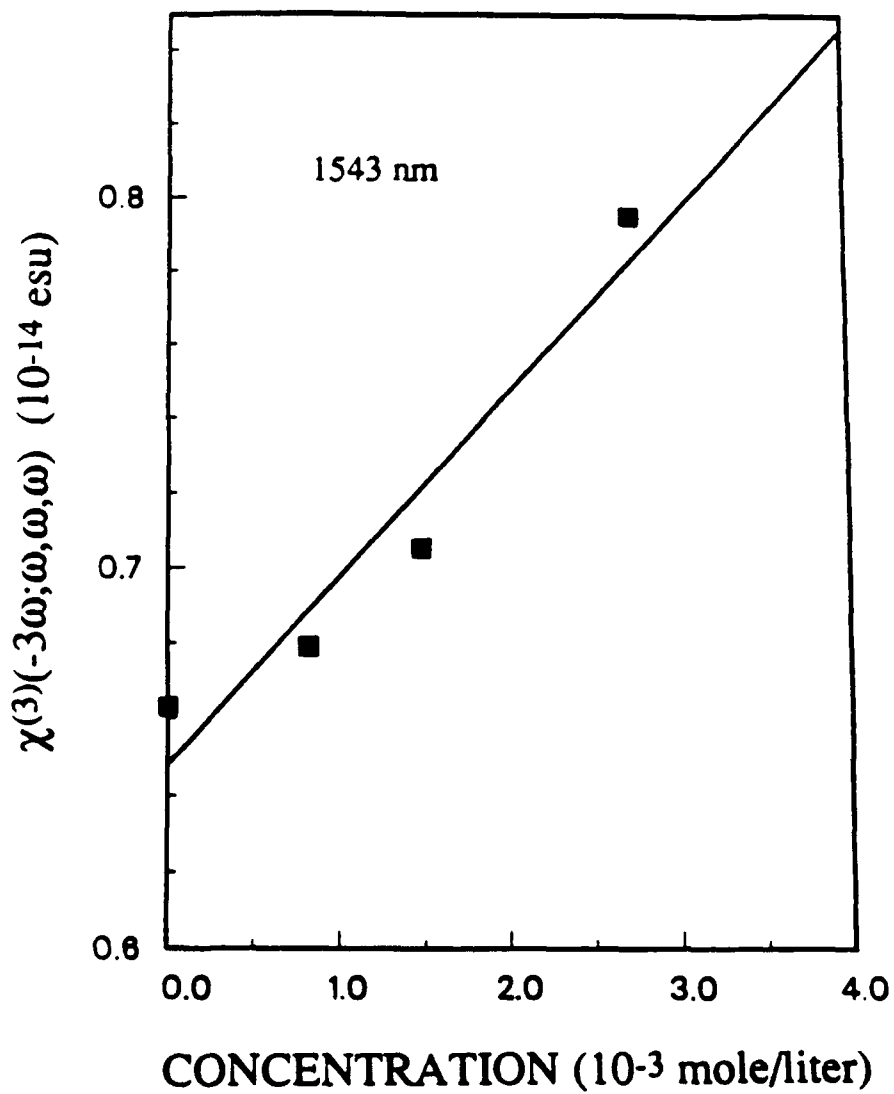
Figure 6-6. Concentration dependence of $\chi^{(3)}(-3\omega;\omega,\omega,\omega)$ for β-carotene in solution with dioxane at $\lambda = 1543$ nm.

222
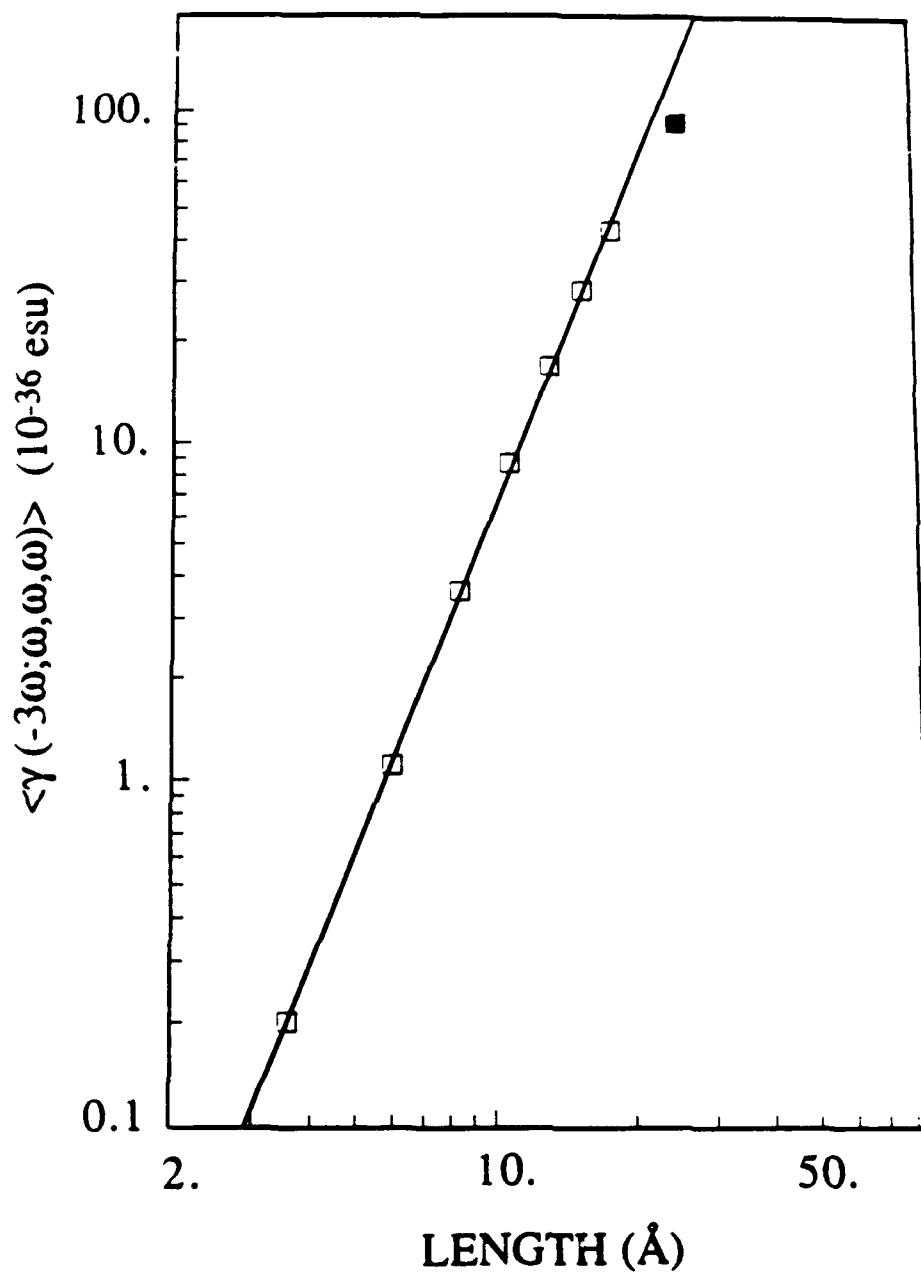
Figure 6-7. The experimental value of $<\gamma(-3\omega;\omega,\omega,\omega)>$ for β-carotene at $\lambda = 1907$ nm ($\hbar\omega = 0.65$ eV) (solid square) compared with the theoretical values for the $N = 4$ to 16 *trans* polyenes (open squares) as a function of chain length L. The β-carotene experimental value is in agreement with the theoretical power law dependence $<\gamma(-3\omega;\omega,\omega,\omega)> \propto L^{3.5}$ represented by the solid line.
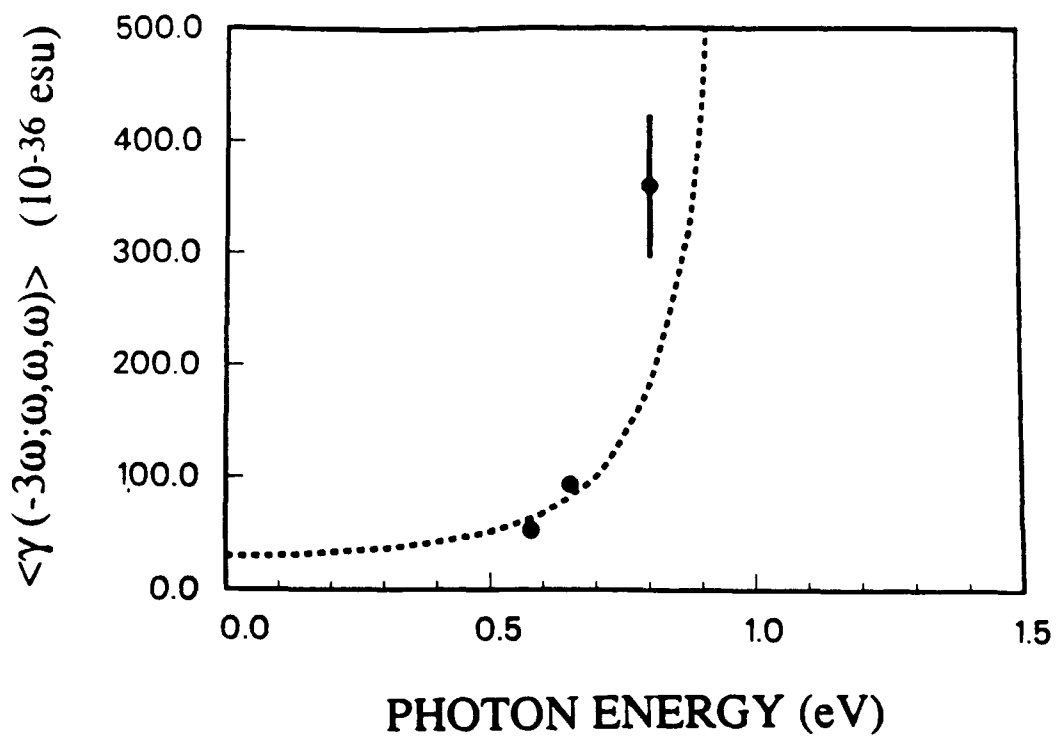
Figure 6-8. The experimentally determined values of $<\gamma(-3\omega;\omega,\omega,\omega)>$ for β-carotene at λ = 2148, 1907, and 1543 nm compared with a three-level model for the dispersion of $<\gamma(-3\omega;\omega,\omega,\omega)>$ of β-carotene (dashed curve).
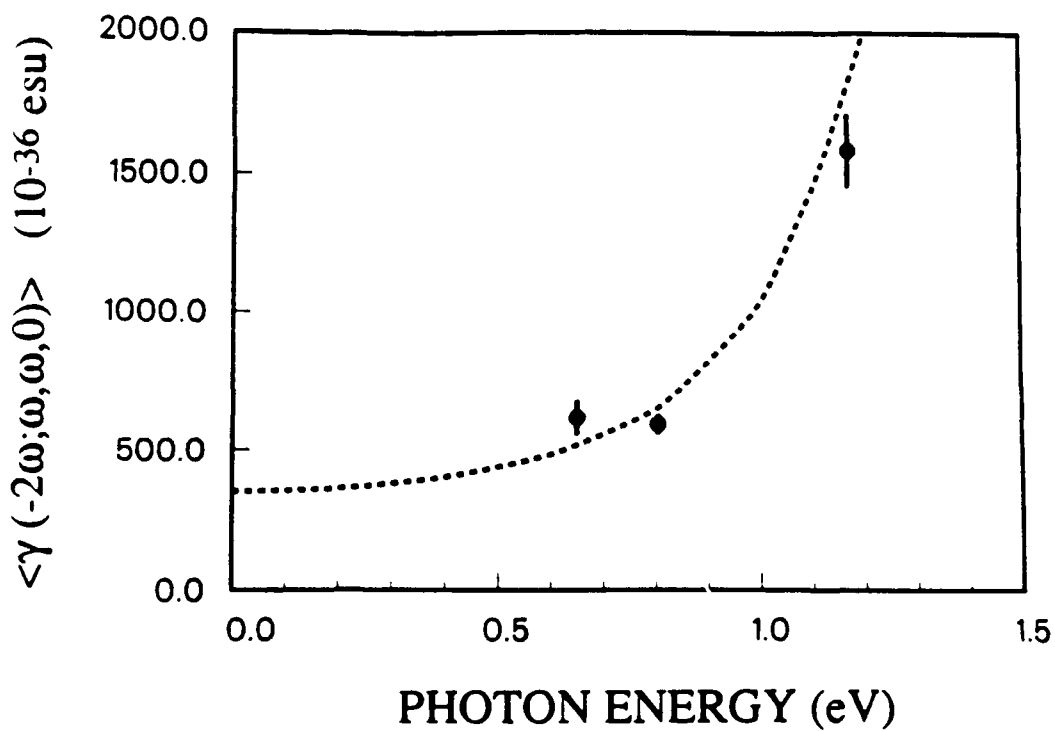
Figure 6-9. The experimentally determined values of $<\gamma(-2\omega;\omega,\omega,0)>$ for β-carotene at λ = 1907, 1543, and 1064 nm compared with a three-level model for the dispersion of $<\gamma(-2\omega;\omega,\omega,0)>$ of β-carotene (dashed curve).

Chapter 6 References

1. G. R. Meredith, B. Buchalter, and C. Hanzlik, J. Chem. Phys. **78**, 1533 (1983).

2. F. Kajzar and J. Messier, Phys. Rev. **A32**, 2352 (1985).

3. F. Kajzar and J. Messier, Rev. Sci. Instrum. **58**, 2081 (1987).

4. G. R. Meredith, B. Buchalter, and C. Hanzlik, J. Chem. Phys. **78**, 1543 (1983).

5. B. Buchalter and G. R. Meredith, Appl. Opt. **21**, 3221 (1982).

6. G. R. Meredith, Phys. Rev. **B24**, 5522 (1981).

7. J. L. Oudar, J. Chem. Phys. **67**, 446 (1977).

8. B. F. Levine and C. G. Bethea, J. Chem. Phys. **63**, 2666 (1975). The reported value has been multiplied by an additional factor of 3/2 to account for the more reliable value $d_{11} = 1.2 \times 10^{-9}$ for quartz that is now taken as the standard.

9. C. C. Teng, Ph.D. Thesis, University of Pennsylvania (1983).

10. R. Adair, L.L. Chase, and S. Payne, J. Opt. Soc. Am. **B4**, 875 (1987).

11. D. Milam and M. J. Weber, J. Appl. Phys. **47**, 2497 (1976).

12. R. W. Hellwarth, Prog. Quant. Elec. **5**, 1 (1977).

Chapter 7

CONCLUSION

We have presented a comprehensive theoretical and experimental study of the microscopic origin of nonresonant third order nonlinear optical processes in conjugated linear chains and demonstrated that electron correlation effects markedly determine the virtual excitation processes and third order nonlinear optical properties of these quasi-one dimensional structures. We first presented a detailed analysis of the molecular third order susceptibility $\gamma_{ijkl}(-\omega_4;\omega_1,\omega_2,\omega_3)$ in conjugated linear chains with a theoretical method that demonstrates the importance of electron correlation due to electron-electron repulsion. Many-electron calculations of $\gamma_{ijkl}(-\omega_4;\omega_1,\omega_2,\omega_3)$ of *trans* and *cis* polyenes reveal the primary role of strongly correlated, energetically high-lying, two-photon ^1A_g virtual states. For short polyene chains, $\gamma_{ijkl}(-\omega_4;\omega_1,\omega_2,\omega_3)$ is dominated by two competing third order virtual excitation processes that involve just three states. For the $N = 6$ site chain hexatriene, for example, the largest virtual excitation process, which makes a positive contribution to $\gamma_{ijkl}(-\omega_4;\omega_1,\omega_2,\omega_3)$, involves a previously unexpected, high-lying 5^1A_g state that is strongly coupled to the large oscillator strength 1^1B_u state and cannot be properly described by uncorrelated, independent particle models. This virtual process, together with a negative virtual process that involves only the 1^1B_u state and the 1^1A_g ground state, determines the sign, magnitude, and dispersion in this archetypal class of conjugated structures. The dominant tensor component of the susceptibility, $\gamma_{xxxx}(-\omega_4;\omega_1,\omega_2,\omega_3)$ with all electric fields polarized along the molecular

227

axis of the conjugation, has been discussed in terms of transition density matrix diagrams that graphically illustrate the large charge separation that occurs upon virtual excitation between the 1^1B_u state and the strongly correlated, high-lying 5^1A_g state.

The same basic mechanism for $\gamma_{ijkl}(-\omega_4;\omega_1,\omega_2,\omega_3)$ holds for all chain lengths calculated from $N = 4$ to 16. For chains of increased length, there are a larger number of virtual excitation processes that make a significant contribution to $\gamma_{xxxx}(-\omega_4;\omega_1,\omega_2,\omega_3)$; but, in all cases, there is always at least one important highly correlated, two-photon ^1A_g state. It is found that $\gamma_{xxxx}(-\omega_4;\omega_1,\omega_2,\omega_3)$ increases dramatically with chain length as evidenced, for example, by the calculated power law dependence of the dc-induced second harmonic susceptibility $\gamma_{xxxx}(-2\omega;\omega,\omega,0)$ on the number N of carbon atom sites in the chain with an exponent of 3.9 for the *trans* polyenes in the range $N = 4$ to 16. The supralinear chain length dependence of $\gamma_{xxxx}(-\omega_4;\omega_1,\omega_2,\omega_3)$ originates in the increased transition moments between the principal virtual states, the decreased excitation energies of those states, and the increased number of significant virtual excitation processes.

Comparison of calculations for the *cis* structural conformation of polyenes with results for the *trans* conformation demonstrates that the fundamental origin of $\gamma_{ijkl}(-\omega_4;\omega_1,\omega_2,\omega_3)$ remains basically the same, irrespective of the structural conformation. The only significant difference in the results for the two conformations is that, in all cases, the value of $\gamma_{xxxx}(-\omega_4;\omega_1,\omega_2,\omega_3)$ for a *cis* chain is smaller than that of the corresponding *trans* chain of the same number of sites. The results are unified by a power law dependence of $\gamma_{xxxx}(-\omega_4;\omega_1,\omega_2,\omega_3)$ on the physical end-to-end length of the chain L with an exponent of 3.5. The *cis* conformation results in a smaller L for a given

N than the *trans* conformation. Conformation affects $\gamma_{xxxx}(-\omega_4;\omega_1,\omega_2,\omega_3)$ only inasmuch as it affects the physical length of the chain. Furthermore, extrapolation of the power law dependence of $\gamma_{xxxx}(-\omega_4;\omega_1,\omega_2,\omega_3)$ on L indicates that the values of $\chi^{(3)}(-\omega_4;\omega_1,\omega_2,\omega_3)$ measured in conjugated polymers correspond to effective lengths of only 50 - 100 Å. We infer that $\gamma_{xxxx}(-\omega_4;\omega_1,\omega_2,\omega_3)$ must therefore deviate from the power law dependence and begin to saturate at a length shorter than 100Å.

Theoretical analysis of a noncentrosymmetric chain heteroatomically substituted with electron accepting groups on one chain end and an electron donating group on the other indicates that the lowered symmetry leads to more than an order of magnitude enhancement of $\gamma_{xxxx}(-\omega_4;\omega_1,\omega_2,\omega_3)$. In noncentrosymmetric structures, virtual excitation processes involving diagonal elements of the transition dipole moment matrix that are forbidden in centrosymmetric structures can contribute to $\gamma_{ijkl}(-\omega_4;\omega_1,\omega_2,\omega_3)$. In the case considered here, 1,1-dicyano-8-N,N-dimethylamino-1,3,5,7-octatetraene (NOT), the virtual excitation process that involves the dipole moment difference of the $2^1A'$ state (analog of the centrosymmetric polyene 1^1B_u state) and the ground state is much larger than even the analogs of the two dominant virtual excitation processes for the centrosymmetric chains and is responsible for the large enhancement of $\gamma_{xxxx}(-\omega_4;\omega_1,\omega_2,\omega_3)$.

Experimental measurements of the dispersion of the isotropically averaged dc-induced second harmonic susceptibility $\langle\gamma(-2\omega;\omega,\omega,0)\rangle$ and the third harmonic susceptibility $\langle\gamma(-3\omega;\omega,\omega,\omega)\rangle$ in two key polyene structures have demonstrated that the electron correlation theoretical description of the nonlinear optical properties of

conjugated linear chains is appropriate and quantitatively correct. The measured values of $<\gamma(-2\omega;\omega,\omega,0)>$ and $<\gamma(-3\omega;\omega,\omega,\omega)>$ at the fundamental wavelengths $\lambda = 1907$, 1543, and 1064 nm for hexatriene (HT), the $N = 6$ site chain, are in excellent quantitative agreement with the calculated magnitude, sign, and dispersion. For example, while the dispersion of $<\gamma(-2\omega;\omega,\omega,0)>$ is found to be weak in this wavelength region, experiment and theory are in agreement in the fact that $<\gamma(-3\omega;\omega,\omega,\omega)>$ at $\lambda = 1064$ nm is 1.8 times larger than the value at $\lambda = 1907$ nm. For β-carotene, a substituted, $N = 22$ site chain, the nonresonant experimental values of $<\gamma(-2\omega;\omega,\omega,0)>$ and $<\gamma(-3\omega;\omega,\omega,\omega)>$ are in agreement with extrapolation of the calculated power law dependence of $<\gamma(-\omega_4;\omega_1,\omega_2,\omega_3)>$ on chain length L. Thus, together with the results for HT, these measurements quantitatively validate the power law dependence on chain length L. Furthermore, based on our theoretical understanding of $\gamma_{ijkl}(-\omega_4;\omega_1,\omega_2,\omega_3)$, we developed a three-level model that adequately describes the experimentally measured dispersion of $<\gamma(-2\omega;\omega,\omega,0)>$ and $<\gamma(-3\omega;\omega,\omega,\omega)>$ for β-carotene.

In obtaining the experimental values of $<\gamma(-2\omega;\omega,\omega,0)>$ and $<\gamma(-3\omega;\omega,\omega,\omega)>$, we have given careful consideration to the values for $\chi^{(3)}(-\omega_4;\omega_1,\omega_2,\omega_3)$, the coherence lengths, and the fundamental and refractive indices of quartz, BK-7 glass, and dioxane that are required for the analysis. Each of these has been carefully measured at $\lambda = 1907$, 1543, and 1064 nm, and the results are presented in detail. In the course of these studies, it was found that the common reference standard for $\chi^{(3)}(-3\omega;\omega,\omega,\omega)$ of BK-7 glass was inconsistent with our results and with measurements of $\chi^{(3)}(-\omega_4;\omega_1,\omega_2,\omega_3)$ by other fundamental nonlinear optical processes. The common reference value was found

to be too large by a factor of 2.0, and an improved reference standard has been proposed.

Finally, the work presented in this report has recently lead to a novel fundamental development in nonlinear optical processes. In general, the real population of the initial state for the virtual electronic excitations can be either the usual singlet ground state S_0, or an optically pumped excited state S_n. This report deals strictly with the case of S_0 ground state population. We have have found, however, that for quasi-one and quasi-two dimensional chain-like and disc-like structures, compared to the ground state, the nonresonant $\gamma_{ijkl}^{S_n}(-\omega_4;\omega_1,\omega_2,\omega_3)$ and second order susceptibility $\beta_{ijk}^{S_n}(-\omega_3;\omega_1,\omega_2)$ can markedly increase, or even change sign, when the first (S_1) or second (S_2), π-electron excited state is optically pumped and then populated for timescales sufficiently long to allow nonresonant measurements of $\gamma_{ijkl}^{S_n}(-\omega_4;\omega_1,\omega_2,\omega_3)$ and $\beta_{ijk}^{S_n}(-\omega_3;\omega_1,\omega_2)$.[1-3] The enhanced magnitude has three principal origins: smaller transition energies $\hbar\omega_{mS_n}$ between the populated state S_n and intermediate virtual states m, many additional accessible virtual excited states with large transition dipole moments, and a larger number of significant virtual excitation processes with a reduced degree of cancellation. These new excited state nonlinear optical processes are currently under extensive experimental and theoretical investigation and will continue into the forseeable future. The microscopic understanding of excited state nonlinear optical processes is based upon the developments for ground state nonlinear optical processes presented in this report.

Chapter 7 References

1. J. R. Heflin, Q. L. Zhou, K. Y. Wong, O. Zamani-Khamiri, and A. F. Garito, Proc. SPIE (1990).

2. Q. L. Zhou, J. R. Heflin, K. Y. Wong, O. Zamani-Khamiri, and A. F. Garito, Phys. Rev. A (in press); and in *Organic Molecules for Nonlinear Optics and Photonics*, F. Kajzar and J. Messier, eds. (NATO ASI, Brussels, 1990).

3. A. F. Garito, OSA Annual Meeting 1989, Technical Digest Series, Vol. **18** (Optical Society of America, Washington, D.C., 1989) p. 22.

Appendix A

COMPARISON OF COMMON

CONVENTIONS FOR $\gamma_{ijkl}(-\omega_4;\omega_1,\omega_2,\omega_3)$

Comparison of theoretical and experimental values for $\gamma_{ijkl}(-\omega_4;\omega_1,\omega_2,\omega_3)$ reported by various authors is complicated by the lack of a universally accepted definition of $\gamma_{ijkl}(-\omega_4;\omega_1,\omega_2,\omega_3)$. In this appendix, we discuss the most common conventions employed for $\gamma_{ijkl}(-\omega_4;\omega_1,\omega_2,\omega_3)$ and relate them to the definition used in this work.

The definition of $\gamma_{ijkl}(-\omega_4;\omega_1,\omega_2,\omega_3)$ is fully specified by the constitutive equation for the nonlinear polarization combined with the convention for the electric field amplitudes. Throughout this report, we have employed the constitutive equation

$$p_i^{\omega_4} = \gamma_{ijkl}(-\omega_4;\omega_1,\omega_2,\omega_3)\, E_j^{\omega_1}\, E_k^{\omega_2}\, E_l^{\omega_3} \qquad (A.1)$$

where the electric field Fourier amplitudes are defined through

$$E_j(t) = \sum_n E_j^{\omega_n} \cos \omega_n t \qquad (A.2)$$

With these definitions, the susceptibilities $\gamma_{ijkl}(-\omega_4;\omega_1,\omega_2,\omega_3)$ for different third order processes (*e.g.* different sets $\{\omega_1, \omega_2, \omega_3\}$) are related in the $\omega \rightarrow 0$ (dispersionless)

limit by the multiplicative factor (c.f. Eq. (2.41)) $K(-\omega_4;\omega_1,\omega_2,\omega_3) = 2^{-m} D$ where m is

the number of nonzero input frequencies minus the number of nonzero output

frequencies and D is the number of distinguishable orderings of the set $\{\omega_1, \omega_2, \omega_3\}$.

The origin of $K(-\omega_4;\omega_1,\omega_2,\omega_3)$ is intuitively illustrated through consideration of the

cube of an optical electric field of amplitude E_i^ω and a dc field of amplitude E_i^0:

$$(E_i^\omega \cos \omega t + E_i^0)^3 = \tfrac{1}{4}(E_i^\omega)^3 \cos 3\omega t + \tfrac{3}{2}(E_i^\omega)^2 E_i^0 \cos 2\omega t$$
$$+ [\tfrac{3}{4}(E_i^\omega)^3 + 3E_i^\omega(E_i^0)^2] \cos \omega t + [\tfrac{3}{2}(E_i^\omega)^2 E_i^0 + (E_i^0)^3] \ . \quad (A.3)$$

Thus, $K(-2\omega;\omega,\omega,0) = 3/2$, $K(-3\omega;\omega,\omega,\omega) = 1/4$, and

$\gamma_{ijkl}(-2\omega;\omega,\omega,0) = 6\,\gamma_{ijkl}(-3\omega;\omega,\omega,\omega)$.

We now list the other common conventions:

1)   Orr and Ward[1]:

The constitutive equation

$$p_i^{\omega_4} = K(-\omega_4;\omega_1,\omega_2,\omega_3)\,\chi_{ijkl}^{(3)}(-\omega_4;\omega_1,\omega_2,\omega_3)\,E_j^{\omega_1}\,E_k^{\omega_2}\,E_l^{\omega_3} \qquad (A.4)$$

is used and the electric field Fourier amplitudes are defined as in Eq. (A.2). The symbol

$\chi^{(3)}$ rather than γ is used by these authors to denote the molecular third order

susceptibility. Since $K(-\omega_4;\omega_1,\omega_2,\omega_3)$ is excluded from $\chi_{ijkl}^{(3)}(-\omega_4;\omega_1,\omega_2,\omega_3)$ in this

234

notation, $\chi^{(3)}_{ijkl}(-\omega_4;\omega_1,\omega_2,\omega_3)$ is equal for all third order processes in the $\omega \to 0$ limit.

$\chi^{(3)}_{ijkl}(-\omega_4;\omega_1,\omega_2,\omega_3)$ is related to our definition of $\gamma_{ijkl}(-\omega_4;\omega_1,\omega_2,\omega_3)$ by

$$K(-\omega_4;\omega_1,\omega_2,\omega_3) \, \chi^{(3)}_{ijkl}(-\omega_4;\omega_1,\omega_2,\omega_3) \; = \; \gamma_{ijkl}(-\omega_4;\omega_1,\omega_2,\omega_3) \qquad (A.5)$$

In particular, we have $\gamma_{ijkl}(-2\omega;\omega,\omega,0) = \frac{3}{2}\chi^{(3)}_{ijkl}(-2\omega;\omega,\omega,0)$ for the measurements of Ward and Elliott.[2]

2)   Kajzar and Messier,[3] Meredith *et al.*,[4] and Hermann and Ducuing:[5]

These authors use Eq. (A.1) for the third harmonic susceptibility $\gamma^{K\text{-}M}_{ijkl}(-3\omega;\omega,\omega,\omega)$, but the electric field Fourier amplitudes are defined as

$$E_j(t) \; = \; \sum_n \; (E^{\omega_n}_j \, e^{-i\omega_n t} + \text{complex conjugate}) \,. \qquad (A.6)$$

We then have

$$\gamma^{K\text{-}M}_{ijkl}(-3\omega;\omega,\omega,\omega) \; = \; 4 \, \gamma_{ijkl}(-3\omega;\omega,\omega,\omega) \qquad (A.7)$$

since the field amplitudes in Eq. (A.6) are defined as only half as large as those in Eq. (A.2). We further point out that the reference values for $\chi^{(3)}(-3\omega;\omega,\omega,\omega)$ of glass and

silica in refs. 3 and 4 were found to be too large by a factor of 2.0 as discussed in section 6.E, and this must also be included for comparison with our results.

3)   Levine and Bethea[6] and Oudar:[7]

$\gamma_{ijkl}(-2\omega;\omega,\omega,0)$ is defined in the same manner as in the present work.

4)   Maker and Terhune:[8]

The macroscopic susceptibility $c_{1111}(-3\omega;\omega,\omega,\omega)$ of these authors is equivalent to our $\chi^{(3)}_{1111}(-3\omega;\omega,\omega,\omega)$, but for degenerate four wave mixing

$$3\, c_{1111}(-\omega;\omega,-\omega,\omega) = \chi^{(3)}_{1111}(-\omega;\omega,-\omega,\omega) \,. \qquad (A.8)$$

5)   Hellwarth, Owyoung, and George:[9]

The electronic contribution to the nonlinear polarization is denoted by σ and is related to our convention by

$$\sigma_{ijkl} = 8\, \gamma_{ijkl}(-3\omega;\omega,\omega,\omega) \,. \qquad (A.9)$$

6)   Soos and Ramasesha:[10]

Inspection of the summation-over-states expression for $\gamma_{ijkl}(-3\omega;\omega,\omega,\omega)$ used by these authors yields

$$2\, \gamma_{ijkl}^{\text{S-R}}(-3\omega;\omega,\omega,\omega) \;=\; \gamma_{ijkl}(-3\omega;\omega,\omega,\omega) \;. \tag{A.10}$$

7)   Finite-field calculations:[11-13]

The third order susceptibility is determined according to

$$W(E) \;=\; W(0) \;-\; \mu_i\, E_i \;-\; \tfrac{1}{2}\alpha_{ij}\, E_i\, E_j$$
$$-\; \tfrac{1}{6}\beta_{ijk}\, E_i\, E_j\, E_k \;-\; \tfrac{1}{24}\gamma_{ijkl}\, E_i\, E_j\, E_k\, E_l \;-\; ... \tag{A.11}$$

where $W(E)$ is the energy of the system in the presence of a static field of amplitude E.

By this definition

$$\gamma_{ijkl} \;=\; 6\, K(-\omega_4;\omega_1,\omega_2,\omega_3)\, \gamma_{ijkl}(-\omega_4;\omega_1,\omega_2,\omega_3) \;. \tag{A.12}$$

237

Appendix A References

1. B. J. Orr and J. F. Ward, Mol. Phys. **20**, 513 (1971).

2. J. F. Ward and D. S. Elliott, J. Chem. Phys. **69**, 5438 (1978).

3. F. Kajzar and J. Messier, Phys. Rev. **A32**, 2352 (1985); Rev. Sci. Instrum. **58**, 2081 (1987).

4. G. R. Meredith, B. Buchalter, and C. Hanzlik, J. Chem. Phys. **78**, 1533 (1983).

5. J. P. Hermann and J. Ducuing, J. Appl. Phys. **45**, 5100 (1974).

6. B. F. Levine and C. G. Bethea, J. Chem. Phys. **63**, 2666 (1975).

7. J. L. Oudar, J. Chem. Phys. **67**, 446 (1977).

8. P. D. Maker and R. W. Terhune, Phys. Rev. **137**, A801 (1965).

9. R. W. Hellwarth, A. Owyoung, and N. George, Phys. Rev. **A4**, 2342 (1971).

10. Z. G. Soos and S. Ramasesha, Chem. Phys. Lett. **153**, 171 (1988); J. Chem. Phys. **90**, 1067 (1989).

11. M. G. Papadopolous, J. Waite, and C. A. Nicolaides, J. Chem. Phys. **77**, 2527 (1982).

12. C. P. de Melo and R. Silbey, J. Chem. Phys. **88**, 2567 (1988).

13. G. J. B. Hurst, M. Dupuis, and E. Clementi, J. Chem. Phys. **89**, 385 (1988).

.

Appendix B

ISOTROPIC ORIENTATIONAL

AVERAGE OF $\gamma_{ijkl}(-\omega_4;\omega_1,\omega_2,\omega_3)$

Chapters 5 and 6 of this report present liquid phase experimental measurements of dc-induced second harmonic generation (DCSHG) and third harmonic generation (THG) for two important conjugated molecular structures. In each of the experiments, the output and all three of the input electric fields are in the same direction in the laboratory coordinate frame, which we will refer to as X. Since the molecules in a liquid are randomly distributed in direction, we must perform an isotropic average of the molecular susceptibility $\gamma_{ijkl}(-\omega_4;\omega_1,\omega_2,\omega_3)$, where lowercase subscripts denote the molecular coordinate frame, to relate it to the measured laboratory frame quantity, which we will write as $\langle\gamma_{XXXX}(-\omega_4;\omega_1,\omega_2,\omega_3)\rangle$, or simply $\langle\gamma(-\omega_4;\omega_1,\omega_2,\omega_3)\rangle$.

The isotropic average is performed by integration of the randomly oriented molecular tensor quantity γ_{ijkl} projected onto the laboratory coordinate frame to obtain $\langle\gamma_{XXXX}\rangle$, where we have omitted the frequency arguments to simplify the notation. For the general case,

$$\langle\gamma_{IJKL}\rangle = \frac{1}{8\pi^2}\int_0^{2\pi}d\phi\int_0^{\pi}\sin\theta\,d\theta\int_0^{2\pi}d\varphi\; R_{Ii}R_{Jj}R_{Kk}R_{Ll}\;\gamma_{ijkl}$$

$$= \sum_{ijkl}\langle\gamma_{ijkl}\,R_{Ii}\,R_{Jj}\,R_{Kk}\,R_{Ll}\rangle \tag{B.1}$$

where the rotation matrix R is given by

$$
R = \begin{pmatrix}
\cos\phi\cos\theta\cos\varphi & \sin\phi\cos\theta\cos\varphi & -\sin\theta\cos\varphi \\
-\sin\phi\sin\varphi & +\cos\theta\sin\varphi & \\
& & \\
-\cos\phi\cos\theta\sin\varphi & -\sin\phi\cos\theta\sin\varphi & \sin\theta\sin\varphi \\
-\sin\phi\cos\varphi & +\cos\phi\cos\varphi & \\
& & \\
\cos\phi\sin\theta & \sin\phi\sin\theta & \cos\theta
\end{pmatrix} . \qquad (B.2)
$$

We note that, by the symmetry conditions for R, $< \gamma_{ijkl} R_{Ii} R_{Jj} R_{Kk} R_{Ll} >$ vanishes for every subscript set $\{ijkl\}$ that has an odd number of any one coordinate.

We now evaluate $<\gamma_{XXXX}>$. Consider, for exmple, the contribution of γ_{zzzz}. One obtains

$$
< \gamma_{zzzz} R_{Xz} R_{Xz} R_{Xz} R_{Xz} > = \frac{\gamma_{zzzz}}{8\pi^2} \int_0^{2\pi} d\phi \int_0^{\pi} \sin\theta \, d\theta \int_0^{2\pi} d\varphi \cos^4\phi \sin^4\theta
$$

$$
= \frac{\gamma_{zzzz}}{8\pi^2} (2\pi) \int_0^{2\pi} \cos^4\phi \, d\phi \int_0^{\pi} \sin^5\theta \, d\theta
$$

$$
= \frac{\gamma_{zzzz}}{8\pi^2} \left(\frac{3\pi}{4}\right) \left(\frac{16}{15}\right)
$$

$$
= \frac{\gamma_{zzzz}}{5} . \qquad (B.3)
$$

Similarly, one finds

$$< \gamma_{xxxx} R_{Xx} R_{Xx} R_{Xx} R_{Xx} > = \frac{\gamma_{xxxx}}{5} \qquad \text{(B.4)}$$

and

$$< \gamma_{yyyy} R_{Xy} R_{Xy} R_{Xy} R_{Xy} > = \frac{\gamma_{yyyy}}{5} \qquad . \qquad \text{(B.5)}$$

Now consider the contribution of γ_{yyzz} to $<\gamma_{XXXX}>$. We must evaluate

$$< \gamma_{yyzz} R_{Xy} R_{Xy} R_{Xz} R_{Xz} > = \frac{\gamma_{yyzz}}{8\pi^2} \int_0^{2\pi} d\phi \int_0^{\pi} \sin\theta \, d\theta \int_0^{2\pi} d\varphi$$

$$(-\cos\phi\cos\theta\sin\varphi - \sin\phi\cos\varphi)^2 \, (\cos\phi\sin\theta)^2 . \qquad \text{(B.6)}$$

The final result is

$$< \gamma_{yyzz} R_{Xy} R_{Xy} R_{Xz} R_{Xz} > = \frac{\gamma_{yyzz}}{15} , \qquad \text{(B.7)}$$

and similar results are obtained for all other subscript sets $\{ijkl\}$ that involve two different pairs of subscripts x, y, or z in any order. The isotropically averaged susceptibility can thus be expressed in the compact notation

$$<\gamma> = \frac{1}{5} \Big[\sum_i \gamma_{iiii} + \frac{1}{3} \sum_{i \neq j} (\gamma_{iijj} + \gamma_{ijij} + \gamma_{ijji}) \Big] . \qquad \text{(B.8)}$$

•

241

Index